IR spectro-electrochemistry of an adsorbed oxygen-tolerant [NiFe] hydrogenase on conductive surfaces

vorgelegt von

Diplom-Chem.

Nina Heidary

geb. in Shiraz

von der Fakultät II - Mathematik und Naturwissenschaften

der Technischen Universität Berlin

zur Erlangung des akademischen Grades

Doktor der Naturwissenschaften

- Dr. rer. nat. -

genehmigte Dissertation

Promotionsausschuss:

Vorsitzender:	Prof. Dr. Schomäcker
Gutachterin:	Prof. Dr. Anna Fischer
Gutachter:	Prof. Dr. Peter Hildebrandt
Gutachterin:	Prof. Dr. Ulla Wollenberger

Tag der wissenschaftlichen Aussprache: 15. Dezember 2016

Berlin 2017

Contents

Abstract **i**

Zusammenfassung **iii**

List of Publications in Peer-Reviewed Journals **v**

Parts of this work are published in the following articles v

Related Publications v

Other publications v

Selected Talks **vii**

Selected Posters **vii**

Danksagung **ix**

Abbreviations **xi**

1 Motivation and Concepts **1**

2 Theoretical Background **3**

2.1 Metalloproteins 4

2.1.1 [NiFe] - Hydrogenases 4

2.1.2 Cytochrome c 11

2.2 Spectroscopic Techniques 12

2.2.1 Theory of Vibrational Spectroscopy 12

2.2.2 Fourier Transform Infrared Spectroscopy 17

2.2.3 UV-Vis Spectroscopy 26

2.2.4 Semiconductor 26
2.3 Transparent Conducting Oxides (TCO) 28
2.3.1 Theoretical Background of TCO's 28
2.3.2 Application / TCO examples 31
2.3.3 Tin-rich Indium Tin Oxide (ITO_{TR}) 31
2.3.4 Tin-doped Antimony Oxide (ATO) 33
2.4 Electrode Interfaces 33
2.4.1 Metal Electrode-Electrolyte Interfaces 33
2.4.2 Self Assembeled Monolayer (SAM) 35
2.4.3 Electrochemistry on Semiconductors 35
2.4.4 Heterogeneous Electron Transfer 39
2.4.5 Protein Film Electrochemistry (PFE) 39
2.5 Microscopic Methods 41
2.5.1 Scanning Electron Microscope 41
2.5.2 Atomic Force Microscope 43

3 Experimental Details **44**

3.1 Chemicals and Preparation Tools 45
3.1.1 Buffer solutions 45
3.1.2 D_2O-buffer 46
3.2 Protein Purification 46
3.2.1 Membrane-Bound Hydrogenase from *Ralstonia eutropha* 46
3.2.2 Cytochrome C 46
3.3 Instrumentation 47
3.3.1 UV-Vis measurements 47
3.3.2 FTIR – Transmission studies 47
3.3.3 Spectro-electrochemical set-up configurations 47
3.4 Protein Sample Preparation 51
3.4.1 Formation of Self-Assembled Monolayer (SAM) on gold electrodes 51
3.4.2 Immobilization conditions of the MBH heterodimer 51

3.4.3 Immobilization of cytochrome c . . . 52
3.4.4 Mediator experiments . . . 52
3.4.5 H-D exchange . . . 52
3.4.6 Desorption studies . . . 53
3.4.7 Electrochemistry . . . 53
3.5 Surface Characterization . . . 53
3.5.1 Conductivity Measurements . . . 53
3.5.2 SEM . . . 54
3.5.3 AFM . . . 54
3.5.4 Ellipsometry . . . 54
3.5.5 Mass spectrometer . . . 54
3.6 Spectra Calculation and Data Processing . . . 54

4 Spectro-electrochemical studies on Membrane-Bound [NiFe] Hydrogenase of Ralstonia eutropha on biocompatible gold electrodes 56

4.1 Introduction . . . 57
4.1.1 Heterogeneous Catalysis . . . 57
4.1.2 Enzyme Adsorption . . . 57
4.1.3 Membrane-Bound [NiFe] Hydrogenase of *Ralstonia eutropha* . . . 58
4.2 Spectro-electrochemical insights into adsorption behavior of the heterodimeric *Re* MBH . . . 61
4.2.1 Probing electrocatalytic efficencies of MBH . . . 61
4.2.2 Surface-Enhanced Infrared Absorption Spectroscopy on adsorbed MBH . 64
4.2.3 MBH coverage determination via Atomic Force Microscopy . . . 73
4.2.4 Summary . . . 75
4.2.5 Conclusions . . . 77
4.3 *Strep*-MBH Orientation . . . 79
4.3.1 Molecular Dynamics Simulation . . . 79
4.3.2 Interaction Energy Landscapes for *strep*-tagged MBH binding . . . 79
4.3.3 MBH orientation on C_6NH_2- Interface . . . 81

4.3.4 MBH orientation on C_5COOH - Interface 84
4.3.5 MBH orientation on C_5COOH/C_6OH - Interface 87
4.3.6 MBH orientation on C_5CH_3- Interface 90
4.3.7 DFT Calculations 92
4.3.8 Conclusions 93
4.4 Mechanistic Impact into MBH 96
4.4.1 Adsorbed MBH under Turnover Conditions 96
4.4.2 Potential Dependent Spectral Changes 98
4.4.3 Oxidation of *strep*-MBH 102
4.4.4 Conclusions and Outlook 103

5 Spectro-electrochemical studies on Cytochrome c - Metal oxide surface interactions 105

5.1 Introduction 107
5.1.1 Immobilization Strategies 107
5.1.2 Protein Denaturation 109
5.2 Antimony-doped Tin Oxide (ATO) thin film electrodes for a stable horse heart Cytochrome c immobilization 111
5.2.1 Reference measurement 112
5.2.2 ATO thin film preparation and characterization 112
5.2.3 Immobilization of horse heart Cytochrome c and his-tagged Cytochrome c on ATO 113
5.2.4 Band assignment of Cytochrome c adsorbed on ATO 116
5.2.5 Conclusions 117
5.3 Tin-rich Indium Tin Oxide (ITO_{TR}) thin film electrodes for his-tagged horse heart Cytochrome c - immobilization strategy 119
5.3.1 Introduction 119
5.3.2 ITO_{TR} thin film preparation and characterization 120
5.3.3 Immobilization of horse heart Cytochrome c and his-tagged Cytochrome c on ITO_{TR} 122
5.3.4 Band assignment of Cytochrome c on ITO_{TR} 126
5.3.5 Conclusion 128

6 Spectro-electrochemical insights into Membrane-Bound [NiFe] Hydrogenase of Ralstonia eutropha on ITO_{TR} electrodes **129**

6.1 Introduction . . . 131

6.2 Adsorption behavior of his-tagged MBH on ITO_{TR} . . . 132

6.2.1 ATR-FTIR on his-tagged MBH on ITO_{TR} . . . 132

6.2.2 AFM studies on his-tagged MBH coverage . . . 134

6.2.3 Desorption experiments of his-tagged MBH on ITO_{TR} . . . 136

6.2.4 Conclusions . . . 136

6.2.5 Under turnover conditions . . . 137

6.2.6 Hydrogen production of hydrogenases . . . 144

6.2.7 His-tagged MBH - semiconductor interface . . . 145

6.2.8 Effect of H_2 on ITO_{TR}-MBH hybrid electrode – Enhanced HER activity 147

6.2.9 Hydrogen affinity towards ITO_{TR}surfaces . . . 148

6.2.10 Shift of the hydrogenases onset potential . . . 148

6.2.11 Reference experiments . . . 151

6.2.12 Preactivation of his-tagged MBH on ITO_{TR} . . . 155

6.2.13 ITO_{TR}stability for electrochemical studies . . . 155

6.2.14 Conclusions . . . 157

6.3 Adsorption behavior of *strep*-tagged MBH on ITO_{TR} . . . 158

6.3.1 ATR-IR studies of immobilized *strep*-tagged MBH on ITO_{TR} . . . 158

6.3.2 Preactivation of *strep*-tagged MBH on ITO_{TR} . . . 160

6.3.3 Conclusions . . . 161

7 Comparison of adsorbed protein on Au-SEIRA and ITO_{TR}-ATR electrodes 163

7.1 Comparisons of spectro-electrochemical surfaces used for Cytochrome c . . . 165

7.2 Comparison of electrode surfaces suitable for spectro-electrochemical studies on Membrane-Bound [NiFe] Hydrogenase from *Re* . . . 166

7.3 Conclusions . . . 170

Bibliography **170**

A Appendix **197**

Abstract

Hydrogenases are metalloenzymes, catalyzing the reversible oxidation of molecular hydrogen into two protons and two electrons. The 'Knallgasbacterium' *Ralstonia eutropha* H16 (*Re*) is one of the few examples, harboring several [NiFe] hydrogenases that established mechanisms to enable catalytic conversion of H_2 in the presence of O_2. In order to exploit the catalytic potential of these oxygen-tolerant hydrogenases, also in view of possible biotechnological applications in biofuel cells, an efficient electronic communication between the enzyme and electrically conducting surface is required. Hence, for optimum performance, an in-depth understanding of the enzyme-surface interactions is needed.

This thesis presents an interdisciplinary approach providing detailed insights into the adsorption parameters of heterodimeric membrane-bound [NiFe] hydrogenase (MBH) species of *Re* on various electrode materials. The first part of this thesis is dedicated to the adsorption studies of oxygen-tolerant MBH onto biocompatibly coated Au electrodes by protein film voltammetry (PFV), surface enhanced IR absorption (SEIRA) spectro-electrochemistry, atomic force microscopy (AFM), and ellipsometry in order to elucidate the enzymes catalytic activity, structure, integrity, and surface coverage. Results were obtained for charged and hydrophobic surfaces. Electrocatalytic efficiencies allowed correlationa with the mode of protein adsorption on the electrode, which provided valuable insights in the orientational configuration. These findings were complemented by molecular dynamics (MD) simulations as well as density functional theory (DFT) calculationa, carried out in collaboration. Hence, different orientational configurations are proposed, discussing the different accessible binding anchors of the MBH., and experimentally could be verified by SEIRA spectro-electrochemical investigations. The obtained results suggested that, in particular, an immobilization of heterodimeric MBH on slightly negatively charged surfaces is most beneficial for an efficient interfacial electron transfer (ET). Hereby, the suggested anchoring via the isolated transmembrane helix still allows a flexibility regarding rotational and translational motions of the large protein backbone relative to the surface. This led to an effective orientation, enabling solely direct ET of the adsorbed active enzymes. In general, applied potentials revealed reorientations under preservation of the enzyme's initial binding anchors. In addition, redox changes at the active site of MBH bound onto a positively charged biocompatible Au electrode were investigated under turnover conditions as well as under the influence of applied potentials.

The second part of this thesis introduces a novel *in situ* IR spectro-electrochemical approach to monitor protein adsorption on two different transparent conductive oxide (TCO) materials, i.e. antimony-doped tin oxide (ATO) and tin-rich indium oxide (ITO_{TR}). Using horse heart cytochrome c (cyt c) as a model system, protein adsorption on planar ATO and ITO_{TR} thin film electrodes were monitored spectroscopically. Within these studies, a selective protein binding via a histidine affinity tag (His-tag) to the unmodified metal oxide surfaces of ATO and ITO_{TR} was shown. Using the advantage of a controlled immobilization via this affinity tag, *Re* His-tagged MBH (his-MBH) was directly adsorbed onto ITO_{TR} and also studied *in situ* by an attenuated total reflection IR (ATR-IR) spectro-electrochemical approach, thereby demonstrating the integrity of the adsorbed protein. Simultaneous PFV studies revealed a remarkable bi-directional activity for H_2 cleavage and formation of his-MBH on ITO_{TR}. The latter effect may be related to the specific semiconductor-enzyme interactions, which are discussed in comparison to the unspecific bound *Re strep*-tagged MBH on the electrode material. Finally, ATR-IR and

SEIRA measurements of cyt c and both MBH variants are compared with respect to the signal enhancement, which eventually allows for an estimation of the catalytic activity of MBH species on different surfaces.

Zusammenfassung

Hydrogenasen sind Metalloenzyme, die reversibel die Oxidation von molekularem Wasserstoff in Protonen und Elektronen katalysieren. Das „Knallgasbakterium“ *Ralstonia eutropha* H16 (*Re*) ist eines der wenigen Beispiele, das mehrere [NiFe] Hydrogenasen besitzt, welche Mechanismen der katalytischen H_2-Umsetzung unter atmosphärischem Sauerstoffgehalt entwickelt haben. Um das katalytische Potential dieser Sauerstoff-toleranten Hydrogenasen zu erschliessen, insbesondere hinsichtlich möglicher biotechnlologischer Anwendungen in biologischen Brennstoffzellen, ist eine effiziente elektronische Kommunikation zwischen Enzym und leitfähiger Oberfläche erforderlich. Dies bedingt ein tiefgreifendes Verständnis der Enzym-Oberflächen-Interaktionen.

In dieser Arbeit wird ein interdisziplinärer Ansatz vorgestellt, der detaillierte Einblicke in die involvierten Adsorptionsparamater der heterodimeren membrangebundenen [NiFe] Hydrogenase (MBH) aus *Re* auf verschiedenen Elektrodenmaterialien ermöglicht. Der erste Teil dieser Arbeit ist der Adsorptionsstudie der Sauerstoff-toleranten MBH auf biokompatibel beschichteten Goldelektroden gewidmet. Anhand der Proteinfilm-Voltammetrie (PFV), der Oberflächenverstärkten Infrarot-Absorptions (SEIRA) Spektroelektrochemie, der Rasterkraftmikroskopie (AFM) und der Ellipsometrie wurde die katalytische Aktivität des Enzyms, sowie dessen Struktur, Integrität und Oberflächenbeladung untersucht. Hierfür wurden Resultate der MBH auf geladenen und hydrophoben Oberflächen erhalten. Die Korrelation zwischen der elektrokatalytischen Effizienz und der Art der Oberflächenanbindung des Enzyms auf der Elektrode lieferte wertvolle Informationen zur Orientierung des Enzymes. Die experimentellen Daten wurden durch Molekular-Simulationen und Berechnungen von IR-Spektren mit Hilfe der Dichtefunktionaltheorie (DFT) komplementiert, die in Kooperation durchgeführt wurden. Die vorgeschlagenen Orientierungskonfigurationen, welche auf unterschiedlichen zugänglichen Bindungsanker der MBH basieren, werden diskutiert und mittels einer SEIRA-spektroelektrochemischen Studie experimentell nachgewiesen werden. Die so erhaltenen Ergebnisse schlagen einen optimierten Elektronentransfer an der Enzym-Elektroden Grenzfläche für die heterodimere MBH Spezies auf leicht negativ geladenen Oberflächen vor. Hierbei wird eine Immobilisierung der MBH über ihre isolierte Transmembran-Helix angenommen, die über diese Anbindung auch eine Flexibilität des Proteingerüsts hinsichtlich Rotations- als auch Translationsbewegungen relativ zur Oberfläche erlaubt. Dies führt zu einer vorteilhaften Orientierung, die zudem einen reinen direkten Elektronentransfer aller adsorbierten und aktiven Enzyme ermöglicht. Angelegte Elektrodenpotentiale führten teilweise zu Reorientierungen unter Erhalt der usprrünglichen Bindungsanker zwischen Enzym- und Elektrodenoberfläche. Zusätzlich konnten auch Änderungen der Redoxzustände des aktiven Zentrums der MBH unter Turnover-Bedingungen sowie unter dem Einfluss angelegter Potentiale untersucht werden.

Der zweite Teil dieser Arbeit führt eine neuen *in situ* IR spektroelektrochemischen Ansatz zur Beobachtung der Proteinadsorption auf zwei unterschiedlichen, transparenten und leitfähigen Oxidmaterialen (TCO) ein, Antimon-dotiertes Zinn Oxid (ATO) und Zinn-reiches Indium Oxid (ITO_{TR}). Unter Verwendung von Pferdeherz-Cytochrome c (cyt c) als Modelsystem wurde die Proteinadsorption auf planaren ATO- und ITO_{TR}-Dünnschichtelektroden spektroskopisch verfolgt. In diesem Zusammenhang konnte eine selektive Proteinanbindung über einen Histidin-Affinitätstag (His-tag) an der isolierten Transmembran-Helix auf unmodifizierten Metalloxid-Oberflächen nachgewiesen werden. Diese Art der Anbindung wurde genutzt, um His-getaggte MBH (his-MBH) von *Re* direkt an die ITO_{TR} Elektroden anzubinden und mittels eines *in*

situ ATR-IR-spektroelektrochemischen Anzatzes zu untersuchen. Hierdurch konnte sowohl der Erhalt der Sekundärstruktur wie auch der strukturellen Integrität des aktiven Zentrums an der Oberfläche demonstriert werden. Simultan ausgeführte PFV-Studien von his-MBH auf ITO_{TR} wiesen eine erstaunliche bi-direktionale Aktivität zur H_2-Oxidation und -Reduktion auf. Die ungewöhnliche H_2-Reduktion der his-MBH wurde auf spezifische Halbleiter-Enzym-Interaktionen zurückgeführt, welche im Zusammenhang mit der unspezifisch gebundenen *strep*-tag MBH auf ITO_{TR} verglichen werden. Zum Abschluß werden Ergebnisse der ATR-IR und SEIRA Spektroskopie von cyt c und beiden MBH Varianten hinsichtlich der Signalverstärkung verglichen und letztendlich eine Abschätzung der katalytischen Aktivität der MBH auf verschiedenen Oberflächen durchgeführt.

List of Publications in Peer-Reviewed Journals

Parts of this work are published in the following articles

1. "Orientation-controlled electrocatalytic efficiency of an adsorbed oxygen-tolerant hydrogenase" N. Heidary, T. Utesch, M. Zerball, M. Horch, D. Millo, J. Fritsch, O. Lenz, R. V. Klitzing, P. Hildebrandt, A. Fischer*, M.A. Mroginski*, I. Zebger*. PLOS ONE, 2015, 10, (11).

2. "IR spectro-electrochemistry to study the influence of the metal oxide support material on the immobilization and function of a [NiFe] hydrogenase" . N. Heidary, A. Guiet, H. K. Ly, S. Frielingsdorf, O. Lenz, P. Hildebrandt, I. Zebger*, A. Fischer*. - in preparation

3. "Orientation-Dependent Catalytic Activity of an O_2-tolerant Membrane-Bound [NiFe] Hydrogenase on Differently Charged Surfaces" N. Heidary, T. Utesch, S. Frielingsdorf, O. Lenz, P. Hildebrandt, I. Zebger*, M.A. Mroginski*, A. Fischer*. - in preparation

Related Publications

4. "Microporous polymer network films covalently bound to gold electrodes" D. Becker, N. Heidary, M. Horch, U. Gernert, I. Zebger, J. Schmidt, A. Fischer*, A. Thomas*. Chem. Com., 2015, 4283-4286.

Other publications

1. "Direct observation of proton coupled electron transfer of immobilized hangman porphyrin complexes on electrodes via surface enhanced vibrational spectroscopy" H. K. Ly, P. Wrzolek, N. Heidary, M. Horch, J. Kozuch, M. Schwalbe*, I.M. Weidinger*. Chem. Sci., 2015, 6, 6999-7007.

2. "Electrochemical and Infrared Spectroscopic Studies Provide Insight into Reactions of the NiFe Regulatory Hydrogenase from Ralstonia eutropha with O_2 and C" P.A. Ash, J. Liu, N. Coutard, N. Heidary, M. Horch, I. Gudim, T. Simler, I. Zebger, O. Lenz, K.A. Vincent*. J. Phys. Chem. B, 2015, 119, 13807–13815.

3. "A One-Pot Approach to Mesoporous Metal Oxide Ultrathin Film Electrodes Bearing One Metal Nanoparticle per Pore with Enhanced Electrocatalytic Properties" A. Guiet, T. Reier, N. Heidary, D. Felkel, B. Johnson, U. Vainio, H. Schlaad, Y. Aksu, M. Driess, P. Strasser, A. Thomas, J. Polte, A. Fischer*. Chem. Mater., 2013, 4645−4652.

4. "A unique iron-sulfur cluster is crucial for oxygen tolerance of a [NiFe]-hydrogenase" T. Goris, A. F. Wait, M.l Saggu, J. Fritsch, N. Heidary, M. Stein, I. Zebger, F. Lendzian, F. A. Armstrong, B. Friedrich, O. Lenz*. Nat. Chem. Biol., 2011, 310–318.

5. "Role of the HoxZ subunit in the electron transfer pathway of the membrane-bound [NiFe] hydrogenase from Ralstonia eutropha immobilized on electrodes" M. Sezer, S. Frielingsdorf,

D. Millo, N. Heidary, T. Utesch, B. Friedrich, P. Hildebrandt, I. Zebger, I. M. Weidinger*. J. Phys. Chem. B, 2011, 115

6. "Mesoporous antimony doped tin oxide thin film electrodes for the stable immobilization of his-tagged proteins" A. Molero Milan, S. Frasca, N. Heidary, H. K. Ly, A. Guiet, U. Vainio, J.Polte , N. Michaela, C. Schulz, I. Zebger, P. Hildebrandt, I. M. Weidinger, U. Wollenberger*, A. Fischer - to be submitted

7. "In-situ spectro-electrochemical studies into the formation and stability of robust diazonium-derived interfaces on gold for the immobilization of electrocatalytic species" . T. Harris, N. Heidary, J. Kozuch, S. Frielingsdorf, O. Lenz, P. Hildebrandt, I. Zebger*, A. Fischer*. - to be submitted

8. "A Graphene Oxide Modified Hybrid Surface as an Alternative Platform for SEIRA Spectro-electrochemical Studies" H. Gatemala, L. Pardo-Perez, C. Querebillo. S. Frielingsdorf, O. Lenz, A. Fischer, I. Weidinger, S. Ekgasit, N. Heidary*, H. K. Ly*, I. Zebger*. - in preparation

first author *corresponding author

Selected Talks

1. "Spectro-electrochemistry of Oxygen-Tolerant Membrane-Bound-Hydrogenase on Conductive Surfaces", Materials Research Society (MRS), San Franciso, USA, 06-10 April 2015.
2. "An Approach towards Enzymatic Biofuel Cells - Spectro-electrochemical Insights into Oxygen-tolerant [NiFe]-Hydrogenase Immobilized on Electrodes", Electrochemistry GDCh Tagung Johannes Gutenberg-Universität, Mainz, 22-24 September 2014.
3. "Spectro-electrochemical approach towards optimization of Ralstonia eutropha (*Re*) membrane-bound-hydrogenase on conductive surfaces", Unicat Symposium, Excellence Cluster Berlin, 2014.
4. "Transparent Nanostructured Conductive Thin Films For Controlled Enzyme Immobilization" Third International Conference on Multifunctional, Hybrid and Nanomaterials, , Sorrento, Italy, 03-07 March 2013.
5. "Spectro-electrochemical approach towards optimization of Ralstonia eutropha membrane-boundhydrogenase on conductive surfaces" UniCat Minisymposium: Biocatalysts – towards Biofuels, Fine Chemicals and Pharmaceuticals, Berlin, 23-24 July 2012.

Selected Posters

1. "Oberflächenverstärkte IR Absorptionsspektroskopie an Enzymen", Tag der Forschung, Albert-Ludwigs-Universität, Freiburg, 25 June 2015.
2. "Spectro-electrochemical Insights into Oxygen-tolerant [NiFe]-Hydrogenase from Ralstonia eutropha immobilized on Electrodes", 7th International Conference on Advanced Vibrational Spectroscopy (ICAVS-7), 25 - 30 August 2013, Kobe, Japan.
3. "Adsorption of the membrane-bound [NiFe] hydrogenase on SAM coated gold electrodes" Tillmann Utesch, Nina Heidary, Maria Ana Castro, Diego Millo, Peter Hildebrandt, Anna Fischer, Ingo Zebger, and Maria Andrea Mroginski. Annual Meeting of the German Biophysical Society, 23 –26 September 2012, Göttingen, Germany.
4. "Hydrophobic Nanoreactor Templating For Nanostructured Metal NP – Metal Oxide-Nanocomposite Electrodes" Amandine Guiet, Nina Heidary, Matthias Driess, Anna Fischer, Third International Conference on Multifunctional, Hybrid and Nanomaterials, , Sorrento, Italy, 03-07 March 2013.

Danksagung

Mein besonderer Dank gilt folgenden Personen, die mich während dieser Zeit unterstützt, begleitet und mir diese Arbeit ermöglicht haben.

Zunächst möchte ich Prof. Dr. Anna Fischer für die Bereitstellung meiner Doktorarbeit danken, sowie für die Betreuung und Unterstützung.

Prof. Dr. Peter Hildebrandt möchte ich für seine Betreuung, seine Unterstützung und das stets offene Ohr danken.

Ich möchte Dr. Ingo Zebger für seine Betreuung und seiner Hingabe für alle seiner „Kinderchen“ danken.

Prof. Dr. Ulla Wollenberger danke ich für die Übernahme des externen Gutachtens und Prof. Dr. Reinhard Schomäcker möchte für die Übernahme des Vorsitzes des Promotionsausschusses danken.

Prof. Dr. Maria Andrea Mroginski und Dr. Tillmann Utesch möchte ich für die umfassende Kooperation, die Ausführung der MD-Simulationen, für die nette, fruchtbare Zusammenarbeit und die wertvollen, wissenschaftlichen Besprechungen danken.

Dr. Oliver Lenz, Dr. Stefan Frielingsdorf und Janna Schoknecht danke ich für die Bereitstellung der Proteinproben und der stets hilfreichen, wissenschaftlichen Gespräche.

Prof. Dr. Arne Thomas und Daniel Becker danke ich für die nette und effektive Zusammenarbeit.

Prof. Dr. Regine von Klitzing und Maximilian Zerball danke ich für die AFM- und Ellipsometrie-Messungen.

Meinen Kollegen: Dr. Anabel (Peluca) Molero Milan, Laura Carito (P like peanuts) Pardo Pérez, Tomos (Helene Fischer) Harris, Martin Rohloff und Dr. Caren Göbel, aka AK FUN möchte ich für die gute und unterstützende Arbeitsatmosphäre danken und der daraus entstandenen einzigartigen Freundschaften.

Besonders möchte ich Dr. Amandine Guiet, Dr. Khoa H. Ly, Dr. Marius Horch und Dr. Jacek Kozuch für ihre wissenschaftliche, aber auch ihrer emotionalen Unterstützung danken. Ihre Freundschaft gab mir während dieser Zeit großen Halt.

Ausserdem möchte ich der gesamten MVL Gruppe für den herzlichen Umgang und die angenehme Arbeitsatmosphäre danken.

Meinen Freunden Elif Kurtulmus, Dr. Andre Körnig, Tabea Hertzog, Laura Klatt, Dr. Murat Sezer, Jenny Misselwitz, Dr. Georg Kröger, Dr. Elisabeth Schulze danke ich, dass sie stets an meiner Seite standen und mir während dieser Zeit mit viel Verständnis und Geduld gegenübertraten.

Meinen Schullehrern Jochen Reder, Otto Essig und Helmar Schirmer danke ich für ihre Förderung, die mich motivierte diesen Weg einschlagen zu können.

Mein herzlichster Dank gilt meiner Familie, meinem Vater Ahmad, meiner Mutter Pari, und meinem Bruder Nima für ihre uneingeschränkte Unterstützung in jeder Lebenslage.

Besonders möchte ich Eduardo Manuel Ferreira da Conceicao für unsere gemeinsame Zeit, für alles was wir außerhalb und innerhalb der Wissenschaft teilen und seine unendliche, liebevolle Geduld und Unterstützung danken.

Abbreviations

A	electron acceptor
Aa	*Aquifex aeolicus*
AFM	atomic force microscopy
Ag/AgCl	silver/silver chloride electrode
AH	actinobacterial hydrogenase
ATR	attenuated total reflection
ATO	anitmony-doped tin oxide
BSE	back scattering electrons
C_5COOH (COOH)	mercaptohexanoic acid
C_5CH_3 (CH_3)	mercaptohexane
C_6OH (OH)	mercaptohexanol
C_6NH_2 (NH_2)	mercaptohexan-amine
CB	conduction band
CV	cyclic voltammetry
cyt c	cytochrome c
E. coli	Escherichia coli
EDC	1-Ethyl-3-(3-dimethylaminopropyl) carbodiimide
E_F	fermi energy level
E_{FB}	flat band potential
EPR	electron paramagnetic resonance
ET	electron transfer
D	electron donor
Dd	*Desulfovibrio desulfuricans*
DET	direct electron transfer
Df	*Desulfovibrio fructosovorans*
DFT	density functional theory
DL	electric double layer
Dv	*Desulfovibrio vulgaris*
FTIR	Fourier transform infrared
H/D	hydrogen/deuterium (exchange)
his-cyt c	his-tagged cytochrome c
his-MBH	his-tagged MBH
H-NMR	proton nuclear magnetic resonance
HPLC	high-performance liquid chromatography
his-tag	hexahistidine-tag (affinity tag)
IR	infrared
IRE	internal reflection element
ITBO	indium(I)tin(II)-*tert*-butyl-oxide
ITO	indium tin oxide
ITO_{TR}	tin-rich indium tin Oxide
M	metal
MB	methylene blue
MBH	membrane-bound hydrogenase
MD	molecular dynamics
MET	mediated electron transfer
MO	metal oxide
MS	mass spectroscopy
NHE	normal hydrogen electrode

OCP	open circuit potential
OHP	outer Helmholtz Plane
OTTLE	optically transparent thin layer electrochemistry
pdb	protein data base
PFE	protein film electrochemistry
PFV	protein film voltammetry
PGE	pyrolytic graphite electrode
PZC	potential of zero charge
Re	*Ralstonia eutropha*
RH	regulatory hydrogenase
SAM	self-assembled monolayer
SCE	saturated calomel electrode
SE	secondary electrons
SEC	spectro-electrochemistry
SEIRA	surface-enhanced infrared absorption
SEM	scanning tunnel microscopy
SERRS	surface-enhanced resonance raman
SH	soluble hydrogenase
SHE	standard hydrogen electrode
strep-MBH	*strep*-tagged MBH
strep-tag	strep-tag II affinity tag
TCO	transparent conducting oxide
UV-Vis	ultraviolet-visible spectroscopy
VB	valence band

Chapter 1

Motivation and Concepts

The 'Knallgas' reaction of molecular hydrogen and oxygen releases a large amount of energy. So far, precious metals, such as Platinum, have been widely used as fuel cell catalysts. Nature, on the other hand, developed specialized metalloenzymes, so-called hydrogenases, that efficiently catalyze the reversible cleavage of H_2 into protons and electrons by using earth abundant metals.[1] Given the worldwide depletion of fossil fuels and anthropogenic global warming, the demand for efficient and sustainable energy conversion approaches involving these biocatalysts has strongly increased. Thus, in recent decades, hydrogenases became a subject of major interest since these enzymes may advance the exploitation of H_2 as an energy carrier, also by serving as blueprints for the design of bio-inspired molecular catalysts. For this reason, this thesis focuses on exploring conditions towards an application of such enzymes.

In practice, the applicability of [NiFe] hydrogenases is often limited by their intrinsic sensitivity towards inactivation by molecular oxygen. Thus, in the field of biological fuel cell development, the focus is laid on oxygen-tolerant [NiFe] hydrogenases, e.g. the membrane-bound hydrogenase (MBH) from the 'Knallgas' bacterium *Ralstonia eutropha* (*Re*). Such enzymes are capable to catalyze H_2 conversion even under ambient oxygen levels,[2] which makes them highly promising candidates for such applications. Hence, *Re* MBH was chosen as a valuable model system for the following studies presented in this thesis.

Typically, the biotechnological utilization of hydrogenases depends on their immobilization on conductive electrode materials. This necessity represents a further major challenge, since large and bulky redox enzymes require orientation-controlled adsorption to enable efficient electronic communication with the electrode surface.[3] Moreover, the enzymatic function relies strongly on the integrity of all cofactors and the overall protein structure. Surface-enhanced infrared absorption (SEIRA) and attenuated total reflection infrared (ATR-IR) spectroscopy are powerful techniques to elucidate enzyme structure and enzyme–surface interactions in a surface-sensitive manner.[4] Specifically, they provide insights into the electronic structure of the [NiFe] active site upon surface interaction by monitoring redox state-dependent frequency changes of highly sensitive reported modes. Moreover, orientation, adsorption, and the integrity of the protein backbone structure can be explored by probing amide I and II vibrations. Last but not least, the electron transfer between the active site and the electrode surface can be studied simultaneously by protein film voltammetry. The aim of the present thesis is to study the factors that govern protein adsorption (and reorientation) by stationary SEIRA and ATR-IR spectro-electrochemistry.

In addition, these techniques were used to gain insights into structural and functional aspects of biocatalysis by surface-bound [NiFe] hydrogenases.

In vivo, the oxygen-tolerant *Re* MBH is incorporated into the cytoplasmic lipid bilayer membrane as a heterotrimeric species via its Cytochrome *b* unit. In order to preserve structure and function of purified heterodimeric MBH subspecies on electrode surfaces, the latter have to be biocompatible and optimized for an efficient binding. Hereby, surface functionality and charge distribution represent central determinants that are also crucial for the accessibility of functional enzyme orientations allowing interfacial electron transfer. In this respect, enzyme-surface interactions depend on possibly charged amino acids patches as well as the overall protein dipole moment. To assess the influence of all these aspects, the efficiency of biocatalytic H_2 oxidation by the oxygen-tolerant *Re* MBH was thoroughly investigated on self-assembled monolayer (SAM)-modified electrodes, and the [NiFe] active site was monitored under catalytic turnover conditions. Furthermore, the electrochemical efficiency of *Re* MBH upon surface interaction with different conductive materials was investigated systematically in order to find the most suitable platform. In more detail, the application potential of transparent conductive oxide (TCO) surfaces as novel substrates for spectro-electrochemistry was explored. In order to gain insights into protein adsorption onto these alternative platforms, the spectro-electrochemical cell for SEIRA investigations was adapted to study TCO thin film electrodes coated onto the ATR Si-prism. In this context, both Cytochrome *c* and *Re* MBH were used as biological model systems, and the corresponding immobilization processes and the enzyme semiconductor interactions were studied in detail.

Chapter 2

Theoretical Background

2.1 Metalloproteins

2.1.1 [NiFe] - Hydrogenases

2.1.1.1 Hydrogen as Alternative Energy Source

The reaction of hydrogen combustion releases large amounts of energy ($\Delta H^o = -286\,kJ\,mol^{-1}$) and hence molecular hydrogen presents a powerful fuel used in biological systems, but has also industrial perspectives.[5, 6, 7] In nature, hydrogenases belonging to the subclass of metalloenzymes, catalyze the reversible cleavage of molecular hydrogen into protons and electrons.[8]

$$H_2 \rightleftharpoons 2\,H^+ + 2\,e^-$$

Hydrogenases are found in a variety of organisms and are essential in their metabolism by catalyzing the oxidation of molecular hydrogen as an energy source. Furthermore, hydrogenases are also capable of the reverse reaction of catalyzing H_2 evolution, which can be established in processes aiming for removal of reducing equivalents. Depending on the required process, hydrogenases function either for hydrogen uptake or hydrogen evolution. Furthermore, several hydrogenases are known as hydrogen sensors for the regulation the gene expression for the biosynthesis of hydrogenases. These regulatory hydrogenases show a very low hydrogen conversion activity during the catalytic process.[9, 10] An example is reported may being involved in establishing transmembrane proton gradients.[11]

In regard of biotechnological applications, hydrogenases are regarded as biological catalysts, which are stable in water, built from earth abundant elements, have high substrate affinities and fast turnover rates.[12] These combined properties have raised the interest towards future H_2 technology.

Renewable H_2 fuel economy presents many advantages. The use of a (bio)fuel cell using H_2/O_2 as energy source under production of H_2O avoids any greenhouse gases. Unlike the energy storage problem of batteries or of solar energy, the fuel cell is a device that provides electrical energy from a chemical reaction, which is sustained as long as oxidants and reductants are present in the fuel cell.[13]

However, the utilization of enzymes on an industrial relevant level requires technical protocols for their sustainable production, efficient enzyme-electrodes preparation and the exploitation of molecular hydrogen aside from the natural gas. In principle, hydrogenases could contribute to both, hydrogen oxidation and hydrogen evolution, according to the observable catalytic bias of the particular enzyme.

Biohydrogen production can be achieved by dark and photo-fermentation of low-cost organic substrates and waste by a diverse group of bacteria or alternatively via direct bio-photolysis of water by green algae.[14] In this respect, research on hydrogenases has grown significantly due to the scientific and technological interest in hydrogen as a clean energy source.[10, 15]

Hydrogenases demonstrate hydrogen catalysis at same efficiencies as platinum.[16] Pt presents the best achieved energy release from hydrogen cleavage using fuel cells that convert chemical to electric energy. However, this precious metal suffers from two major problems. It is resource-limited, thus expensive, which forbids its use in a global scale. Moreover, Pt is poisoned by

traces of impurities of H_2S and CO, which defines typical contaminants of H_2 from steam reforming. In this context, solving the energy problem of our growing society demands alternative catalysts for this particular reaction. Thus, hydrogenases could offer a solution of these limitations due to their active site based on earth abundant metals (Fe and Ni) and their reversible activation after inhibitions by H_2S and CO. Some hydrogenases even exhibit tolerance towards these inhibitors.[17, 18, 19, 20, 21]

The follow enzymatic catalysts for the half cell processes in biological fuel cells are often chosen by hydrogenases for hydrogen cleavage at the anode and by laccase or bilirubin oxidase at the cathode for oxygen reduction to water.[17, 22] In conclusion, a combination of the here outlined biotechnological concepts represent the basis for an integrated approach of emission-free energy supply centered on hydrogen as a clean and sustainable fuel.

Various attempts in the synthesis of molecular catalysts mimicking the active site and/or the funtion of hydrogenases are still under investigation. The importance of its entire complex structure-function-relationship including the protein backbone an other cofactors, may be the obstacle to produce a high efficient catalyst under these physiologic conditions up to today. However, investigations for detailed understanding of their enzymatic reactions on a structural and functional basis can pave the way for the chemical development of artificial hydrogenases.

2.1.1.2 Classification

Hydrogenases are widespread in nature; they occur in bacteria, archaea, and some eukarya.[11, 23, 24, 25, 26] They can be found in the periplasm or cytoplasm, either in soluble form or membrane-bound.[11, 27] Despite the large diversity in size, quaternary structure, electron donors and acceptors, hydrogenases share a common structural motive consisting of a low-spin Fe^{II} ion at the active site that is coordinated by at least one thiolate donor and two diatomic ligands. Commonly hydrogenases can be distinguished based on the metal ion composition and classified in three phylogenetically main groups of [Fe], [FeFe], and [NiFe] hydrogenases.[11, 23, 28, 29] [Fe] hydrogenases are found only in methanogenic archaea. The enzyme catalyzes one of the reaction steps in the metanogenic energy conversion pathway from carbon dioxide with H_2 to methane.[26] They can only activates H_2 in the presence of the a second substrate (methenyltetrahydromethanopterin) and are highly light-sensitive.[30, 31] The classes of [FeFe] and [NiFe] hydrogenases prevail in nature.[32] The [FeFe] enzymes are primarily involved in H_2 evolution under high turnover frequencies.[33] However, [FeFe] hydrogenases are known for their high oxygen sensitivity and are reported to be inactivated irreversibly already upon exposure to traces of oxygen.[34, 35, 36, 37] On the contrary, [NiFe] enzymes are known for catalysis biased towards H_2 oxidation. Besides a group of standard oxygen-sensitive [NiFe] hydrogenases, [NiFe] hydrogenases found in aerobic bacteria are capable of H_2 oxidation even in the presence of O_2, termed as oxygen-tolerant [NiFe] hydrogenases. Turnover rates are reported as high as 10 000 hydrogen molecules per second, which is on the order of platinum based catalysts.[16]

Especially the combined properties of O_2-tolerance and highcatalytic efficiencies raised a major interest for biotechnological applications. This lead to intensive reseach efforts in the last decades towards the understanding of structure, catalytic mechanism and structure-function relationships with respect to the operation of such hydrogenase enzymes.

Group 1 is associated to uptake [NiFe] hydrogenases represented by membrane-bound periplasmic enzymes that supply hydrogen derived electrons to the respiratory chain via quinone reduction, creating a proton motive force for the generation of adenosine triphosphate (ATP). The heterodimer is connected to the quinone pool of the respiratory chain in the membrane by a third subunit, a di-heme cytochrome *b*, which, together with the hydrophobic C-terminus of the small subunit, which anchors the hydrogenase dimer to the membrane. Linked to the potentials of the involved redox components, which is higher than that of the H_2/H^+ couple, they predominantly serve as H_2 uptake hydrogenases. Group 2 includes both cyanobacterial uptake and hydrogen sensing [NiFe] hydrogenases that are involved in energy conversion or regulation of the cellular hydrogen metabolism, respectively. Bidirectional heteromultimeric cytoplasmic [NiFe] hydrogenases (group 3) represent complex multicofactor enzymes that couple the reversible cleavage of hydrogen to the reduction of an additional cofactor substrate, e.g. oxidized nicotinamide adenine dinucleotide (phosphate), $NAD(P)^+$. In principle, these enzymes operate reversibly and thus the catalytic bias and the physiological function depends on the cellular status or the enzyme's metabolic integration.[38, 39, 40, 41, 42, 43] Bidirectional [NiFe] hydrogenases exhibit pronounced sequence homology to the respiratory Complex I and other NADH-linked oxidoreductases.[44, 45, 46] Hydrogen evolving energy-conserving, membrane associated [NiFe] hydrogenases of group 4 generates hydrogen from protons and low potential electrons derived from the oxidation of organic compounds. Recently, a fifth group of cytoplasmic [NiFe] hydrogenases has been identified.[47, 48] Due to high binding affinities, these energy converting enzymes may be able to use atmospheric hydrogen for aerobic respiration in order to maintain basic metabolic functions under nutrient-deficient conditions.[48, 49]

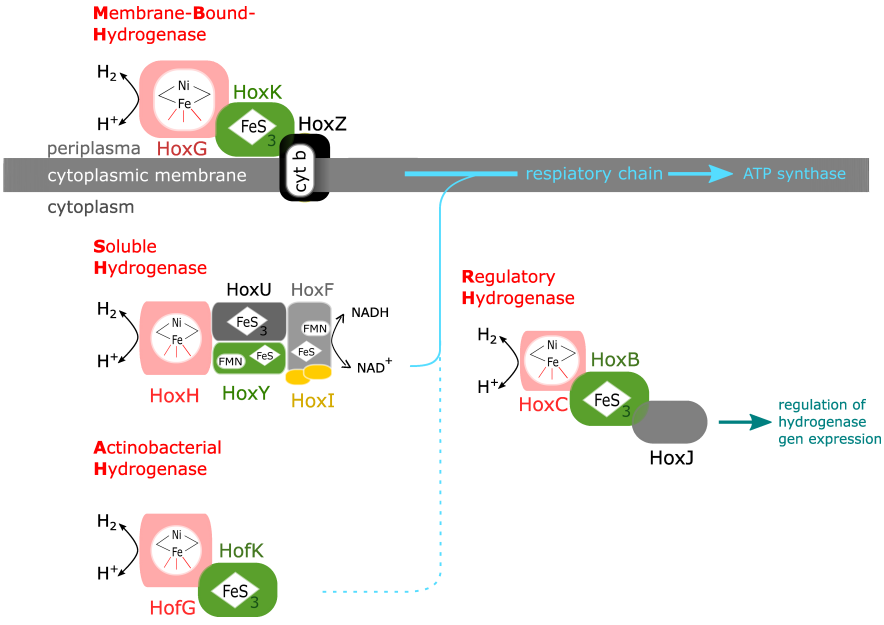

Figure 2.1: Oxygen-tolerant [NiFe] hydrogenases from *Ralstonia eutropha* adapted from reference [50].

The bacterium *Ralstonia eutropha* H16 (*Re*) (see Fig.2.1) is a facultative chemolitoautothropic β-proteobacterium, it is also known as a *Knallgas*-bacterium that can grow on a mixture of CO_2, H_2, and O_2.[38, 49, 39] Hence, all of its four [NiFe] hydrogenases are oxygen-tolerant and presents different subtypes of [NiFe] hydrogenases: the periplasmic membrane-bound hydrogenase (MBH,

group 1),[51, 52] the regulatory [NiFe] hydrogenase (RH, group 2), the soluble hydrogenase (SH, group 3) and a recent discovered Actinobacterial Hydrogenase (AH, group 5). In the following, essential features of the membrane-bound hydrogenase (MBH) will be discussed in this thesis.

2.1.1.3 Structure-Function of Membrane-bound Hydrogenase of *Ralstonia eutropha*

The best studied [NiFe] hydrogenase from *Re* is the MBH.[51, 52] The heterodimeric membrane-bound hydrogenase (MBH) is composed of a 34.6 kDa small subunit containing the Fe-S cluster electron transfer chain and a 67.1 kDa large subunit harboring the [NiFe] active site (Fig. 2.2).[53] The latter functions as the hydrogen converting site,[54] which contains two metal ions, Ni and Fe, bridged by two thiolate donors from highly conserved cysteines. The Ni ion is coordinated by two further cysteine thiolates while the Fe is continuously kept in the low spin (S = 0) ferrous form by its three diatomic ligands, one CO and two CN^-.[54, 32] In addition, a third bridging ligand between the two metals can be found in certain redox intermediates (see Fig. 2.2).[1] Since this active site is deeply buried within the protein, hydrogen is assumed to approach or leave the [NiFe] center via hydrophobic gas channels within the protein matrix.[55] Electrons released or required during catalytic turnover are exchanged with external redox partners via the FeS clusters chain in the small subunit of the enzyme. Concomitant proton transfer is assumed to proceed via intramolecular water molecules or polar amino acid side chains.[56, 57]

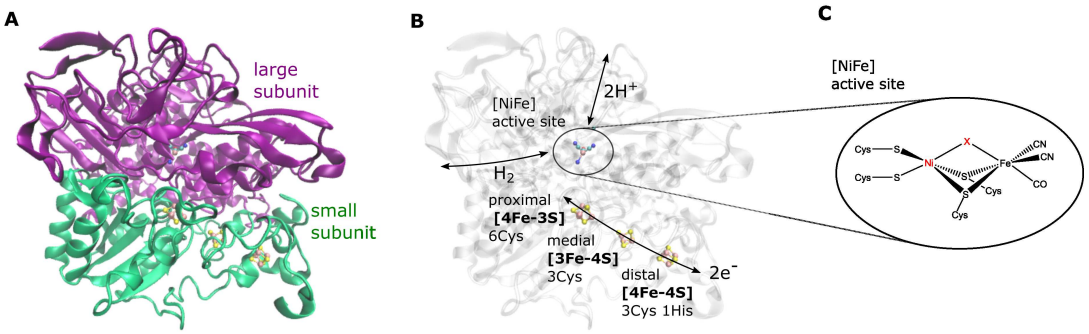

Figure 2.2: Schematic depiction of the membrane-bound [NiFe] hydrogenase from *Re* (pdb code: 3RGW). (A) The large and small subunit are color-coded in purple and green, active site, FeS cluster are shown in yellow and light pink.

Its overall structure appears similar to standard oxygen-sensitive [NiFe] hydrogenases. While the large subunit exposes the typical [NiFe] active site, the electron relay harbored in its small subunit differs essentially. In standard [NiFe] hydrogenases a cubane [4Fe4S] cluster is in the proximal position, which is replaced in the MBH by a six-cysteine coordinated [4Fe3S] cluster, which is crucial for its oxygen-tolerance.[58, 59, 60] Due to its particular structure, this cofactor is capable to provide two electrons in rapid succession. Hence, the formation of an fast activation from the ready oxidized "inactivated" Ni_r-B state is achieved. The observed redox states are discussed in more detail (section *2.1.1.4*). This property allows hydrogen cycling under aerobic conditions. Within the cell, the MBH is linked to the quinone pool of the respiratory chain via a di-heme cytochrome *b* protein. O_2-tolerant MBH can be isolated with or without this auxiliary electron transfer protein,[60, 61] and hydrogenase activity, oxygen sensitivity, and spectroscopic properties can be investigated independent of the presence of this cytochrome subunit.[5, 33, 62, 61, 63, 64] Novel insights into the *Re* MBH's optimized enzyme-surface interaction for biological hydrogen conversion upon adsorption on various electrode surfaces, as well as its resulting catalytic efficiencies are discussed in this thesis.

2.1.1.4 Redox Intermediates of Active Site

Detailed structural information about the active site of [NiFe] MBH has been obtained from spectroscopic measurements using a variety of techniques including EPR[65, 66]and IR.[5, 67, 68, 63] The O_2-tolerant MBH exhibits spectroscopic signatures corresponding to its electrocatalytic properties. The scheme in Figure 2.3 shows the redox transitions between the various states of the enzyme.

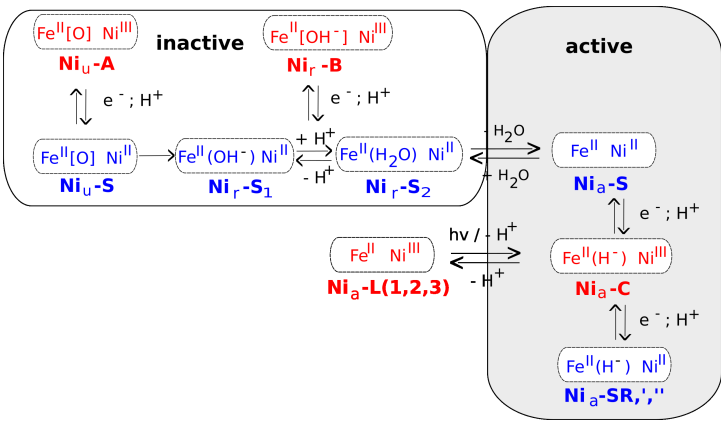

Figure 2.3: Redox states of the active site of oxygen-tolerant [NiFe] hydrogenases in catalytic inactive/active and light-induced processes. All displayed redox states can be observed by IR spectroscopy; EPR-silent states are color-coded in blue. The formal Ni oxidation state is listed for each species, and the presumable nature of the third bridging ligand is given in parentheses.

The unready, only slowly reactivated Ni_u-A state observed in standard [NiFe] hydrogenases is absent in all O_2-tolerant MBHs. The oxidized protein exists only in the Ni_r-B state as observed by electron paramagnetic resonance (EPR) and Fourier transform infrared (FTIR) spectroscopies.[58, 63] This species is accepted to carry a hydroxo ligand at the third bridging position between the two metals.[69, 70, 71, 1]

The redox states in Figure 2.3 are arranged with respect to their redox potential. The proposed chronological order within the catalytic cycle is described in section 2.1.1.5. Formal reduction by one electron of the fully oxidized [NiFe] hydrogenases in its Ni_r-B state yields a set of EPR-silent Ni^{II} species with structural and electronic features are in all cases not explicitly known.[1] Firstly, the inactive intermediates Ni_r-S/ Ni_a-S that contain bridging oxygen species. Through water abstraction from its protonated subform of Ni_r-S is assumed to readily yield the catalytic Ni_a-S intermediate providing a vacant bridging site for hydrogen cycling. A further one-electron reduction of Ni_a-S forms the paramagnetic Ni_a-C state (Ni^{III}, S = 1/2), carrying a bridging hydride ligand.[72, 73, 74, 75] This redox state can be (photo-) converted to another potential catalytic intermediate, Ni-L, which can be reversibly trapped at low temperatures.[72, 73, 74, 75] Within this photoreaction, the hydride ligand is removed from the bridging position as a proton, thereby creating a Ni^{I}(S = 1/2) electronic configuration at the active site.[1, 75, 76, 77] While being formally assigned to the Ni ion, the two hydride-derived electrons may actually form instead a metal–metal bond between Ni and Fe.[78] In this regard, Ni-L might be rather described as a singlet Ni^{III} species, which is in line with X-ray absorption spectroscopy (XAS) studies.[73] The formal addition of another electron to Ni_a-C forms another EPR-silent Ni^{II} species, which is termed as Ni_a-SR, which may exist as a singlet or triplet ground state.[79, 80, 81] This potential

catalytic intermediate is generally assumed to contain a bridging hydride ligand and a protonated terminal cysteine ligand, as confirmed by a recent high-resolution crystal structure.[82] Up to three subforms of Ni_a-SR can be observed by IR spectroscopy, which may differ in terms of protonation, spin state, or the protein environment around the active site. All this one-electron reduction steps are formally coupled each with a proton-transfer step.

2.1.1.5 The Catalytic Cycle

A summary of the proposed key states in the catalytic cycle is given in Figure 2.4. For simplicity, the Figure shows uni-directional H_2 oxidation, although the same states are proposed to occur for H_2 production (H^+ reduction).

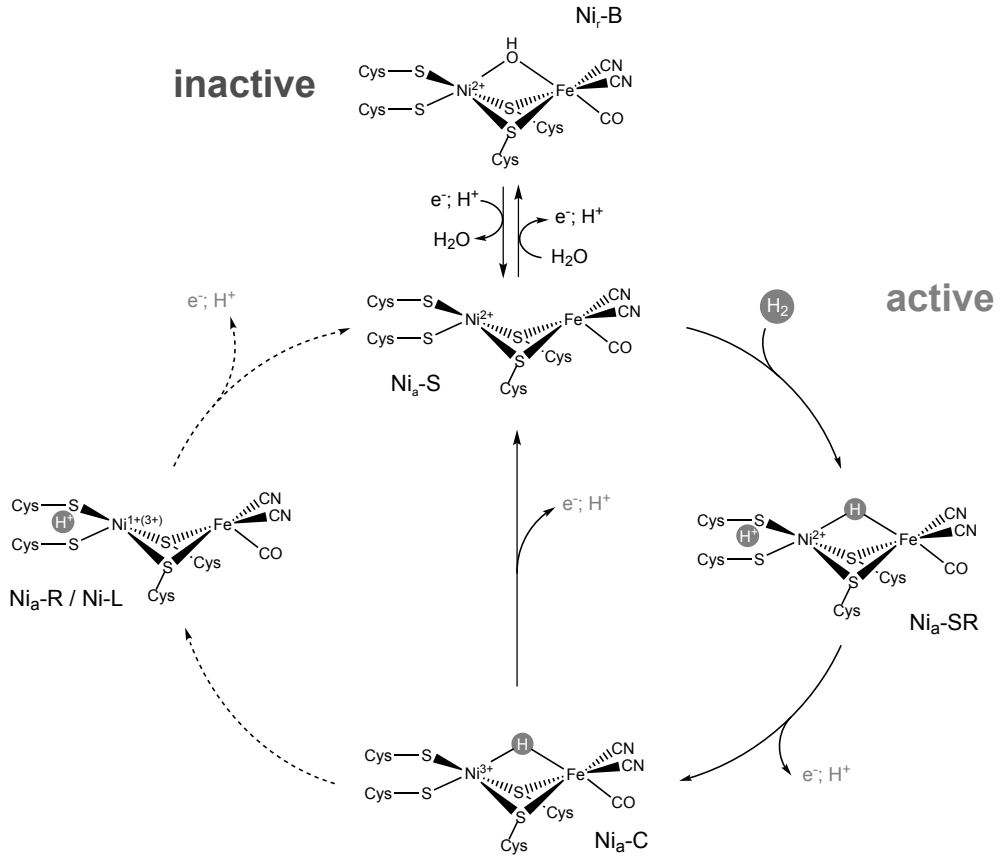

Figure 2.4: Possible mechanism for catalytic hydrogen cleavage at the active site of [NiFe] hydrogenase. The dashed lines indicate a participation of a Ni-L/Ni_a-R as a reaction intermediate in the catalytic cycle of O_2-tolerant MBH.[83]

When catalyzing H_2 oxidation, [NiFe] hydrogenases operate via a heterolytic cleavage mechanism whereby the H_2 initially binds to the Ni_a-S state as a proton and a hydride to form first the most reduced Ni_a-SR state of the active site (Figure 2.4).[82] Under loss of a proton and one electron, the intermediate species of Ni_a-C state is generated. The following step is still unsure. In case of O_2-sensitive [NiFe] hydrogenases the Ni-L state is not considered a catalytic intermediate as it is commonly reported to generate under light exposure at very low temperatures.[84, 85, 86] As denoted by the solid arrows in Figure 2.4, catalysis by O_2 sensitive [NiFe] hydrogenases is thought to proceed via loss of an electron and proton from the Ni_a-C state to give direct regeneration of Ni_a-S. In contrast, for O_2-tolerant hydrogenases a Ni-L state is readily detectable

at room temperature, even when the enzyme has not been illuminated.[68] Figure 2.4 shows an alleged Ni_a-C to Ni-L conversion involving electron and proton rearrangement; thereby Ni^{III} is formally reduced to Ni^{I} with concomitant movement of the bridging hydride to the sulfur of a coordinating cysteine as a proton. Alternatively, another intermediate, Ni_a-R[87] , that is similar or possibly identical to one of the subforms of the light induced Ni-L state may be considered to complete the catalytic cycle via second one-electron/one-proton transfer, forming the initial Ni_a-S intermediate.

2.1.2 Cytochrome c

Cytochromes belong to a subunit of heme proteins consisting of an iron center and primilarily functioning as electron carriers (cyt c) as well as enzymes (cyt P450).[88] Cytochromes are widely spread across animal and plant species playing a crucial role in the metabolism acting as electron or oxygen carriers and signal transducers. The heme groups can be distinguished by the chemical constitution of the porphyrin macrocyle in different types a, b, c and d.[89] In this work cytochrome c was used as a biolocigal reference system as it is a simple, relatively small protein (12 kDa), extensively stuied with ifferent spectroscopic and electrochemical techniques. Cytochrome c is a component of the electron transport chain in mitochondria. The heme group of cytochrome c accepts electrons from the bc1 complex and transfers electrons to the complex IV. Cytochrome c is also involved in initiation of apoptosis.

2.1.2.1 Structure of Monoheme Cytochrome c

Cytochrome c is a small monoheme protein associated with the inner membrane of mitochondrion playing a crucial role in the last step of the respiratory chain (electron transfer chain) able carrying one electron. The heme group of cytochrome c can undergo reduction and oxidation by a Fe^{II}/Fe^{III} change. The iron atom can vary between a ferric and a ferrous oxidation state in which the formal charge on the iron atom is 3+ and 2+, respectively. The transition between the various spin, coordination (or conformational) and oxidation states depends on many factors and can be probed with different spectroscopic, electrochemical and spectro-electrochemical techniques. The protein structure is displayed in Figure 2.5. The heme groups can be distinguished by the ligation, spin and oxidation state at heme iron center atom.

The heme iron center is covalently linked to the protein matrix via cysteine thioether bridges at the vinyl group. The coordination pattern of the heme iron can differ depending on the exogenous or endogenous axial ligands. Either both axial positions are exogenous and endogenous occupied or one position remains vacant assigned to a six fold (6c) or a fivefold (5c) coordination pattern, respectively. Low field ligands coordinated in 5c or 6c form a high spin state (HS) of the iron atom, with an octaedrical complex in which the five d-orbitals split into three degenerated e_g and two lower energetic degenerated t_{2g} orbitals. On the other hand, high field ligands facilitate the formation of a low spin (LS) of the iron state. Both observed states define the nativity of the cytochrome *c* protein. The transition between the various spin, coordination (or conformational) and oxidation states depends on many factors and can be probed with different spectroscopic, electrochemical and spectro-electrochemical techniques.

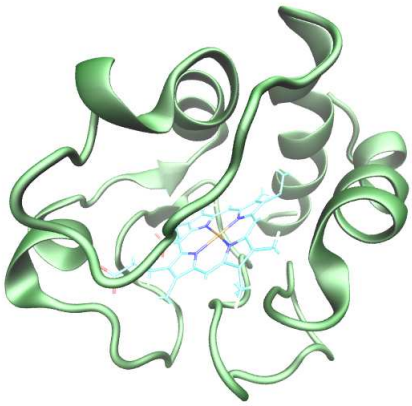

Figure 2.5: Schematic depiction of oxidized horse heart cytochrome c (pdb code: 1AKK). The backbone structure is color-coded in green, covalently attached c-type heme is shown in light blue with the dark red iron center.

2.2 Spectroscopic Techniques

2.2.1 Theory of Vibrational Spectroscopy

Vibrational spectroscopy refers to methods that explore physical and chemical properties from lattice or molecular vibrations, typically frequencies ν range from less than 10^{12} to approximately 10^{14} Hz (or wavenumber $\tilde{\nu} = 10^2 - 5 \cdot 10^3 cm^{-1}; \lambda = 100\,\mu m - 2\,\mu m$). The interaction of electromagnetic radiation with matter results in transitions inbetween its quantized discrete vibrational energy states. This excitation of the molecular vibration can relay on two different physical phenomena, first the absorption of discrete photons, probed by IR spectroscopy and second the inelastic scattering of photons observed with Raman spectroscopy.

The technique of IR spectroscrospy is based on direct absorption of photons, which is achieved by irradiation of polychromatic infrared radiation consisting of a distinct photon energy $h\nu_{IR}$

$$h\nu_{IR} = h\nu_{if} = h\nu_f - h\nu_i \tag{2.1}$$

corresponding to the energy difference $h\nu_{if}$ between the initial ν_i and the excited final vibrational ν_f energy level of a certain normal mode. IR radiation as an energy source can be divided into the regions of near-infrared (NIR: 12500 - 4000 cm^{-1}- combination vibrations and overtones), middle-infrared (MIR: 4000 - 400 cm^{-1}- *i.a.* bending and stretching vibrations) and far-infrared (FIR: 400 - 10 cm^{-1}- metal oxides, lattice vibrations). The energy difference for the most likely transition between the ground state and the first excited state corresponds to an energy in the MIR range.

In contrast to IR spectroscopy, Raman spectroscopy is based on inelastic scattering. Monochromatic light is used to probe and excite molecular vibrational modes and due to the inelastic interaction, the energy of scattered photons ($h\nu_R$) are detected and differs from those of the incident photons ($h\nu_0$) by

$$h\nu_{if} = h\nu_0 - h\nu_R = h\nu_f - h\nu_i \tag{2.2}$$

Both, IR and Raman spectroscopy differ in their underlying mechanisms and generally provide complementary informations. Vibrational transitions are only IR-active when associated with changes in the dipole moment. Whereas, vibrational transitions are Raman -active when associated with changes in polarisability.

In the following sections, the fundamental aspects of molecular vibrations and experimental detection methods will be presented.

2.2.1.1 Molecular Vibrations

To discuss the concept of harmonic vibrations, molecules are considered as an array of point masses interconnected by mass-less springs representing the intramolecular interaction between atoms. A simple picture describes molecules as a dynamic ensemble of N interconnected atoms. Each atom of the molecule has the ability to move in a three-dimensional space resulting with an entire molecule with N atoms obtaining $3N$ degrees of freedom. Three are based on the translational motion in mutually perpendicular directions (in x-,y- and z-axes) and three represent the rotational motion around the x-,y- and z-axes. The remaining $3N - 6$ degrees of freedom correlate with the vibrations of atoms within the molecule. The simplest molecular vibration appears in a diatomic molecule, in which the coupled motion is observable. The molecular vibrations in polyfunctional molecules involve a higher complexity of motions. In case of linear molecules, like CO_2, the rotation around the molecular axis does not vary the position of the atoms in the molecule. Consequently the rotational freedom grades are reduced to two and therefore the total amount of normal modes accounts for $3N - 5$.

Normal modes imply approximately harmonic displacements of the atoms from their equilibrium positions representing well defined motions, in which all atoms posses the same frequency ν, even in different amplitudes. In the case of diatomic molecules Hook's law can be applied:

$$F_x = -f\,\Delta x \tag{2.3}$$

where the force F_x results from a displacement of the atoms Δx and f is the force constant describing the rigidity of the bond.

With this, the potential energy $V(x)$ can be described as

$$V(x) = -\int_0^x F\,dx = \frac{1}{2}\,f\,\Delta x^2 \tag{2.4}$$

The kinetic energy T of the atoms depends on the reduced mass μ and the velocity of their motions $(d\Delta x/dt)$

$$T = \frac{1}{2}\mu\,(\Delta x)^2 \tag{2.5}$$

with

$$\mu = \frac{m_\alpha m_\beta}{m_\alpha + m_\beta} \tag{2.6}$$

The vibrational frequency is governed by the force of f and the masses of the displaced atoms m. For the simplest case, if a diatomic molecule ($m_\alpha \leftrightsquigarrow m_\beta$) solely obtains one vibrational degree of freedom, namely the stretching of the bond. The change of total energy is expressed by the sum of the derivatives of the potential and kinetic energy, which must equal to zero under energy conversation

$$0 = \frac{dT}{dt} + \frac{dV}{dt} = \frac{d^2\Delta x}{dt^2} + \frac{f}{\mu}\Delta x \tag{2.7}$$

which can be solved by

$$\Delta x = A \cdot cos(\omega t + \varphi) \tag{2.8}$$

A presents the amplitude, ω the circular frequency and φ the phase of the respective vibrational motion. Insertion of eq. 2.7 in eq. 2.8, results in the definition for circular frequency in 1/s

$$\omega = \sqrt{\frac{f}{\mu}} \tag{2.9}$$

The conversion into frequencies expressed by division of circular frequency with 2π leads to the oscillation frequency ν ($\tilde{\nu} = \nu/c$ expressed in cm^{-1}) of the spring in relation to the relative mass μ and to the force constant f is defined as

$$\nu_{vib} = \frac{1}{2\pi}\sqrt{\frac{f}{\mu}} \tag{2.10}$$

According to equation 2.10 normal modes frequencies are distingtly linked to the composition configuration and symmetry of the interconnected atoms of a molecule, involving changes of electron densities due to non-bonding interactions. Therefore, vibrational spectroscopic techniques allow sensitive valuable informations of the dynamic molecular structure by excitation of the normal modes, which can be used not only for compositional resolution of molecules, but also more important for fast and small structural changes at certian sites.[90, 91] In many cases of catalysis, the involved active sites are localized within complex molecular structures. Even fast atomic motions, can be detected *in-situ* down to femtosecond timescales without restrictions of the macromolecular sizes.[92] Especially interesting are vibrational spectroscopic techniques in regard of enzymatic biomolecules, in which small active sitesare burried in large macromolecules.

2.2.1.2 Intensities of Vibrational Bands

Besides the frequencies resulting from normal modes, the intensitiy of a vibrational band is a second observable in the vibrational spectrum. Whereas normal mode frequencies are fundamental molecular properties, the intensity of vibrational bands is strongly dependent on the used experimental technique. Derived from the quantum mechanical theory and by excluding the factors of the experimental technique, the integral signal intensity for a certain normal mode is

proportional to the probability of the transition from the initial i to final f vibrational level. The transition probability is given by the square of transitional dipole moment P_{if}, described by the integral

$$P_{if} =< \psi_f^* | \hat{\Omega} | \psi_i > \tag{2.11}$$

where ψ_f and ψ_i are ascribed to the wavefunctions for the vibrational states f and i, and $\hat{\Omega}$ presents the operator defined for perturbating the molecule by electromagnetic radiation. The operator is different for the two different physical processes of IR and Raman spectroscopy. The operator derives from the first- and second-order of time-dependent perturbation theory for IR and Raman, respectively. The transition probability per unit time, the transition rate Γ_{if}, is described according to Fermi's golden rule by

$$\Gamma_{if} = \frac{2\pi}{\hbar} |P_{if}|^2 \, \rho_f \tag{2.12}$$

with ρ_f defined as the density of final states.

2.2.1.3 Infrared Absorption

The IR spectroscopy probes molecuar vibrations by resonant absorption of photons, which is experimentally quantified as the absorbance A by the Lambert - Beer law

$$A = -log \frac{I}{I_0} = \varepsilon \cdot c \cdot d \tag{2.13}$$

deduced from the intensities of incident and transmitted light, I_0 and I, respectively. Or from another perspective, derived from the concentration of the sample c, the optical path length d as well as from ε the proportionality constant, which depends on the quantum mechanical probability of the transition between initial and final vibrational state (see eq.2.11). In IR spectroscopy, the transition probability is governed by the electrical dipole moment operator $\hat{\mu}_q$ for the transition $i \rightarrow f$ as following

$$\hat{\mu}_q = \sum_{\alpha} e_\alpha q_\alpha \tag{2.14}$$

where e_α is the effective charge of the atom α, and q_α presents the distance to its center of gravity of the molecule in cartesian coordinates *(q=x,y,z)*. The perturbation with the IR radiation can be described as a scalar product of the electric field vector of the radiation and $\hat{\mu}_q$. Considering the components for all molecular orientations, the intensity of IR transitions can be expressed by

$$I_{if,IR} \propto \left([\mu_x]_{if}^2 + [\mu_y]_{if}^2 + [\mu_z]_{if}^2 \right) \tag{2.15}$$

with $[\mu_q]_{if}$ described by the integral

$$[\mu_q]_{if} =< \psi_f^* | \hat{\mu}_q | \psi_i > \tag{2.16}$$

The vibrational transition $i \rightarrow f$ occurs in the IR spectrum only if it results from a non-zero transition dipole moment $[\mu_q]_{if} \neq 0$. To identify the prerequisites for an IR-active absorption, the operator of the electric dipole moment $\hat{\mu}_q$is expanded with respect to the normal coordinates Q_k by a Taylor series, which can be aborted after the second term as a harmonic approximation, which is considered by involving only linear terms, and results in

$$\hat{\mu}_q = \mu_q^0 + \sum_{k=1}^{3N-6} \hat{\mu}_q^k Q_k \tag{2.17}$$

with

$$\hat{\mu}_q^k = (\frac{\partial \mu_q}{\partial Q_q})_0 \tag{2.18}$$

By implementing (eq. 2.17) in (eq. 2.16): the respective transitional dipole moment can be expressed as

$$[\mu_q]_{if} = \mu_q^0 < \psi_f^* \psi_i > + \sum_{k=1}^{3N-6} \hat{\mu}_q^k < \psi_f^* | Q_k | \psi_i > \tag{2.19}$$

From this expression, the quantum mechanic description for the absorption process, can be derived in the following way: the first term of equation 2.19 equals to zero based on the orthogonality of both wavefunctions, therefore the second term must be unequal to zero in order to define a transitional probability as non-zero. This means (1) the dipole moment must change during the vibration, i.e. given that the first derivative of the electric dipole moment with respect to the normal coordinates Q_k is unequal to zero. (2) the integral$< \psi_f * | Q_k | \psi_i >$ must also differ from zero, which is the case when i and f vibrational states differ by one. Conclusively, assuming an harmonic oscillator, the vibrational quantum number varies about ± 1 during the transition. This consideration holds for all three components of the cartesian coordinates *(q=x,y,z),* meaning that the absorbance A of unpolarized light of randomly oriented molecules evolves from the sum of transition probabilities along all thee components (*see* eq. 2.15). However, linear polarized IR radiation on oriented samples addresses individual components of the transition dipole moment and enables thereby the access to specific details of the investigated systems.

2.2.2 Fourier Transform Infrared Spectroscopy

The remarkable performance advantages of a FTIR spectrometer lead to drastically reduced measuring time and an improved signal-to-noise ratio compared to the previously used dispersive technique. The concept of FTIR is based on the implementation of a Michelson interferometer (see Figure 2.6).

2.2.2.1 The Michelson Interferometer

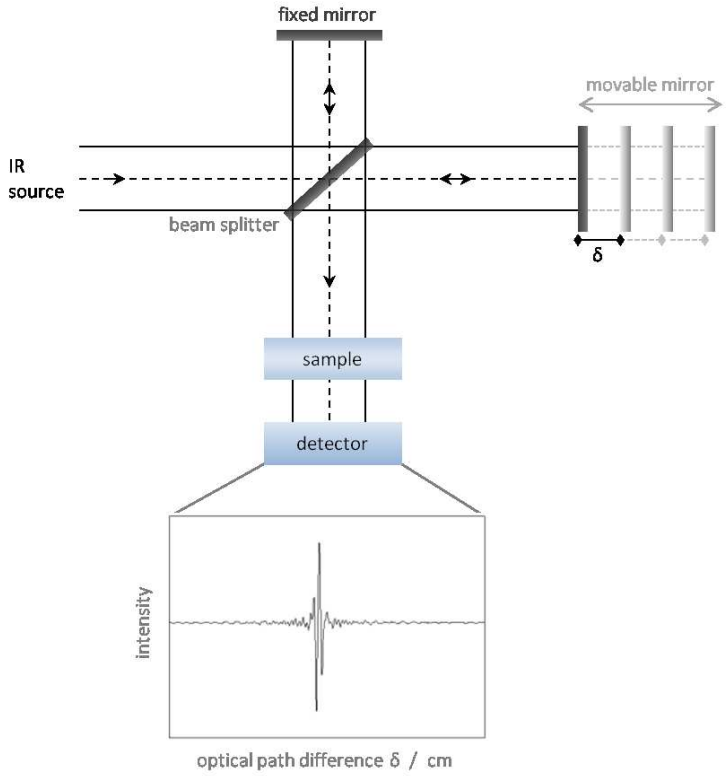

Figure 2.6: Sketch of Michelson Interferometer. IR radiaton passes the semi-transparent beam splitter, which is divides the beam in two parts and are subsequently recombined at the sample and guided via the sample onto detector, while the movable mirror varies optical path differences between the two beams and generates an interferogram of the detected IR radiation.

The radiation of the infrared source is divided by a semitransparent beam splitter into two beams directed to a stationary mirror and a movable mirror, the latter varies the optical path difference by a continuous displacement. The recombination takes place at the beamsplitter and is guided via the sample onto a detector. The movement of the slideable mirror leads to an alternating interference. Thus, the resulting interferogram displays the radiation intensity of the mirror position calculated relatively to the position of stationary mirror. Both variables, distance and frequency can be interconverted by applying a Fourier transformation as expressed by the following equation

$$I(\tilde{\nu}) = \int_{-\infty}^{+\infty} I(\delta)\, cos(2\pi\tilde{\nu})\, d\delta \tag{2.20}$$

thereby $\widetilde{\nu}$ refers to the corresponding wavenumber, while the retardation δ is known as the optical path difference between the two mirrors. The Fourier transformation converts the corresponding $I(\delta)$ information in the interferogram to an $I(\bar{\nu})$ plot of the light intensity versus wavenumber. Therefore, the so called single beam spectrum reveals absorption bands only at wavenumbers at which the sample adsorbs IR radiation. These specific values are characteristic for certain molecular functional groups within its molecular environment. Vibrational dipole moment changes are sensitive to variations on the structure, conformation as well as the physical state and can be even differentiated for similar groups in a complex biological matrix.

Fourier Transform Infrared Spectroscopy offers several advantages compared to the dispersive technique including

- Multiplex or Fellgett advantage is based on the simultaneous measurement of all frequencies leading to an improved signal to noise ratio. In dispersive spectrometers the respective intensity is recorded at each spectral data point. Using a FTIR spectrometer, the total noise is distributed over the entire spectral range, which results in a signal-to-noise (S/N) ratio increased by a factor of √N for a spectrum comprised of N resolved elements.

- Throughout or Jacquinot advantage arises from the fact that the circular apertures used in FTIR spectrometers has a larger area than the slits used in grating spectrometers that determine the resolution, thereby enabling higher throughput of radiation.

The combination of the Jaquinot and Fellgett advantages leads to improment of both, the time required to the speed recording and the signal-to-noise of an FT spectrometer, thereby enabling *in-situ* measurements as well as spectral detections at much lower light levels.

- Connes advantage is provided by an internal calibration based on a simultaneaously measured interferogram of a HeNe laser, which precisely determines the mirror position and thus also the precise wavnumber of spectral features.

2.2.2.2 Attenuated Total Reflectance – Infrared Spectroscopy

Figure 2.7 displays a schematic representation of a Single-ATR-setup focusing thereby on the internal reflection element (IRE), i.e. ATR prism, as central building block. The phenomenon of total reflection takes place at the interface to an optical less dense medium under an angle of incident higher than the critical angle θ_c. Generally, the IRE consists of an IR transparent material with a refractive index considerably higher than those of the sample. The refrection index of biological systems is generally about $n_1 \sim 1.44$, while silicon (n_{Si}= 3.42), germanium ($n_{Ge} = 4.0$) or zinc selenid ($n_{ZnSe} = 2.43$) are typically used as materials for IRE.[93, 94, 95, 96] In this work metal oxides are used ITO ($n_{ITO} \sim 1.6 - 2.5$), ATO ($n_{ATO} \sim 4$).[97, 98]

Decay pattern of the evanescent wave under ATR condition

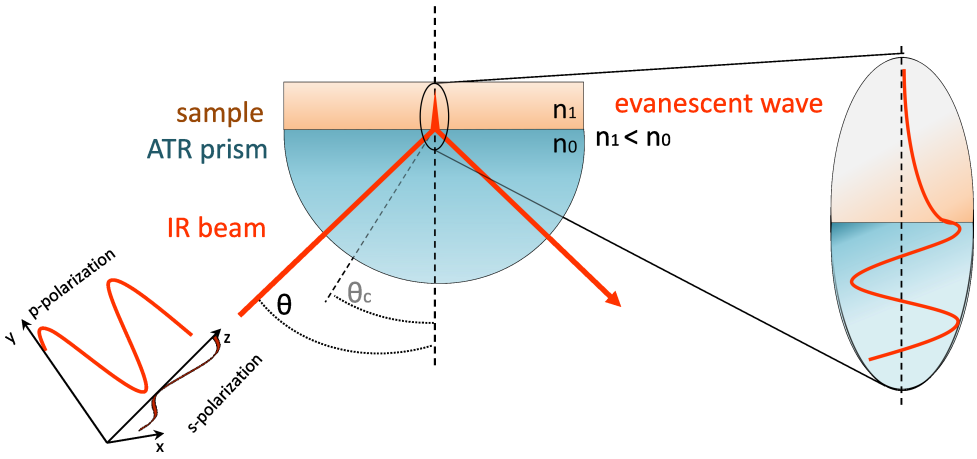

Figure 2.7: Schematic representation of attenuated total reflection IR (ATR-IR) spectroscopy. Incoming unpolarized IR beam, defined by perpendicular (s) and parallel (p) component relative to the plane of incident of electromagnetic field results in total reflection at the interface to an optical less densed medium, i.e. sample, if incident angle exceeds critical angle θ_c. Illustrated magnification displays the descent of electromagnetic field at interface to optically rare medium presenting the progress of an evanescent wave.

ATR is the effect of the total reflection of an evanescent wave through the interface into the less dense medium without carrying any energy. In this process, the amplitude of the electric field decays exponentially in the direction normal to the surface.

$$E = E_0 exp\left(-\frac{z}{d_p}\right) \tag{2.21}$$

Thereby, d_p defines the penetration depth at which the amplitude decayed to ca. 37 % ($\sim e^{-1}$) of its initial value and depends on the angle of incident ϑ, the wavelength of the radiation λ and the ratio of the refractive indices $n_1/n_0$of IRE and the optically rare medium, respectively:

$$d_p = \frac{\lambda}{2\pi\sqrt{sin^2\theta - \left(\frac{n_1}{n_0}\right)^2}} \tag{2.22}$$

Generally, the penetration depth lies in the range of the wavelength of the incident radiation. In case of a Si-prism, an incident angle of 60° and a spectral region of 1000 – 4000 cm^{-1} (10 – 2.5 µm) the penetration depth of the evanescent wave is between 2.6 and 0.7 µm, respectively. Hence, absorbing species on the surface of the IRE medium can be probed by the interaction with the electric field of the evanescent wave. Absorbants of multi, but also of single layers can be probed *in-situ* by ATR. Furthermore, it provides the possibility to measure a wide variety of solid and liquid samples without any complex sample preparation.

2.2.2.3 Surface-Enhanced Infrared Absorption Spectroscopy

An important variant of IR-spectroscopic investigations is the so called surface enhanced infrared absorption (SEIRA) spectroscopy, which was developed in the 1980s.[99] Molecules which are adsorbed on nanostructured metal island film or metal colloids exhibit a more intense IR absorption. Similar to the surface-enhanced Raman spectroscopy (SERS) the enhancement effect is based on two different mechanisms: an electromagnetic (EM) and a chemical contribution.[100] The total enhancement provide a factor of 10 to 100 times higher intense IR absorption. Whereas SERS presents enhancement factors in a range up to 10^6 times. However, the sensitivity of this IR technique is high enough to allow quantitative and qualitative analyses of components in the range of picogram to micrograms close to the surface. Studies correlating the metal thickness and the enhancement, proved a short-range enhancement effect within ca. 8 nm from the metal surface.[101] The surface can be characterized in vacuum, air, gas and solution phases. In addition to the use of metals for signal enhancement, they can function also as a working electrode for electrochemical studies on the same sample, therby allowing spectro-electrochemical investigations. Hence, SEIRA spectroscopy is a powerfull tool for a wide range of applications including biological systems. So far, SEIRA spectroscopical investigations had been shown for peripheral and integral membrane proteins such as cyt c,[102, 103] cyt c oxidase,[104] sensory rhodopsin II,[105] membrane-bound anion channel,[106] hydrogenases,[67, 62, 107] just to mention a few. A variety of immobilization strategies were developed for the protein binding either directly on the surface as well as embedded in artificial bilayer membranes.[106, 108, 109]

Similar to SERS, a roughened structure of the metal surface plays a crucial role with respect to the surface enhancement effects in SEIRA spectroscopy. The most common metal used for SEIRA is gold, because of its properties exposing plasmon resonance in the range of IR, but also a nobel metal, ehich is inert for oxidaziation, easily modified to a biocompatible surface by self assembled monolayers.

The observed total surface-enhancement consists of the sum of different individual effects.

- **Electromagnetic (EM) Mechanism**

  Plasmon Resonance

  Surface plasmons can be excited by an electromagnetic radiation, resulting in an enhanced electromagnetic field at the surface [110, 111]. The metal can be polarized by an interaction with the incident photon field via excitation of the collective electron resonance (localized plasmon modes). The dipole p which is induced in the particles generates a local electromagnetic field around the particles. The induced EM field is polarized perpendicular to the surface at every point in the metal particle. The magnitude of the localized EM field E_{local} depends on the induced dipole p and the distance from the metal d with the sixth power

  $$|E_{local}|^2 = \frac{4p^2}{d^6} \tag{2.23}$$

  The decrease of the localized EM field with distance by the sixth power results a the short-range enhancement effect.

  As shown in Figure 2.8, the local EM field is much stronger than the incident EM field.

The polarization of the local EM field along the surface normal results in a surface selection rule. In general an oscillation of dipoles perpendicular to the surface leads to a three times higher intensity than randomly oriented dipoles. [101]. Thereby, enhancement effect can be described according to the following distance dependency

$$F_{SEIRA}(d) = F_{SEIRA}(0) \cdot (\frac{a_0}{a_0 + d})^6 \tag{2.24}$$

with $F_{SEIRA}(0)$ the enhancement factor of the surface, a_0 the diameter of spherical metal islands and d the distance from the metal surface. For a adequate enhancement the diameter of the islands must be in the range of the incident radiation wavelength. The extent of the enhancement is dependent from the dimensions and also shape of the metal particles.

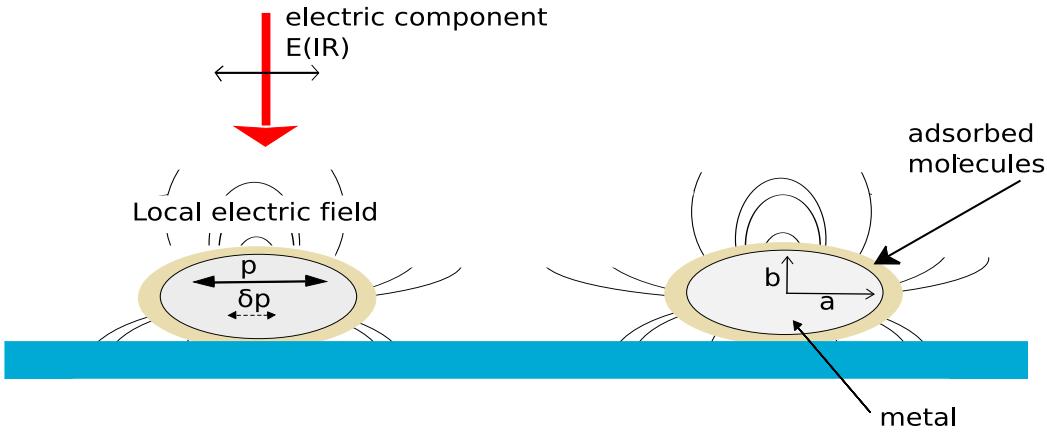

Figure 2.8: Schematic representation of the EM and chemical mechanism on an island metal film; p: dipole moment; a, b: dimensions of the ellipsoid metal particles; δp: additional induced dipole of the metal island denoted to the molecular vibration of the adsorbed molecules.Adapted from[112].

Perturbation of Optical Properties of the Metal

Additionally, a perturbation caused by oscillating dipoles of surface molecules can contribute to the total enhancement factor. The oscillating dipoles of adsorbed molecules enable an induction of dipoles in the metal particles resulting in a change of the dielectric function of the metal, which modulates the transmittance and reflectance of the metal film at the wavenumbers of the vibrations. The perturbation is larger at frequencies of molecular vibrations. Therefore, the molecular vibration is observed by the change in transmittance or reflactance of the nano-structured metal island film [101].

- **Chemical Mechanism**

  Another contribution to the overall enhancement is given by the so called chemical mechanism. Chemisorption can also change the vibrational polarizability of adsorbed molecules due to donor-acceptor interaction between the adsorbed molecules and the underlying metal. Strongly polarizable groups of adsorbats achieve a larger enhancement than others [113]. This effect is similar to a charge transfer process between molecular orbitals and those of the metal, thus can cause an increase of the adsorption coefficient.

- **Unifromal Orientation**
  Molecule adsorption at the metal surface usually leads to a preferential and more homogenous orientation due to an alignment of molecular dipoles within the exposed electric field. Vibrations perpendicular to the surface are enhanced maximal by the enhanced IR radiation propagating perpendicular to the surface. In comparison to statistical random distribution of orientations in solution, this alignment gives rise to an enhanced signal.

SEIRA displays a strong dependency on the angle of the incidence of IR light, hence on the contribution of polarisation component of radiation. P-polarized IR radiation progagating perpendicular to the surface leads to the highest plasmon resonance due to the most intense interaction with the metal inducing the strongest dipole moment of the metal. However, the geometry of s-polarized radiation to the surface does not yield any surface enhanced IR signals. These properties of SEIRA effects are discussed and reviewd by Osawa.[112]

2.2.2.4 FTIR Spectroscopy on Proteins

The main feature of an protein in the IR spectrum is related to of the polyamide backbone with its secondary and tertiary structure, involving residues of each single amino acid side chain,[114] and prosthetic groups. The latter two components can usually only be derived in difference spectra, emphasizing even small changes in the IR spectra.[115] The protein backbone structure, however, contributes to a predominant part to the protein related IR signals, denoted as various amide bands. Their respective vibrational spectroscopic features mainly derived from the secondary structure elements are shown in scheme (Fig. 2.9) and Table 2.1.

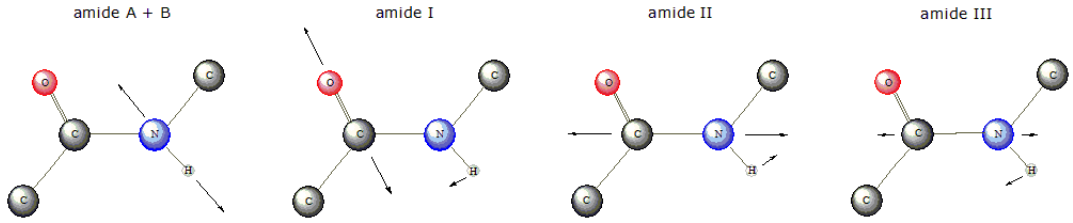

Figure 2.9: Scheme of protein amide vibration of predominant group modes indicated by arrows and assigend to correpsonding wavenumbers in Table 2.1.

Table 2.1: Assignment of protein amide vibrations to wavenumber regions, which correspond to the predominant group modes illustrated in Fig. 2.9.

designation	wavenumber / cm^{-1}	group vibrations
amide A	3310 - 3270	N-H stretching; 1st Fermi resonance with first overtone of amide II
amide B	3010 - 1600	N-H stretching; 2nd Fermi resonance with first overtone of amide II
amide I	1700 - 1600	C=O stretching with minor contributions of N-H bending
amide II	1580 - 1480	combination of N-H bending and C-N stretching
amide III	1300 - 1230	combination of N-H bending and C-N stretching

The focus with respect to the protein backbone vibrations is formally directed to the amide I and amide II bands, which can be predominantly ascribed to the stretching vibration of the C=O combined with minor N-H bending and to N-H bending combined with C-N, respectively. So far, amide I band is the most extensively studied one and can provide valuable information. Thus, e.g. vibration for different secondary structures can be discriminated due to different hydrogen bonds in between the structures. Both vibrational contributions, namely the C=O stretching and N-H bendings can be easily effected by their interacting hydrogen bonds. Therefore, components can be assigned to their structural fragments.

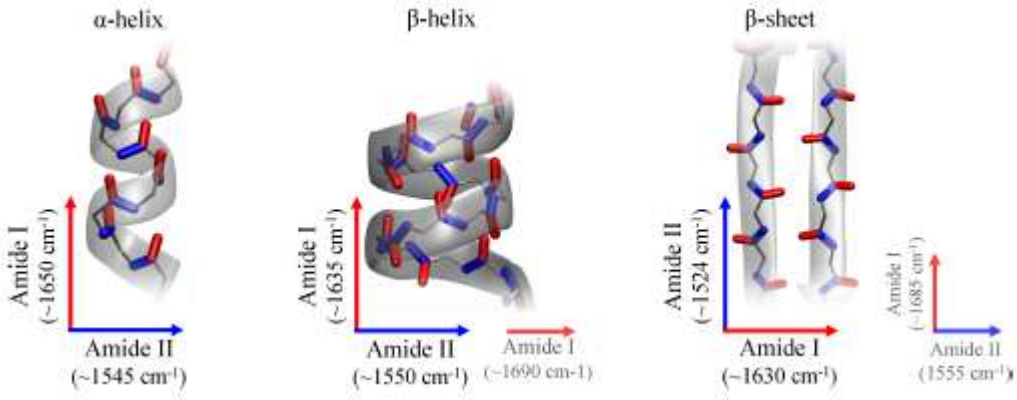

Figure 2.10: α-helix (left), β-helix (center), and β-sheet (right) composed of C=O and C-N bonds, which are highlighted in red and blue, respectively. Due to the periodical alignment of these bonds, the total dipole moments of amide I and amide II of the secondary structure elements are orientated perpendicular to each other as indicated by the arrows for amide I (red) and amide II (blue). (PDB: 1KdL, 1MAG, and 1JY4, respectively. Graph depicted from reference [116]

α-helix consists of N-H forming hydrogen bonds sequencely with the C=O group four residues earlier. The α-helix exhibits a sole amide I IR absorption usually in a range between 1657 cm^{-1} and 1648 cm^{-1}. The transition dipole moment is oriented in parallel to the helix axis. The amide II band is located at ca. 1545 cm^{-1} with a perpendicular polarization relative to the helox axis.

3_{10}-helix exhibits similar structure to α-helix, but forms hydrogen bonds with each third residue. The corresponding helical structure is packed slightly tighter.

β-sheet is connected laterally by backbone hydrogen bonds, forming a twisted, pleated sheet. Due to the dipole moment coupling, the amide I band splits into two components. The main absorption occurs ar 1630 cm^{-1} with a dipole moment oriented perpendicular to the propagation direction of the chain. The weaker absorption is located at ca. 1685 cm^{-1} revealing a dipole moment parallel along its chain. The related amide II band of β-sheets is split in two components showing a strong absorption at 1524 cm^{-1} and a weaker at 1555 cm^{-1} as well.

β-helix shows similar features as observed for β-sheet and exhibit in such way one weaker and one stronger component, perpendicular and parallel dipole moments relative to the helical axis, at 1635cm^{-1} and 1690 cm^{-1}, respectively.

Turn differ significantly in their hydrogen bonding network and therefore show an unspecific absorption in a range between 1690 cm^{-1} and 1630 cm^{-1}. However, most often the amide I band can be found between 1686 and 1662 cm^{-1}.

Random Coil overlaps with the observable positions of α-helices and is located at around 1650 cm^{-1}. Membrane proteins rarely harbour such segments.

Surface-Selection Rule is based on the local EM in the surface enhancement effect, which is polarized perpendicular (along the z-axis) to the metal surface at every point at the mtal surface. Besides the enhancemnt of IR signal, the alignment of the vibrational mode relative to the surface determines observable IR intensity. This allows to characterize orientation of adsobed molecules, but also gives insights into possible reorientations. Structural elements with a dipole moment change associated with an excited vibrational transition oriented parallel to the metal surface (in the xy-plane) do not exhibit any effective IR absorption $I_{\parallel} = 0$; those oriented perpendicular to the surface display the highest intensity of the IR band ($I_{\perp}$; along z-direction). For orientations in between both of these two extremes, the intensity depends on the z-component of the dipole moment change and, hence, on the angle relative to the surface normal:

$$I_{IR,\theta} = I_{IR,\perp} \cdot cos\,\theta \tag{2.25}$$

As mentioned above, the amide I and amide II vibrations are comprised mostly of C=O and C-N stretchings, respectively. These groups appear in a periodical orientation in helices and sheets and experience a coupling of their dipole moments. This leads to a coupled oscillating system of amide I and amide II vibrations, respectively,[114] characterisitc for the entire secondary structure unit (see Figure 2.10). Consequently, the total dipole moment changes of these amide bands show a specific orientation for helices and sheets.

2.2.2.5 Infrared spectroscopy of *Re* MBH/active site of MBH

[NiFe] hydrogenases harbours three inorganic diatomic ligands coordinated to the Fe atom of the bimetallic active site: one carbonyl monoxide and two cyanides [117]. In the IR, these stretching vibrations occur in a specific spectral region free of other vibrations, e.g. from protein backbone. The exact band positions are sensitive to small changes of electron density related to varying ligation or changes in the surrounding amino acid environment of the active site. In more detail, the observable shifts of the characteristic frequencies of CO and CN^- ligands are mainly based on the distinctive π-acceptor capabilities [118]. In this context, a higher electron density at the Fe atom would cause a stronger backbonding into an antibinding "π" orbital, which leads in turn to a shift to higher stretching frequencies. Furthermore, changes of the stretching vibrations of the ligand can also result from varying hydrogen bonding interactions with surrounding amino acids in the second coordination sphere e.g. caused by point-/ site-directed mutagenesis [119, 120].

Generally, most coordinated carbonyl and cyanide functionalities exhibit strong and sharp bands. The typical spectral regions for [NiFe] hydrogenases are 1970-1890 cm^{-1} for CO stretchings and

2120-2040 cm^{-1} for CN vibrations. Free CO in aqueous solution absorbs at 2155 cm^{-1}, while the corresponding band for free CN^- is localized at 2080 cm^{-1}.[54, 121]

The typical IR spectral regime are displayed from *Re* Membrane-Bound [NiFe] Hydrogenase in Figure 2.11, where the absorption bands of the CO and CN ligands of the active site are found. In cases of samples with low protein concentrations or when band positions of different redox states are located in close vicinity, a visual resolution enhancement can be achieved by displaying the absorbance spectra as the corresponding second derivatives. This allows a better differentiation of the absorption band as sharp peaks because broader background modulation and baseline drifts are suppressed.

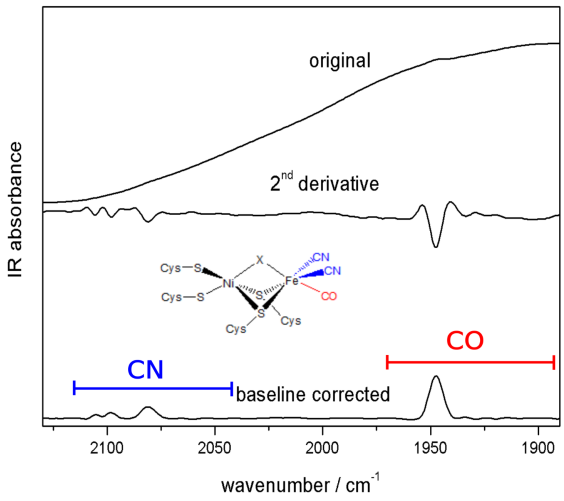

Figure 2.11: FTIR absorbance spectra, the second derivative and the baseline corrected spectrum of a sample from a [NiFe]-hydrogenase, exhibiting a mixture of several redox states. Each state is normally characterized by one CO and two CN stretching vibrations, suggesting some bandoverlaps.

By means of IR spectroscopy all redox states of the active site can be examined, which cannot be accomplished by EPR (see section *2.1.1.4*). In contrast to X-ray crystallography, dynamic structural changes in the ligation can be detected by IR spectroscopy. In combination with electrochemistry, so called IR-SEC, detailed information about the redox potentials, the number of electrons and protons involved in redox transition as well as slow kinetic might be determined.

The kinetic behavior of the enzyme adsorption within the immobilization time can be derived from plotting IR absorption intensity (A) of amide I, amide II or CO band as a function of time (t). These will be described in the following chapters by a mono-/ or biexponential processes, i.e. a first or second order decay of adsorbent, defined as

$$A = A_0 + A_1 \exp(-t/\tau_1) \text{ or } A = A_0 + A_1 \exp(-t/\tau_1) + A_2 \exp(-t/\tau_2).$$

with A_0, A_1 and A_2 present the absorbance intensities of amide I or amide II band at the final adsorption time, at the first and the second completed adsorption process, respectively. Further, τ_1 and τ_2 present time constants for the first and the second adsorption process, respectively. Therefore, the kinetic processes and time scales of *Re* MBH adsorption and surface interaction can be distinguished in more detail.

2.2.3 UV-Vis Spectroscopy

In the UV-Vis range (UV: λ= 1-400 nm; Vis: λ=400-800 nm), absorption of light causes vibronic transitions inducing simultaneously electronic, vibrational and rotational excitations. Due to the strong interactions between molecules in solution, the electronic transitions occur as broad bands. The rotational transitions can not resolved even in gas phase. Hence, these transitions are in most cases neglected. The intensity of a transition from an electronic (n) and vibrational (ν) ground states $S_{0,0}$ to the corresponding excited state $S_{n,\nu}$ is proportional to the square of the transition dipole moment M, which can be separated into the electronic $M_{0;\nu}$ and the vibrational contribution $F_{0,0;n,\nu}$

$$M = M_{0;\nu} F_{0,0;n,\nu} \tag{2.26}$$

where $F_{0,0;n,\nu}$ exhibits the vibrational overlap integral of the corresponding vibronic wave functions $\chi_{0,0}$ and $\chi_{n,\nu}$

$$F_{0,0;n,\nu} = \chi_{0,0}\chi_{n,\nu} dr \tag{2.27}$$

thereby r is the internuclear distance. The transition probability between the vibrational ground S_0 and an excited state S_n is given by the Franck-Condon factor which is defined as the square of $F_{0,0;n,\nu}$.

The electronic transition dipole moment $M_{0;n}$ with the wave functions ψ is determined as

$$M_{0,n} = \psi \mu \psi dq_e \tag{2.28}$$

During the scan of an UV-Vis spectrum, the wavelength of the incident light is continuously varied. The observed absorption bands in the UV-Vis spectrum can be preferentially interpreted as energy-rich electronic transition at significant wavelengths. Due to the excitation of the molecules, the light intensity of the UV-Vis source I_0 is reduced to an intensity I and subsequently detected. Assuming a reasonable low concentrations c of the sample this intensity-loss obeys the law of Lambert-Beer

$$A = log \frac{I_0}{I} = \epsilon c d \tag{2.29}$$

where d is the thickness of the sample, which is passed by the light beam and ϵ is the extinction coefficient of the investigated samples.

2.2.4 Semiconductor

The properties of semiconductor electrodes and their differences to metallic electrodes can be understood by examining the electronic strucutres of the material. The highest and lowest energy levels of a band are referred to as the band edges. The energy bands of intrest are the highest occupied (valence band) and the lowest unoccupied (conduction band). It is the energy gap between these bands (band gap) that determines the properties of the material.

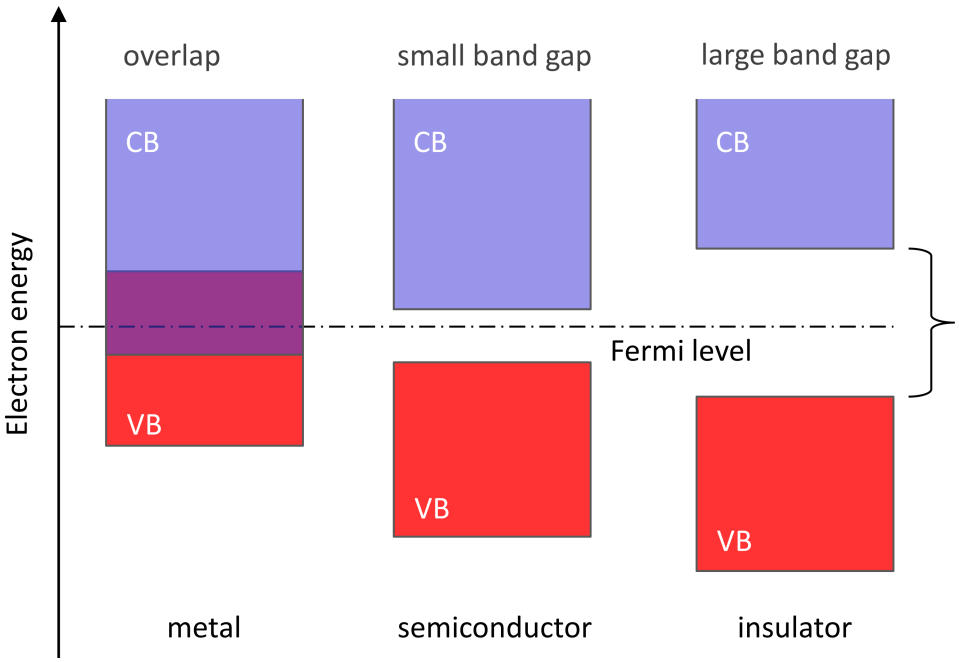

Figure 2.12: Band structure diagrams for relative energetic position of valence band (VB), conduction band (CB) of metal, semiconductor and insulator materials.

Conductivity of a solid state material requires that the electrons occupy partially filled orbitals. This is achieved by occupancy of the conduction band. For metals, the conduction and valence bands overlap, so the conduction band can be readily occupied.

For insulators, the band gap is sufficiently large that electrons cannot be promoted from the valence band to the conduction band. However, for semiconductors, the band gap is not as large, and electrons can be moved into the conduction band. The promotion of electrons leaves a positively charged vacancy in the valence band, which is referred to as a hole. These holes can be moved through space by the transfer of an electron to the vacancy; therefore, holes are considered to be mobile. Electrons can be excited to the conduction band either thermally or photochemically. However, there is another method for generating charge carriers (i.e. electrons or holes) within a semiconductor, referred to as doping. Doping involves the addition of a different element into the semiconductor. The simplest example of this involves the introduction of a group V element (e.g. P) or a group III element (e.g. Al) into a group IV element (e.g. Si). The addition of P into Si introduces occupied energy levels into the band gap close to the lower edge of the conduction band, thereby allowing facile promotion of electrons into the conduction band. The addition of Al introduces vacant energy levels into the band gap close to the upper edge of the valence band, which allows facile promotion of electrons from the valence band. This leads to the formation of holes in the valence band. Undoped semiconductors are referred to as intrinsic semiconductors.

The characterization of semiconductor electrodes is defined by the dominant (or majority) charge carriers. In case of majority charge carrieres being electrons, the materials are referred to as n-type semiconductor, whereas those in which holes are the majority charge carriers are referred to as p-type semiconductors (see section. 2.3.1)

The following sections will discuss transparent conducting oxides, which belong to a subgroup of

semiconductor materials and are used in this work as electrode material. Further, an introduction to the electrochemical properties at the semiconductor/eleytrolyte interface will be given in section 2.4.3.

2.3 Transparent Conducting Oxides (TCO)

Most TCO's belong to a subspecies of n-type semiconductors which exhibit high electric conductivity (10^3 ~ 10^4 S cm^{-1}) and high optical transparency (> 80%).[122, 123, 124] Typically, values of high electric conductivity are associated to metals owning a high density of free charge carriers. The latter exhibit high optical absorptions of electromagnetic radiation and hence prevent an optical transmission. On contrary, insulators are known for transparency provided by their large band gaps, but posses low or no conductivities. Transparent conducting oxides have the particular property of owning both of these characteristics. TCO's are wavelength dependent optical resistors as they are capable of generating mobile electrons as well as they are dopant dependent electrical conductors. Transparent conductive electrodes play important roles in information and energy technologies, as their optical transparency in the visible region is combined with a controllable electrical conductivity. These materials, particularly transparent conductive oxides, are widely used as transparent electrodes across technical fields such as low-emissivity coatings, flat-panel displays, thin-film solar cells and organic light-emitting diodes. The first TCO, cadmium oxide (CdO), was discovered 1907 by Badekar.[125] The research in the fields of transparent conductor materials grew intensively in the last decades.[126] In the last half century, systems such as indium oxide (In_2O_3), tin oxide (SnO_2) and zin oxide (ZnO) as well as related binary, ternary and quaternary systems have been developed and applied in modern technology.[127, 128]

2.3.1 Theoretical Background of TCO's

In all semiconductors, there is a forbidden energy region or gap in which energy states cannot exist. Energy bands are only permitted above and below this energy gap. The upper bands are called the conduction bands, while the lower ones are called the valence bands. Figure 2.13 illustrates perfect isolators such as oxide glasses with a high transparency due to their large energy bandgap, usually $E_g > 4$ eV, and a low amount of free charge carriers hindering an electrical conductivity. However, high free charge concentration can be introduced within the forbidden zone intrinsically by defects such as oxygen deficiencies or extrinsically by substitutional dopant in the host matrix.

As displayed in Figure 2.13, when a semiconductor is doped with donor or acceptor atoms, the donor level close to the conduction band or the acceptor level close to valence band can be filled, respectively. The donor level is defined as being neutral if filled by an electron, and positive if empty. An acceptor level is neutral if empty, and negative if filled by an electron. Depending on the distance of the donor and acceptor levels with respect to the corresponding bands, electrons can be thermally excited into the conduction band as well as holes into the valence band thereby achieving conductivity. Most of the TCO materials are n-type semiconductors such as Sn-doped In_2O_3 (ITO) and Sb doped SnO_2 (ATO), which are used in this work.

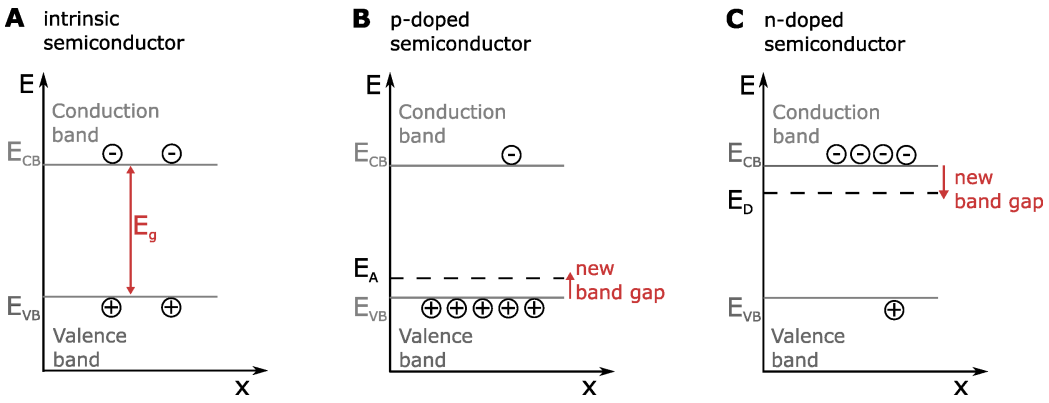

Figure 2.13: Band diagrams of (A) a undoped intrinsic semiconductor (B) an p-doped semiconductor (C)a n-type semiconductor.

The charge carrier concentration (density) can be obtained by approximating the Fermi-Dirac integral by a Boltzmann distribution for holes (p):

$$p = N_{VB} \exp\left(-\frac{(E_F - E_{VB})}{kT}\right) \tag{2.30}$$

The number of electrons (n) occupying levels in the conduction band is given by

$$n = N_{CB} \exp\left(-\frac{(E_{CB} - E_F)}{kT}\right) \tag{2.31}$$

where N_{CB} presents the effective density of states at valence band maximum, E_{F} is fermi level, $E_{\mathrm{VB}}$is valence band edge, k is Boltzmann constant and T is temperature.

where N_{CB}, N_{VB}- effective density of energy states *(DOS)* of conduction and valence band, respectively, and are defined at valence band maximum by

$$N_{VB} = 2\left(\frac{m_h^* kT}{2\pi\hbar^2}\right)^{2/3} \tag{2.32}$$

and at conduction band minimum by

$$N_{CB} = 2\left(\frac{m_e^* kT}{2\pi\hbar^2}\right)^{2/3}. \tag{2.33}$$

Here, $m^*_{(e,h)}$ denotes the effective mass of electrons or holes; deviation of from free particles behavior- to describe the energy band structure of solid.

The Fermi level is euqivalent to the total chemical potential for electrons. In a band structure picture, the Fermi level can be considered as a hypothetical energy level of an electron, such that at thermodynamic equilibrium this energy level exhibits the probability of the half occupied level. The position of the Fermi level can then be calculated from

$$E_F = \frac{(E_{VB} + E_{CB})}{2} + \frac{kT}{2} ln \frac{N_{VB}}{N_{CB}} \tag{2.34}$$

The electrochemical potential of electrons is given by the Nernst equation (eq. 2.41) in relation to the standard hydrogen reference electrode as displayed in Figure 2.14. A theoretical absolute scale is defined by the vacuum level as a reference point.

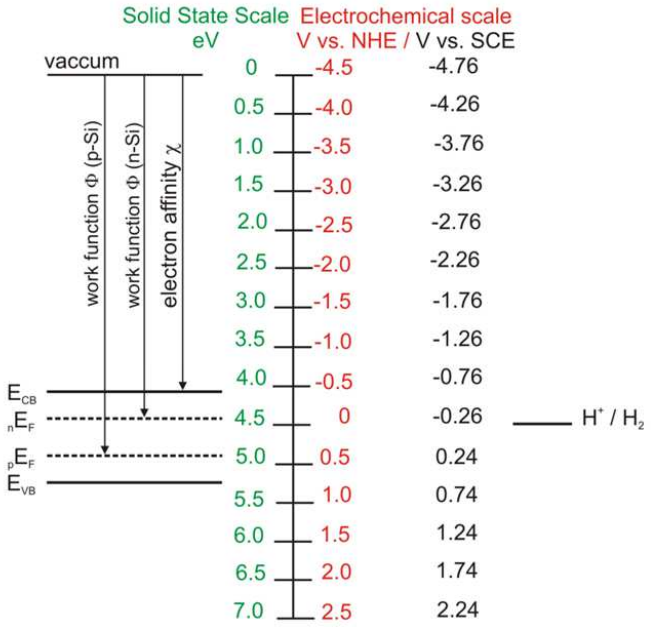

Figure 2.14: Schematic illustration of semiconductor band position in repect to energy level of solid state (eV), compared to electrochemical scale (NHE and SCE), and compared to redox couple of H^+/H_2. depicted from reference [129].

The vacuum level is the energy of an electron far from the influence of the potential of the solid. The electron affinity for a semiconductor is the energy required to remove an electron from the bottom of the conduction band to the vacuum level. The work function is the energy required to take an electron from the Fermi level to the vacuum.

Electrical and optical properties

The electrical conductivity and visible transparency are the two characteristics of semiconductors, which strongly relate on another.[123] The electric conductivity depends on the charge carrier density and charge carrier mobility in the presence of elemental charge and hence is described as

$$\sigma = n_e \cdot \mu \cdot e \tag{2.35}$$

where μ represents the charge carrier mobility, n_e the charge carrier density, and e the elementary charge. The material resistivity ρ can be expressed as

$$\rho = (n_e \cdot \mu \cdot e)^{-1} \tag{2.36}$$

From the resistivity and the film thickness d the films sheet resistance Rs can be derived as follows:

$$R_s = \frac{\rho}{d} \tag{2.37}$$

The transparency can generally be defined following the Lambert-Beer law as already described after same principle as UV-Vis Absorption (*see* eq. 2.13). The absorption coefficient of a semiconductor material at a given wavelength determines the spatial region in which most of the light is absorbed. Depending on the electronic band structure, band gaps of metal oxides count to the group of indirect absorption band gaps, which usually exhibit only low absorptions.

2.3.2 Application / TCO examples

Tin-doped Indium Oxide (ITO) is a very common TCO material. This material has extremely complicated refractive indices with optical absorptions in both the UV and the NIR regions. Each manufactured ITO film can show widely varying refractive indices depending on production conditions.[130] In comparison to pure In_2O_3, tin-doped In_2O_3 exhibits higher electrical conductivity due to the substitution of indium atoms (3+) by tin atom (4+). This cation substitution process generates one additional electron contributing to the formation of a lower energy level of the conduction band, *vide supra* (section 2.3.1). The incorporation level of Sn atoms into the In_2O_3 lattice counts usually 5-15 mol%.[131] Its high visible transparency (T > 85 %) combined with its good electrical conductivity (10^3 ~ 10^4 S cm^{-1}) makes ITO coatings a very attractive materials for an application as transparent electrodes, flat panel display construction[132] for gas sensing,[133] or enzyme immobilization.[134, 135] Since natural resources of indium are limited and the ITO coating production has increased drastically in the last decades, indium becomes more and more precious. In the last years, the development of reduced indium content TCO materials became necessary in regard of sustainability. However, comparable electrical conductivity and optical transparency challenges productions for ITO alternatives. Some examples of "indium saving" alternatives were recently developed. Besides hetero-bimetallic systems such as Zn-In-O[136]and In-Cd-O [137], also indium-free materials have gained relavance as like doped SnO_2 (Sb -, Nb- and Ta-doped SnO_2).[138, 139] Since parts of this thesis focus on alternative ITO materials such as Sn-rich In_2O_3 (ITO_{TR}) and Sb-doped SnO_2 (ATO) (see section 2.3.4), the following section describes their material characteristics briefly.

2.3.3 Tin-rich Indium Tin Oxide (ITO_{TR})

One promising example of an ITO alternative was recently reported by Veith et al.,[140, 141, 142] and Aksu et al. [143]. The synthesis of this novel tin-rich ITO material was established with a largely reduced indium content (from 90% in ITO down to 50% in tin-rich ITO).[143] The synthesis route for tin-rich ITO (ITO_{TR}) is based on a single source precursor approach. This is accomplished by the thermal decomposition of a single source precursor molecule, namely indium(I)tin(II)-*tert*-butyl-oxide (ITBO), containing a ratio of 1:1 of the required elements.[141] The single source precursor enables the fabrication of thin films with homogenousdistribution of the incolved elements as well as the fine tuning of the final material morphology.[141] This approach provides a great advantage over the traditional processes such as sol-gel, which are usually based on different single metallic precursors.

The thermal decomposition of deposited ITBO thin films at 400°C leads to homogenous coatings with a final indium and tin content of 1:1, reflecting the initial composition of the single source

precursor (Sn:In ratio of 1:1). Besides high transparency (98%),[144] ITO_{TR} thin films exhibit surprisingly high conductivities (10^3 S cm^{-1})[143] in the amorphous state. Those properties make ITO_{TR} thin films an interesting alternative for regular ITO coatings, which could be used as transparent conductive platform for the immobilization and spectro-electrochemical investigation of electrocatalysts such as enzymes. The following chapter section will first describe the preparation and characterization of the heterobimetallic indium tin precursor ITBO as developed by Veith and coworkers,[145] followed by the synthesis of ITO_{TR} coatings as prepared by Aksu et al.,[143] and Guiet et al. [146, 147].

The synthesis of indium(I) tin(II) tris-*tert*-butoxide, $InSn(OtBu)_3$ (ITBO), has been reported by Veith and Kunz in 1991.[145] The compound was obtained from $Na(OtBu)_3Sn$(II) in a heterogeneous salt elimination reaction with In(I)Br as following

$$Na(OtBu)_3Sn + InBr \xrightarrow{-NaBr} In(OtBu)_3Sn$$

The complex has a distorted trigonal bipyramidal InO_3Sn structure with In and Sn in apical positions and the three oxygen in equatorial positions (Figure 2.15). The metal ions harbor both, a lone electron pair and occur in their lowest oxidation states (In^{+1} and Sn^{+2}). Therefore, ITBO could react as a double Lewis base towards electrophilic metal centers under formation of covalent binding with Sn and In.

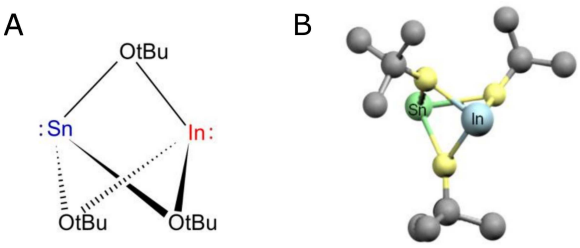

Figure 2.15: Representation of (A) structural formula and (B) molecular structure of indium(I) tin(II) tris-tert-butoxide, $InSn(OtBu)_3$ determined by x-ray analysis.[145] Gray spheres are carbon atoms. Hydrogen atoms are not shown. Depicted from reference [148].

The high solubility of ITBO in organic solvents, e.g. until 800 mg/mL in toluene, allows a simple synthesis by spin-coating of homogenous ITO_{TR} thin films directly from its precursor solutions. As reported of the group of Prof. Driess (TU Berlin),[143, 135] thin film ITO_{TR} deposition can be achieved from a concentrated ITBO solution in toluene by spin-coating under controlled inert conditions ($<$ 1 ppm H_2O, $<$ 1 ppm O_2). After solvent evaporation, the deposited thin film is exposed to a subsequent thermal treatment under air, which leads to the formation of homogeneous transparent ITO_{TR} thin films. A second thermal treatment under forming gas results in long-term stable and highly conductive homogenous thin film electrodes. The first calcination step under air atmosphere leads to a complete oxidative combustion of the organic *tert*-butyl groups. Thus, under thermal decomposition and release of carbon dioxide and water, the formation of a material solely composed of a metal-oxygen matrix, $InSnO_x$ with In^{3+} and Sn^{4+}, is achieved.

$$In(OtBu)_3Sn \xrightarrow[-CO_2,-H_2O]{O_2,25-600^{\circ}C} InSnO_x$$

Guiet et al [146, 147, 148] exemplified the immense flexibility of 3D material design and reported a great variety for different ITO_{TR} nanoparticle compositions, which are highly relevant in nowadays heterogeneous catalysis. A more detailed insight of the material can be found in reference [146, 147].

2.3.4 Tin-doped Antimony Oxide (ATO)

Besides ITO_{TR} films, an alternative, commonly used, well-crystallized material, which is based on SnO_2 doped with Sb or F. These materials can be found among others in applications for transparent, electrical conductors, low-emittance coatings and frost-preventing surfaces .[149, 150] Tin oxide is known as a wide band gap material (e.g. between 3.6-4.0 eV) and crystallizes in the rutile cassiterite structure. Due to its unique physical properties such as high electrical conductivity, high transparency in the visible part of the spectrum and high reflectivity in the IR region [151], this system has gained high interest and was extensively studied in the last years.[152, 130, 153, 154, 155] Particularly, they are stable up to high temperatures, exhibit an excellent resistance to strong acids and bases at room temperature and displays very good adhesion to many substrates as well as perform as electrode platforms for biocatalyst adsorption.[156, 157] All these properties have promoted an intense research on SnO_2 coatings over the past few decades. Tin oxide films have been prepared by various techniques such as sputtering [152], spray-pyrolysis [130], electron-beam from bulk samples [153], sol gel [154] dip coating of precursor solutions.[155] It is well described in literature that the film conductivity increases largely without losing optical transparency with a small amount of dopant.[158] Alternatively, the preparation of Sb- doped SnO_2 (ATO) thin films can be also easily prepared by evaporation induced self-assembly (EISA) of crystalline ATO nanoparticles (NPs) sols. [139, 157] The preparation of the ATO NPs is described in more detail reference [157].

2.4 Electrode Interfaces

2.4.1 Metal Electrode-Electrolyte Interfaces

Inserting a bare metal electrode into an aqueous solution leads to redistribution of charges and thus to a charged interface.[92] Depending on the kind of metal and electrolyte, the electron density of the metal is either reduced or increased which results in an excess concentration and even adsorption of oppositely charged ions at the electrode surface under formation of an electric double layer (DL). This phenomena does not require externally applied potentials and takes place already at open circuit conditions. The charge distribution at the solid/water interface, shown in Figure 2.16 (A), can be described by a combination of the Helmholtz and the Gouy-Chapman concept. According to this, the first layer in direct contact at the electrode surface defines a compact film of absorbed ions and/or a highly ordered water matrix.

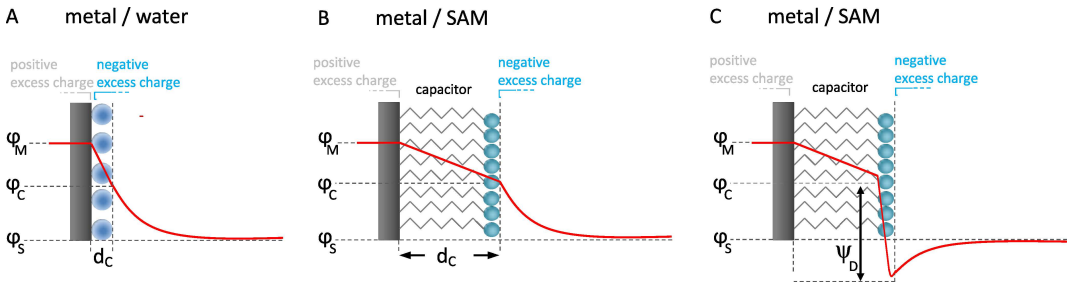

Figure 2.16: Scheme of potential profiles in the electrical double layer at (A) a metal-electrolyte interface with absorbed ions, (B) a metal coated by self-assembled monolayer with polar funtional groups in contact with electrolyte presented in a simplified model and (C) in an advanced model including the dipole potential ψ_D deduced by the polar functional group. The potential of metal φ_M , the inner Helmholtz layer φ_C and of the solution φ_S, as well as the thickness of the inner Helmholtz layer d_C are illustrated in each model (A-C).

The interactions between the ions in solution and the electrode surface are asssumed to be electrostatic and result from the fact that the electrode holds a charge density (σ_M) arising from either an excess or deficiency of electrons at the electrode surface. In order to preserve a neutral interface, the charge at the electrode is balanced by the redistribution of ions close to the electrode surface. The overall results are two layers of charges, known as the double layer, and a potential drop which is confined to only this region, finally reaching the outer Helmholtz Plane (OHP) in solution. This can be regarded analogous to an electrical capacitor, which are two plates of charge separated by a distance. The outer Helmholtz or diffuse double layer represents the region in which the ions can diffuse freely underlying a concentration gradient, which is determined by the interfacial electric field.

The potential distribution in the proximity of a metal can be described on the basis of a simple electrostatic model in which the charge densities at each interface have to be considered (see [159]).

The charge density of the inner Hemholtz layer σ_C is defined by the requirement of charge neutrality of the complete system :

$$\sigma_M + \sigma_C + \sigma_S = 0 \tag{2.38}$$

Under potential applications, the potential of the metal electrode can be set and a charge redistribution and ion reformation in the water matrix at the surface takes place under maintanace of charge neutrality of the complete system. Hereby, the potential of zero charge (E_{PZC}) can be understood as the absolute charge density equals zero, $\varphi_M = \varphi_S$. In this conext, no effective field perturbates the solution and no DL formation occurs. Coating the electrode with an amphiphilic self-assembled monolayer (SAM), as shown in Figure 2.16B, introduces a hydrophobic layer functioning as capacitor and a hydrophilic polar funtional group facing the solution. The hydrophobic layer lowers the dielectric constant ($e_r \sim 2-3$). The potential drops linearly along the capacitive layer similar to Figure 2.16B. This model disregards the influence of the charging functional group. Therefore, a more elaborate model contemplates the dipole potential ψ_D deduced by the polar functional group and can be displayed as shown in Figure 2.16C.[160]

2.4.2 Self Assembeled Monolayer (SAM)

The direct adsorption of proteins at metal surfaces is known to cause denaturation of the protein, i.e. the loss of its structure and thus the distruction of its function. Due to the strong electric felds at the metal/water interface proteins may unfold.[161] Self-assembled monolayers (SAMs) are a simple and variable way to cover the metal surface, resulting in high compact, organic monolayer films, thereby establishing a biocompatible electrode. The self-assembly of amphiphilic alkanethiols are structured as R-$(CH_2)_n$-SH chains, where n denotes the length of the alkyl chain. The sulfur species can adsorb spontaneously under covalent binding at a variety of noble metals, especially Au and Ag electrodes can be easily coated in such way. The organic chain interacts leading to a highly ordered monolayer by self-assembly based on van der Waals forces.[162, 163] The strength of thiol-metal bonds is in the order of 100 kJ/mol, which make it fairly stable with respect to variations of temperature, solvents, and potentials.[164] The specific properties such as the packaging density, the degree of order or the angle between the metal-S-chain of the assembled monolayer depend on the particular type of the employed SAM, i.e. on the number of n and the nature of R, which represents a functional group. Depending on the properties of the protein, e.g. its charge distribution or dipole moment, R is selected correspondingly to ensure an efficient adsorption. Thus, cytochrome *c* with a positive binding patch can be effectively adsorbed using a negatively charged SAM (R: carboxylic acid group) via electrostatic forces.[165]

Figure 2.17 illustrates common mechanisms for protein adsorption using different kind of functional groups. The most complex immobilization strategy refers to the cases in Fig. 2.17E and F where adsorption of the protein is achieved via formation of covalent or coordinative bonds between the SAM and the biomolecule.[166, 167] Besides direct adsorption of protein at the surface, strategies for the formation of phospholipid membran films have been recently established to embedd membrane-integral enzymes and investigate these in their natural environement.[168, 169] The choice of R in combination with pH of the electrolyte reflects the charge density at the interface. A more profound introduction to SAMs can be found in the cited literature.[170, 171]

2.4.3 Electrochemistry on Semiconductors

There is a fundamental difference between electron-transfer reactions on metals and on semiconductors. On metals the variation of the electrode potential causes a related change in the molar Gibbs energy of the reaction. Due to the comparatively low conductivity of semiconductors, the positions of the band edges at the semiconductor surface do not change with respect to the solution as the potential is varied. However, the relative position of the Fermi level in the semiconductor is changed, and so are the densities of electrons and holes on the semiconductor surface. The periodic pattern of chemical bonds in the crystal is interrupted at the surface, resulting in unsaturated bonds, which can rearrange (surface reconstruction). This results in a change of both, the surface crystal structure and the allowed energies. The electronic surface structure is not related with the bulk structure.

2.4.3.1 Energy States in Solution

When a semiconductor electrode is brought into contact with an electrolyte solution a spatial separation of charges at the surface as well as a potential difference is established at the interface.

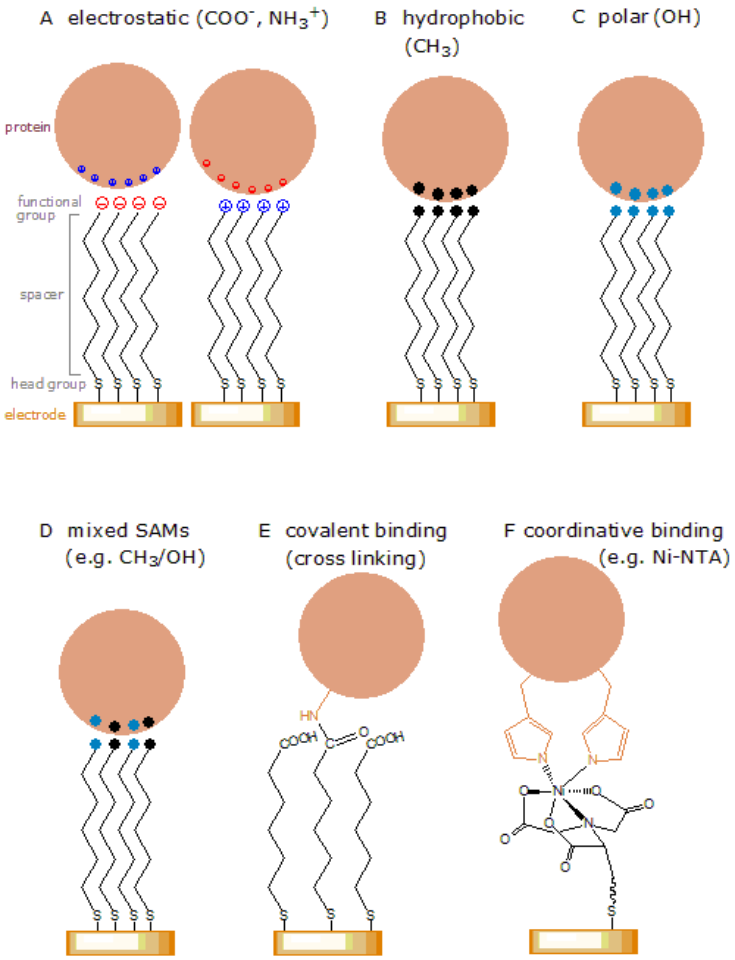

Figure 2.17: Illustration of different protein (flesh colored sphere) immobilization strategies as presented in (A) electrostatic, (B) hydrophobic and (C) polar forces as well as (D) combinations of mixed SAMs, (E) covalent bonds or (F) coordinative binding strategies, such as examplified by protein affinity-tags, which are used for high-performance liquid chromatography.

The conductivity of doped semiconductors is usually below that of an electrolyte solution, so that the entire potential drop occurs in the boundary layer of the electrode denoted as the space charge region and only to a minor extend on the solution side of the interface. This space charge region has an associated electrical field. However, the energetic position of the band edges at the surface of each material remains unaltered. The opposed behavior is observed for metal electrodes-electrolyte interfaces (see section 2.4.1) (Schottky-like junction). While metals exhibit a charge distribution within a range of 0.1 Å, semiconductors distribute the charge over a certain distance below the surface in nm scale. The electrochemical potential of the solution is determined by the redox potential (chemical potential) of the electrolyte solution itself, and the redox potential of the semiconductor determined by its Fermi-level. The electrochemical potential $\bar{\mu}_{e,redox}$ is defined for solutions by the Nernst equation (eq. 2.41) and is equivalent to a Fermi level of a redox system, $E_{F,redox}$, under the condition that the same reference level is used for the solid electrode and the redox system, as first introduced by Gerischer.[172, 173] Hence it is defined as

$$E_{F,redox} = \left(\frac{e}{F}\right) \bar{\mu}_{e,redox} \tag{2.39}$$

The Gerischer model introduces a model for charge transfer processes at the semiconductor-electrolyte interface. Following this model, band diagrams can be constructed to understand the state of electronic surface states, fundamental for ET processes, *vide infra*.

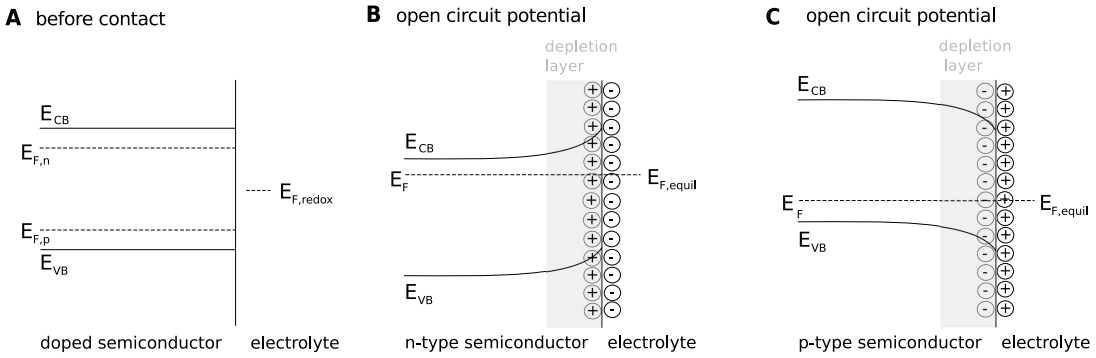

Figure 2.18: Energy level diagrams for semiconductor-electrolyte junctions. Schematic depiction of band bending in equilibrium with the electrolyte for (A) a n-type semiconductor and (B) a p-type semiconductor.

The energy schemes of an n-and p-type electrode prior and after contact with an aqueous solution of a redox system, at equilibrium are shown in Figure 2.18. For an n-type semiconductor electrode at open circuit potential, the Fermi level is typically higher than the redox potential of the electrolyte and hence electrons will be transferred from the electrode into the solution. Therefore, a positive charge is associated with the space charge region, whikle is reflected in an upward bending of the band edges (see Figure 2.18B). Since the majority charge carrier of the semiconductor has been removed from this region, the space charge region is also referred as depletion layer. For a p-type semiconductor, the Fermi layer is generally lower than the redox potential of the solution . Thus, electrons must be transferred from the solution to the electrode to obtain an equilibrium. This generates a negative charge in the space charge region, which causes a downward bending in the band edges (see Figure 2.18C). Since the holes in this area are removed by this process. This space charge region is again referred as depletion layer, but in this case with a opposed charge distribution along semiconductor-electrolyte interface.

2.4.3.2 Electron Transfer Processes

The Fermi level concept is very useful for a quantitative description of reactions on semiconductor electrodes, as described in section 2.4.3.1. Besides the Fermi level, also energy states for a a redox system can be defined. Any variation of the electrode potential occurs across the space charge layer which leads to an equivalent change of the band bending in the energy diagram ($\Delta(eUE) = \Delta(e\Delta\varphi sc)$).

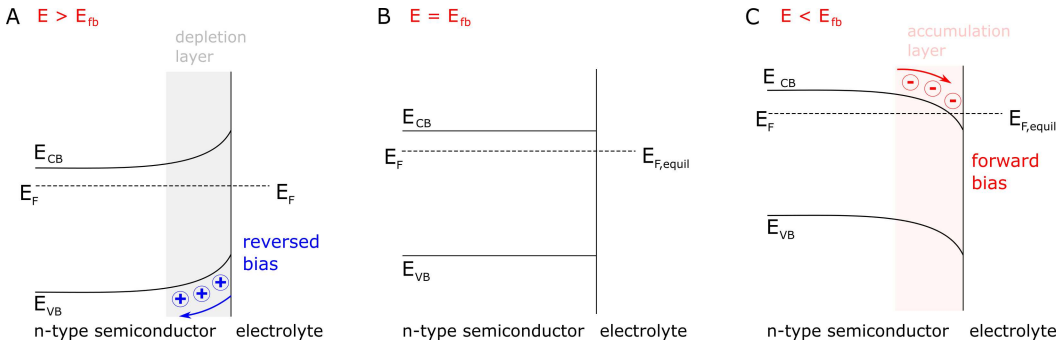

Figure 2.19: Energy diagram for a n-type semiconductor under conditions of (A) more negative potentials, (B) potential equal and (C) more positive potentials compared to the flat band potential (position).

As observed for metallic electrodes, a change in the potential applied to the electrode shifts the Fermi level. The band edges of the semiconductor also vary with the applied potential in the same way as the Fermi level. However, the energies of the band edges at the interface still remain unaffected even under applied potentials. Therefore, the magnitude and direction of band bending varies with the applied potential. Three different conditions have to be considered and are displayed for an n-type semiconductor. Figure 2.19A displays a depletion region, which arises at potentials more positive than the semiconductor flat-band potential. The flat-band potential can be considered equal to the potential of zero charge defined for metal/electrolyte interfaces. For semiconductor/electrolyte barriers, the flat band potential lies at a certain potential, at which the Fermi energy equals those of the solution redox potential (Figure 2.19B). As there is no net transfer of charge, no band bending is observed. This potential is therefore referred to as the flat-band potential, Efb. Potentials more negative than the flat-band potential provides an excess of the majority charge carrier (electrons) in this space charge region denoted as an accumulation region (Figure 2.19C). The different electronic surface states at the semiconductor interface are presented in a potential ranges in Figure 2.20.

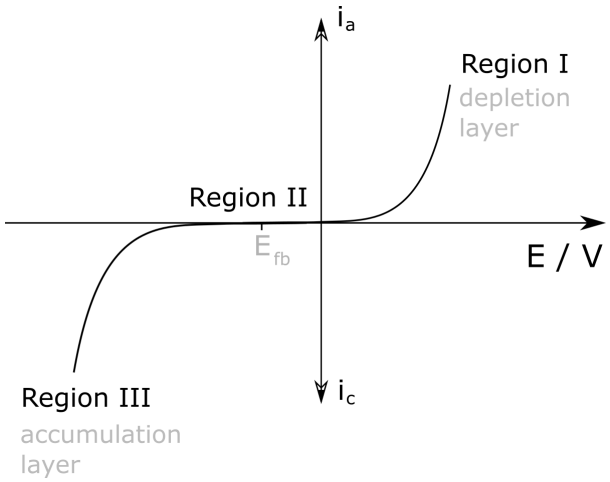

Figure 2.20: Space charge region observed throughout a wide potential range, which can be divided in three different regions with respect to the band bending trend.

The here discussed energy diagram models can be also applied for enzymes adsorbed on metal oxides to investigate the related enzyme-semiconductor interaction, which is discussed in this thesis (section 6.2.7).

2.4.4 Heterogeneous Electron Transfer

In heterogeneous ET reactions, one of the reaction partners is replaced by an electrode. The driving force of these heterogeneous reactions is given by the applied overpotential η.

$$\eta = E - E^0 \tag{2.40}$$

E denotes the applied electrode potential and E_0 represents the redox potential of the surface ET reaction defined by the Nernst equation

$$E = E^0 - \frac{k_B T}{n\, e}\, ln\left(\frac{c_{red}}{c_{ox}}\right) \tag{2.41}$$

c_{red} and c_{ox} denote the respective concentrations of the electrochemically active species while n represents the number of transferred electrons per reaction formula.

2.4.5 Protein Film Electrochemistry (PFE)

To study electrochemical reactions in enzymatic redox systems protein film voltammetry (PFV) is often applied. Upon adsorption of a protein monolayer, the electrode surface can serve as redox-partner. The protein adsorption is commonly established either on a SAM-coated metal electrodes or on pyrolytic graphite electrodes (PGE), which contains a rough, oxidized surface, effective for electrostatic adsorptions. The electron transfer between metal electrode and adsorbed enzyme occurs reversible, whereby the catalytic activity can be controlled by the applied electrode potentials. In studies of catalytic electron transport, mainly two methods, the cyclic voltammetry and the chronoamperometry, are used.[174] During cyclic voltammetry, the pontetial is cycled between two defined values for each scan and the resulting currents are monitored. In chronoamperometry, the current is monitored as a function of time after applying a fixed potential value and injecting gases in the PFV cell. By scanning or stepping the electrode potential, the rates and direction of electron flow can be changed and specific redox states of the enzyme can be interconverted. In such way, also activation or inactivation processes can be also induced. A typical PFV study on oxygen-tolerant hydrogenases is presented in Figure 2.21.

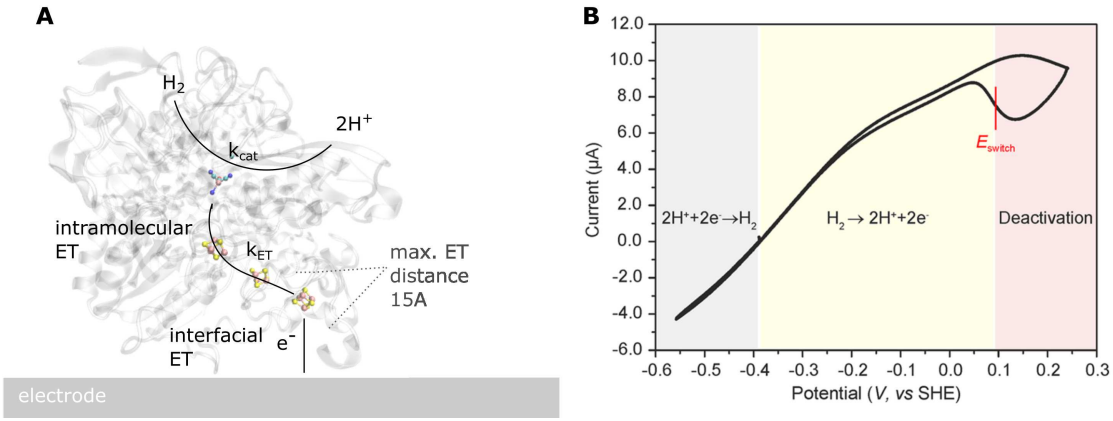

Figure 2.21: (A) In protein film electrochemical experiments , the hydrogenase has to be immobilized on the electrode with the distal [4Fe-4S] cluster facing the electrode surface to obtain direct electron transfer (ET) between protein and electrode. As electrons are part of the catalytic reaction of hydrogenases, the monitored electric current generated by the enzyme on the electrode in the presence of substrate allows the direct determination of the turnover frequency of the enzyme as a function of the electrode potential. (B) Cyclic voltammogram (CV) of a [FeFe] hydrogenase from *Desulfovibrio desulfuricans* covalently attached to a pyrolytic graphite electrode (PGE) under H_2 atmosphere, color-coding the ability for hydrogen evolution (HER) (grey area), H_2 oxidation (yellow area), and the anaerobic inactivation of hydrogenase and its switch potential for reactivation (red area and red vertcal line, respectively). Panel (B) is depicted from reference [1].

The voltammogram of hydrogenases can be divide in three distinct regions. At low potentials, usually below thermodynamic potential of H_2/H^+ the region of negative current corresponds to H^+ reduction. The current trace cuts the zero-current line at the thermodynamic potential of the H_2/H^+ couple, where the enzyme catalyzes both H_2 oxidation and H_2 production. Above, two different regions of positive current can be distinguished, defined as active and inactive/deactivated region. The hydrogenase deactivation occurs through strict redox control via the electrode, leading to an anaerobic oxidation on the active site via formation of the reversible inactive $Ni_r - B$ state, thereby the catalytic current starts to drop. Generally, this state can be also formed upon O_2 addition. On the return scan, the electrocatalytic current recovers as the enzyme reactivates at lower potentials. In the presence of hydrogen, the potential, at which the activity returns is highly sensitive to the conditions of the experiment, and a characteristic quantity, the so called switch potetnial (E_{switch}). It is defined as the potential of maximum slope in the reductive activation direction, determined from a derivative plot. The E_{switch} varies depending on pH and temperature. An higher switch potential is expected by decrease of pH and/or increase of temperature [33].

The catalytic current recorded in the voltammetric trace corresponds to enzymatic activity. The catalytic current i_{cat} can be directly correlated to the turnover rate (k_{cat}) of the enzyme as following:

$$i_{cat} = k_{cat} \cdot nFA\Gamma \tag{2.42}$$

where A, F and Γ define electrode surface area, Faraday's constant and enzyme coverage density,

respectively.

The bidirectional catalytic activity of [NiFe] hydrogenases can be clearly revealed in cyclic voltammetry experiments such as that shown in Fig. 2.21. Biased hydrogenases show a shift of onset potential in the correponding to the direction of their bias. This observation shows that hydrogenases operate 'reversibly' and require only the smallest overpotential to work in either direction. For the understanding of the catalytic bias of hydrogenases, two effects should be considered. First, H_2 can be a strong inhibitor as at it has been commonly found in [NiFe]-hydrogenases, particulary in oxygen-tolerant species. [FeFe]-hydrogenases generally do not exhibit strong H_2 inhibitions, for which typical values of inhibitory constants (K_i) are in the order of several mM of H_2. Second, hydrogenases with high Michaelis constants (K_m) for H_2 can show high activity for H_2 oxidation only at high partial pressure andare therefore not reflecting the extent of bias towards H^+ reduction that would be observed under low H_2 concentrations.

Generally, [FeFe]-hydrogenase have higher K_m values than [NiFe]-hydrogenases, so that under 1bar H_2 the current for H_2 oxidation may be higher than the current for H^+ reduction as observed for [FeFe]-hydrogenases from *C. reinhardtii* and *D. desulfuricans.[175, 1, 176]* Therefore, the common statement that [FeFe]-hydrogenases are more active than [NiFe]-hydrogenase requires qualification because of the effect may not reside only in turnover frequencies k_{cat}, but also refelcts the affinity with which H_2 is captured from the environment. [NiFeSe]-hydrogenases are generally are good H_2 producers, which is also related to their weak product inhibition. Cyanobacteria, which contain [NiFe]-hydrogenase were shown by protein film electrochemistry to be proficient in H_2 production.[177]

2.5 Microscopic Methods

In this work, microscopic methods such as Scanning Electron Microscopy (SEM) and Atomic Force Microscopy (AFM) were performed on metal oxide thin films and immobilized MBH on SAM-coated Au, respectively. SEM was carried out on conductive electrode surfaces to characterize their structure, morphology and thickness, while AFM was used for detection of the distribution of a adsorbed protein molecules on the electrode surface, allowing also a determination of the protein coverage. The SEM images presented in this thesis were recorded by Dr. Amandine Guiet/Fischer group, while AFM images were collected by Maximilian Zerball/von Klitzing group. A brief introduction for both methods will be given in the following section.

2.5.1 Scanning Electron Microscope

SEM imaging is based on scanning a sample in a raster scan pattern with a focused electron beam. In an ideal case, the incident electron beam is highly monochromatic and coherent. Based on the electron-matter interaction various process are generated as summarized in Figure 2.22 (A). Interesting for SEM are two particular phenomena which are discriminated as secondary electrons (SE) and back-scattered electrons (BSE) (Figure 2.22).

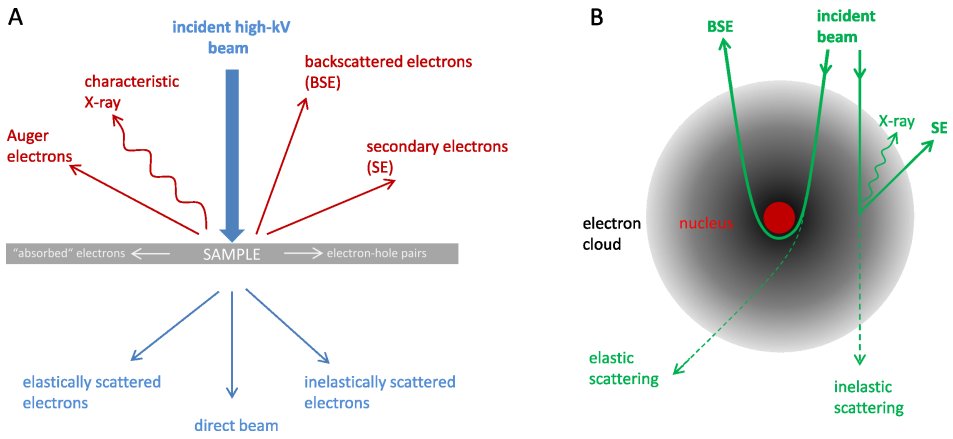

Figure 2.22: Schematic representation of phenomena on electron-matter interaction applying a high voltage electron beam onto (A) a thin sample and (B) on atomic scale level.

BSE are related to an electron diffraction phenomena, an elastic scattering without any energy loss. Since heavy elements backscatter electrons more strongly than light elements, they appear brighter in the recorded image. Therefore, the detection of BSE is used to elucidate the contrast of areas with differing chemical compositions. The condition for constructive interference can be described by Bragg's law

$$n\lambda = 2d\,sin\,\theta \tag{2.43}$$

where θ is the scattering angle, λ is the wavelength of incident wave and n is a positive integer. For a crystalline solid, the waves are scattered from lattice planes separated by the interplanar distance d. When the scattered waves interfere constructively, they remain in phase since the path length of each wave is equal to an integer multiple of the wavelength. The path difference between two waves undergoing constructive interference is given by $2d\,sin\,\theta$.

However, SE is the most common imaging mode, collecting low energy (< 50 eV) and originates from the inelastic scattering due to interaction with the k-shell of the atom. The brightness of the signal depends on the number of secondary electrons reaching the detector. In this regard, the detection of beam position and reflected electrons provides information on the sample surface topography as well as its composition, in the imaging contrast.

Generally, SEM can be used on materials with a certain conductivity. Due to the high-voltage electron beam, the sample is locally excited, which can be equilibrated by dispersed throughout the sample by fast re-combinations. The detection of non-conductive organic sample is challenging as the locally excited sample tends to overcharge without the ability of release, thus leading to a noisy SEM image, which is difficult to analyze. A microscopic method for suitabke imaging of non-conductive samples such as proteins is the often used Atomic Force Microscope.

2.5.2 Atomic Force Microscope

In contrast to electron microscopy, atomic force micrscopy (AFM) does not use lenses or an electron beam and is solely based on a mechanical tapping of the surface with an sharp peaked tip, ideally with a tip apex consisting of one atom. With this, the surface can be scanned under maintanance of a constant distance between probe-sample interaction. The distance remains via a steadily controlled and measured force between sample and tip apex (see Figure 2.23A). Tip and oscillating cantiliver are connected to a piezoelectric element, with which accurate and precise movements resulting in small and highly defined steps can be controlled.[178, 179] The topography of the sample surface achieved by raster scanning the position of the sample with respect to the tip, thereby recording the height of the sample. Since the cantilever is displaced caused by deflection, a laser beam reflected on the cantilever and recorded by a photodiode detector can translate the detected, displaced laser beam in a topographic image. The surface topography is commonly displayed as a pseudocolor plot.

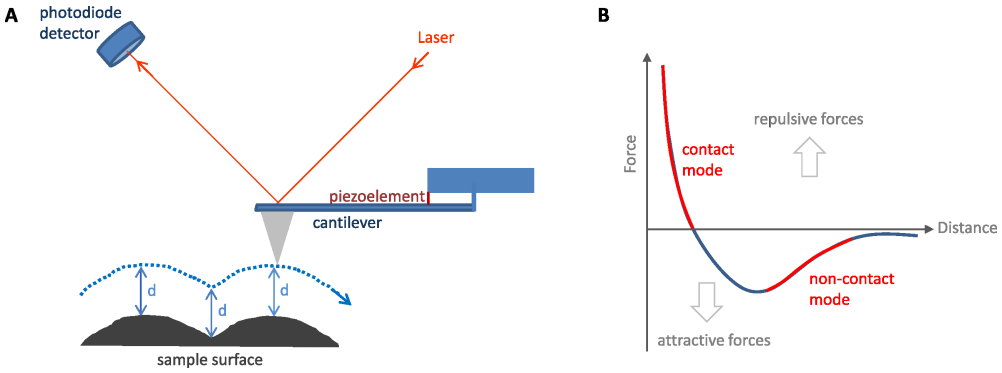

Figure 2.23: (A) Illustration of an Atomic Force Microscopy configuration using beam deflection detection for recording a topographic image and (B) force-distance plot of particle-particle interaction such as surface-cantilever representing the commonly applied AFM contact and non-contact modes.

Commonly two operation modes are used for AFM, contact- and non-contact mode (see Figure 2.23B).[180] Contact mode is performed in a short-range interaction (Å), measuring the repulsion between tip and sample, thereby using a cantilever with low stiffness. This method results in high resolutions, but the excessive tracking forces which are applied by the probe to the sample can become a problem for non-rigid samples. On the other hand, non-contact mode measures the attractive forces (van der Waals) between tip and sample with larger sample-tip distances.[180] For these measurements a stiff cantilever is used under the application of high amplitudes. However, non-contact mode exhibits slightly lower resolutions, and can not be measured in fluid. Experimentally, the resolution of AFM is also depended on the size of the tip apex, which in standard is often found to be around 5-10 nm.

Chapter 3

Experimental Details

3.1 Chemicals and Preparation Tools

The following chemicals listed in Table 3.1 were used for all experiments.

Chemical	distributor
6-mercaptohexanoic acid (99.3%)	Dojindo
6-amino-1-hexanethiol hydrochloride	Dojindo
6-mercapto-1-hexanol	Sigma Aldrich
1-mercaptohexane	Sigma Aldrich
Ag/AgCl DriRef (reference electrode)	World Precision Instruments, Inc.
Alumina oxide slurries (1-5 µm)	Pieplow & Brandt GmbH
Ammonium chloride (NH4Cl)	Sigma Aldrich
Ammonium fluoride (NH4F)	Sigma Aldrich
Antimony (III) acetate	Sigma Aldrich
Anhydrous benzyl alcohol	Sigma Aldrich
Cytochrome c (wild type horse heart)	Sigma Aldrich
D_2O (99.9 atom % D)	Sigma Aldrich
Ethanol (LiChrosolv, purity $\geq$ 99.9%)	Merck
Hydrofluoric acid (HF)	Fluka
Hydrochloric acid (HCl)	Merck
Imidazole	Sigma Aldrich
ITO coated glass slides (8-12 Ω/square)	Sigma Aldrich
KCl	Sigma Aldrich
K_2HPO_4 ($\geq$ 99%)	Merck
KH_2PO_4 ($\geq$ 99%)	Merck
Methylene blue hydrate	Sigma Aldrich
Pluronic F127	Sigma Aldrich
Sodium sulfite (Na_2SO_3)	Merck
Sodium tetrachloroaurate ($NaAuCl_4 \cdot 2\ H_2O$)	Sigma Aldrich
Sodium tetrachloroaurate ($NaAuCl_4 \cdot 2\ H_2O$)	Sigma Aldrich
Tris(hydroxymethyl)aminomethane (Tris)	Serva Electrophoresis GmbH

Table 3.1: Chemicals and substrate used in this work. All solutions were prepared using MilliQ water (> 18 MΩ cm).

3.1.1 Buffer solutions

Strep- and his-tagged MBH samples were in diluted 10 mM potassium phosphate buffer solutions (PBS), prepared by mixing adequate volumes of 10 mM K_2HPO_4 and 10 mM KH_2PO equivalents to obtain PBS solutions at pH 7.0 and pH 5.5.

Cytochrome c and his-tagged Cytochrome c samples were immobilized in 5 mM Tris-buffer at pH 7.5. The pH-values were adjusted by addition of HCl. All pH adjustments were controlled by a pH meter.

3.1.2 D_2O-buffer

For H-D exchange experiments, 10 mM $K_2HPO_4$and 10 mM KH_2PO_4 solutions were prepared-solved in D_2O. A pD of 5.5 was adjusted by adding slowly K_2HPO_4 – D_2O to the KH_2PO_4 – D_2O solution under pH control to obtain a D_2O phosphate buffer solution (PBS-D_2O). For measurements in D_2O, the pD was estimated according to pH meter reading and the addition of a value of 0.4.[181]

3.2 Protein Purification

3.2.1 Membrane-Bound Hydrogenase from *Ralstonia eutropha*

was cultured and the MBH heterodimer (HoxGK) was purified via a *strep*-tag II, which was attached by genetic engineering to the small subunit of the MBH (HoxK). The growth conditions and the purification are described in detail in Goris et al. [58]. The samples were purified by Dr. Stefan Frielingsdorf/ Lenz group as described previously.[182] The purified MBH heterodimer samples were buffered in 50 mM KPO_4 buffer at pH5.5 containing 150mM NaCl and stored in liquid N_2.

The heterodimeric his-tagged MBH was prepared by Janna Schoknecht/Lenz group as reported previously.[67] The purified samples in solution were buffered in 50 mM K-PO_4 buffer at pH 5,5, including 150 mM NaCl, 20 % glycerol and stored in liquid N_2.

3.2.2 Cytochrome C

Wild type horse heart Cytochrome c (cyt c) was purchased from Sigma Aldrich and purified by Ion-Exchange Chromatography (IEC) on a mono-S-column (GE Healthcare).

His-cyt c was obtained using a technique described by Pollock et al..[183] We used a system with codon optimized DNA for horse-cyt c and yeast Cytochrome c heme lyase, inserted in Plasmid pQE12 and harboured in Xl1-blue E.coli. cyt c is equipped with a N-terminal his-tag, followed by a TEV cut site,[184] showing the start sequence: MGSSHHHHHHSSG-ENLYFQ-cyt c. After expression cells were lysed by french press. His-cyt c was purified by affinity chromatography on Ni^{2+}-NTA-Agarose column.

3.3 Instrumentation

3.3.1 UV-Vis measurements

UV-Vis spectroscopy was performed in the transmission mode on protein solutions. Furthermore, UV-Vis studies in reflection mode were carried out on metal oxide coatings. These data were recorded in a (chemie/Lensen) spectrometer at room temperature.

3.3.2 FTIR – Transmission studies

The sample compartments of the IR-spectrometer(s) were purged with N_2 or dry air during all measurements. Before each measurement all devices were equilibrated for several hours to obtain a stable atmosphere and temperature. The detectors were cooled with liquid nitrogen at least 30 min before starting the measurement. Spectra acquisition was accomplished by using the OPUS 5.5 software from Bruker. For all transmission measurements of buffered protein samples, a Bruker Tensor 27 spectrometer was used, equipped with a globar infrared source, a ROCKSOLID interferometer and a liquid nitrogen cooled photoconductive detector. The liquid sample cell was temperature-controlled (at 10°C), gas-tight, and equipped with CaF_2 windows. It provided a volume of approximately 7 µL and an optical path length of 50 µm. The temperature was stabilized by peltier-elements and cooled by a thermostat/cryostat device. The spectral resolution for the measurements was 2 cm^{-1}.Typically 200 scans were accumulated for each spectrum which was evaluated using the OPUS 5.5 software.

3.3.3 Spectro-electrochemical set-up configurations

For the spectroscopic studies a Bruker IFS 66v/S and a Bruker Tensor 27 spectrometer, equipped with an ATR set-up (Kretschmann configuration), a liquid N_2-cooled MCT detector (HgCdTe) and a globar IR radiation source were used. In case of the IFS 66v/S spectrometer the globar and Michelson Interferometer as well as the photoconductive MCT-detector were operated under vacuum. The sample chamber was purged continuously with nitrogen gas for all hydrogenase related experiments. For the ATR measurements, a trapezoidal Si crystal (Lx W x H = 25 mm x 20 mm x 10 mm) was used under an angle of incidence of 60° with an aperture setting of 3 mm. Spectra were acquired in the spectral region between 4000 and 1000 cm^{-1} with a spectral resolution of 4 cm^{-1}. Each spectrum is in total composed of 400 scans, requiring an accumulation time of 3 min. To perform Surface Enhanced IR Absorption (SEIRA) experiments, the Attenuated Total Reflection (ATR) prism was coated with a nanostructured Au film. Metal oxide coatings deposited on the Si-prism (see synthesis details in the following section 3.3.3.2) were used for spectro-electrochemical ATR experiments as depicted in Figure 3.1. SEIRA and ATR spectra were evaluated using the OPUS 5.5 software.

3.3.3.1 Spectro-electrochemical cell

Depending on its coverage (Au or metal oxide thin film), the Si-prism was implemented either in a homemade SEIRA and / or ATR cell, respectively, as depicted in Figure 3.1. Spectro-electrochemical experiments were performed using a three-electrode configuration with a gold plate contacted Au film or metal oxide film as working electrode (for SEIRA or ATR experiments, respectively), a platinum mesh as counter electrode and a DriRef Ag/AgCl (3 M KCl) as reference electrode (+0.21 V vs SHE and -0.0591V * pH vs RHE). All potentials cited in this work refer to the SHE electrode.

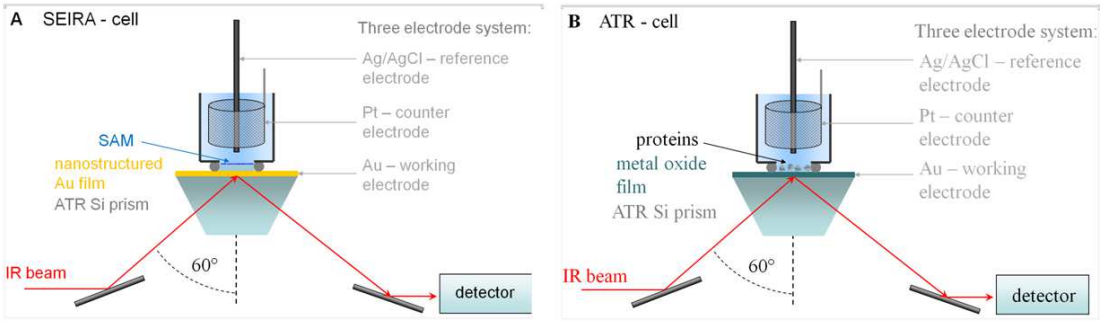

Figure 3.1: Schematic representation of the spectro-electrochemical cell in (A) SEIRA/ATR mode with a nanostructured Au coating as surface enhancing IR signal amplifier and working electrode and in (B) ATR mode with transparent, conductive metal oxide thin film adsorption layer and transparent working electrode for *in situ* spectro-electrochemical characterization of immobilized enzymes.

Electrochemical set up

Pure electrochemical measurements were performed either on Au pen electrodes or on metal oxide thin film electrodes coated on commercial ITO glass slides. The metal oxide thin film electrodes were contacted using a cupper tape. Note: The cupper tape must be adjusted in such a way that it does not get in contact with the electrolyte.

3.3.3.2 Gold thin film for SEIRA

Chemical (electroless) deposition of nanostructured gold film for SEIRA

A nanostructured gold film was obtained by electroless (or chemical) deposition of $HAuCl_4$.[185] Therefore, the reflecting plane of the silicon prism was polished by finer grade alumina oxide slurries with a particle size between 1-5 µm and rinsed with Milli-Q water (< 18 MΩ cm). The surface was covered with a solution of 40 m% NH_4F for 2 min in order to remove the oxide layer on the Si surface and to terminate it with hydrogen. The prism was rinsed and placed in a water bath at 65 °C and the plain side was covered by drop-casting the Au plaiting solution, which consists of 240 µL of 2 vol% aqueous HF-solution , 240 µL of aqueous 0.03 M $NaAuCl_4$ -solution, and 240 µL of aqueous reduction solution containing 0.3M $Na_2SO_3 + 0.1$ $Na_2S_2O_3 \cdot 5\,H_2O + 0.1M\,NH_4Cl$. The gold deposition on the Si surface is accomplished via the reduction of the gold precursor and the simultaneous oxidation of the Si surface, according to the following reactions.

$$Si^0(s) + 6F^-(aq) \longrightarrow SiF_6^{2-}(aq) + 4e^-$$

$$AuCl_4^-(aq) + 3e^- \longrightarrow Au^0(s) + 4Cl^-$$

The reaction was stopped after 1 min by rinsing the prism with Milli-Q water.

Electrochemical cleaning of nanostructured gold film

Prior to the actual measurements, the Au surface was cleaned electrochemically in the SEIRA cell , as shown in Figure 3.2 by repeating potential scans between 0.0 and 1.4 V in 0.1 M H_2SO_4 as electrolyte. The cell was rinsed several times with Milli-Q water before the immobilization procedure. The electrochemical cell containsa gold plate which is contact with the gold film and defines the working electrode, a platinum mesh is used as the counter electrode gauged by a Ag/AgCl (3 M KCl) reference electrode (+0.21 V vs SHE). During the cleaning process, the cell was purged with Argon. The voltammetric cycles were repeated.

Immediately after the chemical deposition, the Au surface was cleaned electrochemically. Six subsequent cyclic voltammograms displaying Au oxidation and reduction peaks were recorded with a scan rate of 50 mV s^{-1} between 0.1 V and 1.4 V vs Ag/AgCl (0.21 and 1.61 V vs SHE) in 0.1M H_2SO_4. The electrolyte was purged with Ar to remove all O_2 residues. The last cycle was used to determine the real area of the Au electrode via the Au-oxide reduction charge density method.[186, 187] A real area of ca. 1.65 cm^2 (geometric area of 0.79 cm^2 corrected by the roughness factor of 2.1) was determined for each deposited Au film. The cell was rinsed several times with Milli-Q water before the immobilization procedures were started.

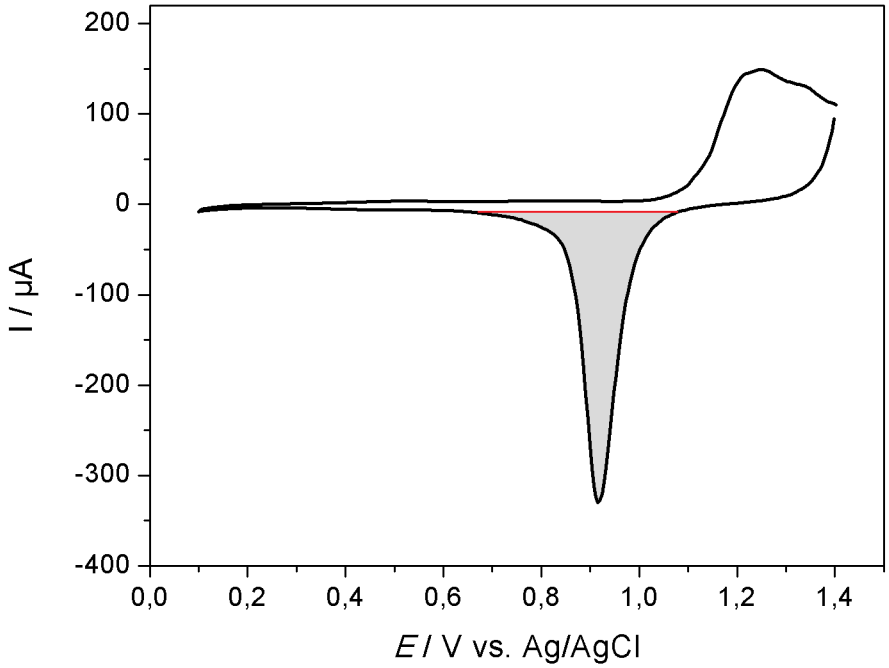

Figure 3.2: Electrochemical cleaning of the nanostructured Au electrode with cyclic voltammetry in 0.1 M H_2SO_4. The real area of the Au electrode is obtained from the Au-oxide reduction charge by calculating the area under the reduction peak at E_{red} = 917 mV (grey area).

Example calculation of the real Au surface of a SEIRA Au electrode:

The geometrical area of the exposed Au surface to the electrolyte of the SEIRA cell is A_{geo} = 0.79 cm^2 . The charge transferred for the reduction of an ideal planar (111) Au surface with

a roughness factor $R_f = 1$ is reported in [187] and accounts for $Q_{lit} = 400$ C/cm². The charge transferred for the considered Au SEIRA electrode in Figure 2 is Q_{exp}= 664 C. In the following a calculation for the determination of the real surface area of Au (A_{real}) is exemplified:

(1) $$Q_{(R_f=1)} = Q_{lit} \cdot A_{geo} \qquad \Rightarrow Q_{(R_f=1)} = 316C$$

(2) $$R_f = \frac{Qexp}{Q_{(Rf=1)}} \qquad \Rightarrow R_f = 2.1$$

(3) $$A_{real} = A_{geo} \cdot R_f \qquad \Rightarrow A_{real} = 1.66\,cm^2$$

3.3.3.3 Metal oxide thin film for FTIR-ATR

The synthesis of indium(I) tin(II) tris-tert-butoxide (ITBO, $InSn(OtBu)_3$) was carried out by Dr. Amandine Guiet (Fischer group). All experiments and manipulations were carried out under dry, oxygen-free nitrogen atmosphere by using standard Schlenk techniques or in a MBraun glove box purged with dry and oxygen free nitrogen (<1 ppm H_2O and <1 ppm O_2). Anhydrous solvents were used for all synthesis. The single source heterobimetallic $In(OtBu)_3Sn$ precursor was synthesized as previously reported.[143, 145] The obtained precursor was characterized by 1H-NMR (C_6D_6, 200.13 MHz, δ = 1.36 ppm [1s, 27 H, $OC(CH_3)_3$]) and 119Sn-NMR (C_6D_6 ,149.21 MHz, δ = – 78 ppm).

Before coating, the surface of the Si-prism was cleaned by polishing the Si surface with fine grade alumina oxide slurry with a particle size ranging from 1 to 5 µm followed by subsequent ultra-sonication in EtOH and water. Planar ITO_{TR} thin films were prepared according to a modified procedure of the procedure reported by Aksu and coworkers.[143] In a dry, oxygen-free nitrogen glovebox, solid $InSn(OtBu)_3$ (ITBO) was dissolved at room temperature in anhydrous toluene (200 mg mL^{-1}) and stirred for 10 min. 10 µL of the as-obtained colorless solution were then immediately dropped onto an ATR Si-prism, (mounted on a spin-coater) and constantly and slowly spread over the complete top surface of the prism. Note: This procedure is necessary as the ITBO precursor dissolved in toluene is highly hydrophobic and does not tend naturally to homogenously wet the Si surface. After 2-3 minutes a "gel-like" viscous solution was obtained on the prism surface. The prism was then spinned at 6000 rpm for 30 s. After drying, additional 10µL of the precursor solution were drop-cast / spin-coated in the same manner as just described. This step-wise procedure lead to very thin (thickness = 40 nm) and homogenous, grey-colored thin films. The as-obtained layers remained for 30 min of drying inside the glove box, slowly turning to grey. After drying, the films were taken out of the glovebox and calcined first under air (400 °C - 2h, heating rate = 5 °C min^{-1}) and second under reducing atmosphere (300 °C - 90 min, 10 % H_2, 90 % N_2, 20 °C min^{-1}).

Planar antimony-doped tin oxide thin films (ATO) were produced by Dr. Anabel Molero (Fischer group). ATO nanoparticles with a doping level of 8 mol% of Sb (Sb(8%):SnO_2) were synthesized as reported previously[157] via evaporation-induced self-assembly (EISA) of preformed crystalline

ATO nanoparticle sols (ATO NP). For the deposition of the planar ATO thin film on the Si-Prism, 10 mg of ATO NPs were suspended in 0.9 ml of THF. To solubilize the NPs, 30 µl of HCl (37% w/w) were added. To improve the film adherence to the Si-prism a small amount of F127 (0.1 mg) dissolved in 0.05 ml of THF was added. The solution was stirred at room temperature for 2 h. 50 µl of the transparent solution were then drop-cast on the Si-prism covering the complete area of substrate, and immediately spin-coated with a customized adapted spin-coater. Subsequently, all films were aged for minimum 6h at 100 °C, followed by calcination at 450 °C for 30 min (heating ramp = 0.6 °C min^{-1}). After implementing the Si-prism into the ATR set-up, the films were rinsed with EtOH, MilliQ-water, and the buffer used in the respective experiment. Finally the prism surface was dried under N_2.

3.4 Protein Sample Preparation

3.4.1 Formation of Self-Assembled Monolayer (SAM) on gold electrodes

Au electrodes were immersed for 8 to 12 h in solutions of ω -substituted mercaptanes to form self-assembled monolayers (SAM) on the electrode surface. 1 mM of each C_6NH_2, C_5COOH - , C_6OH - , C_5CH_3- SAM were dissolved in ethanol. Two-component SAMs consisting of C_6NH_2/C_6OH and C_5COOH/C_6OH were obtained by mixing the respective SAMs in a volume ratio of 1:9 (1mL of C_6NH_2 or C_5COOH and 9 mL of C_6OH).

3.4.2 Immobilization conditions of the MBH heterodimer

Immobilization of the *strep*-tagged MBH heterodimer (HoxGK) on SEIRA Au electrodes was accomplished by incubating the SAM-coated Au electrodes in the SEIRA cell with a 1 µM solution of *strep*-tagged MBH prepared in 10 mM potassium phosphate buffer (PBS). The MBH remains stable in a pH range between pH 7 and pH 5.5. Therefore, only these two pH values were chosen for immobilization studies. For all spectro-electrochemical experiments, both the SEIRA and the ATR-cell, the immobilization was performed under atmospheric conditions and under temperature control at 4 °C. For all electrochemical experiments using the gold pen electrodes, the electrodes were cooled on dry ice during the immobilization.

(1) SAM-covered Au electrodes:

- C_6NH_2, C_6NH_2/C_6OH, C_5CH_3- SAM: 10mM PBS at pH 7 was chosen for immobilization of *strep*-tagged MBH at 4 °C/ice.
- C_5COOH - and C_5COOH/C_6OH - SAMs: 10mM PBS at pH5.5 was used for immobilization of *strep*-tagged MBH at 4 °C/ice.

(2) ITO_{TR}-films electrodes:

- 10mM PBS at pH 7 or pH 5.5 was used for immobilization of *strep*- and his-tagged MBH at 4 °C/ice.

10 mM potassium phosphate buffer at pH 5.5 was chosen as electrolyte solution for the MBH studies as the highest H_2 oxidation activity is reported at this pH [5, 17]. For the electrochemical analysis, the temperature was increased as the catalytic activity of enzyme increases. The temperature in the SEIRA-cell was set to 25°C, using a thermostat from Thermo Fisher Scientific. For the investigations performed on Au-Pen electrodes the measurements were carried out at room temperature.

3.4.3 Immobilization of cytochrome c

Cyt c and his-cyt c were immobilize on ITO_{TR}- and ATO thin films. For protein adsorption on the planar ATO slides were incubated for 2 h with a buffered 7 µM cytc or his-cyt c solution at room temperature. The protein solution was then exchanged several times by pure buffer to remove non-bound protein species. If not stated else wise 5 mM Tris-buffer at pH 7.5 was used for these experiments. All electrochemical experiments, if not stated otherwise, were conducted using 120 mM Tris-buffer at pH 7.5 and at room temperature.

3.4.4 Mediator experiments

Determination of mediated electron transfer was performed by the addition of methylene blue (MB) to the electrolyte to reach a final mediator concentration of 10 µM. MB was chosen as mediator as its redox couple potential overlays with the potential range in which the H_2 oxidation efficiency of the MBH is maximal, therefore ensuring by its oxidation-reduction via MBH abstracted / MBH delivered electrons proper electron transfer between non-electro-contacted MBH and the electrode. 10 µM was chosen as optimum MB concentration, as any further increase of the MB concentration did not further increase the mediated catalytic currents. In addition, higher mediator concentrations interfere with the catalytic signal of MBH impeding proper data evaluation due to the appearance of the redox transitions of MB in the CV.

3.4.5 H-D exchange

For H-D exchange experiments, a 10 mM PBS-D_2O solution at pH 5.5 was purged and saturated with Ar or H_2 in a gas-tight electrochemical glass cell. Afterwards, chronoamperometry for 1h at different reductive potentials ranging from -0.19 V to -0.44 V (vs SHE) were applied for his-tagged covered ITO-glass slides. Subsequently a volume of 2 ml from the sample solution was subjected to MS analysis. Thereby, the corresponding solution was continuously stirred at room temperature with a magnetic bar rotating at 1,250 rpm. For a correction of the gas consumption by the mass spectrometer (first-order function of the gas partial pressure), control measurements were carried out without his-tag bound MBH. Data collection was accomplished with the software package Quadstar 32-bit, and further processing was carried out using SigmaPlot 10.

3.4.6 Desorption studies

The stability of the adsorbed protein on Au-SAM and metal oxide surfaces was investigated by desorption experiments. These involve repetitive washing of the enzyme-covered electrodes either with 3 M KCl or 750 mM imidazole dissolved in 10 mM PBS at pH 5.5 to release protein species bound to the electrode surface via electrostatic interactions or his-tagged mediated complexation, respectively.

3.4.7 Electrochemistry

Spectroscopic and electrochemical measurements of metal oxide thin films

Electrochemical characterizations were conducted using a µAutolab III and an Autolab PG-Stat12 potentiostats from Metrohm controlled with the General Purpose Electrochemical System (GPES) software (version 4.9) or with a CH Instruments potentiostat. The potentiostats are specified with current ranges down to 10 nA and even down to sub pA range for the latter.

The electrolyte solutions used for the electrochemical and/or spectro-electrochemical experiments were adjusted to the pH value, where the highest protein stability or activity was reported. In none of the experiments detergent has been added. The electrochemical measurements were performed at 25 °C. Current densities j [µA cm^{-2}] are reported with respect to the geometric surface area of the electrode. ITO_{TR} can be approximated to a perfect planar surface with a roughness factor of $R_f = 1$, as its intrinsic surface nano-roughness in the range of 2 nm can be neglected compared to proteins of 5-9 nm in size. All experiments were performed under Ar or H_2 gas atmosphere (high-purity grade 5.0, with implemented Oxygen filters from Agilent). 10 mM potassium phosphate solutions at pH 5.5, pH 7.0 and 10 mM Tris-buffer at pH 7.5 were used as electrolyte solutions. The temperature for Protein Film Voltammetry (PFV) was set to 25°C by using a thermostat from Thermo Fisher Scientific. All experiments were reproduced at least 3 times. Spectroscopic parameters were set as reported above.

3.5 Surface Characterization

3.5.1 Conductivity Measurements

Conductivity measurements were performed by 4-point probe measurements at room temperature with a resistivity meter Loresra-GP model MCP-T610, PSP 1.5 mm from Mitsubishi Chemical Analytech. The specific resistivity (Ω cm) of the films was calculated by multiplying the sheet resistance (Ω/□) by the film thickness. For these investigations, the ITO_{TR} thin film was deposited onto the non-conductive, undoped (ATR) Si-prism and each film was measured at three different points and the average value calculated.

3.5.2 SEM

Scanning Electron Microscopy (SEM) was performed by Dr. Amandine Guiet (/ Fischer group) using a JEOL 7401F electron microscope equipped with an inlens secondary electron detector or at the ZELMI/ TU Berlin with a Hitachi SU8030. For these measurements, films were either prepared on Si (ATR) prisms, Si wafers or ITO coated glasses.

3.5.3 AFM

AFM micrographs were recorded on a commercial Cypher AFM instrument (Asylum Research, Santa Barbara USA) by Maximilian Zerball (Klitzing group). The topographic imaging was performed in non-contact-mode with a standard tip size of 7 nm in diameter, purchased from Olympus. The z-axis profile reveals the lateral information rather than the height information due to tip size induced height limitations. Au coated silicon wafers for AFM measurements were purchased from Sigma Aldrich.

3.5.4 Ellipsometry

Ellipsometry has been applied to determine the thickness of the protein layer adsorbed on the gold electrodes surface, in particular gold electrodes coated with an amino-terminated SAM. The ellipsometric measurements were performed with a PCSA (polarizer-compensator-sample-analyzer) ellipsometer from Optrel GbR (Sinzing, Germany). The experiments were carried out at a constant wavelength of 632.8 nm and a fixed angle of incidence of 70° (near the Brewster angle of the Si/air interface). The layer thickness was calculated with the software "Ellipsometry: simulation and data evaluation" (Optrel, v. 3.1). For the protein a one-box model was assumed, in which the continuum media were air (n=1.000) and gold (n=0,144; k=3,178). The refractive index and the absorption constant of gold were determined by measuring 5 different spots on the bare gold surface. With respect to its small thickness, the SAM layer was neglected.

3.5.5 Mass spectrometer

H-D exchange measurements were carried out as described in [188] in a setup consisting of a modified Hansatech DW2/2 Liquid-Phase Oxygen Electrode Chamber (Hansatech, United Kingdom) which was connected to the vacuum line of a gas analysis quadrupole mass spectrometer (Omnistar GSD 301; Pfeiffer Vacuum, Germany). The vacuum line connected to the mass spectrometer was heated to 160 °C to prevent water condensation, the detector type was set to channeltron, the secondary electron multiplier voltage was set to 980 V, and the dwell was set to 50 ms. m/z 2, 3 and 4 were recorded revealing the detection of H_2, HD and D_2, respectively. Additionally, m/z 18 and 28 corresponding to H_2O and N_2, respectively, were recorded as control parameters.

3.6 Spectra Calculation and Data Processing

Spectra calculation and data processing were performed by using the Bruker OPUS software 4.2, 5.5 and 6.5. The absorbance spectra were calculated according to

$$S_A = -lg\frac{s_{SC}}{r_{SC}}$$

where A corresponds to the absorbance and s_{SC} and r_{SC} to the respective single channel spectrum of the sample and reference, respectively. In order to obtain a higher signal to noise (S/N) ratio, n sample- and n reference single channel spectra were averaged and used as background spectra. For purified enzyme fractions, a salt/buffer-solution was recorded as reference. Positive bands are related to increasing amounts of certain species, whereas negative bands describe the corresponding decrease of species. The spectra calculation was carried out along with an atmospheric compensation of H_2O and CO_2 (OPUS software algorithm) in order to avoid significant contributions of the respective absorptions. Further data analysis for baseline corrections and visualization were performed by using the Win-IR-Bio-Rad, Bruker OPUS 5.5, and Origin 9.1 software.

Chapter 4

Spectro-electrochemical studies on Membrane-Bound [NiFe] Hydrogenase of Ralstonia eutropha on biocompatible gold electrodes

4.1 Introduction

4.1.1 Heterogeneous Catalysis

Enzymes can be used as efficient electrocatalysts of redox reactions when attached to a conductive surface (electrode). Despite their large size and electronical insulation through most of their bulk, enzymes can catalyze selectively electrochemical reactions at useful kinetic rates and at low overpotentials. Therefore, enzymes are promising candidates for biological fuel cells: they perform (bio)catalysis under mild operating conditions such as ambient temperature and near-neutral pH. Further advantages are their low costs, renewability, and biodegradability. An enzymatic biofuel cell is defined by at least one half reaction taking place by the reaction of the redox enzyme, commonly the H_2 oxidation at the anode. The first biofuel cell was reported in 1964 by Yahiro et al. [189] and even though this field has been developed since then, there is still scope for improvement. Especially, with the growing awareness of the sustainable energy problem, biofuel cells gained a great attention in the last decade. Fundamental research on mechanistic aspects of hydrogen oxidation by hydrogenases have been carried out for more than 20 years [12, 190, 191, 174, 192, 33]. However, their application in H_2/O_2 biofuel cells only recently emerging is in particular because of the high sensitivity to O_2 of many known hydrogenases. By the identification of O_2-tolerant hydrogenases [59, 58, 193, 194], the limitation in their application could be lately overcome. Armstrong's group accomplished the proof of concept of a H_2/O_2 biofuel cell using O_2-tolerant [NiFe] hydrogenases for the hydrogen oxidation reaction and copper enzymes (laccase or bilirubin oxidase (BOD)) to reduce oxygen.[195, 196, 197]

4.1.2 Enzyme Adsorption

Immobilization of enzymes on the electrode must be sufficiently strong to facilitate the electron transfer, but still suitable to not cause denaturation. Additionally, the enzyme must be properly oriented with respect to the electrode surface in such way that the redox center is located within an acceptable distance for the electron transfer to occur.[198, 199] In an optimal way, the electrode surface should be designed to resemble the surface characteristics of its native environment, e.g. regarding surface charge distribution or hydrophilic/hydrophobic properties, which facilitates an efficient interaction between enzyme and electrode surface without major conformational changes.[200] Among different enzyme immobilization strategies (see chapter 2), self-assembled monolayers (SAMs) on metal electrodes offer an attractive approach for enzymes with given distinct surface groups, which makes them suitable for chemisorption directed towards defined orientations. Despite the large record existing on enzyme-based electrochemistry, the fabrication of bio-catalytically modified electrodes with enzymes is still in early stages, particularly due to so far limited enzyme stability and power output. Since the early studies of direct enzyme coupling on pyrolytic graphite electrodes,[33] researchers have made substantial progress in designing biocompatible surfaces to study different hydrogenases, ranging from self-assembled monolayers (SAMs) [67, 62, 64] to protein-tethered lipid bilayer [168, 107] or polymeric scaffolds [201]. Previous work on standard hydrogenases on Au-SAM electrodes demonstrated that the ratio of direct electron transfer (DET) or mediated electron transfer (MET) processes for H_2 oxidation by a soluble, O_2-sensitive [NiFe] hydrogenase from Desulfovibrio species could be controlled by electrostatic interactions.[62, 202] The presence of a defined acidic patch of amino acids, coupled to a strong dipole moment, pointing towards the distal Fe-S cluster allowed an optimal enzyme orientation onto positively charged surfaces. This immobilization strategy

enables direct electron transfer between enzyme and surface. In contrast to standard hydrogenases, recent studies on a more relevant hydrogenase, oxygen-tolerant *Aa* MBH, could not obtain any specific orientation by electrostatic interaction on a variety of Au-SAM electrodes, and thus control of the electron-transfer process was not possible. An alternative important example of oxygen-tolerant hydrogenases is known by the membrane-bound [NiFe] Hydrogenase (MBH) of Ralstonia eutropha (*Re*), which in the last years was studied mechanistically via spectroscopy by the group of Hildebrandt [5, 203, 76, 204, 58] and electrochemically on graphite electrodes by Armstrong/Vincent's group [17, 205] In order to elucidate oxygen-tolerant *Re* MBH interaction on surfaces, the following chapter combines Surface-Enhanced IR Absorption (SEIRA) spectroscopy, Atomic Force Microscopy (AFM), Protein Film Voltammetry (PFV), and Molecular Dynamic (MD) simulations. Thereby, comprehensive insights into a bio-electronic hybrid system established on *Re* MBH could be provided. *Re* MBH was immobilized on SAM-modified Au electrodes, involving various natures of the functional end groups of the thiol derivate. The presented multidisciplinary approach is shown to successfully identify parameters that control enzyme adsorption and orientation on electrodes, thus ensuring structural integrity and highest catalytic efficiency.

4.1.3 Membrane-Bound [NiFe] Hydrogenase of *Ralstonia eutropha*

The oxygen tolerant membrane-bound [NiFe] hydrogenase (MBH) of *Ralstonia eutropha* (*Re*) is an outstanding example of an enzymatic catalyst with a potential for biofuel cell applications. At its bimetallic active site hydrogen is split into protons and electrons. Via the three Fe-S cluster relay, these electrons can be transferred towards the enzyme surface to an attached natural redox partner (cytochrome *b*). Alternatively, they can be also shuttled to the electrode, if the distance between distal Fe-S cluster and the electrode is less than 15-20 Å, which allows electron tunneling.[206, 207]

Naturally, the *Re* MBH is a heterotrimeric species, which consists of two subunits and one cytochrome *b* unit. Purifications of *Re* MBH as a heterodimeric protein detached from cyt *b* is achieved by means of affinity tags such as *strep*- or polyhistidine- (his-) tag systems, henceforth specified as *strep*-MBH and his-MBH. As illustrated in Figure 4.1B, the heterodimeric MBH relies on the large subunit (HoxG), harboring the [NiFe] active site, and a small subunit (HoxK), which contains the corresponding electron transfer chain. This electron relay consists of one [4Fe4S], one [3Fe4S], and an unusual proximal [4Fe3S] cluster, the latter of which is crucial for the oxygen-tolerance of the enzyme.[208, 209, 34] The Ni and Fe ions of the bimetallic catalytic center are coordinated by four cysteine residues. In addition, one CO and two CN^- ligands are bound to the Fe.[210] The C-terminal α-helical transmembrane extension of HoxK is not illustrated in Fig. 4.1B, but is essential for both, anchoring the hydrogenase to the membrane and a tight connection to cytochrome *b*.[60, 51] The isoelectric point (pI) of MBH can be assumed of a value around 7.32, which was calculated with the propka method by Dr. Tillmann Utesch. The lack of a distinct acidic patch of amino acids at the enzyme surface in the vicinity of the distal Fe-S cluster, accompanied by a comparable weak dipole moment, which is tilted relatively to the ET chain axis (see Fig. 4.1B),

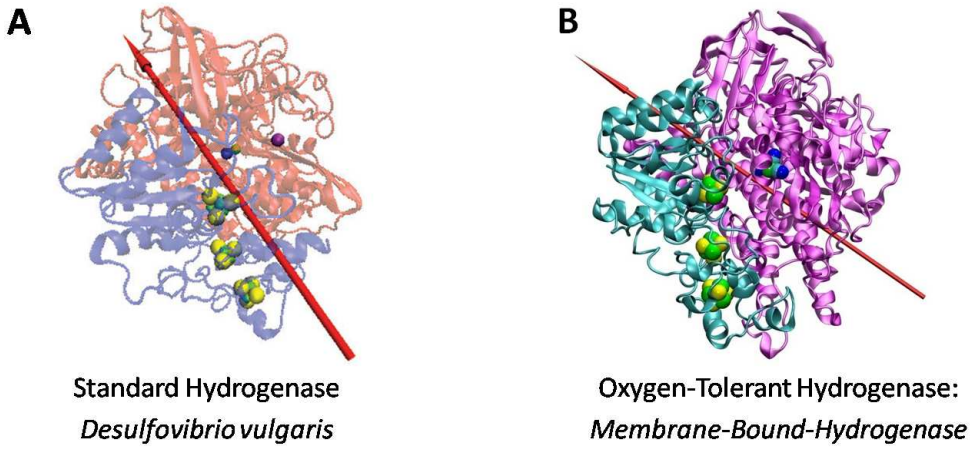

Figure 4.1: Structure and dipole moment of (A) a standard [NiFe] hydrogenase from *Desulfovibrio vulgaris* (illustration reprinted from reference [211]); and (B) the MBH of *Ralstonia euthropha*.

prevents a simple estimation of an optimal orientation of the enzyme for electron transfer from distal Fe-S cluster towards the electrochemical interface.[62] In the case of DET from enzyme to the surface, access to thermodynamic and kinetic information of enzymatic reactions can be provided. Whereas mediated electron transfer (MET) allows an electron transfer process of unfavorably oriented enzymes with the distal Fe-S cluster too far away for direct electron tunneling towards the electrode. Mediators are redox couples, which assist as electron acceptors and donors, shuttling electrons via a two-step electron reaction process between the terminal Fe-S cluster and the electrode surface via a diffusional path.

A controlled immobilization of redox enzymes on electrode surfaces, which would result preferentially in DET, emerged as an attractive goal in bioelectrochemical research for fundamental studies of enzymatic catalysis as well as biotechnological applications. To achieve this, a good structural knowledge of the investigated redox enzymes and the development of efficient methods regarding electrode derivatization are required.

Previously, electrochemical and/or SEIRA studies of adsorbed O_2-sensitive, so-called standard [NiFe] hydrogenases on electrodes were carried out for different organisms as like those of *Desulfovibrio vulgaris* Miyazaki F (*Dv*MF) [62], *Desulfovibrio gigas* (*Dg*) [208], *Desulfovibrio fructosovorans* (*Df*) [202] as well as O_2-tolerant membrane-bound hydrogenase of *Aquifex aeolicus* (*Aa* MBH).[64] For the Desulfovibrio O_2-sensitive hydrogenases dipole moments are calculated, resulting in similar magnitudes from 1050 to 1200 Debye [208, 209]. Due to the strong dipole moment along the axes of the Fe-S relay and their specific negative binding patch close to the distal Fe-S cluster, these enzymes exhibit a strong attraction to positively charged surfaces enabling high electrocatalytic efficiencies. This selective binding, however, could not be achieved with *Aa* MBH ascribed to a lower dipole moment of 1000 D [211]on Au-SAM systems, instead showing high contributions of MET processes. Alike *Aa* MBH, the *Re* heterodimer MBH is characterized by a weaker dipole moment (Figure 4.1) (680 D) and exhibits only a slightly negatively charged surface patch in the vicinity of the distal Fe-S cluster. These two aspects preclude an intuitive prediction of a preferential electrostatically determined binding orientation. This challenges the rational choice of optimal surface functionalities and charges for an adsorption leading to one favored orientation suitable for DET. The specific alignment is crucial for the bio-catalyst on the

electrode, as it controls the rate of the electron transfer. The key to the reliable function and quantification of the output data is the ability of the electrodes to immobilize sufficient amounts of redox enzymes in electro-active orientations. Therefore, a systematic variation of determining parameters which control the heterogeneous ET is essential; such as the ET distance, driving force, charge distribution in the SAM-protein interface, ionic strength, pH in the bulk solution and immobilization temperature are required for the formations of an optimal surface. Some of the most relevant aspects are varied within this work to aim towards finding optimized surface properties for MBH immobiliztion.

Besides its buried active site and its interconnecting electron relay, *strep*-MBH carries also an isolated, and highly flexible transmembrane α-helix at the C-terminus with the extension of *strep*-tag II, which may interfere within the surface binding process. The catalytic efficiencies depend strongly on the turnover number, which is based on the amount of adsorbed catalyst as well as the interfacial electron transfer from the catalyst to the electrode, which is usually the rate determining step of the ET process [212, 213]. The latter is defined by the distance for electron tunneling between terminal Fe-S and surface and therefore depends on the enzyme orientation. According to standard hydrogenases, an ideal binding for *Re* MBH for optimal electron transfer from the distal Fe-S cluster as exit point for the electrons, which are gained from the H_2 splitting at the enzyme's active site to the surface, might be accomplished via the interaction of the weak negatively charged patch close to the terminal Fe-S cluster to a positive charged Au-surface. So far, extensive works on heterodimeric *strep*-MBH on PGE electrodes carrying negatively charged surfaces with carboxylic and hydroxyl functional groups, have been reported. Thereby, successfully adsorbed *strep*-MBH exhibited an efficient direct electric contact between surface and enzyme.[207, 19] To understand this type of interaction and the underlying enzyme orientation(s), (i) different kind of functional groups exposing charges as well as (ii) various charge distributions were selected for electrode modifications to monitor possible overall electrostatic interactions of *strep*-MBH with the electrode surface. In this work, gold electrodes were used, which can be easily modified by biocompatible self-assembled monolayers (SAMs), thereby offering a variety of different functional groups.

4.2 Spectro-electrochemical insights into adsorption behavior of the heterodimeric *Re* MBH

4.2.1 Probing electrocatalytic efficencies of MBH

For electrochemical experiments, gold electrodes were modified with SAMs to form hydrophobic or charged surfaces depending on their functional groups and adjusted by the pH of the solution. Negatively charged 6-mercaptohexanoic acid (C_5COOH), positively charged 6-amino-1-hexanethiol (C_6NH_2) and a hydrophobic surface introduced by 1-pentanethiol (C_5CH_3) SAM were used. Dilutions of the surface charge density of carboxylic and amino-terminated SAMs were achieved by incorporation of a 6-mercapto-1-hexanol SAM with a hydroxyl functional group (C_6OH). A similar length of carbon-hydrogen chains was selected for all SAMs. Longer aliphatic chains reveal more compact monolayers in high ordered structures,[165, 163] however, the related enhancement of the SEIRA signals decreases with increasing distance from the Au electrode [112] and also the corresponding interfacial electron transfer rate. Therefore, a medium C_6/C_5 chain length was used for all the experiments as a good compromise. The experiments for a series of diluted charge densities using a C_6OH SAM were carried out by varying the ratios of the C_5COOH/C_6OH - SAMs by Dr. Nastaran Ranjbar/ Strasser group. Thereby, the highest enzyme activities were observed with a ratio of 1:9 (v:v) (see appendix Fig. A.2). In addition, different protonation degrees were applied by a variation of the corresponding buffer pH, covering the respective monolayer-surface on gold pen electrodes (see appendix Fig. A.5), in order to reveal the best immobilization parameters for *strep*-MBH on each SAM. Thus, the best immobilization conditions for the *strep*-MBH were screened, as shown in appendix (Fig. A2-A6). The corresponding protonation degrees are related to the chosen pH-values in Table 4.1 for the optimized surface immobilization.

Table 4.1: pKa and resulting (de)protonation degree of selected SAMs*

SAMs	pka value	working pH	(de)protonation degree	reference
C_5COOH	6.3 ± 0.1	5.5	16 ± 5 % -COO^-	this work/appendix
C_5COOH/C_6OH (1:9; v:v)	5.7 ± 0.1	5.5	37.5 % -COO^-	this work/appendix
C_6NH_2	6.0 ± 0.2	7.0	ca. 8 % -NH_3^+	[208, 214]
C_6NH_2/C_6OH (1:9; v:v)	7.2 ±0.01	7.0	38.7% -NH_3^+	[215]

*pKa values of SAM functional groups determined electrochemically according to procedures reported in Degefa et al. [216], while the related (de)protonation degree for negatively charged carboxyl and positive charged amino functional groups, respectively, were estimated for chosen immobilization phosphate buffer solution (PBS) at pH 5.5 for C_5COOH-, C_5COOH/C_6OH- and at pH 7.0 for C_6NH_2-, C_6NH_2/C_6OH-terminated SAMs. For pKa value determination of negatively charged-SAMs see appendix (Fig.A4.9).

Surface pKa values of the SAMs were determined by the peak current (i_p) of a given probe redox couple in buffers varying the pH. In this context, Zhao et al. [217] proposed a simple method, in which cyclic voltammetry is used to measure i_p values of $[Ru(NH_3)_6]^{3+/2+}$ for negative charged SAMs and $[Fe(CN)_6]_3^{3-/4-}$ for positive charged SAMs as a function of pH.
It should be noted, that the surface pKa for carboxylic acid terminated SAMs are typically more basic and amino-terminated SAMs more acidic than reported for their respective compound

in solution.[218] These shifts of pka values originate from the closely-packed surface-confined functional groups of adsorbed SAM. Thereby, intramonolayer hydrogen bonding effects and also electrostatic repulsions of surface charges can occur at the functional groups. Thus, the surface pKa value of the diluted C_5COOH/C_6OH – SAM shifts in comparison to the pure C_5COOH – SAM to a lower pka value. Similar trends have been previously reported by the Whitesides [219] and Crooks groups [220]. According to these authors, removal of acidic protons results in a closely packed monolayer of negative charge which appears, however, thermodynamically unfavorable due to the strong electrostatic repulsion of the charged carboxylate groups. In the case of mixed C_5COOH/C_6OH (1:9; v:v) SAM, COO^-- groups can structurally arrange favorable low-energy configurations, which reduce the effect of repulsive electrostatic interactions and allows an entire ionization for all available carboxylic groups. In this regard, a similar trend for positive charges of a diluted C_6NH_2 – SAM is observed by Marmisollé et al. [215] showing an increase of pka value for a C_6NH_2/C_6OH – SAM (1:1; v:v). Hereby, it can be assumed that the used higher diluted C_6NH_2/C_6OH – SAM (1:9; v:v) also presents a higher protonation degree than its corresponding C_6NH_2 – SAM.

Cyclic voltammograms recorded under the optimized conditions for a *strep*-MBH adsorption, derived from the pre-screening process as described above and are displayed in Figure 4.2.

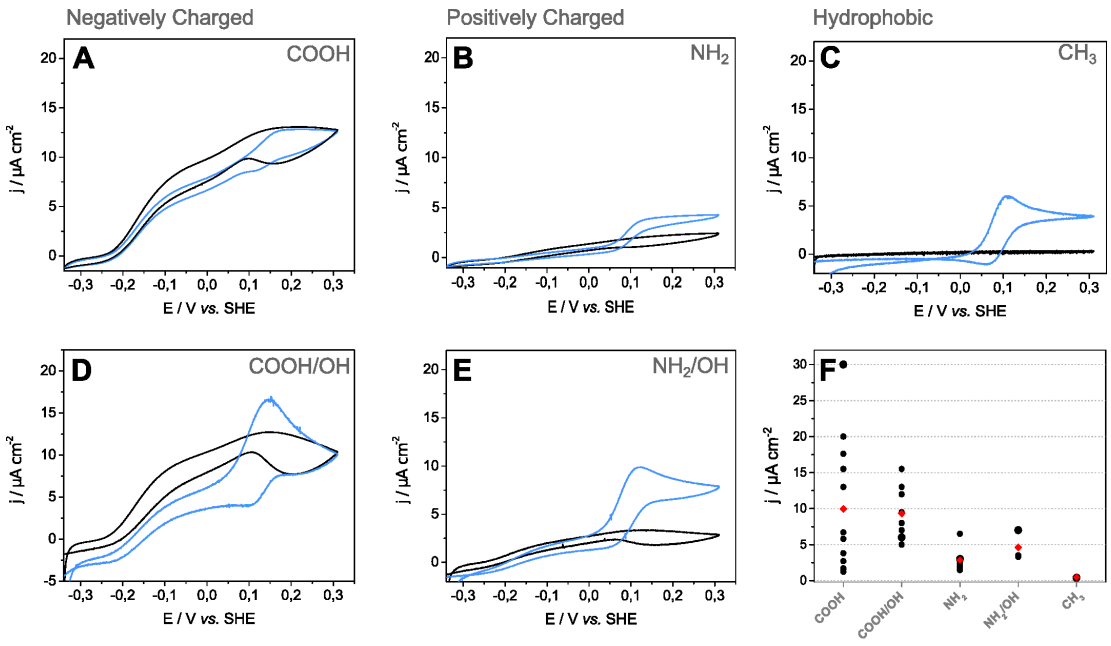

Figure 4.2: Cyclic voltammograms (CVs) recorded under H_2 atmosphere at room temperature for H_2 oxidation of *Re strep*-MBH on SAM covered gold electrodes in the presence of H_2-saturated buffer before (black lines) and after addition of 10 µM methylene blue (blue lines) for (A) C_5COOH, (B) C_6NH_2 (C) C_5CH_3, (D) C_5COOH/C_6OH (1:9) and (E) C_6NH_2/C_6OH. (F) shows the statistical evaluation of the current densities for each SAM, thereby displaying each experimental result (black) and the averaged current density (red). Scan rate: 5mV/s; 10 mM potassium phosphate solution at pH 5.5 was used as the electrolyte.

Figure 4.2 displays voltammetric traces recorded in the presence of H_2-saturated buffer, thereby revealing current densities similar to those previously observed for all purification variants of the *Re strep*-MBH heterodimer immobilized on pyrolytic graphite edge (PGE) electrode and the *Re*

MBH heterotrimer on Ag electrodes under H_2 atmosphere (Fig. 4.2A).[203, 205, 17] The characteristic sigmoidal shape reflects the electrocatalytic activity of the immobilized enzyme for H_2 oxidation, including the typical current drop at higher potentials, related to the reversible oxidative inactivation of this particular enzyme.[33] These results indicate that the catalytic activity of the heterodimer *strep*-MBH is preserved upon adsorption on SAM-coated Au electrodes, with preferential orientations towards the electrode surface suitable for DET and therefore within a distance below 15 Å. However, differences in current densities can be detected with respect to the DET efficiencies. *Strep*-MBH on negatively charged C_5COOH- and C_5COOH/C_6OH-SAM (Figure 4.2A, 4.2D) yields the highest current densities of about 10 µA cm^{-2}. Subsequently, methylene blue was added as a redox mediator to the buffer solution to investigate the homogeneity of the enzyme adsorption. Interestingly, the orientation of the individual enzyme molecules obtained on the negatively charged SAMs does not result in any mediated electron transfer with methylene blue (MB). This suggests a binding of exclusively favored orientations locating the distal Fe-S cluster close to the surface of the Au electrode, which enables solely DET of all adsorbed active enzymes. In contrast, *strep*-MBH bound on positively charged C_6NH_2- and C_6NH_2/C_6OH-SAMs involves both, DET and MET processes, resulting in current densities of 2 µA cm^{-2} (mediated: 4 µA cm^{-2}) and 3.3 µA cm^{-2} (mediated: 9.8 µA cm^{-2}), respectively. On C_6NH_2 covered surfaces none of the two ET processes is favored. In the case of mixed SAM (C_6NH_2/C_6OH) with a diluted charge distribution, the fraction of MET is higher (compared to the DET). It even exhibits higher current densities compared to the pure C_6NH_2 covered surface. These findings strongly suggest that the electro-enzymatic H_2 oxidation originates from various MBH orientations on the surface. *Strep*-MBH adsorption on a hydrophobic C_5CH_3 SAM results in an even stronger effect of the redox mediator. In this case, the MET is clearly favored over the DET process with a current density of 6 µA cm^{-2} compared to only 0.3 µA cm^{-2}, respectively, thereby revealing 20 times higher mediated current densities.

Figure 4.2F gives an overview on all cyclic voltammetric experiments recorded on gold pen electrodes, including deviations between different protein purifications and various purchased SAM batches. Thereby, the following general trend can be observed: Both negatively charged SAMs exhibit major current density variances throughout all performed CVs. In particular, *strep*-MBH on C_5COOH-SAM reveals values between 1.6 µAcm^{-2} and 30 µAcm^{-2}. This broad distribution can presumably be related to variations in the C_5COOH-SAM quality. In particular, the short C_5-COOH-SAM might be more strongly affected by an oxidative degradation process over time. Generally, SAMs can oxidize over time and particularly the here used C_5COOH-SAM seems to be affected by oxidation during its long-term storage. Although the mixed C_5COOH/C_6OH-SAM also exhibits a significant deviation in the detected current densities, the SAM consists only of a 1/9 (v/v) fraction of C_5COOH-SAM and therefore the observable variance might cover only a smaller range (between 5 and 15 µA cm^{-2}).

Strep-MBH immobilized on both positively charged SAMs, C_6NH_2- and C_6NH_2/C_6OH-SAMs, exhibits reproducible values for the recorded current densities in DET as well as MET. The hydrophobic C_5CH_3-SAM exhibits reproducibly hardly any DET and rather high values for the MET in all experiments.

The cyclic voltammetric data displays an adsorption of *strep*-MBH on all screened SAM-modified surfaces, exhibiting the typical electrocatalytic H_2 oxidation. As the catalytic current densities of the same *strep*-MBH preparation differ drastically depending on the surface charge of the SAM-covered Au surface, discriminative binding sites between *strep*-MBH and the various SAM

surfaces can be assumed. To gain deeper insights into the binding processes, SEIRA spectroscopy was applied to study the adsorption process and possible correlations with the observable catalytic current densities.

4.2.2 Surface-Enhanced Infrared Absorption Spectroscopy on adsorbed MBH

4.2.2.1 Amide Region

In line with the electrochemical data (see section 4.2.1) the adsorption of the *strep*-MBH on different SAM surfaces was monitored *in situ* by SEIRA spectroscopy. Thereby, the protein backbone structure can be particularly resolved in regions between 1700 – 1600 cm^{-1} and 1600-1500 cm^{-1} by means of the so-called amide I and amide II bands, respectively. The amide I band derives almost exclusively from the C=O stretching vibration of the backbone peptide bond, whereas the amide II band originates from an out-of-phase combination of N-H in-plane bending and C-N stretching vibrations of peptide bonds, see chapter 2.2.2.4. Figure 4.3 A shows the immediate adsorption of *strep*-MBH indicated by the amide I and amide II bands, centered at 1660 cm^{-1} and 1550 cm^{-1}, respectively, hence confirming the sustained integrity of the backbone structure. The comparison of amide I and amide II bands on different SAMs and in solution is given in section 4.3.7). Adequate signal intensities of amide I and II on all SAM surfaces are observed already in the first spectrum, finalized after 3 min. The intensities of the amide I and amide II bands monitored in the respective absorbance spectra as a function of time show a gradual increase within the first 30 min (Figure 4.3A).

These results are in good agreement with previous spectroscopic studies on hexahistidine-tagged *Re* MBH (his-MBH). However, no electric contact between enzyme and electrode surface was established by this immobilization strategy on a Ni-Nitrilotriacetic acid (NTA)-SAM [67], presumably related to a too large distance between the distal Fe-S cluster and the electrode surface, thereby impeding a DET. Adsorbed *strep*-MBH on SAM-modified gold surfaces, however, exhibits DET on all SAM structures under sustained overall protein backbone integrity, revealed by its amide patterns and more importantly by the state of the active site. The analysis of amide I and amide II band intensities as well as the corresponding amide I/amide II ratios gives an idea about the enzyme coverage, enzyme-surface distance dependencies and relative enzyme orientations on the surface. All observable amide I and II band intensities and the respective amide I/amide II ratios show in Figure 4.3 C are summarized in Table 4.2.

Surprisingly, the positively charged SAMs (C_6NH_2 and C_6NH_2/C_6OH) reveal very low overall values for DET and MET, whereas the SEIRA spectra display the highest amide I band intensities of 6.2 mOD and 11.4 mOD, respectively. The negatively charged C_5COOH-SAM, on the other hand, exhibits the lowest amide I band intensity of 3.7 mOD in Figure 4.3A. However, previous results (see 4.2.1) already revealed that in particular, this type of surface modification exhibits strong variances due to the inherent instability of the SAM. *Strep*-MBH on a mixed C_5COOH/C_6OH SAM displays moderate amide I band intensities of around 4.5 mOD. On the hydrophobic surface of C_5CH_3, similar intensity values of about 4 mOD can be detected.

Table 4.2: Amide I, II band intensities and related ratios of *strep*-MBH adsorbed on various SAMs*

SAMs	amide I intensity (mOD)	amide II intensity (mOD)	amide I / amide II ratio ± deviation
C_5COOH	3.7	3.6	1.00 ± 0.1
C_5COOH/C_6OH (1:9; v:v)	4.5	3.9	1.14 ± 0.2
C_6NH_2	6.2	4.8	1.27 ± 0.01
C_6NH_2/C_6OH (1:9; v:v)	11.4	8.9	1.26 ± 0.01
C_5CH_3	3.9	4.0	0.98 ± 0.2

*Amide I and II band intensities values [in 10^{-3} OD] extracted from SEIRA spectra displayed in Figure 4.3A and mean values and standard deviations (±sd) of amide I/ amide II band intensity ratios extracted from all experiments.

Naturally, the *strep*-MBH is composed of a mixture of unordered secondary structure elements, namely 42.5 % helices, 14.8 % sheets: 42.7% others (turns and random coils), determined by secondary structure assignment program STRIDE.[221] A second secondary structure assignment program, DSSP, revealed similar values.[222] Hence, it is not possible to distinguish *per se* specific orientations solely based on the evaluation of the amide mode region in the SEIRA spectrum by means of the angular dependent surface enhancement as for example membrane proteins which harbor uniform parallel transmembrane helices.[108] Monitoring the amide I/amide II ratio, in such manner, provides an understanding of similarities in orientations and ratio changes of the same sample allow comparisons of the occurring surface processes, i.a. reorientations.

The finally recorded spectra of *strep*-MBH on C_5COOH and on C_5COOH/C_6OH, measured after a 30 min adsorption process exhibit amide I/amide II band intensity ratio of 1 and 1.14, respectively (see Table 4.2). *Strep*-MBH samples immobilized on C_6NH_2 and mixed C_6NH_2/C_6OH-SAMs, both representing the highest absorbance intensities for adsorbed *strep*-MBH, display identical amide band ratios with a value of around 1.3. It has to be emphasized, that on these particular surfaces the respective amide I to amide II proportions are significantly higher compared to both, negatively charged (1.0 and 1.14) and hydrophobic (0.98) SAMs. These values suggest different final orientations on positively charged surfaces compared to the other ones. As the *strep*-MBH molecules are bound in multiple orientations, as derived from the observed MET processes described in section 4.2.1, their amide I/amide II value of 1.3 may be related to a spectral overlap of the differently oriented enzyme fractions. For comparison the corresponding amide I/amide II band ratio of isotropically oriented *strep*-MBH in solution was determined within a thin IR- transmission cell to 1.38, which is indeed close to *strep*-MBH adsorbed on C_6NH_2- and C_6NH_2/C_6OH-terminated SAMs.
A further, more detailed discussion of this matter is provided at the end of this chapter (see section 4.3.7). The amide I/amide II ratio changes during adsorption are discussed in detail in section 4.2.2.3.

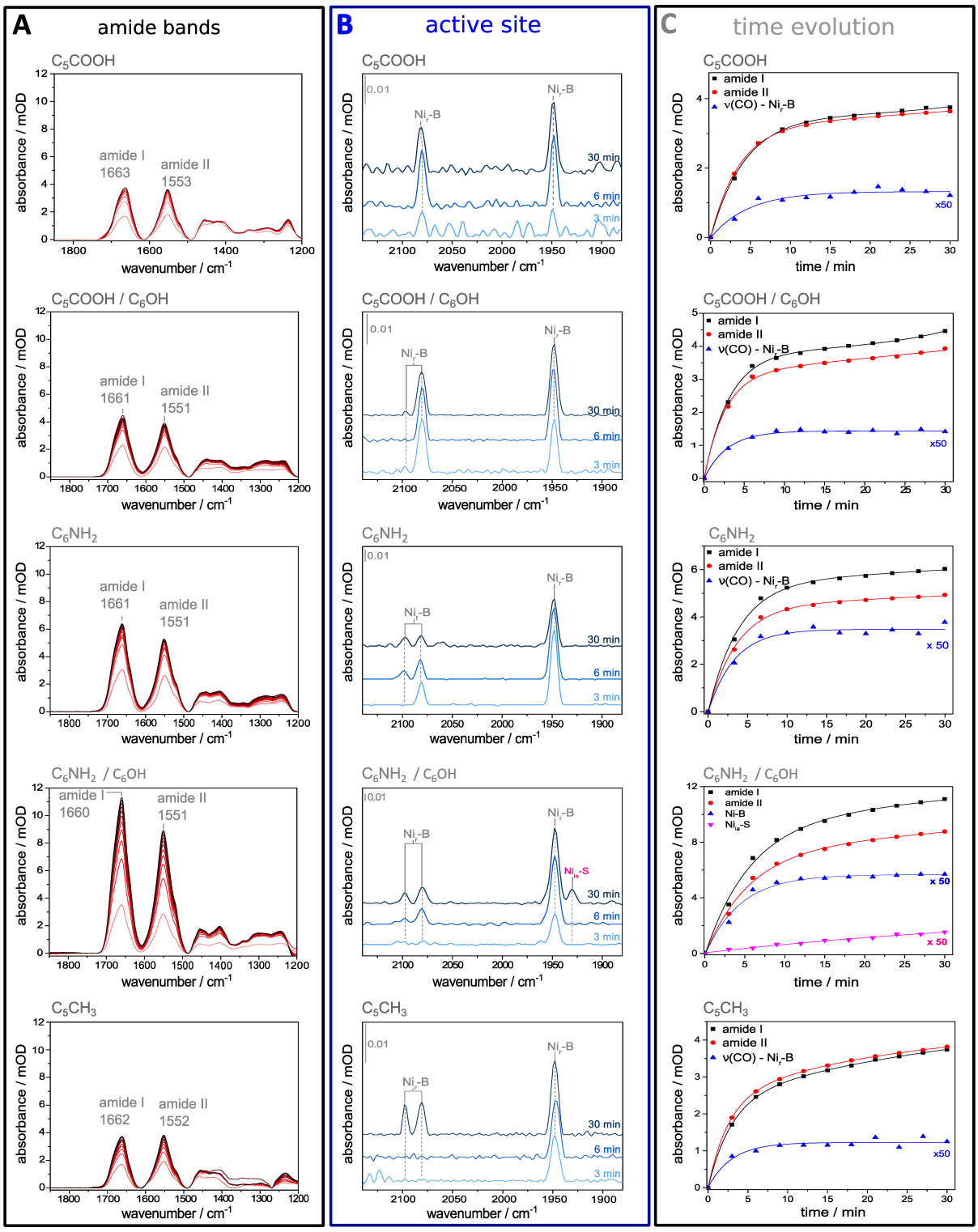

Figure 4.3: SEIRA spectra of *strep*-MBH, immobilized on a nanostructured, SAM-covered Au electrode surface resulting in five different surface charge distributions. From top to bottom: C_5COOH, C_5COOH/C_6OH, C_6NH_2, C_6NH_2/C_6OH and C_5CH_3. SEIRA spectra (A) displaying the amide mode region, (B) SEIRA spectra showing the region characteristic for CO and CN stretchings of the active site and (C) time evolution of band intensities derived from the SEIRA spectra for amide I, II modes and active site CO absorption (in Ni_r-B, Ni_{ia}-S state) The latter were multiplied by a factor 50 for better comparability. Biexponential fits ($A = A_0 + A_1 \exp(-t/\tau_1) + A_2 \exp(-t/\tau_2)$) could be applied in the time period of $0 < t < 30$ min and are displayed as solid lines. Incubations with *strep*-MBH on C_5COOH and C_5COOH/C_6OH-SAMs were performed in 10 mM phosphate buffer solution (PBS) at pH 5.5 and on C_6NH_2,C_6NH_2/C_6OH and C_5CH_3 covered surfaces in 10 mM PBS at pH 7. All experiments were carried out at 4°C.

4.2.2.2 Active Site

The SEIRA spectra of *strep*-MBH immobilized on SAM-coated electrodes at open circuit potential (OCP) reveals a characteristic vibrational band at 1948 cm^{-1}, assigned to the CO ligand coordinated at the [NiFe] active site, together with the conjugate CN_1 and CN_2 stretching vibrations at 2081 cm^{-1} and 2098 cm^{-1}, respectively. These three bands are assigned to the Ni_r-B species of *Re* MBH,[5] a readily oxidized state, typical for the as-isolated enzyme. The Ni_r-B state is observed for all adsorbed *strep*-MBH preparations displayed in Figure 4.3B, which suggests an intact catalytic center upon enzyme-surface interaction. The corresponding vibrational modes of the CO and CN^- ligands can be detected already in the first spectrum recorded after 3 min. Band intensities and selected ratios of the related CO, CN_1 and CN_2 absorptions taken from of the final spectra of the immobilized protein are displayed in Table 4.3. Calculation of Rippers et al. [210] based on the MBH homology model showed, that the vibrational modes related to the observed cyanide bands derive indeed from localized movements of the individual ligand with varying amino acid environments. Not all spectra exhibit the three ligand bands assigned to Ni_r-B: The active site absorptions of the *strep*-MBH (Figure 4.3B) on C_5COOH- and C_5COOH/C_6OH-SAMs display the CO and only one CN^- stretching vibration at lower frequencies, i.e. CN_1 stretching at 2081 cm^{-1}. This is still indicative of a native active site, although the intensity of the CN_2 band at 2098 cm^{-1} band is too weak for an obvious detection. The latter observation can be interpreted as a consequence of the angular dependence of the SEIRA spectral intensities, namely the surface selection rule, which states that vibrational modes with changing transition dipole moments parallel to the surface cannot be detected; those with preferentially perpendicular orientations are maximal enhanced. This distinct absence in the SEIRA spectrum indicates a homogeneous orientation of the MBH and also correlates with the observed unaffected current densities after the addition of a redox mediator, which have been determined in the electrochemical experiments (see section 4.2.1).

Table 4.3: Band intensities of the CO and CN^- ligands at active site*

SAMs	intensities of active site absorptions (10^{-5} OD)			ratio	ratio
	CO	CN_1	CN_2	CO/ CN_1	CO/ amide I
C_5COOH	2.4	1.7	–	1.4	0.006
C_5COOH/C_6OH (1:9; v:v)	2.4	1.5	–	1.6	0.006
C_6NH_2	4.5	1.0	0.8	4.5	0.010
C_6NH_2/C_6OH (1:9; v:v)	11.6	2.6	1.7	4.5	0.011
C_5CH_3	2.3	0.92	0.75	2.5	0.006

*CO (1948 cm^{-1}), CN_1 (2081 cm^{-1}), CN_2 (2098 cm^{-1}) intensities, as well as CO/ CN_1, CO/ amide I ratios of *strep*-MBH adsorbed on different SAMs, as exhibited in Figure 4.3B.

The absolute intensities for the active site ligands are a factor of 10^{-2} smaller than the amide I band intensities, in all cases of *strep*-MBH bound onto various SAMs. The intensity values for the observed diatomic ligands on different SAMs evaluated from Figure 4.3B and their band intensity ratios of active site ligands those of CO/CN_1 as well as CO/amide I are summarized in Table 4.3. The latter, CO/ amide I band intensity ratio derived from Ni_r-B species reveals similar value ranges of approximately 0.01 on all SAM surfaces. *Strep*-MBH on the positively charged surfaces

C_6NH_2- and C_6NH_2/C_6OH reveal again almost identical ratios of 0.01 and 0.11, respectively, whereas the negatively charged and hydrophobic surfaces, which displayed already similar amide I/amide II band intensity values show the exact same ratios of 0.006. Under the assumption that the signal intensity originates solely from the enhanced IR radiation a signal decrease of d^{-6} can be supposed. For an understanding of the enzyme orientation on the particular surfaces, the CO/ CN_1 ratios are contemplated for further interpretation, since these ratios depend strongly on the angular dependent selection rule. The intensity of enhancement involves two factors: distance dependency relative to the Au surface and second the angular dependence of vibrational modes, which are maximal enhanced for adsorbates exhibiting transition dipole moment changes in perpendicular direction to the Au surface. Since all three ligands are coordinated to the Fe atom, and are in very similar distance to the Au electrode, different enhancement factors due to different ligand to Au-surface distance could be rather excluded. Hence, the ligand absorption intensity ratios are suggested to originate mainly from their angular enhancement dependence.

The CO/CN_1 ratio for *strep*-MBH in solution at pH 5.5 is about 4.2, representing a statistical distribution of orientations. *Strep*-MBH adsorbed on C_6NH_2– and C_6NH_2/C_6OH–SAMs represent identical values of 4.5, underlining the similar orientation scenarios on both surfaces and in agreement with the results for amide I/amide II intensity ratios, also CO/CN_1 ratios are close to those found in bulk solution (4-5). Furthermore, electrochemical data, *vide supra*, underlines adsorption scenario of mixtures of more than one orientation by their monitored processes of both, DET and MET (see section 4.2.1). A contrary trend to those observed on positively charged surfaces is found for *strep*-MBH on the C_5COOH-and C_5COOH/C_6OH-surface with a CO/CN_1 ratio of 1.4 and 1.6, respectively, which is significantly smaller than *strep*-MBH in solution. The complementary electrochemically derived data exhibits only a DET, suggesting a homogenous adsorbed MBH with a preferential orientation in this case. *Strep*-MBH adsorbed on C_5CH_3-SAM exhibits a CO/CN_1 ratio of 2.5, while the related electrochemical data suggest the presence of several orientations shown by the high fraction of favored MET process.

4.2.2.3 Adsorption Kinetics

The adsorption kinetics in Figure 4.3 C displays the time-dependent evolution of amide I, II and CO band intensities within the entire process. The spectra collection of *strep*-MBH immobilization on all SAMs was started immediately after addition of the *strep*-MBH solution.

Amide Band Region

While the positions of amide I and amide II bands remain unchanged, their intensity changes follow a biexponential increase consisting of a fast and a slow kinetic process. Parameters of exponential processes are defined in section 2.4.5. The corresponding time constants are determined from the applied fits on the experimental data and are summarized in Table 4.4.

Figures 4.3 C displayed the amide I and amide II band intensities as a function of adsorption time. The underlying kinetic processes exhibit the expected biexponential increase as often reported for slow monolayer adsorptions.[67, 223, 208] The adsorption processes differentiate evidently in their time constants, resulting in various biexponential behaviors depending on the investigated surface charges. The time constants derived from the related fits are summarized in Table 4.4.

Upon immobilization, both, the two amide bands and the CO stretching band(s) increase concomitantly as a function of time (see Fig. 4.3). Table 4.4 summarizes the resulting parameter values from a biexponential fit of the time course of amide I and amide II band intensities. For

all adsorption processes of *strep*-MBH on selected SAMs, a first fast and a second slow time constant have been determined.

Table 4.4: Kinetic parameters of the adsorption process derived from the time course of amide I and amide II band intensities*

amide band	A_0 (mOD)	A_1 (mOD)	τ_1 (min)	A_2 (mOD)	τ_2 min
C_5COOH					
1663 cm^{-1}	3.49 ± 0.2	3.52 ± 0.14	4.28 ± 0.30	0.02 ± 0.07	10.35 ± 12.96
1553 cm^{-1}	3.41 ± 0.5	3.21 ± 0.13	3.56 ± 0.17	1.48 ± 0.71	114.50 ± 32.17
C_5COOH/C_6OH (1:9; v:v)					
1661 cm^{-1}	4.76	3.28 ± 0.25	2.63 ± 0.34	1.49 ± 0.24	23.56 ± 4.75
1551 cm^{-1}	4.16	2.96 ± 0.18	2.43 ± 0.27	1.20 ± 0.17	22.89 ± 4.14
C_6NH_2					
1661 cm^{-1}	6.24	5.04 ± 0.53	3.63 ± 0.46	1.22 ± 0.53	18.58 ± 6.56
1551 cm^{-1}	5.12	4.19 ± 0.30	3.59 ± 0.20	0.95 ± 0.30	20.15 ± 5.81
C_6NH_2/C_6OH (1:9; v:v)					
1661 cm^{-1}	11.90	8.73 ± 2.76	5.44 ± 1.45	3.29 ± 2.81	22.81 ± 16.24
1550 cm^{-1}	9.40	2.55 ± 2.06	5.26 ± 1.37	2.80 ± 2.09	21.70 ± 13.09
C_5CH_3					
1662 cm^{-1}	3.95	1.81 ± 0.14	2.30 ± 0.26	2.13 ± 0.13	14.06 ± 0.76
1552 cm^{-1}	4.00	2.0 ± 0.08	2.10 ± 0.14	2.00 ± 0.08	13.59 ± 0.46

*Fit parameters obtained from the biexponential function ($A = A_0 + A_1 \exp(-t/\tau_1) + A_2 \exp(-t/\tau_2)$) to the time-dependent evolution of amide I band (around 1660 cm^{-1}) and amide II band (around 1550 cm^{-1}) intensities of the *strep*-MBH adsorption on C_5COOH, C_5COOH/C_6OH, C_6NH_2, C_6NH_2/C_6OH and C_5CH_3 SAMs derived from the related data in Figure 4.3.

The first and faster adsorption process lies in time scales between 2.3 min and 5.5 min. The fastest time constants are determined for *strep*-MBH binding on hydrophobic C_5CH_3-SAM coated surface, revealing values for τ_1(amide I) = 2.3 min and τ_1(amide II) = 2.1 min. These values are followed by the ones obtained within the time constant determination of C_5COOH/C_6OH with τ_1(amide I) = 2.63 min and τ_1(amide II) = 2.96 min. *Strep*-MBH adsorbed on C_5COOH exhibits slightly slower time constants, as found for the previous mentioned mixed C_5COOH/C_6OH-SAM with τ_1(amide I) = 4.28 min and τ_1(amide II) = 3.56 min. The slowest growth time constants were derived for the *strep*-MBH on a mixed C_6NH_2/C_6OH surface with values of τ_1(amide I) = 5.44 min and τ_1(amide II) = 5.26 min. Figure 4.4 displays the ratios, which are considered to be most interesting during the adsorption processes, presumably indicating reorientation processes at the surface, i.e. amide I/amide II and CO/amide I ratios, evaluated from Figure 4.3C. As displayed in Figure 4.4, the value of amide I/amide II ratio varies from 0.98 to 1.26 for *strep*-MBH on different SAMs, a similar tendency of the time course can be reported for all: Starting with a lower amide I/amide II ratio in their first recorded spectra, i.e. 3 min, the subsequent detected spectra show amide I/amide II values equilibrating at slightly higher ratios. Two different time-dependent course behaviors are observed during the residual immobilization time. Amide I/amide II ratios of *strep*-MBH samples on C_6NH_2- and mixed C_6NH_2/C_6OH-SAMs remain constant after the

first 20 min within the contemplated immobilization time, whereas in case of immobilization on C_5COOH-, C_5COOH/C_6OH-, C_5CH_3–SAMs a secondary and subordinate slowly, but steady increase of amide I/amide II can be observed within the complete adsorption time.

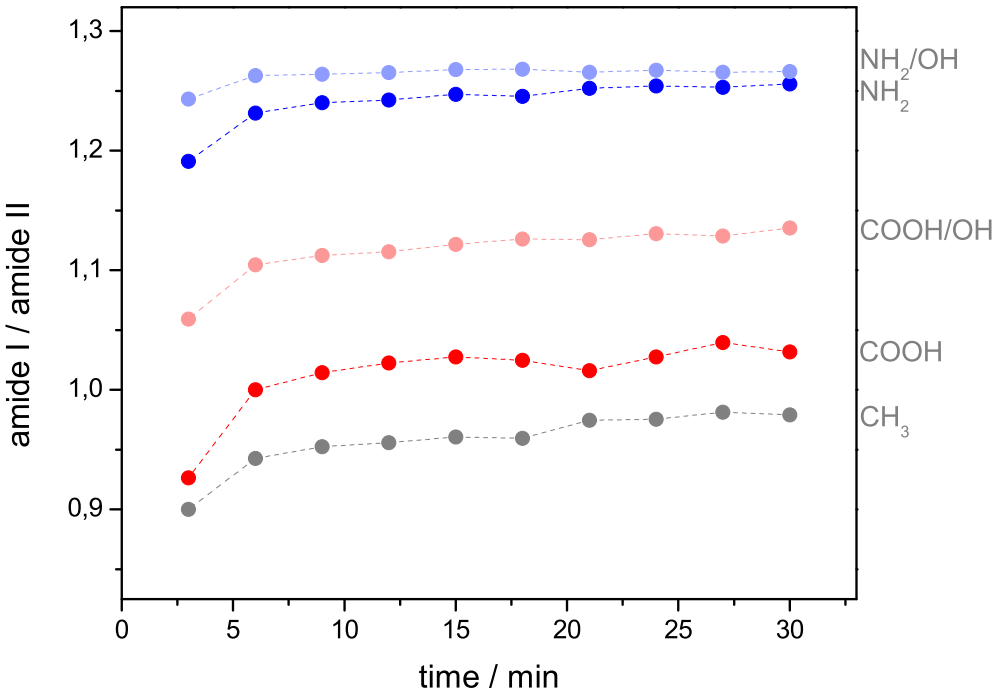

Figure 4.4: Ratios over adsorption time of amide I/ amide II; data evaluated from Fig. 4.3C: SEIRA spectra of *strep*-MBH, immobilized on a nanostructured, SAM-covered Au surface: C_5COOH, C_5COOH/C_6OH, C_6NH_2, C_6NH_2/C_6OH and C_5CH_3.

This change is accompanied by a small shift (from 1665 cm^{-1} to 1663 cm^{-1}) in the amide I position, while the position of amide II remains constant. While the ratio changes also over the adsorption time of 30 min, this could be the indication of a steady reorientation process. Since MET processes were not observed on C_5COOH-, C_5COOH/C_6OH-SAMs, enzyme multi-layer formation can be excluded here.

Active Site Region

As discussed previously, the active site could be monitored for *strep*-MBH immobilized on all SAMs used in the present study and revealed predominately the presence of an oxidized, ready Ni_r-B state, which intensity is studied over time. Figure 4.3C displayed the time course from the band intensities of the corresponding CO absorptions, characteristic for the redox states Ni_r-B and Ni_{ia}-S, if present. Interestingly, only a mono-exponential adsorption process is found for the Ni_r-B state (see Table 4.5), although the related amide bands follow a biexponential binding behavior.

Hereby, the amount of Ni_r-B reaches a constant value within few minutes indicating the completion of *strep*-MBH adsorption, implying a saturation of binding sites at the surface and therefore

most likely monitoring only the *strep*-MBH directly bound to the surface, i.e. (sub)monolayer formation. The initial kinetic process of amide bands intensity growth and the corresponding Ni_r-B formation exhibit both similar time constants for each essayed SAM, see Table 4.4. The initial adsorption process monitored by the intensity growth of the two amide bands is likely to be associated to an initial direct enzyme-SAM interaction, as the mono-exponential time course of the Ni_r-B formation derives.

Table 4.5: Kinetic parameters of the adsorption process derived from the time course of CO stretching vibration band intensity of the active site *

CO absorption (active site)	A_0 (10^{-2} mOD)	A_1(10^{-2} mOD)	τ_1(min)
C_5COOH			
1948 cm^{-1}	2.6 ± 0. 1	2.7 ± 0.2	4.7 ± 0.9
C_5COOH/C_6OH (1:9; v:v)			
1948 cm^{-1}	1.4 ± 0.02	1.44 ± 0.05	4.4 ± 0.4
C_6NH_2			
1551 cm^{-1}	4.5 ± 0.1	4.6 ± 0.2	4.4 ± 0.4
C_6NH_2/C_6OH (1:9; v:v)			
1948 cm^{-1}	11.4 ± 0.2	11.6 ± 0.2	4.4 ± 0.4
1930 cm^{-1}	3.2 ± 0.9	3.1 ± 0.9	46.2 ± 20.1
C_5CH_3			
1948 cm^{-1}	2.5 ± 0.1	2.4 ± 0.2	3.0 ± 0.6

* Results obtained, using the mono-exponential function ($A = A_0 + A_1 \exp(-t/\tau_1)$) to fit the time course of the CO stretching bands at 1948 cm^{-1} (Ni_r-B) and at 1930 cm^{-1} (Ni_{ia}-S) of *strep*-MBH immobilized on C_5COOH, C_5COOH/C_6OH, C_6NH_2, C_6NH_2/C_6OH and C_5CH_3 SAMs; evaluated from data shown in Figure 4.3.

The further increase in the biexponential time course of amide band intensities does not seem to be related to the coverage of the *strep*-MBH bound directly at the SAM-surface, since no further increase of the Ni_r-B state intensity can be observed after the initial process. Thus, the second process derived from the amide band intensities course might be therefore rather related to a reorientation of the (sub)monolayer species, which would lead to a slow amide band intensity change due to the enhancement effect by its angular- dependency.

Fig. 4.5 displays the CO/amide I band intensity ratio over the entire immobilization time. While the corresponding CO/amide I band intensity ratio of *strep*-MBH on both positively charged surfaces, NH_2- and C_6NH_2/C_6OH-SAM, slowly decrease over time, the amide band intensity ratios reach a maximum intensity and remain thereafter constant within the contemplated time scale.

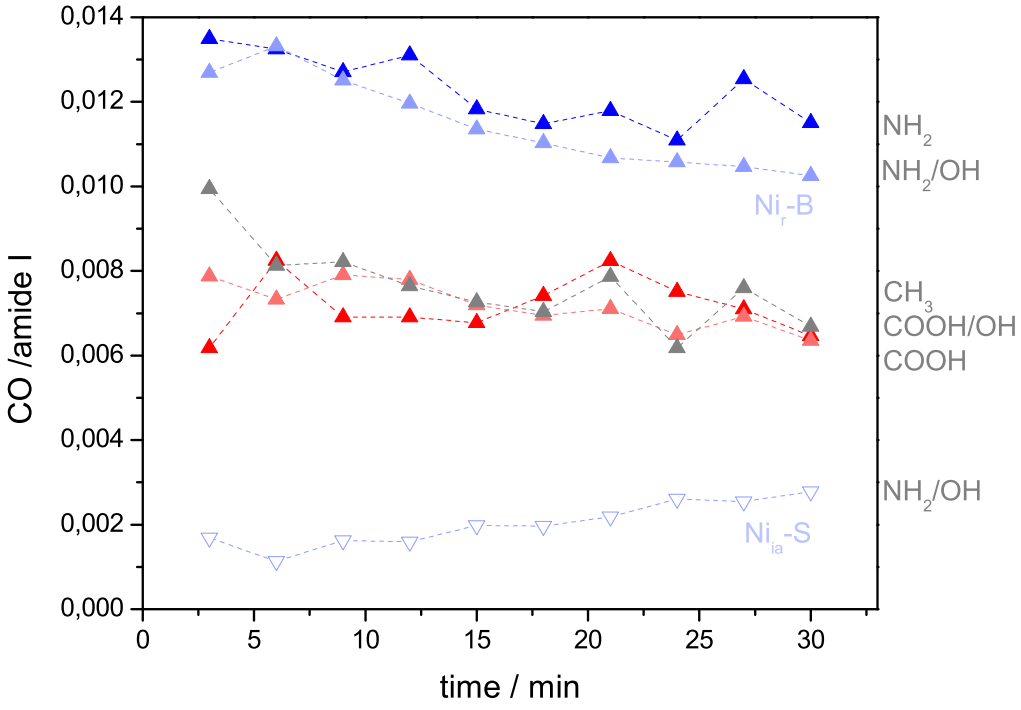

Figure 4.5: Ratios over adsorption time of CO/ amide I from CO stretching vibration characteristic for active site absorption (in Ni_r-B state, and if present Ni_{ia}-S state). Data evaluated from Fig. 4.3C: SEIRA spectra of *strep*-MBH, immobilized on a nanostructured, SAM-covered Au surface: C_5COOH, C_5COOH/C_6OH, C_6NH_2, C_6NH_2/C_6OH and C_5CH_3.

The CO/amide I band intensity ratio for the Ni_r-B state of *strep*-MBH on C_6NH_2/C_6OH-SAM displays a decay in a slightly faster regime than on a pure NH_2-SAM and is accompanied by the formation of the irreversibly inactive state, Ni_{ia}-S (1930 cm^{-1}).[224, 5] It might be here formed, when the active site is in certain enzyme orientations exposed to the high local electric field on uncovered Au, which also lead to protein denaturation.[225, 226, 227] Normally it is formed only for the *Re* heterodimer MBH in the presence of residual oxygen (traces) and hydrogen. Presumably, electrons cannot be fast enough provided to the active site during O_2-reduction, whereby reactive oxygen species remain at the active site leading to oxidative damage. Indeed, spectroelectrochemical studies of immobilized *strep*-MBH on both positively charged SAMs support this hypothesis, as here also enzyme fractions are present, where the enzyme is not electronically wired to the surface. Thereby, a higher amount of MET and also Ni_{ia}-S state is observed on the C_6NH_2/C_6OH-SAM (see section 4.2.1).
In fact, the CO/amide I band intensity ratio of *strep*-MBH on negatively charged SAMs remains constant within the immobilization time. Since electrochemical data (see Fig. 4.2) only exhibits DET between *strep*-MBH and the electrode surface, electrons required for a complete O_2 reduction at the active site can be provided directly from the electrode. In agreement, no loss of Ni_r-B can be derived from the CO/amide I band intensity ratio.
In line with these observations, *strep*-MBH on a CH_3-SAM, which is mainly not electronically wired to the Au electrode reveals a relative decay of the Ni_r-B state monitored via the CO/amide band intensity ratio over time. However, no CO absorption characteristic for Ni_{ia}-S was observ-

able. Here, the overall intensity might be only too low for a detection at this stage or the progress of an oxidative damage not far enough.

4.2.3 MBH coverage determination via Atomic Force Microscopy

For a more accurate comparison of *strep*-MBH adsorption on these diverse surfaces, the origin of the observed amide band intensities was analyzed in more detail. SEIRA spectroscopically recorded band intensities depend on the amount of adsorbed enzyme molecules and the surface enhancement effect, which decreases strongly with increasing distance from the surface $I \propto d^{-6}$.[100] To understand the contribution of enzyme coverage to the intensity values observed in SEIRA spectra comparative AFM measurements were performed to determine the latter . In this context, Au surfaces coated with pure C_5COOH- and C_6NH_2-SAMs, which were exemplarily studied after enzyme incubation. In such manner, besides the variation of amide band intensities, also different amide I/amide II band intensity ratios were observed, suggesting diverging orientations. Since a huge variance was observed in particular for the previously described studies on C_5COOH-SAMs, the present experiments were prepared and performed on the same day on identical *strep*-MBH and SAM incubation solution for SEIRA and AFM measurements.

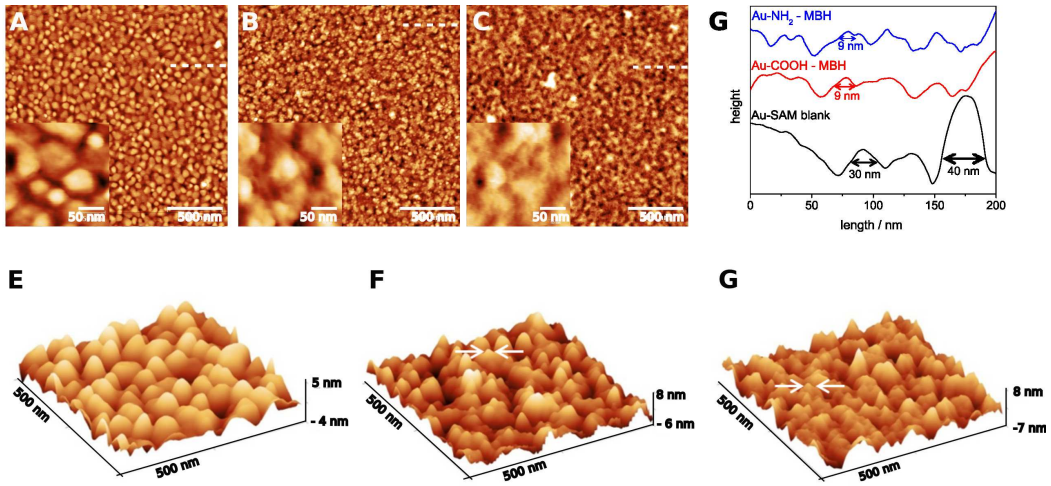

Figure 4.6: Top: Topographic AFM mapping in non-contact mode of the SAM-modified Au surface (A) before and (B-C) after completed *strep*-MBH immobilization on (B) C_5COOH-modified, and (C) C_6NH_2-modified, SAM covered Au electrodes. Insets display high magnification AFM images. The dashed horizontal lines indicate the course of the height profiles shown in (D) for immobilized *strep*-MBH on a C_5COOH-SAM (red line), on a C_6NH_2-SAM (blue line) and prior to immobilization (black line). Bottom: 3D illustrations of the higher magnifications of (E) before and after completed MBH immobilization (F) on C_5COOH-modified Au electrodes, (G) C_6NH_2-modified Au electrodes. The colored arrows indicate one *strep*-MBH enzyme unit of 9 nm size.

AFM measurements on the C_5COOH-surface and on C_6NH_2-surface were performed before after enzyme incubation (Figure 4.6A-C). Figure 4.6A displays the rough nanostructured Au surface with lateral size values between 30-50 nm for the Au surface aggregates, coated with SAM. Figure 4.6B shows the AFM image of *strep*-MBH adsorbed on C_5COOH-coated Au after 30 min, which clearly deviates from the bare SAM-covered Au-surface exhibiting smaller structural units on the rough surface, which can be attributed to the *strep*-MBH. Consistently, structural units can be observed for the *strep*-MBH on C_6NH_2-SAM coated Au. The diameter of a single unit is determined by the lateral periodicity of ca. 9 nm in the corresponding height profile of *strep*-

MBH on C_5COOH- and C_6NH_2-SAM (Figure 4.6D). Recorded surface depths of these samples yield an average value between – 6 nm and 8 nm for enzyme-covered Au-SAM surfaces, whereas blank Au-SAM surfaces, exhibit average depths of -6 and 5. Due to the limiting width of the AFM pits the corresponding tip could not reach surface depths, which cannot be considered as representative for the real depth. In addition, the thickness of the MBH layer was determined by ellipsometric measurements for both monolayers revealing layer thicknesses of ca. 7 nm, which is indicative of a preferential protein monolayer formation (see appendix Fig. A.10). *Strep*-MBH on C_5COOH-SAM covered Au surface exhibits a lower coverage than on the corresponding C_6NH_2-SAM coated surface. The determination of the molecular units on the individually screened sample in low (2µm x 2µm) and high magnification (500nm x 500nm) on least 3 different spots per sample, revealed coverages of 0.09 pmol cm^{-2} for C_5COOH- and 0.44 pmol cm^{-2} for C_6NH_2-SAM surfaces. Thus, the coverage on an amino-terminated surface reveals a 5-fold higher enzyme coverage than on C_5COOH-terminated surface. This result correlates well with the observable absolute band intensities of amide I and amide II bands measured on these particular surfaces by SEIRA spectroscopy, shown in Figure 4.7. This finding suggests that a distance dependence of spectral intensities due to the surface enhancement effect can be ruled out as the dominating reason, at least for large biomolecules such as MBH. However, the latter should be still considered in the further data evaluation for same films.

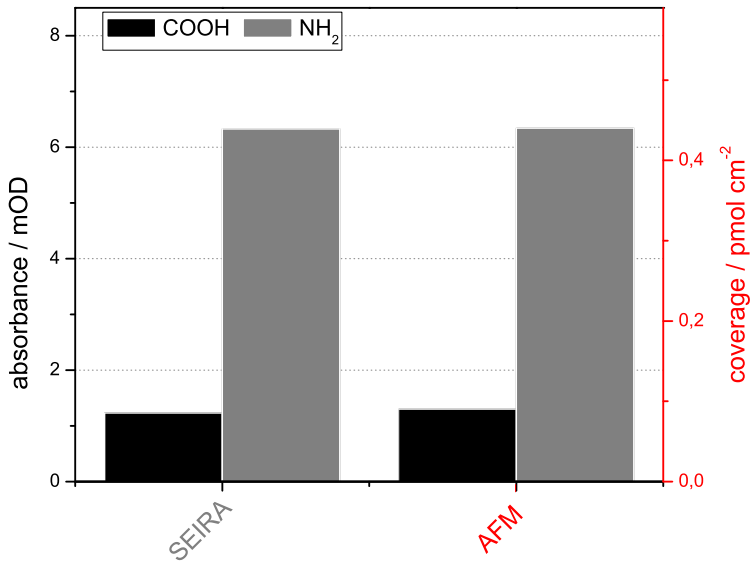

Figure 4.7: Exemplary comparison between SEIRA derived amide I band intensities and the surface coverage deduced from AFM studies on C_5COOH- (black) and C_6NH_2-SAMs (gray).

4.2.4 Summary

To summarize the obtained data on all different presented SAM surfaces, Figure 4.8 displays the occurring variances in all performed experiments. The detected electrochemical activity of the SEIRA measurements for *strep*-MBH is plotted in Figure 4.8A in form of black dots and reveals for the C_5COOH-SAM the highest variance presumably due to the instability of the SAM. Contrarily to the pure electrochemical data displayed in Figure 4.2 (violet triangles), the observable current densities are consistently lower for all performed experiments on SEIRA electrodes. This might be related to the use of an "older" C_5COOH-SAM for the SEIRA experiments and the utilization of a recently purchased batch for electrochemical measurements. The variances of electrochemical activities on the other SAM surfaces are similar to the previously observed in Figure 4.2 (see section 4.2.1) and deviate only within a small range. The CV measurements performed in the SEIRA-setup reveal reproducible results. The highest averaged current density is observed for *strep*-MBH on mixed C_5COOH/C_6OH-SAM as detected also in exclusive electrochemical studies on Au pen electrodes. Thereby, the lowest current densities were recorded for *strep*-MBH on C_5CH_3 coated Au surfaces. Also here, the data obtained for both positive charges C_6NH_2- and C_6NH_2/C_6OH-SAMs are comparable to the ones previously recorded on Au pen electrodes (violet triangles) coated with the respective SAMs. The variances in the amide I band intensities in the individual SEIRA experiments (Fig. 4.8B) correlate well with the data scattering observed for C_5COOH-terminated surfaces. MBH on C_6NH_2-treminated surface exhibits small variations compared to a C_5COOH-SAM. Interestingly the lowest amide I band intensities are observed on all negatively charged surfaces, C_5COOH- as well as C_5COOH/C_6OH-SAM, although *strep*-MBH on C_5COOH/C_6OH-SAM exhibits consistently high electrocatalytic activity. *Strep*-MBH adsorbed on both positively charged surfaces, C_6NH_2- and C_6NH_2/C_6OH-SAM, displays the highest amide I band intensities, with its maximum intensity observed on the mixed C_6NH_2/C_6OH-SAM. The amide I band intensity values on the hydrophobic surface are situated between those of positive and negative charged surfaces. Although *Re strep*-MBH on a CH_3-terminated SAM exhibits almost no activity for the DET, high current densities are monitored for the MET. To correlate the band intensities with the current density Figure 4.8C was plotted from the averaged data of each SAM surface. *Strep*-MBH on C_5COOH/C_6OH-SAM exhibits the highest ratio of current density over amide I band intensity.

Table 4.6: Comparison of average values for current densities (j), amide band intensities obtained in SEIRA experiments *

SAMs	average values for j / µA cm^{-2}	average values for amide I intensity (mOD)	ratio j / amide I band
C_5COOH	1.72	3.37	0.5
C_5COOH/C_6OH (1:9; v:v)	8.71	3.84	2.3
C_6NH_2	2.62	6.33	0.4
C_6NH_2/C_6OH (1:9; v:v)	4.49	11.41	0.4
C_5CH_3	0.50	4.51	0.1

* Results obtained from average values of the entire data from SEIRA experiments of *strep*-MBH immobilized onC_5COOH, C_5COOH/C_6OH, C_6NH_2, C_6NH_2/C_6OH and C_5CH_3 SAMs; evaluated from data shown in Figure 4.8.

As shown by the comparison between SEIRA intensity of the amide I band and the corresponding *strep*-MBH coverage determined by AFM, which was exemplified on the two highest oppositely charged SAM surfaces, see Fig. 4.8, the predominant spectral contribution of the amide I band intensities seems to be related to the *strep*-MBH coverage rather than the distance and orientation dependency of the surface enhancement. Hence, amide I band intensities of *strep*-MBH on different SAMs will be correlated to enzyme coverage, in a first crude estimation. Thus comparing their ratio of current densities obtained from DET to amide I band intensity presents a value for comparing the efficiency of the surface for *strep*-MBH catalysis. These results are displayed in Table 4.6. In this sense, the C_5COOH/C_6OH-SAM surface presents the most efficient surface for *strep*-MBH adsorption by far. In contrast, *strep*-MBH on mixed C_6NH_2/C_6OH-SAM shows the utmost amide I band intensity, thereby suggesting the highest enzyme coverage, and reveals second highest current densities by DET process.

Taking into account that the *strep*-MBH catalytic activity (k_{cat}) is defined by its current density relative to enzyme coverage, the corresponding value for *strep*-MBH on mixed C_6NH_2/C_6OH-SAM appears low compared to the mixed C_5COOH/C_6OH SAM and therefore represents a less efficient platform. Within the SEIRA experiments, *strep*-MBH on the pure C_5COOH– and NH_2–terminated SAMs exhibit also low current densities for DET, as well as low amide I band intensities compared to their corresponding mixed SAMs, C_5COOH/C_6OH- and C_6NH_2/C_6OH-SAMs. In contrast, *strep*-MBH on C_5CH_3–SAM with an averaged amide I band intensity of 4 mOD does hardly show any DET activity and thus presents the less efficient surface.

MET processes can be excluded for *strep*-MBH onto C_5COOH- and C_5COOH/C_6OH- SAMs, suggesting that every electrocatalytically active *strep*-MBH enzyme molecule, adsorbed at the surface, experiences a DET process and is therefore is electronically wired to the electrode surface with a distance small enough for electron tunneling from the distal Fe-S cluster. For both positive charged C_6NH_2- and C_6NH_2/C_6OH-SAM surfaces, however, MET processes are found by an increase of 50% and 30% increase relative to DET, respectively.

Strep-MBH on C_5CH_3-SAM shows mainly MET and hardly any DET processes. The amide I band intensities suggest an adequate coverage of *strep*-MBH at this surface. However, the major fraction of the enzyme molecules seems to be adsorbed in unfavored orientations for a direct transfer of electrons from the distal Fe-S cluster to the electrode surface.

4.2.5 Conclusions

In summary, an appropriate orientation is the most crucial aspect for an efficient and direct interfacial ET when an enzyme is immobilized on a biocompatible electrode surface. Thus, in the case that there is a distribution of orientations (involving significant fractions of electronically unwired enzyme molecules), even a high overall enzyme coverage can result in rather low catalytic efficiency and therefore a significant loss of power output.

In this context, the catalytic H_2 oxidation efficiency of immobilized *strep*-MBH depends strongly on its orientation at the electrochemical interface and not only on the enzyme coverage. In the present study, an interdisciplinary methodological approach using electrochemistry, SEIRA spectroscopy, AFM and ellipsometry reveals that *strep*-MBH on negatively charged interfaces adopts a preferential orientation with the distal Fe-S cluster located close to the electrochemical interface, hence promoting high DET processes. Previous studies on the electrostatic immobilization of standard hydrogenases used positively charged surfaces to direct the Fe-S cluster towards the electrode surface, thereby giving an efficient interfacial ET.[213] Oxygen-tolerant *strep*-MBH, with its significantly weaker dipole moment, gives fairly low catalytic efficiencies when adsorbed on positively charged surface, where H_2 oxidation proceeds through both DET and MET processes. Corresponding SEIRA spectra and AFM, however, show large amounts of adsorbed *strep*-MBH.

The adsorption of *strep*-MBH on a hydrophobic surface, which mimics the membrane core of a lipid bilayer with which the *Re* MBH natively interacts, shows mainly MET processes and hardly exhibits any surface-wired enzyme orientations. This type of unspecific binding might originate from the presence of the transmembrane helix and a possible interaction of the hydrophobic sequence of the C-terminal membrane anchor with the hydrophobic interface. The corresponding SEIRA spectra provide sufficient band intensities for monitoring the protein backbone and the active site. The amide I/amide II band intensity ratio indicates an ensemble of multiple orientations, exhibiting another type of binding of the *strep*-MBH on C_5CH_3-SAM than observed on positively charged SAMs.

Comparable to *strep*-MBH on C_5CH_3-SAM, the adsorption *strep*-MBH on C_5COOH-SAM interface reveals a comparable amide I/amide II band intensity ratio, although different *strep*-MBH orientations prevail for both C_5COOH- and C_5CH_3-SAM, as shown by the corresponding electrochemical data. While *strep*-MBH on C_5COOH-SAM demonstrates only DET process, the immobilization on C_5CH_3-SAM results in predominantly MET processes. In agreement with observations on C_5COOH-SAM, electrochemical studies of *strep*-MBH on C_5COOH/C_6OH-SAM reveal optimized homogenous orientational distribution, as shown by the prevailing of solely DET processes. However, the amide I/amide II band intensity ratio of *strep*-MBH adsorbed on a C_5COOH/C_6OH-SAM displays a value in between C_5COOH- and the positively charged SAMs. Comparison of orientation estimations by means of amide I/amide II band intensity ratios and electrochemical behavior demonstrates a discrepancies the case of *strep*-MBH immobilized on negatively and hydrophobic surface.

In order to understand the origins of the similar amide I/amide II band intensities, and hence differentiate various *strep*-MBH binding anchors on these different types of charged and hydrophobic surfaces, DFT calculations were used. This will be further discussed in section 4.3.7.

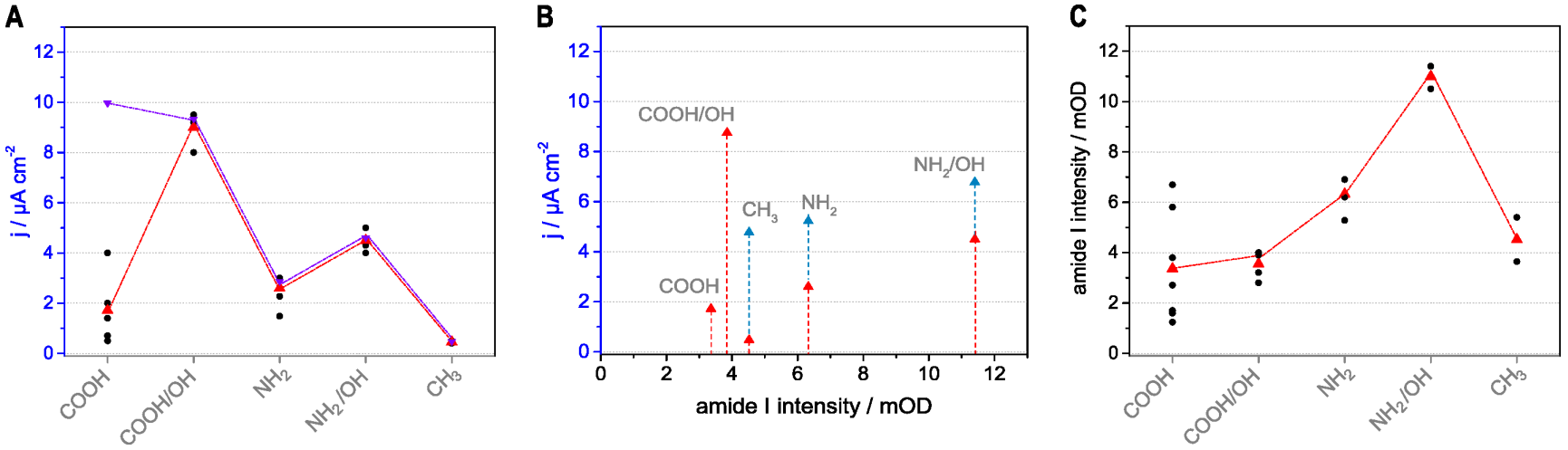

Figure 4.8: Summary of SEIRA investigations on *strep*-MBH: (A) electrochemical activities on various SAMs obtained by cyclic voltammetry derived from SEIRA experiments, for comparison pure electrochemical studies from section 4.2.1; (B) amide I band intensities derived from SEIRA spectra on different SAM surfaces. Each single experiment is displayed by black dots (●), while the averaged values of entire SEIRA experiment data (▲) are compared to the previously obtained electrochemical activities on gold pen electrodes (▲). (C) The averaged electrochemical activities are correlated to the mean amide I intensities for all SAM surfaces.

4.3 *Strep*-MBH Orientation

4.3.1 Molecular Dynamics Simulation

As mentioned previously, the *strep*-MBH is characterized by a weaker dipole moment compared to O_2-sensitive 'standard' hydrogenases and lacks a distinct negatively charged surface patch in the vicinity of the distal Fe-S cluster, which prevents a straightforward prediction of the adsorption behavior. Experimental studies showed opposing results for adsorbed *strep*-MBH on differently charged surfaces and non-charged SAM surfaces. Low catalytic activities with high enzyme loadings and high catalytic activities with small enzyme loadings were observed (see Table 4.6), which shows that for an efficient interfacial electron exchange between enzyme and electrode, the protein orientation plays the most important role when attempting to achieve high current densities. In this context, molecular dynamics (MD) simulations can be applied as an accurate, well-established and computationally cheap technique to investigate the initial adsorption processes of biomolecules on surfaces,[208, 228, 229] thereby allowing coarse predictions of protein orientations. MD provides insights into protein adsorption on an atomic level under the assumption of a rigid protein structure, which cannot be resolved experimentally.

Protein-surface interaction energy landscapes were constructed for the most interesting interfaces: C_5COOH-, C_5COOH/ C_6OH-, C_6NH_2-, and C_5CH_3-SAM coated Au surfaces. The energetically most favorable orientations were determined and used as the initial configuration for the MD simulations. It should be noted that the resulting initial calculations are established for a rigid MBH structure and can change dramatically when dynamic processes are taken into account, such as changes in the protein's dipole moment upon surface contact. [208] MD simulations were therefore performed using both the experimental conditions and the solved crystal structure of the purified hetero-dimeric *strep*-MBH in its reduced state as an input; these simulations suggested one or more preferential orientation. , The C-terminal transmembrane α-helix and the *strep*-tag were both not resolved crystal structure of the protein, presumably due to their high flexibility.[59] This transmembrane α-helix consists of of 3 sequences: a hydrophobic membrane anchor, a hydrophilic polar part and an additional *strep*-tag II peptide, which in total comprises of 54 amino acids. The membrane anchor represents the first part of the C-terminal helical extension of the small subunit HoxK and is essential for anchoring both the hydrogenase to the membrane and to the cytochrome b unit, which is the natural electron acceptor. In the present structural *strep*-MBH model, the hydrophobic membrane anchor, the hydrophilic polar transmembrane extension and the *strep*-tag II are modeled as an α-helix and as such included in the MD simulations. In this way, all possible binding sites of the protein are taken into account for when predicting surface adsorption on differently charged surfaces, thereby contributing to a better understanding of this rather complex adsorption process.

4.3.2 Interaction Energy Landscapes for *strep*-tagged MBH binding

According to the energy landscape theory the protein folding and molecular binding are both essential thermodynamically controlled processes. Electrostatic forces play an important role in protein-surface interactions. Due to electrostatic interactions with charged amino acids, the enzyme is attracted to the opposed surface charge. These long-range electrostatic interactions provide a charge to charge related stabilization that funnels the landscape for binding and also helps to steer the docking of statistically disordered proteins from the bulk to the surface.

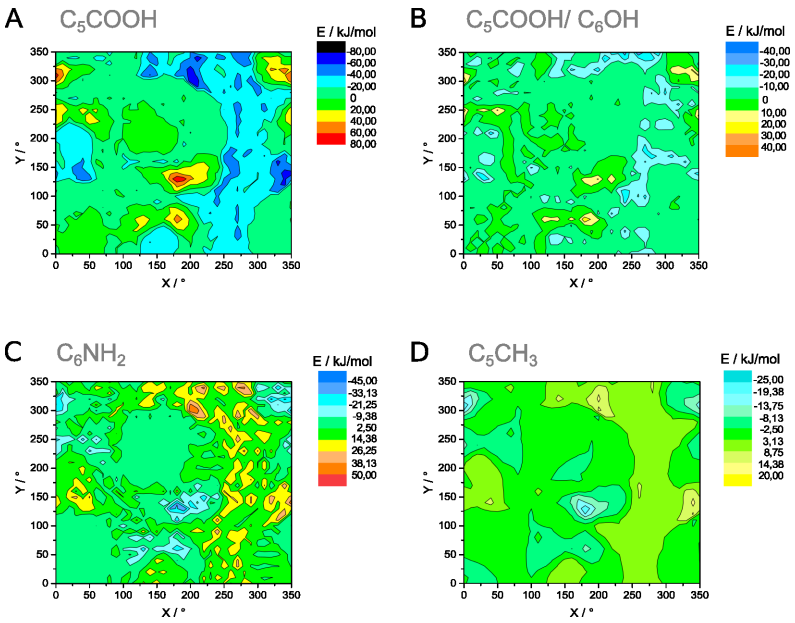

Figure 4.9: Interaction energy landscape between the *strep*-MBH and SAM-coated Au surface covered by the following (A) C_5COOH, (B) C_5COOH/C_6OH (C) C_6NH_2 and (D) C_5CH_3 monolayers. The in vacuo interaction energy between rotated *strep*-MBH (in a 5 Å distance to the SAM) in y- and x-axis to the surface was calculated with the NAMD energy plugin for VMD provided by Dr. Tillmann Utesch/ Mroginski group.

Figure 4.9 shows the interaction energy landscape mapping all rotational conformations of *strep*-MBH on various SAM-coated Au surfaces. Each conformation was constructed by rotating the enzyme in 10° steps around the x-axis (Φ angle) and the y-axis (Ψ angle), thereby remaining in a constant separation distance of 5 Å to the SAM. The blue areas represent the negative energetic values, while red peaks define energy barriers.

The C_5COOH –SAM covered surface clearly exhibits the widest spreading energy minima areas in light and dark blue. The excitation energy from the local dark blue minima to the light blue energetic level is around 20 kJ/mol, which could be already transcended at room temperature. The carboxyl-terminated SAM (pKa=6.3) is negatively charged, due to the deprotonation degree of 16% under the chosen incubation conditions at pH5.5 (see section 4.2.1; Table 4.1).

The C_5COOH/C_6OH–SAM coated Au surface exhibits a lower charge density at the surface compared to the C_5COOH-SAM. The corresponding energy landscape shows, in general, a flatter distribution with respect to the entire rotation conformations. However, the related flatter energy funnels are located at same positions in the energy landscape as observed for the interaction of *strep*-MBH with a C_5COOH-SAM coated Au surface. The mixed C_5COOH/C_6OH–SAM (ratio of 1:9, pKa=5.7) is slightly negatively charged, with a deprotonation degree of 37.5 % of the carboxylic functional groups (-COO-) under the chosen incubation conditions at pH5.5 (see section 4.2.1; Table 4.1).

The energy landscape of *strep*-MBH on a C_6NH_2-SAM coated surface shown in Figure 4.9C represents the inverse landscape of the opposed charged C_5COOH-SAM coated surface. In this regard, the C_6NH_2–SAM energy landscape exhibits a wide area with high energy barriers. Three distinctive funnels can be observed and are separated by energy barriers of 45 – 60 kJ/mol, which are required to transcend for a protein reorientation. Also, two of the three funnels reveal

a similar initial protein orientation. The amino-terminated SAM (pKa=6.8) is mainly uncharged under the chosen incubation conditions at pH7, which leads only to a protonation degree of only 8% (see section 4.2.1; Table 4.1).
Figure 4.9D shows the interaction energy landscape of *strep*-MBH with the hydrophobic C_5CH_3-SAM coated surface. Although some local minima are exhibited, the landscape appears particularly flat. One explanation for the observed flatness in the energy landscape could arise from a broad interaction area between the *strep*-MBH and the C_5CH_3-SAM surface. Besides, the trend of the energy landscape is comparable to the pattern found for adsorbed *strep*-MBH on a C_6NH_2-SAM coated surface.
The similarity of the generated energetic patterns for C_6NH_2- and C_5CH_3-SAMs might result from the very low charge of the NH_2 functional groups and the non-charged CH3 ones. However, the observed overall flat energy landscape suggests a rather unspecific protein conformation on the C_5CH_3-SAM, which is in sharp contrast to those of the C_6NH_2-species.
In summary, the most negative energetic minimum is found for the C_5COOH-SAM surface with -80 kJ/mol, even though this energy minima valley is distributed over a wider area. The C_5CH_3-SAM covered surface, on the other hand, exhibits the flattest energy minimum of only -20 kJ/mol. The most defined local minima are displayed for the NH_2-SAM coated surface due to the height of the surrounding energy barriers.

4.3.3 MBH orientation on C_6NH_2- Interface

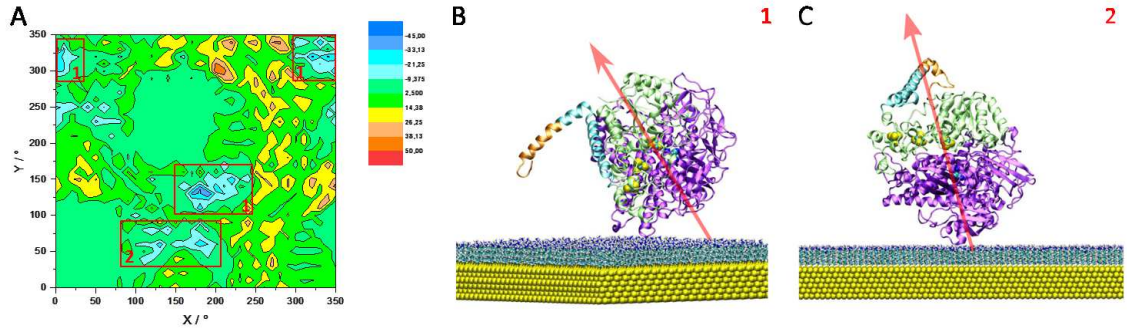

Figure 4.10: (A) Interaction energy landscape between the *strep*-MBH and the C_6NH_2-SAM coated Au surface generated by stepwise rotation of *strep*-MBH around the x-axis (Φ angle) and the y-axis (Ψ angle) under maintenance of the separation distance to the SAM of 5 Å. Additionally, funnels are surrounded by red boxes in the energy map, which corresponds to the most favorable configurations simulated for 50 ns resulting in two orientations (1 and 2) shown in (B) and (C), respectively. The protein backbones of the large and small subunits are colored in magenta and green, respectively. The Fe-S clusters (yellow/cyan) and the [NiFe] active site (dark blue/cyan) are indicated as spheres. The C-terminal transmembrane helix consisting of a hydrophobic and a hydrophilic sequence including *strep*-tag II are highlighted in cyan and orange, respectively. The SAM is depicted as blue-tipped sticks and the Au film as yellow spheres. The resulting overall dipole moments of the differently adsorbed enzyme molecules are displayed as red arrows (both exhibiting 800D). Simulated graphs are kindly provided by Dr. Tillmann Utesch / Mroginski group.

In Figure 4.10A, the three favored initial orientations are comprised in the interaction energy landscape by red boxes. Two of which are similar initial orientations, representing mirror images

of each other and are labeled with the orientation number one (1). Another initial orientation is displayed and marked by number two (2), which exhibits slightly higher energy minima than orientation one (1).

MD simulations of these initial geometries were carried out for 50 ns and lead to two distinct different *Re* MBH orientations adsorbed on the C_6NH_2-SAM as displayed in Figure 4.10B-C. Both orientations suggest an adsorption of the *strep*-MBH via the large subunit HoxG, while the entire C-terminal transmembrane α-helix is repelled by the surface. The MD simulations demonstrate the stability of the immobilized MBH dimer on the surface by the root-mean-square deviation (rmsd) values, which were found to be less than 3.0 Å compared to the initial state.[230] This is consistent with the SEIRA spectroscopic results, thereby ruling out any denaturation of the immobilized enzyme in both orientations. The interaction with the surface significantly reduces the directional fluctuation of the enzyme's dipole moment,[230] while its overall magnitude increases during the adsorption process.[230] This finding emphasizes the necessity to consider the entire enzyme-surface interaction in the MD simulation. However, further reorientations on larger time scales cannot be entirely excluded. However, a reasonable stability of these states is indicated by a quasi-static orientation of the enzyme's dipole moment with respect to the surface.

In orientation 1 (Fig. 4.10B), the *strep*-MBH binds through its small adjacent large and small subunits to the surface, is facing towards the monolayer with by facing its distal iron-sulfur cluster and theits slightly negative charged encompassing patch are facing towards the monolayer. This seems to represent an orientation still appropriate for a slow direct electron transfer between *strep*-MBH and the electrode, which experimentally was observed. Orientation 2 (Fig. 4.10C) binds again via its large subunit to the surface, contrarily to orientation 1, its distal iron-sulfur cluster pointing towards the solution and away from the electrode surface. Thus, the underlying electro-catalytic processes in an orientation like No. 2 would require the presence of redox mediators in the bulk solution to shuttle electrons between the distal Fe-S cluster and the electrode. Consequently, orientations 1 and 2 might be attributed to the fractions of *strep*-MBH molecules undergoing direct and mediated electron exchange with the electrode, respectively, as observed experimentally for *strep*-MBH adsorbed on C_6NH_2-coated Au-electrodes previously, *vide supra*. As depicted in Figure 4.11A, also SEIRA experiments indicated a mixture of different orientations, which might relate to those capable for direct and mediated electron transfer.

However, when the electrode potential was set to -340 mV [versus the standard hydrogen electrode (SHE)] for five minutes prior to the voltammetric measurements, a slight but reproducible increase (15%) of the catalytic current related to direct electron transfer was observed (Figure 4.11B). This pretreatment step was accompanied by a change of the amide I/amide II band intensity ratio in the SEIRA spectrum (Figure 4.11C), reflecting a potential-induced reorientation of the immobilized protein at -340 mV. This potential is still sufficiently positive to prevent reductive SAM desorption (see appendix Fig. A.7). Obviously, as a result of this preactivation step, some initially electro-inactive enzyme molecules have adopted an orientation that allows now direct electron transfer. Consistently, the catalytic current remained virtually unchanged upon

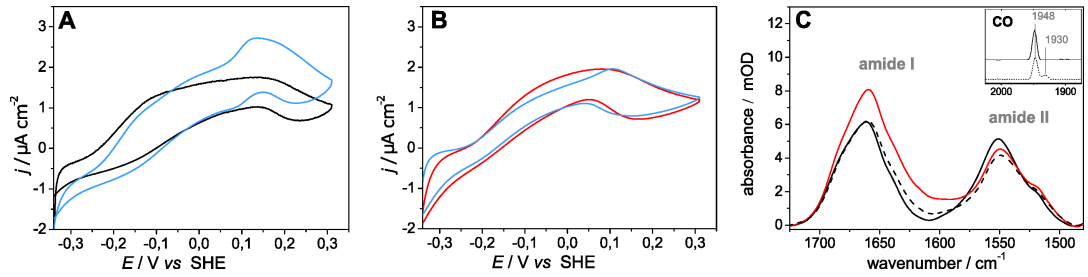

Figure 4.11: Voltammetric traces of *Re* MBH immobilized on C_6NH_2-coated Au electrodes in the presence of H_2-saturated buffer: (A) measured before (black) and after (blue) addition of methylene blue; (B) measured before (red) and after (blue) addition of methylene blue with a subsequent 5 min preactivation step at -340 mV in the presence of H_2. All voltammetric measurements were carried out at room temperature with a scan rate at 5 mV s^{-1}. (C) SEIRA spectra characteristic for the amide region recorded before (solid black), after (dashed black), and during (red) the preactivation at -340mV under H_2. The inset shows the corresponding stretching vibration of the CO ligand bound to the active site prior (solid line) and after (dashed line) preactivation in oxidized state. Black spectra were recorded at OCP (+260 mV). Potentials are given with respect to the standard hydrogen electrode (SHE). All CVs and SEIRA spectra were monitored at 25 °C.

subsequent addition of a redox mediator (Figure 4.11B, blue trace), pointing towards a more homogeneous orientation of throughout electro-active adsorbed enzyme molecules. Subsequent to the CV measurements, a buffer exchange was carried out, with the aim to remove all residual H_2 gas and to change the atmosphere to oxygen (air). In such way, the solution potential was again increased to oxidizing conditions [OCP: +260 mV]. Thereby, the reorientation of the protein was reversed as suggested by the corresponding SEIRA spectrum, restoring a similar spectrum to those recorded before preactivation (Figure 4.11C). During the entire processes, the integrity of the active site was almost fully preserved (up to 75%), which could be derived from the relative intensity change of the CO stretching mode of the Ni_r-B state (inset of Figure 4.11C).

Such as for the *strep*-MBH adsorption on NH_2-terminated SAM, also the corresponding interaction with C_6NH_2/C_6OH–coated surfaces revealed high amide band intensities, as well as major MET contributions compared to those of DET in ratios of 1.5:1 and 4:1, respectively. By means of AFM, it could be verified that the protein loading is correlated with the amide band intensities and the protein molecules are well distributed on the surface in form of single *strep*-MBH units. Thus, it can be assumed that all MBH molecules are directly adsorbed onto the surface. This is in line with the related MD simulations for *strep*-MBH immobilization on a C_6NH_2-SAM suggesting two orientations as displayed in Figure 4.11. Since different time constants can be considered for either a direct, one-step ET or a two- or even multi-step and diffusion limited MET process, an accurate quantification for each enzyme fraction in orientation 1 and 2 cannot be determined here. Therefore, the effect of the orientation 1 and 2 on the interaction pathway with the electrode could only be discussed qualitatively. In general mixed C_6NH_2/C_6OH–coated surfaces behave very similar to the pure C_6NH_2–coatings and were therefore not further investigated on a theoretical level.

4.3.4 MBH orientation on C_5COOH - Interface

Contrarily to the previously described scenario, when the enzyme is placed on the C_5COOH-SAM, the subsequent MD simulation predicts an adsorption of the *strep*-MBH via the positively charged anchor points at the *strep*-tag (Figure 4.12B). Further, the hydrophilic part of the transmembrane α-helix is also positively charged and might also interact with the surface. The distance between distal Fe-S cluster and Au surface is suggested quite large due to the repulsion between the surface charges and those of the dimer subunit with its weak negative patch located closely to the terminal Fe-S cluster. In this case, the distances of the active site Ni-atom and the distal Fe-S cluster to the Au surface are calculated to be 73.9 ± 1.0 Å and 65.1 ± 1.2 Å, respectively. In this illustrated model, the presence of any direct electron transfer reactions should be ruled out. Figure 4.12B displays the simulated conformation after 100 ns. During the 100 ns MD simulation, the heterodimer MBH subunits were rotating around the bound helix under retention of the tail-SAM interaction.

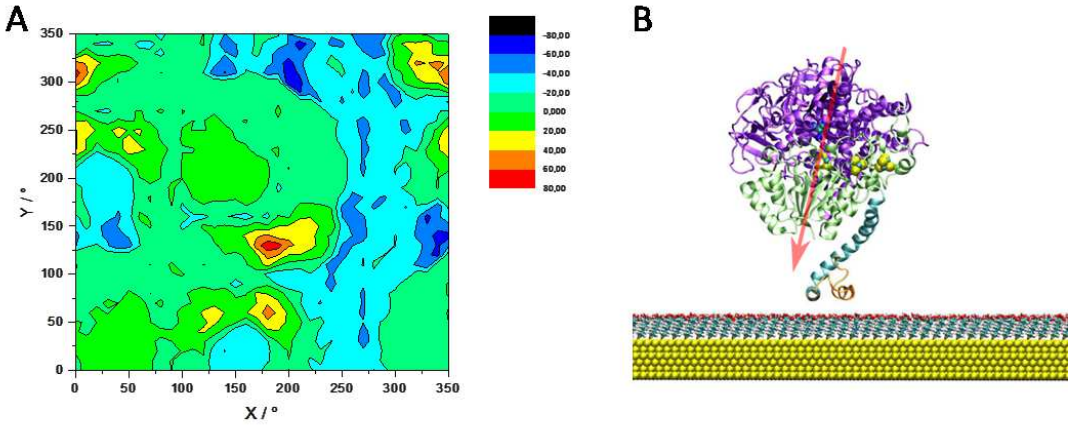

Figure 4.12: (A) Interaction energy landscape between the *strep*-MBH and the C_5COOH-coated Au surface. (B) Predicted structure of *strep*-MBH adsorbed on C_5COOH–coated Au surface after 100 ns MD simulation starting from the initially most favored configuration. The protein backbones of the large and small subunits are colored in magenta and green, respectively. The Fe-S clusters (yellow/cyan) and the [NiFe] active site (dark blue/cyan) are displayed as spheres. The C-terminal transmembrane helix consisting of hydrophobic and hydrophilic sequence including *strep*-tag II are highlighted in cyan and orange, respectively. The SAM is depicted in form of cyan colored sticks with red tips (indicating the oxygen) and the Au film as yellow spheres. The resulting overall dipole moment of the adsorbed enzyme molecule is displayed as a red arrow (814 D). Graphs were provided by Dr. Tillmann Utesch/ Mroginski group.

This suggests a high flexibility of the α-helix allowing translational and rotational motions of the protein backbone itself without direct interaction with the surface. This observed freedom with respect to smaller motions of the MBH subunits, which does not affect the binding interaction of the dimer. This can be particularly important for the involved ET processes if the enzyme can vary its relative distance to the Au surface. Preliminary studies of Dr. Tillmann Utesch/ Mroginski group based on coarse-grain simulations, which allow longer simulation times, indeed indicate such a dynamic behavior for the bound MBH. By such motions, the distance between distal Fe-S cluster and surface could in principle be reduced to levels which allow electron tun-

neling so that DET should be observable depending on the strength of repulsion between surface and enzyme. Results from the electrochemical studies, clearly reveal that exclusively DET takes place, *vide supra*. On the other hand, a binding via the *strep*-tag tail to the surface would involve only a few anchor points, which in turn raises questions regarding the amount of adsorbed enzyme and the binding strength, which however experimentally seems to be stable. In general, the energy landscape exposes more an energetic minimal area of possible orientations than a global or local minimum for a specific orientation. It should be noted, that the simulation was carried out under the assumption of a rigid protein structure, however, the *strep*-tag helix itself exhibits a high inherent flexibility and could thus change the energy landscape drastically. Preliminary results from coarse-grain simulations by Dr. Tillmann Utesch/ Mroginski group also revealed a certain flexibility of *strep*-MBH upon the adsorption process, when the transmembrane α-helix, carrying the in sum positively charged hydrophilic part including the partially with positively charged residues equipped *strep*-tag tail, docks to the C_5COOH-coated Au surface. The positively charged key residues which can be involved in the binding are such as for example within the *strep*-tag: arginine (K318), tryptophan (K321), serine (K322), histidine (K323), glutamine (K325), lysine (K328).

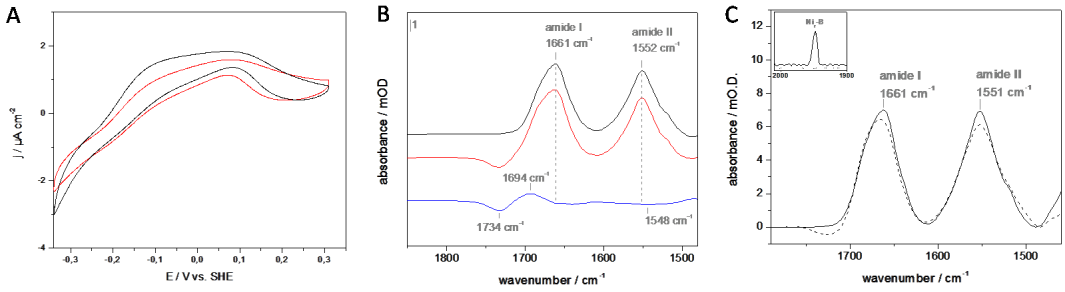

Figure 4.13: Voltammetric traces of *Re strep*-MBH immobilized on C_5COOH -coated Au electrodes in the presence of H_2-saturated buffer: (A) measured before (black) and after (red) a 5 min preactivation step at -340 mV. All voltammetric measurements were carried out at room temperature with a scan rate at 5 mV s^{-1}. (B) SEIRA spectra displaying the amide I and II band region, which were recorded before (black) and during (red) the preactivation step at -340mV under H_2 and the related blue-colored difference spectra [red - black]. (C) SEIRA spectra shown in the same amide band region, which were taken before (solid black) and after (dashed black) the preactivation step at -340mV under Ar. The inset shows the corresponding stretching vibration of the CO ligand at the active site prior (solid line) and after (dashed line) preactivation in oxidized state. These spectra were recorded at OCP (+260 mV). All CVs and SEIRA spectra were monitored at 25 °C.

As previously described for the *strep*-MBH binding process on NH_2-terminated surface (see section 4.3.3), also in the present case of *strep*-MBH immobilization on a C_5COOH-SAM, a potential step is applied prior the CV investigations, as shown in Fig. 4.13A. Contrary to the earlier findings on positively charged surfaces, the current density is not affected by the "preactivation" step (Fig. 4.13A). SEIRA spectroscopy reveals only slight changes in the spectral region of the amide bands before activation (black curve) and during activation (red curve) displayed in Figure 4.13B. The potential-dependent difference spectrum (blue trace), derived from the subtraction of the spectrum of adsorbed *strep*-MBH on C_5COOH-SAM after adsorption at OCP (+260 mV)

from the corresponding spectrum at -340mV, confirms a maintenance of the *strep*-MBH binding to the surface under preservation of the native protein structure via the integrity of the amide bands. After the potential was switched to -340 mV, a negative band at 1734 cm^{-1} and a positive band at 1694 cm^{-1} are observed, which can be assigned to the C=O stretching mode of the protonated species of the carboxylic end group. Already in the work of Natt Wisitruangsakul the pure C_5COOH-SAM was studied under potential influence, whereby bands occurred at 1690 cm^{-1} and 1734 cm^{-1}. Thus, it can be concluded that these bands detectable within the potential step, derive only from structural changes the C_5COOH-SAM functional group. As described by the electrostatic model of Smith and White, applied positive potentials at the Au electroe induce a charge compensation, involving the C_5COO^- functional groups and thus result in a change of the protonation degree.[159, 231] In this respect, a potential above the PZC will lead to a deprotonated C_5COOH-surface. Whereas, with decreasing potentials, in particular, below PZC, the charge compensation will form a protonated C_5COOH-SAM. This phenomenon can be spectroscopically detected on the basis of the negative band formation at 1734 cm^{-1}, which is observable at negative potentials, already below +130 mV (vs SHE).[232] This is in line with the determined PZC around -0.13 mV (vs SHE).[233, 234] The increasing band at 1694 cm^{-1} suggests the formation of a second protonated species, exhibiting this particular ν(C=O) stretching mode frequency. It might be related to the case of a missing hydrogen bridging to the C=O group, when the SAM is only partially deprotonating, as sketched in Figure 4.14A. Unfortunately, frequencies around and below 1470/1430 cm^{-1}, which are representative of the deprotonated carboxyl functional group ($-COO^-$), could not be accurately analyzed as the spectral contributions of the Si-O stretching modes of the prism interfered strongly in this range. This is due to a reduced transmission of the prism at lower frequencies, leading to an enhanced sensitivity with respect to temperature fluctuations. However, a weak negative band at 1548 cm^{-1}, characteristic for asymmetric stretching vibration of the deprotonated carboxylic anion species was observed by Wisitruangsakul in her work on potential-dependent changes in an Au bound C_5COOH-SAM monitored by SEIRA difference spectroscopy.[232]

Subsequently to the CV measurements, a buffer exchange was carried out with an air-saturated buffer solution in order to remove all residual H_2, thereby the potential reached oxidizing conditions [OCP: +260 mV]. As a consequence, the reorientation of the protein was reversed, as indicated by the corresponding SEIRA spectrum. However, a permanent change in the deprotonation degree of the SAM could be observed in comparison to the situation before the potential step, which can be monitored by the negative band at 1734 cm^{-1} (Figure 4.13C). Furthermore, the amide I and II bands lost slightly in intensity after this treatment, suggesting a certain potential induced protein loss as a consequence of the long-term application of an external potential. During the entire processes also the integrity of the active site seems to be strongly affected, shown by the absence of CO and CN stretching modes of the Ni_r-B state proposes a complete loss (inset of Figure 4.13C). Alternatively, and more likely, due to an electrochemically monitoring of the enzyme activity just before spectrum acquisition, the modified surface charge may have enlarged the distance from the enzyme to the surface, which would according to the distance dependence of the surface enhancement lead to an intensity decrease of amide I/amide II bands as well as active site bands.

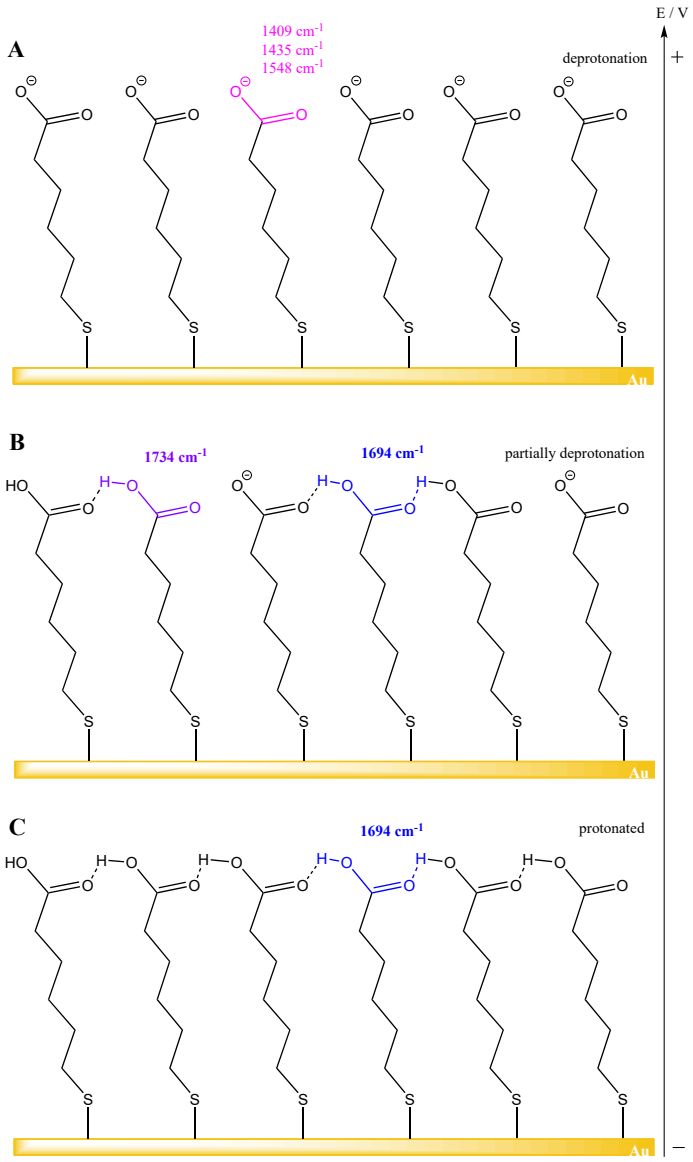

Figure 4.14: Sketch of the deprotonation process taking place at the C_5COOH-SAM: (A) fully deprotonated SAM with characteristic bands corresponding to asymmetric and symmetric stretching modes for carboxylate anion, 1548 cm^{-1} and 1409 cm^{-1}, respectively, as well as a combinatory vibration at 1435 cm^{-1} of symmetric $\nu(COO^-)$ and CH_2 scissors bending, (B) partially deprotonated SAM revealing two (C=O) stretchings of the protonated species at 1694 cm^{-1} and 1734 cm^{-1}, (C) fully protonated SAM exhibiting a (C=O) stretching vibration at 1694 cm^{-1}.

4.3.5 MBH orientation on C_5COOH/C_6OH - Interface

Experimentally, the C_5COOH/C_6OH-surface presented previously the highest catalytic current densities involving DET of the adsorbed *strep*-MBH on all studied surfaces. This negatively charged surface contains a less dense charge distribution at the SAM surface, i.e. only 1/9 are carboxylic functional groups, in comparison to the pure C_5COOH-SAM. When the enzyme is placed on the C_5COO^-/C_6OH-SAM as observed on the pure C_5COOH-SAM, several positive charged amino acids can act as anchor points on the slightly negative charged surface.

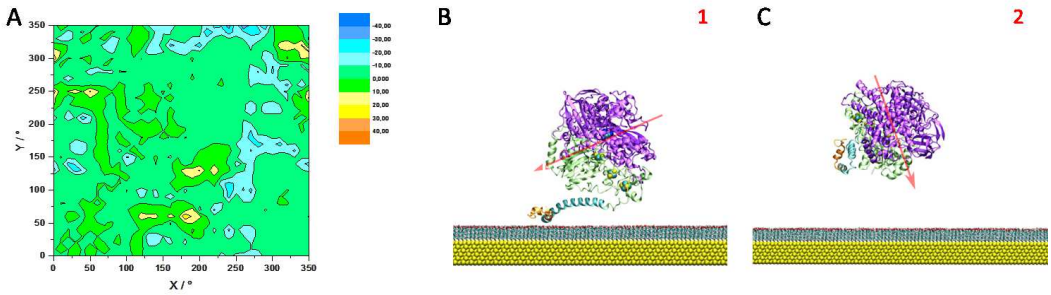

Figure 4.15: (A) Interaction energy landscape between *strep*-MBH and the C_5COOH/ C_6OH-SAM coated Au surface. (B,C) Predicted structures of *strep*-MBH adsorbed on a mixed C_5COOH/C_6OH-SAM originating from two oppositely oriented initial configurations derived from the energetic minima in (A) and simulated for 15 ns (B) and 100 ns (C), respectively. The protein backbones of the large and small subunits are colored in magenta and green, respectively. The Fe-S clusters (yellow/cyan) and the [NiFe] active site (dark blue/cyan) are indicated as spheres. The C-terminal transmembrane helix consisting of hydrophobic and hydrophilic sequence including *strep*-tag II are highlighted in cyan and orange, respectively. The SAM is depicted in form of cyan colored sticks with red tips (indicating the oxygen) and the Au film as yellow spheres. The resulting overall dipole moments of the adsorbed enzyme orientation 1 and 2 are displayed as red arrows (603 D and 695 D, respectively). Graphs were provided by Dr. Tillmann Utesch/ Mroginski group.

Similarly to the pure C_5COOH -SAM, MD simulation predicts an adsorption of the *strep*-MBH via the positively charged *strep*-tag extension on C_5COOH/C_6OH-SAM. Figure 4.15B and C exhibit snapshots after 15 ns and 100 ns simulation time, respectively, which originate from the two most diverging initial orientations predicted by the energetic minima in Figure 4.15A. Figure 4.15B displays an interaction of the transmembrane helical extension with the surface even after short simulation times. Contrarily, the simulation with an initial orientation, where the transmembrane helix points towards the solution, seems to be still not completed within the time frame of 100 ns (Figure 4.15C). However, ongoing axial rotation of the MBH molecule around its axis indicates the tendency to continuously turn in such way that the transmembrane helix is moved towards the electrode surface and might finally bind via the affinity-tag as shown in orientation 1.

The orientation 1 in Fig. 4.15B suggests a significantly reduced distance between the protein backbone and SAM-covered Au surface, compared to *strep*-MBH on pure C_5COOH–SAM. Hereby, the lower charge density at the surface might result in a weaker repulsion between surface and in particularthe slightly negative charged patch close to distal Fe-S cluster. Therefore, the distance for the interfacial ET pathway decreases and DET between *strep*-MBH and the electrode surface is expected to be increased. As a result, *strep*-MBH on C_5COOH/C_6OH-coated surface should yield higher current densities compared to *strep*-MBH on pure C_5COOH–SAM, which was then indeed observed in the CV studies (see section 4.2.1).

It should be noted that the configuration in Fig. 4.15B is suggested only after a 15 ns long MD simulation, therefore additional changes in distance, occurring after these 15 ns, still have to be considered.

Besides the effect of a faster interfacial ET, the reduction in distance also would also increase the

option of additional anchor sites by the hydroxyl functional groups for a polar surface interaction of the *strep*-MBH backbone structure. In addition, interactions with hydrophobic sides as well as van der Waals forces could potentially contribute to a stronger binding of the enzyme, as desorption experiments at higher ionic strengths did not show any significant desorption effect. The interacting binding anchors of the *strep*-MBH are the same as suggested by MD simulation for *strep*-MBH on C_5COOH-SAM. Additionally, as in the vicinity of the distal Fe-S cluster, present amino acids with negatively charged residues can interact with the polar, but neutrally charged functional groups of the hydroxyl functional groups of the mixed C_5COOH/C_6OH-SAM.

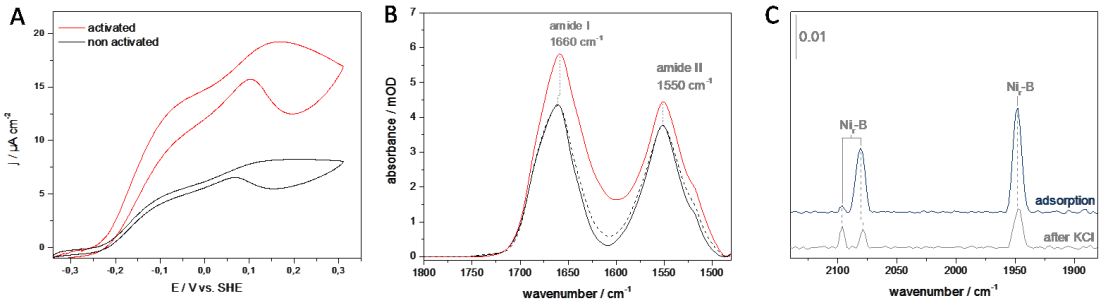

Figure 4.16: Voltammetric traces of *Re strep*-MBH immobilized on C_5COOH/C_6OH-SAM coated Au electrodes in the presence of H_2-saturated buffer: (A) measured before (black) and after (red) a 5 min preactivation step at -340 mV in the presence of H_2. All cyclic voltammetric measurements were carried out at room temperature with a scan rate at 5 mV s^{-1}. (B) SEIRA spectra displaying the characteristic region of amide I and II bands recorded at OCP (+260mV) before (solid black), during the preactivation at -340mV under H_2 (red) and after buffer exchange OCP (+260mV) and additions of KCl buffer (3M) at (dashed black). (C) Corresponding SEIRA spectra displaying CO and CN stretching vibrations from the active site prior (blue) and after additions of KCl buffer (grey) in the oxidized state. Both spectra were recorded at OCP (+260 mV). All CVs and SEIRA spectra were monitored at 25 °C.

When the electrode potential was set to -340 mV [versus SHE] for five minutes prior to the voltammetric measurements, a tremendous and reproducible increase (2.3 times higher) of catalytic current related to direct electron transfer was observed (Figure 4.16A). This current rise was accompanied by an increase of the amide I and amide II band intensities of 33% and 14%, respectively, see Fig. 4.16B. Besides the observable band increase, also the corresponding amide I/amide II ratio changes from 1.15 to 1.34 during the potential pretreatment. In line with the distance dependence of to the enhancement effect, these two observations, an intensity increase of the amide bands and a change of their relative ratio, in the SEIRA spectra suggest a rearrangement in which the entire enzyme with its flexible tail is brought closer to the surface. Further, the remarkable increase in current density indicates a convergence of the *strep*-MBH towards the electrode including a rearrangement resulting in a more favored orientation of the distal Fe-S cluster for faster DET. The close surface proximity of the *strep*-MBH is revealed in the subsequent desorption experiment after the CV studies (Figure 4.16B). Only by an addition of KCl buffer (3M), a recovery of the original amide band intensities and the corresponding ratio could be accomplished. The need of higher ionic strengths demonstrates the presence of a potential-induced electrostatic interaction between surface and MBH. The fact that the re-

orientation process, which resulted in a closer binding towards the surface, could be reversed, demonstrated by the retrieval of the initial values of amide band intensities prior to the potential step, implies the initiation of an additional electrostatic binding interaction to the *strep*-MBH. The latter is presumably related to an anchor patch, which is located in close proximity to the Fe-S cluster, thereby allowing lower energy barrier for electron tunneling, i.e. DET. A protonation of the carboxyl functionalities in this mixed C_5COOH/C_6OH-SAM within the potential steps down to -340 mV could not be unambiguously monitored by spectroscopy due to its limited amount in the 1:9 carboxylic to hydroxyl mixed SAM. However, it is very likely that this effect will take place, just as observed for the pure C_5COOH. In such way, the negative charge distribution will be reduced at the surface and thereby the repulsion with respect to the slightly negative charged patch close to the distal cluster will be further decreased and might therefore provide further binding anchors for the *strep*-MBH.

By the increase of the ionic strength of the buffer solution, the reorientation of the protein could be completely reversed, as indicated by the corresponding SEIRA spectrum, which is very similar to that, was measured prior to the preactivation step (Figure 4.16B). Figure 4.16C displays the corresponding spectral region characteristic for the active site, before preactivation and after KCl additions, thereby showing that the integrity of the active site is preserved up to 30%. Interestingly, as derivable from the inherent and changed relative ratio of the CO and in particular the CN stretching modes, it is likely, that a different conformation of *strep*-MBH at the surface is formed.

4.3.6 MBH orientation on C_5CH_3- Interface

The orientation of *strep*-MBH on a C_5CH_3-surface is of particular interest; as such a surface mimics the hydrophobic membrane chore of the lipid bilayer, in which native *strep*-MBH is attached via the membrane anchor of the transmembrane helix. The previous SEIRA studies indicated similarities with the adsorption processes carried out on C_5COOH- and C_5COOH/C_6OH-SAM covered surfaces based on the observable amide I/amide II ratios (see section 4.2.2.1). Although the energy landscape shown in Figure 4.17A, displays an energetic pattern similar to the one for *strep*-MBH on a C_6NH_2-SAM, however with a flatter energy distribution, the subsequent MD simulation reveals a hydrophobic interaction between the membrane anchor of the transmembrane helix within the uncharged surface (Figure 4.17B).

In such way, MD simulations suggest an interaction of the entire flexible helix tail consisting of the large hydrophobic membrane anchor and a shorter *strep*-tag II tail with the surface, exhibiting a similar scenario as observed for *strep*-MBH immobilized on C_5COOH- or on C_5COOH/C_6OH - SAMs. In the present case, the anchor points derive from the hydrophobic helical membrane anchor, which interacts with the hydrophobic surface. Although the specific snapshot displayed in Figure 4.17B exhibits a distal Fe-S cluster close to the surface, this is only one of the possible orientations, as the energy minima clearly imply a broad orientation distribution, in all of which the helical membrane tail retains his function as a binding anchor to the C_5CH_3-hydrophobic surface.

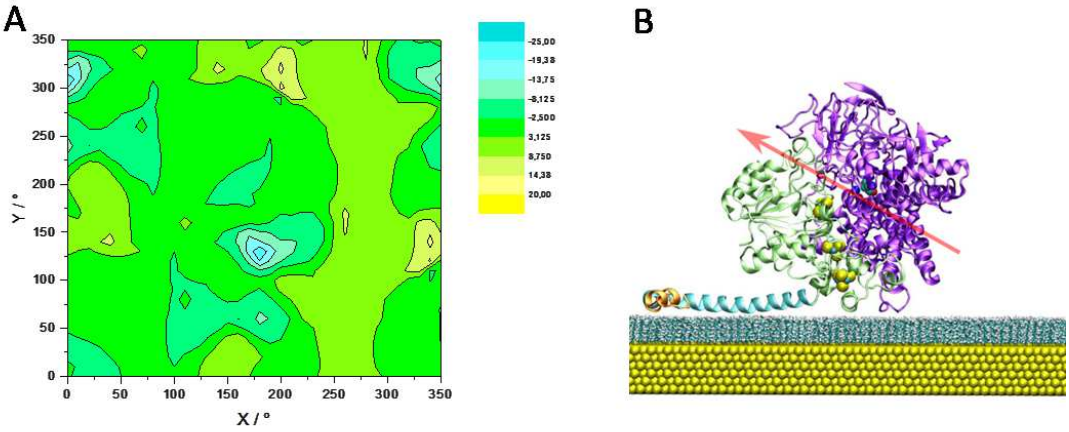

Figure 4.17: (A) Interaction energy landscape between the MBH and the C_5CH_3-coated Au surface. (B) Predicted structure of *Re strep*-MBH, which corresponds to the most favorable configuration in (A) after 50 ns simulation time. The protein backbones of the large and small subunits are colored in magenta and green, respectively. The Fe-S clusters (yellow/cyan) and the [NiFe] active site (dark blue/cyan) are indicated as spheres. The C-terminal transmembrane helix consisting of hydrophobic and hydrophilic sequence including *strep*-tag II are highlighted in cyan and orange, respectively. The SAM is depicted as white-tipped sticks and the Au film as yellow spheres. The resulting overall dipole moment of the adsorbed enzyme molecule is displayed as a red arrow (263 D). Graphs are provided by Dr. Tillmann Utesch/ Mroginski group.

Experimental data indicated mainly MET processes with almost no contributions of DET (ratio of DET:MET ~ 1:6) (see section 4.2.1) and also the SEIRA spectra display amide band intensities revealing a binding affinity of the enzyme for this type of surface (see section 4.2.2), leading to reasonable protein adsorption. Only lower energy barriers, which might be easily transcended at working temperature (277-298 K), are presumably the reason for such a broad distribution of different orientations. Further, it can be taken under consideration that an incorporation of the hydrophobic tail into the hydrophobic spacer of the SAM is possible. This scenario was also under consideration in the in the studies of *Aa* MBH immobilization on Au-SAMs in the work of Ciaccafava et al. [64], where also an adsorption of *Aa* MBH on hydrophobic SAM surfaces was observed.

4.3.7 DFT Calculations

The large, isolated C-terminal α-helix, which consists of 54 C-terminal amino acids (˜6 kDa), defines about 7% of the whole MBH (98 kDa), and therefore represents a considerable fraction of this enzyme. Preliminary Density Functional Theory (DFT) calculations of polarization dependent IR spectra were carried out exemplarily on a α-helix, which consists of a sequence of 10 amino acids (alanines), performed by Dr. Jacek Kozuch/ Hildebrandt group, which are in line with the work on α-helix orientation by Marsh.[235]Figure 4.18B displays the calculated spectrum which is polarized parallel to the long axis of the α-helix (xy-plane) and the other one with a polarization direction perpendicular to the α-helix (z-axis). These spectra correspond to the related s- and p-polarized ATR spectra of an orientated α-helix sample and can be compared to the large isolated transmembrane α-helix of *strep*-MBH. The direction of the dipole moment of the α-helix is practically identical with the helix axis of the C-terminal transmembrane tail. The calculated spectrum of α-helix is generated by averaging the spectra which were calculated for an alignment of the α-helix in the xy-plane. Spectra calculated in such way for xy-plane and z-axis polarizations are suitable for a comparison with the SEIRA spectra. The α-helical structure is similar to the present inherent C-terminal α-helix structure which is located as the transmembrane tail close to the distal Fe-S cluster of *strep*-MBH, and consists of a 54 amino acids sequence, including the affinity *strep*-tag as an extension. The respective calculated spectra are displayed in Figure 4.18 and reveal high amide I/amide II band intensity ratios around 10-20 to 1 for a dipole axis of α-helix which is perpendicularly oriented onto the surface. In the case of an orientation of the α-helix dipole axis parallel to the surface the corresponding amide I/amide II band intensity ratio becomes smaller than 1, around 0.9-0.8. Hence, an interaction of the isolated transmembrane α-helix with the Au-SAM surface or just a very close proximity could already affect the amide I and amide II ratio in the SEIRA spectrum due to distance dependence of the surface enhancement effect of the nanostructured Au electrode.

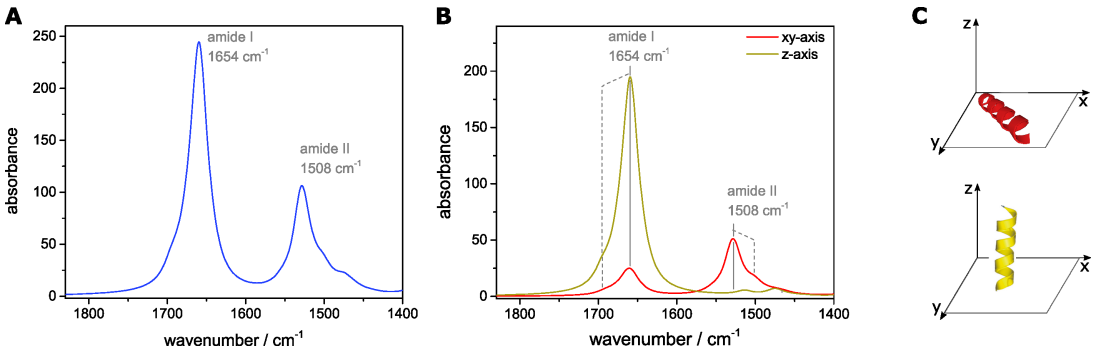

Figure 4.18: DFT calculated (A) IR spectrum of an isolated 10 alanine α-helix, (B) polarization dependent IR spectra of the isolated α-helix in its xy-plane (red) and along the z-axis (yellow), respectively. (C) The corresponding illustration of this α-helix when it aligned in xy- (red) or z-plane (yellow), respectively.

As the *strep*-MBH harbors a mixture of various secondary structure elements, an unambiguous and absolute determination of the *strep*-MBH orientation cannot be accomplished. However, a comparison of amide I/amide II band ratios between *strep*-MBH adsorptions on various SAM surfaces indicates similarities regarding the enzyme orientation. The contribution of amide I and amide II intensities in the SEIRA spectra of the adsorbed *strep*-MBH are based on the

combination of the predominantly unordered secondary structure elements of enzyme backbone as well as the loose and quiet large transmembrane α-helix. Hence, by means of the distance- and angular-dependencies of the surface enhancement effect, the helix can contribute to a greater extent to the SEIRA spectrum and thus the difference in amide I/amide II ratios on various SAMs can indicate the involvement of helix-surface interactions.

Figure 4.19 displays the spectral amide I and II band region of the MBH in solution (A) with an isotropic orientational distribution as well as those of adsorbed enzymes on an oxidized Si-prism in the absence of the gold film monitored in the ATR mode with unpolarized IR light (B). In this case, the applicability of any surface selection rule can be excluded, and therefore also the presence of any orientational selectivity. Both displayed spectra reveal an amide band intensity ratio of 1.38 and 1.36, respectively. The adsorbed *strep*-MBH on C_6NH_2- and C_6NH_2/C_6OH-terminated surfaces (Fig. 4.19C,D) exhibit similar ratios of 1.3, close to the ratio observed for the MBH in solution. Unlike the positively charged surfaces, the specific amide band intensity ratios for an enzyme binding on C_5COOH- and C_5CH_3– terminated SAMs exhibit values of 1.0 and 0.98, respectively. The larger spectral contribution of amide II for the latter two surfaces compared to the positively charged SAMs could indicate a parallel helix in close to the enhancing Au surface, as suggested in Fig. 4.18B. This correlates very well with the proposed orientations by MD simulations in which the *strep*-MBH binds directly via the partially positive charged hydrophilic sequence of the transmembrane helix to the on C_5COOH- and C_5CH_3-surfaces. In contrast, the higher values of amide I/amide II on positively charged SAMs would therefore exclude the helix interaction accordingly to the DFT calculations (Fig. 4.18). The similarity of the amide I/amide II ratios of *strep*-MBH on positively charged SAMs and *strep*-MBH in solution may confirm the far distance from helix to surface, as well as representing the heterogeneous orientational distribution originating from the predominantly unordered secondary structure of enzyme backbone rather than the transmembrane helix. The conducted MD simulations suggest already a direct interaction between protein backbone and surface, excluding any binding via the helical tail, always in a significant distance from the Au-SAM surface.

The amide I/amide II band intensity ratio of 1.14 observed for the *strep*-MBH bound to a C_5COOH/C_6OH terminated surface lies in between the two previously discussed scenarios. As discussed in section 4.2.2.1, comparing to *strep*-MBH on pure C_5COOH- SAM, the *strep*-MBH on C_5COOH/C_6OH-SAM binds also via the transmembrane helix to the surface, although the enzyme backbone is suggested in closer surface proximity due to the lower enzyme-surface repulsion by the lower negative charge density of the diluted SAM surface. Therefore, a higher spectral contribution of enzyme backbone can be assumed, which agrees well with the MD simulation as well as with the suggested spectral contribution for a parallel and in close surface vicinity located transmembrane helix by DFT calculations.

4.3.8 Conclusions

MD simulations suggest either an electrostatic binding directly to the MBH backbone or a binding via the transmembrane α-helix and its *strep*-tag extension. None of the conducted MD simulations indicate a denaturation of the protein structure, which is reflected by a rmsd value comparable to the non-adsorbed protein.[230] The large variations in the protein-cofactor-to-surface distances have a significant effect on the intensity of the spectroscopic signals for both the protein backbone and the active site, as well as on the observable catalytic currents.

This suggests that the *strep*-MBH, with its partially negatively charged amino acids in close

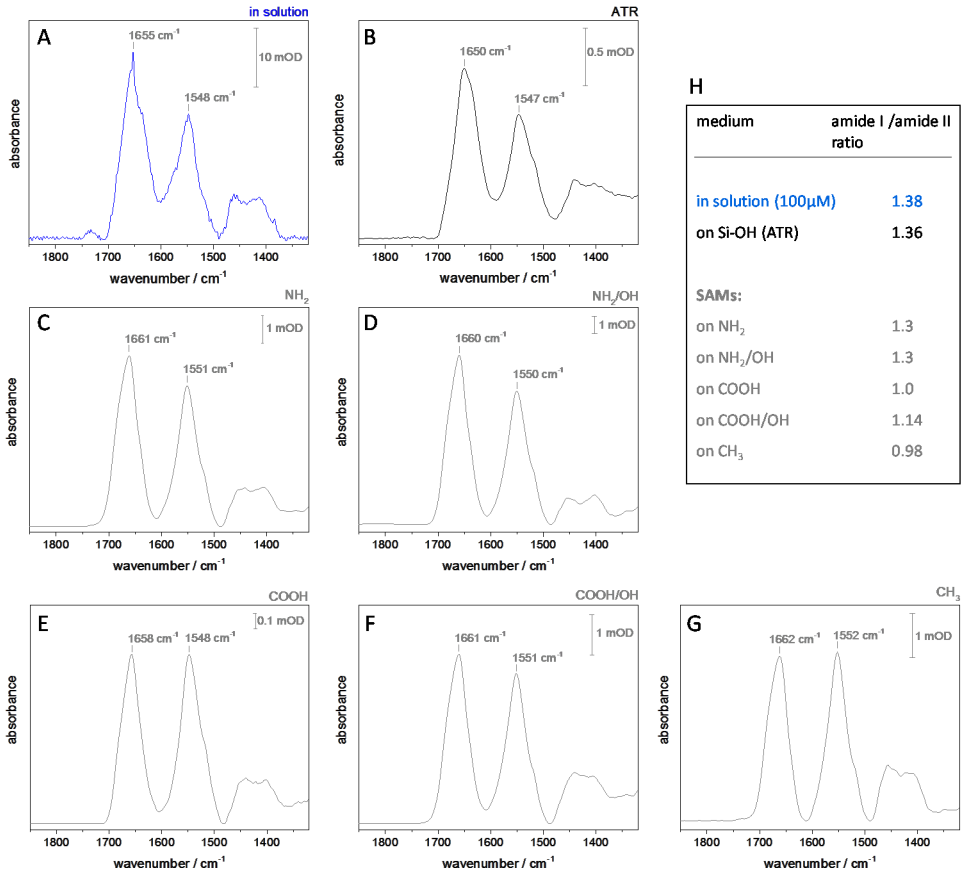

Figure 4.19: Spectra displaying the IR region characteristic for amide I and II modes of *strep*-MBH recorded via (A) a thin layer transmission cell in solution, (B) the ATR mode after adsorption on an oxidised Si-prism and SEIRA spectroscopy after immobilisation on a nanostructured Au surface coated with (C) C_6NH_2,(D) C_6NH_2/C_6OH,(E) C_5COOH,(F) C_5COOH/C_6OH, (G) C_5CH_3. All amide I/ amide II ratios derived from this spectra are depicted in a small Table (H).

vicinity of distal Fe-S cluster, would be better immobilized on a positively charged surface in terms of both the electrochemical and spectroscopic response. It is also anticipated that a binding to negatively charged surfaces can be accomplished via the partial positively charged hydrophilic sequence and *strep*-tag extension of the transmembrane helix, thereby also providing good electrocatalytic function.

A binding via the latter exhibits the highest observable enzymatic efficiencies, explained by the restricted but sufficient flexibility for rotation and slight translation movements as observed for *strep*-MBH on the C_5COOH/C_6OH-terminated SAMs. This SAM revealed the highest current densities during electrochemical probing and the highest amount (100%) of DET by a stable and selective binding, therefore the distal Fe-S cluster is situated close to the electrode surface during potential application.

A further binding mechanism of the *strep*-MBH on C_5COOH-terminated SAMvia the flexible transmembrane tail is suggested by the MD simulations and supported by DFT calculations regarding spectral proofs for such an orientation. The widely spread energetic valleys represent a broad range of favorable *strep*-MBH conformations on the surface via a transmembrane helical

binding. This was confirmed by recent coarse grain simulations by Dr. Tillmann Utesch (AK Mroginski). The 1:9 mixture of C_5COOH/C_6OH-terminated SAM and the concomitant decrease of negative charges, however, lead to moderate enzyme coverage and resulted in reproducible highest current densities.

Strep-MBH adsorbed on C_6NH_2– and on C_6NH_2/C_6OH–terminated SAMs reveals in both cases a narrow distribution of binding modes to the surface, which is represented by the well-defined energy landscape for the NH_2–terminated SAM with distinct energetic minima. Experimentally it can be observed that these modes can be homogenized by slight potential-induced rearrangements on the surface leading to increased and solely DET. These surfaces display the highest protein coverages of all studied SAM-surfaces. The potential-induced rearrangements and hence resulting DET current densities remain small compared to overall efficiencies for lower loadings of *strep*-MBH on C_5COOH/C_6OH-SAM

Strep-MBH adsorbed on C_5CH_3-terminated SAM displays a binding via the hydrophobic sequence of the transmembrane tail, as indicated by MD simulations as well as the correlation of the low amide I/amide II ratio exhibited in the SEIRA spectra with DFT calculations. Due to the extremely flat energy landscape for enzyme orientations on the surface, axial rotations under maintenance of the surface interaction with the hydrophobic tail would allow a broad distribution of *strep*-MBH orientations and this is supported by the observably predominant MET contribution. DFT calculations of polarization dependent IR spectra on an isolated α-helix indicate an arrangement of such a helix parallel to the Au surface. In summary, the correlation of MD simulations with the observed experimental data indicates a binding anchor via the isolated transmembrane tail, and this was further confirmed by DFT calculations.

For such large and complex proteins such as the *strep*-MBH which even harbors a flexible, C-terminal tail and an additional affinity-tag, it is not feasible to relate to a simple linear correlation between enzyme loading on the electrode surface and recorded catalytic efficiency; in the present case the experimental data even reveals the opposite trend. What is much more important in this context is an understanding of the underlying orientation mechanisms as the key for an efficient energy output in the field of enzyme-based fuel cells. In its native environment the *Re* MBH is somehow constricted by the incorporation of its cytochrome b unit into the cell membrane; according to MD simulations the purified hydrogenase heterodimer however exhibits increased flexibility regarding rotational and slight translational motions on the SAM-coated electrode.

The results obtained in this work demonstrate that the diluted negative charges as displayed by the C_5COOH/ C_6OH-terminated SAM surface are beneficial for high performances with respect to H_2 oxidation and future biotechnological applications, such as in bio-fuel cells. In this regard, metal oxides exhibiting inherently negatively charged surfaces might provide an alternative platform as biocompatible, low-cost electrodes for *strep*-MBH immobilization. High current densities at low over-potential can be accomplished when the enzyme molecules are directly connected to the electrode, which is feasible with various metal oxide materials and should be studied as an alternative platform. The related investigations will be discussed in chapter 5 and 6.

4.4 Mechanistic Impact into MBH

The majority of spectro-electrochemical studies have used hydrogenase in solution either with [12, 63, 209] or without [236, 237] redox mediators. However, solutions are likely to suffer from substrate depletion and limited electron delivery despite mediators.[33] SEIRA spectro-electrochemical studies combine the options of an electrochemical control of a protein film with the structural insight provided by surface-enhanced IR spectroscopy.

Recently, another spectro-electrochemical approach has been developed in the group of Vincent applying a typical FTIR–ATR set-up for *in situ* spectro-electrochemical studies on enzymes adsorbed on carbon particles.[236] SEIRA spectroscopy has been widely used to study redox enzymes immobilized on gold electrodes. [209, 106, 67, 104, 238, 239, 107] Notably, the activation of the membrane-bound NiFe hydrogenase from *Desulfovibrio vulgaris* Miyazaki F (*Dv*MF) in the presence and absence of H_2 was monitored with this technique, thereby proving the redox transition Ni_r-B/Ni_a-S by probing the corresponding IR bands.[62]

Since *Re strep*-MBH on NH_2-terminated SAMs resulted in reproducible high enzyme loadings at the surface, concomitant with high active site absorption intensities (see section 4.2.2), this adsorption condition is used for the following studies, exemplary for mechanistic insights into *Re* MBH.

4.4.1 Adsorbed MBH under Turnover Conditions

Table 4.7 displays the characteristic wavenumbers of the stretching vibrations assigned to the active site diatomic CO and CN- ligands in different redox states, which are discussed in the following section in more detail. The proposed catalytic cycle is described in more detail in chapter 2.1.1.5.

Table 4.7: Characteristic wavenumbers of the corresponding CO and CN stretching vibrations assigned to the various redox states of purified MBH samples as described in literature

redox states	ν_{CO} / cm^{-1}	ν_{CN_1} / cm^{-1}	ν_{CN_2} / cm^{-1}	reference
Ni_u-S	1943	2082	2104	[5]
Ni_r-B	1948	2081	2098	[5, 240]
Ni_r-S	1936	2075	2092	[204, 240]
$Ni_{r/a}$-S	1936	2075	2093	[5]
Ni_a-C	1957	2074	2094	[5]
Ni_a-SR	1948	2068	2087	[5]
Ni_a-SR'	1926	2049	2075	[5]
Ni_a-SR"	1919	2047	2071	[5]
Ni_{ia}-S	1930	2060	2076	[224, 5]
	1930	ND[a]	ND[a]	[224]
	1954	ND[a]	ND[a]	[240]

[a] ND means not determined.

Figure 4.20 displays characteristic region for the active site of *strep*-MBH adsorbed on the C_6NH_2-SAM in the SEIRA spectrum with the corresponding ν_{CO} and ν_{CN} stretching vibrations. Subsequently, after the adsorption process under Ar atmosphere, the catalytic center of *strep*-MBH

resides preferentially in its oxidized, catalytically inactive state, known as Ni_r-B state, which is formed at high potentials (see chapter 2.1.1.4). The observed open circuit potential is about +130 mV (under Ar). The measured electrode potential at zero net current is represented by the open circuit potential (OCP). Adsorbed *strep*-MBH on C_6NH_2-coated surfaces reveal an OCP under air of about +310 mV, which decreases under anaerobic conditions, i.e. under Ar, to a value of +130 mV and under H_2 atmosphere to an untypical high value of -40 mV. Assuming only DET between an enzyme and an electrode, an OCP under turnover conditions, i.e. with H_2 supply, would be expected to be close to the H_2/H^+ redox couple (-325 mV). Also, the enzyme loading is expected to affect the OCP to a minor extent.[241] Since AFM studies on *strep*-MBH on C_6NH_2-surfaces revealed adequate enzyme coverage of 0.4 pmol/cm^{-2} (see section 4.2.3), this effect seems to be not the reason for the unusual high OCP value, but however, it seems to be rather related to maximal feasible direct electron transfer at the enzyme-electrode interface. This is already suggested by the observation of an orientational distribution of adsorbed enzymes and the detected low DET current densities compared to the good enzyme coverage values. In contrast, *strep*-MBH adsorbed on negatively charged surfaces, i.e. C_5COOH and C_5COOH/C_6OH, exhibits higher DET current densities und related OCPs under H_2 of about -240 mV. This is in consistent with the observed onset potential of -240 mV in the CVs (see section 4.4.2).

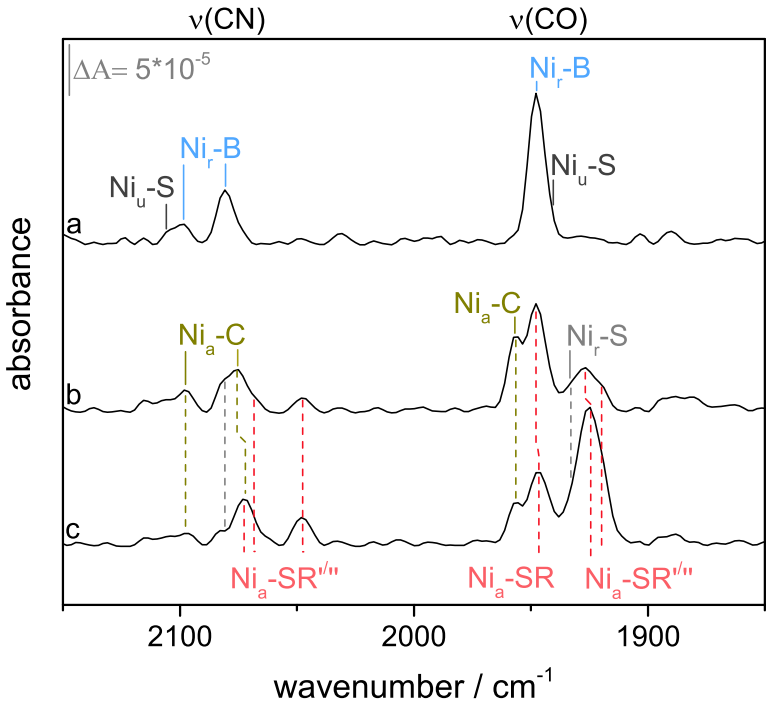

Figure 4.20: SEIRA spectra of *strep*-MBH on C_6NH_2 showing the characteristic region for ν(CO) and ν(CN) of the active site (a) after adsorption under Ar (open circuit potential OCP + 130 mV), (b) under H_2 (OCP ˜ -40mV) and (c) at the lowest applied potential of -340 mV under H_2. Potentials are quoted relative to the standard hydrogen electrode (SHE).

Generally, the value of the OCP characterizes the substrate/product redox reaction occurring at the enzyme-electrode interface and given by the Nernst equation. However, it does not give

any insights into intrinsic properties of the enzyme itself. Information about the latter can be derived by the value and shape of the voltage dependent current courses.

Under H_2 atmosphere, the *strep*-MBH is rapidly activated and the recorded ν_{CO} and ν_{CN} vibrations exhibit values related to the reduced states of the active site already after the first spectrum. Upon constant substrate supply, spectra of the catalytic center in the respective redox equilibrium can be recorded within a few minutes. The corresponding ν_{CO} and ν_{CN} bands observed spectra (b) and (c) in Fig. 4.20, reveal a set of redox states of the adsorbed *strep*-MBH consistent with the respective states observed for *strep*-MBH in solution and his-tag -bound MBH on a comparable Au surface under H_2.[5, 67]

As H_2 substrate is supplied, the open circuit potential shifts to a potential at -40 mV within few minutes. Simultaneously, the amount of the oxidized Ni_r-B state decreases and the reduced intermediate state Ni_a-C is predominantly formed. The most reduced species reported for the *Re* MBH, the so-called Ni_a-SR states, can be detected in minor fractions in spectrum (b) (Fig. 4.20). At the most negative applicable potential (-340 mV), at which no reductive SAM desorption occurs, the amount of Ni_a-SR states enriches, with Ni_a-SR' and Ni_a-SR" as the dominating species. Three sub-states of the most reduced redox Ni(II) species are reported, which can be identified by their characteristic ν_{CO} absorptions (see Table 4.7). Generally, these Ni_a-SR states have been suggested to be formed due to different protonation states in the close environment of the active site.[34]

Notably, none of the so-called "irreversible inactivated" Ni_{ia}-S_x states has been monitored by its characteristic ν_{CO} or/and ν_{CN} bands within this series of experiments.

4.4.2 Potential Dependent Spectral Changes

Figure 4.21 shows SEIRA spectra in the corresponding region characteristic for the CO stretching recorded at selected electrode potentials, either under constant Ar or H_2 flow (see Figure 4.21 A or B), as displayed exemplarily on two samples of adsorbed *strep*-MBH on C_6NH_2-coatings. The adsorbed enzyme was initially activated at low potentials under the corresponding gas atmosphere (Ar or H_2) before the potential was raised stepwise.

Displayed are four relevant potentials, which are also marked in the corresponding CV courses. Under H_2 atmosphere, the current increases in magnitude, as the electrochemical driving force is raised (Figure 4.21B). At the most positive applied potential (+310 mV), the current under H_2 decays over time ascribed to the slow anaerobic, oxidative inactivation of [NiFe] hydrogenases and related to the formation of Ni_r-B. Generally, *strep*-MBH is reported to exhibit a low ability for proton reduction.

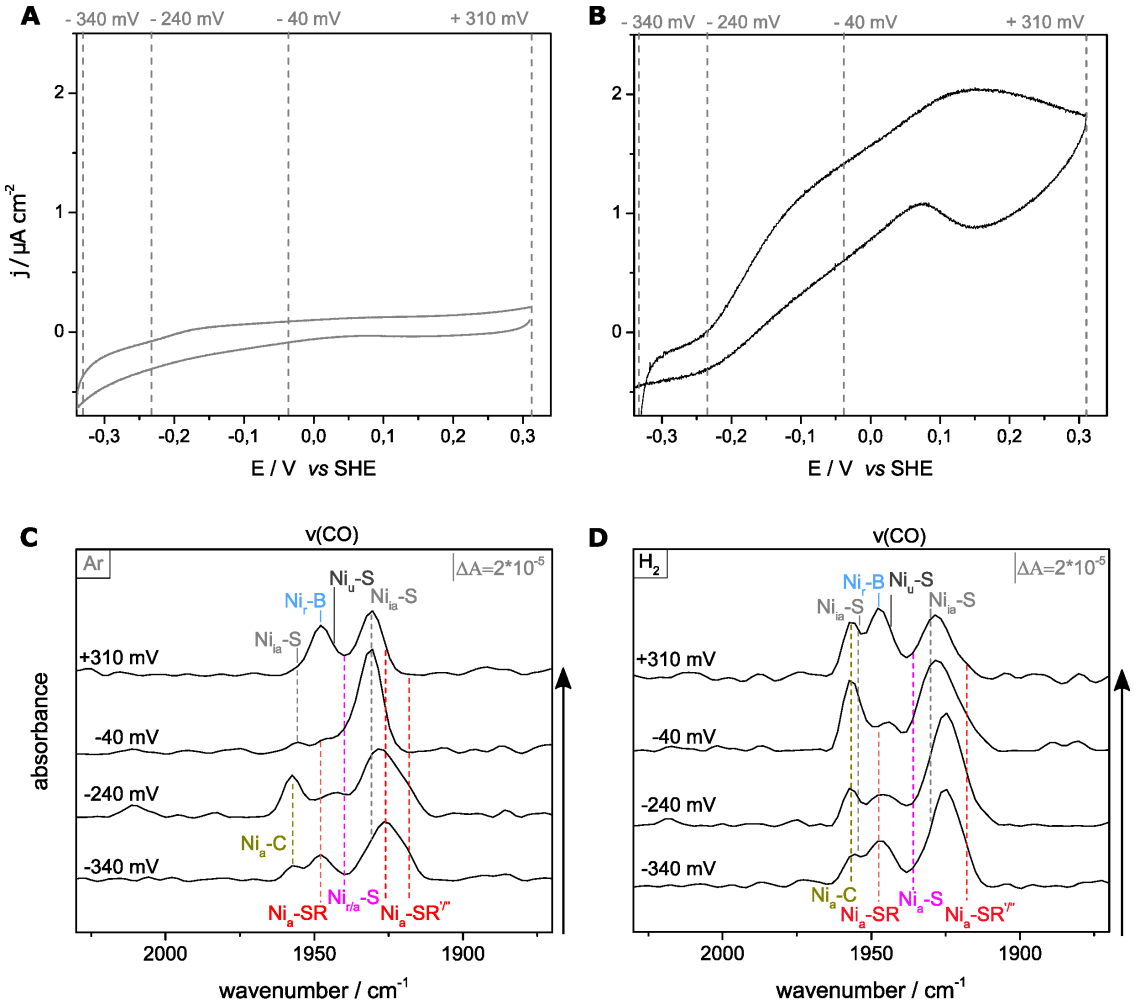

Figure 4.21: Voltammetric traces of *strep*-MBH on C_6NH_2 in (A) Ar and (B) H_2-saturated in and SEIRA spectra showing characteristic spectral ν(CO) region of the active site at different applied potentials under (A) Ar and (B) H_2-saturated electrolyt. Potentials are quoted in V relative to the standard hydrogen electrode (SHE). Measurements were performed in 10 mM phosphate buffer solution at pH 5.5; CVs (A,B) were recorded at 25°C and SEIRA spectra (C,D) at 4°C.

However, upon Ar at lowest applied potential (-340 mV), typically a low electrocatalytic current is detected in the CV, which is ascribed to H_2 evolution. The enzymatic H_2 production is suppressed under H_2 atmosphere due to substrate inhibition.[33] An onset of -240 mV is observed - in the recorded CVs as shown in Figure 4.21A and B. An OCP of -40 mV is found for *strep*-MBH on C_6NH_2-SAM under H_2.

Only for the isolated MBH heterodimer, a for H_2 (as substrate) seemingly "irreversibly inactivated" species, the so-called Ni_{ia}-S state with a CO absorption at 1930 cm^{-1}[5], is formed under certain conditions, e.g. in the presence of residual oxygen and substrate excess. This state is accumulated during the different potential steps within the present experiments as derived from the respective SEIRA spectra. Therefore, occurring changes in the redox state composition of the catalytic center were analyzed by calculating suitable difference spectra and determining the corresponding state populations via the corresponding CO absorptions by component fits. Hence, even under continuous changes in the Ni_{ia}-S CO-ligand band intensity, the analysis could

be carried out accurately. At the lowest applied negative potential (-340mV), the most reduced Nia-SR states are preferentially populated under Ar as well as H_2 atmosphere. The populations of the Ni_a-SR states decrease slightly at the observed onset at -240mV, while the amount of Ni_a-C is enriched to its maximum population. Under Ar atmosphere (see appendix Fig. A.12), the highest Ni_a-C state population is found at around -240mV. Under H_2 atmosphere the maximum Ni_a-C state enrichment occurs at more positive applied potentials, i.e. instead of -240 mV under Ar it is found to be -40 mV under H_2. As stepping to -40mV under Ar, the populations of Ni-SR decreases and Ni_{ia}-S, as well as the $Ni_{a/r}$-S species increase are obtained as main states. In consistence with the SEIRA studies on DvMF, the redox transition from Ni_a-S to Ni_r-B could be shown under potential control. This particular transition is triggered here by switching the potential to the most positive value of +310 mV: Thereby, a significant fraction of Ni_r-B is slowly formed under Ar atmosphere besides the Ni_{ia}-S species within 30 min. Under H_2 atmosphere, the corresponding SEIRA spectrum displays a different redox state composition, since substrate conversion still occurs despite applied potentials. At -40 mV a significant fraction of the Nia-SR states is already transformed to the Ni_a-C state. At a potential of +310 mV, where an oxidative inactivation is expected, the amount of detectable Ni_r-B increases significantly, however, all reduced states are still observable in the spectrum, despite in slightly minor fractions. This means that the applied positive potential cannot transform all adsorbed, SEIRA detectable *strep*-MBH enzymes at the C_6NH_2 surface to the oxidized state. This is related to different orientations of the immobilized *strep*-MBH. Thus, also a fraction of unwired enzymes, which only can interact with the H_2 substrate, are present at the C_6NH_2-terminated surfaces, as already discussed in section 4.2.1. The application of negative potentials, however, induces a reorientation of the *strep*-MBH molecules, leading in consequence to a homogenous DET for all electrochemical active enzymes at the electrode surface. This might be also an explanation for the observed shift of about +200 mV for the maximum Ni_a-C population under H_2. Since a fraction of the adsorbed enzyme molecules might not be able to release electrons directly to the electrode, certain prevail reduced at the active site and the Fe-S cluster, preferably in a Ni_a-C state. In order to illustrate the role of the previously discussed potential dependent enzyme rearrangement at the surface, the intensity and the relative ratio of the amide I and II band are shown as a function of the applied potential in Fig 4.22.

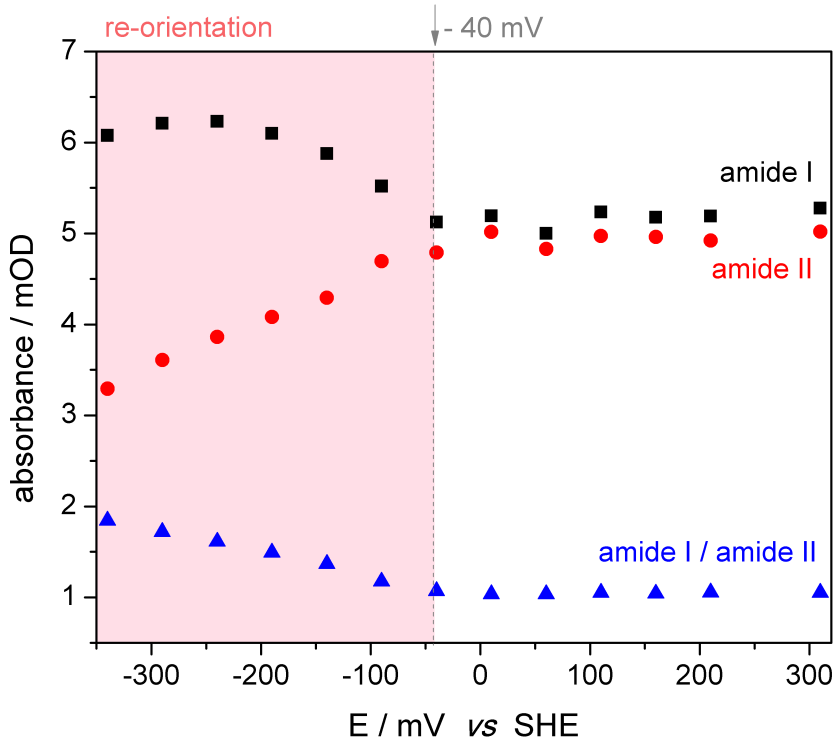

Figure 4.22: Potential dependent change of *strep*-MBH on C_6NH_2-SAM showing the amide I (black) and amide II (red) band intensity as well as in the amide I / amide II ratio (blue) of *strep*-MBH adsorbed on a C_6NH_2-SAM.The potential,where reorientation is observable is indicated in by a grey arrow and a grey dashed line at -40 mV (vs SHE). Measurements were performed in 10 mM phosphate buffer solution at pH 5.5 under Ar atmosphere, thereby decreasing the applied potential stepwise from positive to negative values. Measurements carried out at 4°C.

Indeed, by monitoring the potential dependent course of the amide I and amide II band intensities shown in Fig. 4.22, a reorientation is detectable at potentials below -40 mV. At -40 mV and above, the amide I and amide II band intensity ratio remain constant and can be compared to the initial one, where two different orientations were suggested by MD and the related experiments where a redox mediator was added to monitor the mediated current [230], vide supra. Below -40mV the reorientation is directed towards an optimized direct electron exchange between enzyme and surface and thus will allow the potential control of *strep*-MBH at low potentials, consistent with the observed redox states from the active site under different gas atmospheres and potential control, *vide infra*.

In contrast to the work of Hidalgo et al. [68] on Hyd-1, no clear evidence for Ni-L species could be identified in the corresponding SEIRA spectra of the *Re strep*-MBH. This does not exclude a possible participation of this state in the catalytic cycle of MBH per se, but rather suggests a higher thermodynamic instability of this state in the catalytic cycle of *Re* MBH compared to the findings of Hyd-1.[68]

4.4.3 Oxidation of *strep*-MBH

The highest oxidized state of oxygen-tolerant [NiFe] hydrogenases, namely Ni_r-B, is formed upon exposure with O_2, as well as under anaerobic potential control (under Ar) and H_2 as displayed in section 4.4.2. The latter shows, that at least to a certain extent, Ni_r-B could be slowly recovered at high positive potentials. (+310 mV) even under anaerobic conditions, although the presence of traces of O_2 cannot entirely be excluded even during long exposure times with Ar.

The mechanism of O_2 conversion in this type of oxygen-tolerant hydrogenases and the its function as O_2-reductase upon formation of the Ni_r-B species is still discussed. One possible reaction pathway involves O_2 binding at the active site followed by reduction by four electrons and three protons to form water and a hydroxide molecule ($O_2 + 3H^+ + 4e^- \rightarrow H_2O + OH^-$).[242] The water molecule originating from O_2 conversion can diffuse out of the enzyme via a solvent channel, while the hydroxide ion remains bound to the oxidized active site. The consideration that Ni_r-B formation arises from O_2-binding at the active site, has been studied in various works. Lauterbach et al. showed for the soluble hydrogenase of Ralstonia eutropha, that O_2 reduction takes place in the vicinity or directly at the catalytic [NiFe] center via the reuse of electrons produced during H_2 cleavage by mass spectroscopic detection of labeled compounds.[243]

However, an exclusive aerobic Ni_r-B formation by O_2 has been questioned in other isotope labeling studies, which suggested alternatively a solvent derivation of the bridging OH− ligand in Ni_r-B.[244] Thereby, no oxygenic species originating from O_2 were observable in the first coordination sphere of the nickel.[72] Based on these studies, the authors claim that inactivation can also occur under O_2-free oxidizing conditions, i.e. anaerobic inaction.[245]

In this context, SEIRA spectro-electrochemcial studies on *strep*-MBH in different gas atmospheres were carried out to investigate the enzyme's redox state composition under formally (re)oxidizing, aerobic as well as anaerobic conditions. Figure 4.23 shows the corresponding SEIRA data in the spectral region characteristic for the ν_{CO} and ν_{CN} vibrations recorded under these terms, namely under Ar at OCP or under H_2 at applied positive potential, and performed on the same sample of *strep*-MBH adsorbed on a C_6NH_2-SAM, successively.

The adsorbed enzyme remains after completed adsorption process under Ar (OCP: +130 mV) in its Ni_r-B state. Upon H_2 exposure, the *strep*-MBH is firstly activated, before the re-oxidation process is initiated by positive applied potentials or exposure to air without potential control. Only upon reduction at negative applied potentials of about -50mV or an exposure to H_2, a clear redox transition between Ni_r-B and $Ni_{a/r}$-S can be observed. As shown in 4.4.2, also fractions of the reduced states are found under H_2. Under the additional negative potential, certain reduced states are more populated. The application of a positive potential under H_2 atmosphere leads to so-called "anaerobic inactivation", thereby forming oxidized ready species (Figure 4.23b). This process is also observed in cyclic voltammetric traces at high positive potentials (see chapter 2.4.5). As already discussed in 4.4.2, the slow formation of the Ni_r-B state takes place even under H_2 atmosphere, suggesting a solvent derived hydroxyl-binding at the active site.

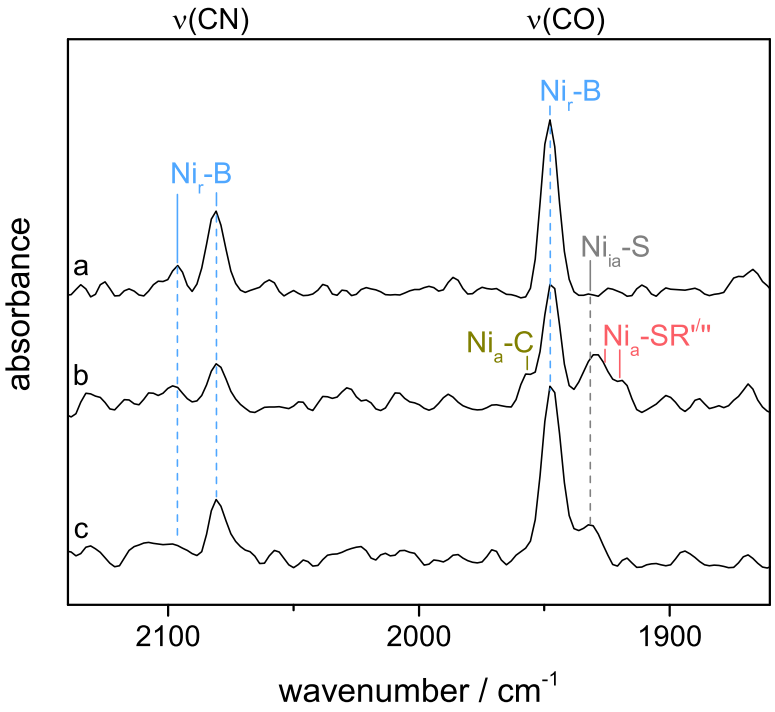

Figure 4.23: SEIRA spectra of *strep*-MBH on C_6NH_2 showing the characteristic spectral region for ν(CO) and $\nu(CN)_{CN}$ vibrations of the active site under aerobic and anaerobic oxidizing conditions: (a) oxidized under Ar atmosphere at OCP after *strep*-MBH adsorption, (b) re-oxidized under H_2 atmosphere with applied potential of +310 mV and (c) re-oxidized with air at OCP (+310 mV). Potentials are quoted in mV relative to the standard hydrogen electrode (SHE). All spectra were recorded at 4°C.

Consistently, reduced species are still present at this positive potential, which is presumably related to *strep*-MBH molecules bound in unfavored orientation, preventing a direct electric contact with the working electrode, vide supra. However, half of the initially observed Ni_r-B state shown in spectrum (a) (Fig. 6.10) could be recovered upon anaerobic inactivation. Successively, a second activation of *strep*-MBH by reduction under H_2 at OCP was carried out, before a final re-oxidation step under air was performed (Fig. 6.10c). Figure 6.10c shows the formation of Ni_r-B under air exposure, thereby a fast and almost complete re-oxidation could be observed. Besides the Ni_r-B formation, another state is formed, namely Ni_{ia}-S, presumably an irreversibly inactivated state.

As shown here, under optimized adsorption condition, high intensities of active site characteristic bands are obtained, which allow important mechanistic insights. However, not all enzyme molecules are in direct contact with the electrode surface. As discussed above, it might be possible to address the still discussed mechanism for MBH oxidation as well as the enzymes function as O_2-reductase by SEIRA spectroscopy in more detail in future.

4.4.4 Conclusions and Outlook

The active site of *strep*-MBH on C_6NH_2-SAM surface was successfully monitored by spectroelectrochemical IR studies in the SEIRA mode under turnover and non-turnover conditions.

The observed redox states are consistent with those found for purified hetero-dimer *strep*-MBH in solution, and thus reveal the integrity of the MBH molecule after adsorption on the surface. Even though a seemingly irreversible inactive state in the presence of H_2 as well as residual oxygen was formed upon potential application and increased as a function of time, the analysis of the native redox states of the enzyme could be processed. Observations of the corresponding amide I and II bands of the protein backbone relate to the detectable changes at the active site at applied potentials, confirming the prior discussed reorientation of the enzyme at the surface: At negative potentials, a homogenous MBH orientation is found on the electrode which favors direct electric contact of all active enzymes with the electrode. In contrast, at high positive potentials, the contact between enzyme and surface appears partially disrupted due to a fraction of unfavorably orientated immobilized molecules. However, the enzymes active site could still be probed under turnover conditions as well as aerobic and anaerobic re-oxidation processes. As a function of the externally applied potential various redox states of the catalytic active and also the oxidized, inactive states and their principle inter-conversions could be monitored at least on a qualitative level. This is a significant advantage compared to the potential-dependent titration of *strep*-MBH dimer in solution with substochiometric amounts of dithionite, preferentially forming in large amounts Ni_{ia}-S species at pH 7 (not published data. Other works on potential titration of *strep*-MBH in solution in the presence of mediator cocktail have been carried out in a OTTLE cell by Elisabeth Siebert.[224] The results obtained for adsorbed enzyme molecules might define a more promising approach for the determination of midterm potentials for the redox transition of the active site since the electron exchange is faster, potentials can be established more precisely and possible diffusion limitations (from the enzyme via mediator to the electrode) do not have to be considered. A great advantage of this approach is the easy simultaneous exchange of various gas atmospheres, i.e. to study the effect of the relative amount of oxygen or hydrogen on irreversible inactivation and other mechanistic implications. However, a drawback of SEIRA spectroscopy is the lower spectral resolution 4 cm^{-1} compared to that in solution (2 cm^{-1}), to achieve a comparable S/N ratio. Due to the orientational distribution of *strep*-MBH on C_6NH_2-surface, the negatively charged surfaces discussed in section 4.3.3 should be also considered for mechanistic studies, even with the drawback of higher variations in absorbance intensities and catalytic activity. In this context, SEIRA spectro-electrochemical studies on immobilized *strep*-MBH was shown to be a powerful future tool for a deeper understanding of the underlying mechanistic processes at the active site, such as for example the still unknown mechanism of observed H_2 evolution by the Re MBH upon non-physiological conditions as shown in electrochemical studies,[246] even if it is mainly known to be biased towards H_2 oxidation. A further example is function of the enzyme as O_2-reductase.

Chapter 5

Spectro-electrochemical studies on Cytochrome c - Metal oxide surface interactions

5.1 Introduction

Direct electron transfer between redox proteins or enzymes and conductive materials has been demonstrated for a number of proteins and (semi)conductors and has proven to be promising both in mechanistic studies as well as in the development of emerging nanotechnologies such as biosensors and enzymatic fuel cells.[207, 213, 247]

Up to date, studies on protein-surface interactions have been extensively performed on standard electrode platforms, which commonly are based on self-assembled monolayer (SAM) coated metal systems as presented in chapter 4 and are in particular applied in spectro-electrochemical studies (SEIRA, SERS). Also, pyrolytic graphite edge (PGE) electrodes are commonly used, but they are used mainly for electrochemical investigations and hardly in a spectroscopic approach due to their high radiation absorbance. To overcome these limitations, an Attenuated Total Reflexion–IR (ATR-IR) spectroscopic approach on graphite NPs covered by adsorbed protein was recently developed by the group of Vincent for spectro-electrochemical studies on enzymes.[68] In order to obtain reasonable spectroscopic signals, carbon NPs are used in this set-up to achieve high enzymatic loading, at the expense however of the electrode conductivity due to the particles low interparticle electric contact. The used graphite NPs are interconnected by a Nafion films, while the electric contact is established by a carbon paper sheet pressed on top of the NP film.[236]

In particular, Transparent Conductive Oxides (TCO), belonging to a group of semiconductors, attracted attention with respect to the adsorptions of a redox protein for electrochemical applications in the last years. Since TCOs show transparencies in the visible range as well as in some cases in the IR.[248] Hereby, they may offer a promising platform for spectro-electrochemical investigations. In contrast to noble metal electrode materials, metal oxides represent a low-cost alternative, with a wider electrochemical accessible potential range compared to standard metal-SAM systems, and provide also a certain biocompatibility for protein adsorptions due to their surface functionalities. Protein adsorption on metal surfaces normally requires surface modifications of the electrode surface to retain the protein structure and function after immobilization. In this context, SAMs are frequently chosen for surface functionalization of metal surfaces. These suffer however from their intrinsic instability in terms of surface desorption under oxidative and reductive potentials, thermal instability, and aging effects.[163]

Of particular interest from a nanotechnology perspective is the possibility of controlling the orientation, conformation, and function of a surface adsorbed protein through the physicochemical properties of the nanomaterial and its surface. The protein orientation can be affected by its size, shape, and functionality of the respective surface.[249, 250] The latter is discussed in regard to electrostatic interactions in chapter 4. The surface charge is a crucial component for the protein coverage and orientation. In this sense, also metal oxides are investigated towards an optimal adsorption strategy.[250, 251]

5.1.1 Immobilization Strategies

Wiring of redox proteins on electrode surfaces with a fast electron transfer between the electrode surfaces and the redox protein is crucial for an efficient outcome. Analogue to the immobilization strategies on standard electrodes, different immobilization strategies of protein on metal oxides have been investigated.

5.1.1.1 Surface Modifications

To enable directed electrostatic binding of proteins at metal oxide surfaces, SAMs for metal

oxides have been established such as n-alkanoic acids and alkylphosph(on)ates. Both groups are believed to bind through direct coordination between carboxylate or phosphate and the metal cation within condensation processes. Both, mono- and bi-dentate bindings have been suggested to take part in the coordination.[252] However, some reported drawbacks for these SAMs are pointed out, repeatedly. The precondition for a complete monolayer formation is a widely hydroxylated metal oxide surface,[253] which is usually, even in contact with water, only formed to a certain extent. The amount of a hydroxylation coverage formed in contact with aqueous solution depends on the material composition and the applied pretreatment steps. In addition to the challenge of the formation of a homogenous monolayer, there is also an adsorption-desorption of metal-oxygen-phosphor (M-O-P) species.[253] Further disadvantages of such type of SAMs may be their inferior stability in aqueous solutions and the difficulty to introduce functionalities in alkylphosph(on)ates chains for the attachment of biomolecules.[254] Therefore, covalent grafting processes for SAM formations at metal oxides have been studied. One well-known strategy is the silanization of metal oxide surfaces.[255] However, this type of modification is restricted to a handful of metal oxides.[256] Another strategy is based on the generation of radicals in alkyne chains for a direct binding to the surface. This process has been recently applied to form homogenous monolayers with a well-spread charge distribution at the metal oxide surface. The biggest challenge up to date is the controlled formation of monolayers, involving the reduction of the amount of defect sites [257]as well as an inhibition of a likely SAM branching, which would generate a thicker spacer layer between metal oxide and protein.

In addition, immobilization strategies for covalent binding between proteins and metal oxides via multi-step synthesis have been studied, which usually require an engineering of the metal oxide surface and may also introduce a further synthesis step on the protein site, such as amide coupling surface binding.[258] A common disadvantage hereby is the broad distribution of orientations resulting from an undirected amide coupling at all suitable functional groups at the enzyme's surface. In the case of large proteins, this drawback does hardly allow an accessibility of the protein functionality by electronic communication to the electrode surface.[258]

5.1.1.2 Direct Adsorption

TCOs contain a high amount of oxygen functionalities at the surface and may thus allow a protein-friendly environment even without any modifications.[134, 157, 259, 260] In contact with an aqueous solution at neutral pHs, metal oxide films form preferentially hydroxyl groups,[261] thereby inducing surface charges that allow application of specific adsorption strategies for protein binding.[262, 250] Metal oxides are generally characterized by their amphoteric nature based on the Protonation deprotonation ability of hydroxyl groups at the metal surface (-MOH^{2+} $\leftrightarrows$ -MOH $\leftrightarrows$ -MO^{-}). The pH at which the net surface charge vanishes refers to the isoelectric point (IEP). The IEP of metal oxides is also equal to their potential of zero charges (PZC). Thus, depending on pH, either above or below IEP, the surface is negatively and positively charged, respectively. Both charges present on the electrode surface and on the proteins will affect the adsorption behavior of the protein on the electrode surface.
The surface coverage of redox proteins on metal oxide films is shown to depend on the surface charge of the films similar to the adsorption of proteins on SAM-coated metals (see chapter 4. Hereby, the isoelectric point (IEP) plays a crucial role for electrostatic protein-surface interaction. In this chapter, the focus is directed on two proteins, Cytochrome c (cyt c) and Membrane-Bound-Hydrogenase (MBH), which will be discussed as examples for protein-metal oxide interactions. In this sense, cyt c and dimeric MBH have isoelectric points of 10.5 and ˜7.2, respectively,

meaning that cyt c and MBH are positively charged below pH 10.5 and 7.2, respectively.[259] In this regard, an effective protein surface loading depends on the counterpart charges between surface and protein given by the pH of the solution as shown for cyt c on TiO_2.[259] This work indicates, that the closer the pH value is to the corresponding surface IEP, the more probable are hydrophobic interactions between protein and metal oxide surface. The biocompatibility of directly adsorbed protein on metal oxide may be given, but its compatibility under the force of electric fields cannot be completely understood without more profound spectro-electrochemical studies and is therefore often only estimated.

Besides planar, low surface area TCOs, mesoporous structures of TCOs including mesoporous Titanium Dioxide (TiO_2), Tin Dioxide (SnO_2), Tin doped Indium Oxide (Indium Tin Oxide (ITO); $Sn:In_2O_3$) and Antimony doped Tin Oxide ($Sb:SnO_2$, ATO) have been recently examined as high surface area substrates for the immobilization and voltammetric investigations of proteins.[134, 157] Although metal oxides are often claimed as biocompatible surfaces, in many cases, adsorption upon incubation of nano- and mesoporous structures were found to modify the protein properties.

Durrant discusses the immobilization of cyt c on nanoporous TiO_2 (with pores sizes between 10 and 20 nm), thereby claiming no occurrence of protein denaturation upon immobilization. However, the relatively slow electron mobility due to a lack of conductivity within the nanocrystalline electrodes precluded the use of these nanostructured TiO_2 electrodes for a cyclic voltammetric determination of protein/electrode electron transfer kinetics.[263, 264] Indeed protein voltammetry exhibited only the cyt c reduction peak at -0.55 V (vs Ag/AgCl) and no oxidation peak. The authors claimed that the observed irreversibility and negative shift of the redox transition relative to the solution redox potential, which usually is observed at around 0 V vs Ag/AgCl [102, 265, 134] is due to the limited conductivity of the TiO_2 film.[259] However, this shift of the observable redox potential indicates the formation of a non-native cyt c species, which is often found at such negative potential values. Even if the authors claim that cyt c is preserved in its native state with respect to the presented UV-Vis spectra, a band overlap with non-native cyt c species cannot be excluded due to the high spectral similarity between native and denaturated states. Thus, a quantification of the state composition appears challenging. In contrast, as reported by Wollenberger/Frasca et al., cyt c adsorbed in mesoporous Indium Tin Oxide was immobilized in its native state monitored by protein film voltammetry, displaying no significant potential shifts.[134]

5.1.2 Protein Denaturation

Basically, the function of a protein is strongly related to its structure which can be highly affected by changes with respect to its native environment.[266] Generally, proteins can unfold and become inactive upon changes in pH, temperature, ion concentration and surface interaction. Depending on the specific denaturating conditions, the observed conformational modifications of the ternary / quaternary structure can be reversible or irreversible. In this context, protein adsorption onto nano- or mesoporous metal oxides,[250] can in some cases lead to an irreversible denaturation

of the protein.[267] In order to investigate the protein-metal oxide interactions, testing its biocompatibility and a to gain a deeper understanding regarding the influence of specific metal oxide properties on proteins, more sophisticated spectroscopic and spectro-electrochemical approaches are required. With the gained knowledge, a further development of biohybrid-electronic devices towards optimized applications will then be possible on the basis of a knowledge-based optimization of the electrode material as well as of the enzyme-electrode interface.

Hence, this following section describes an ATR-FTIR spectroscopic set-up for investigation of metal oxide – protein interfaces. Therefore, planar metal oxide surfaces were chosen to test the specific setup. For probing the protein-semiconductor interactions [268, 269, 251, 270] two proteins were investigated, cyt c as a "benchmark" model redox protein, which was already extensively studied in the past, and the Re MBH, an oxygen-tolerant [NiFe] hydrogenase, representing a complex enzyme catalyst, used for bio-fuel cell application. An insight into their adsorption behavior, their interaction behaviors with transparent conducting oxide electrode materials can only be gained by *in situ* spectroscopic studies.

Surface enhanced spectroscopic techniques are powerful techniques, which allow the monitoring of adsorbed species in surface selective manner. Among others, SERRS-, SEIRA- and some multiple reflection ATR-IR approaches are suitable to probe adsorbed species down to pmol/cm^2 concentrations. However, conventional spectroscopy on a protein (sub)monolayer as obtained on planar surfaces might be not sensitive enough for detailed spectroscopic studies due to low sample concentration. IR spectro-electrochemical studies on thin TCO films might be in principle feasible due to their transparency in the IR region. Surface selective observations required for fundamental studies of direct protein-semiconductor interactions [268, 269, 251, 270] might be challenging.

Among the different available TCOs, Indium Tin Oxide (In_2O_3/SnO_2 90/10 wt% - ITO) is the most widely used TCO due to its high transparency (85% in the visible region) and high conductivity (104 S cm^{-1}).[271] However, one major disadvantage of ITO is the relatively low natural abundance of indium and its high price. Therefore, in an attempt to decrease the indium content, Sb-doped SnO_2 (ATO) and amorphous tin-rich Indium Tin Oxide (ITO_{TR}, with In-Sn ratio close to 1) TCOs have emerged as promising alternatives to regular ITO, see 2.3.2. In the present work, two of these promising examples, namely ATO and ITO_{TR}, are discussed and used as spectro-electrochemical platforms to study the immobilization of biomolecule (sub)monolayers.

5.2 Antimony-doped Tin Oxide (ATO) thin film electrodes for a stable horse heart Cytochrome c immobilization

As mentioned before a promising alternative material for ITO is an antimony-doped tin oxide (Sb:SnO_2, ATO), which is briefly introduced in section 2.3.4. It benefits from a comparatively low cost (when compared to ITO), a high conductivity (in the range of 10^2 S cm^{-1}), a high transparency (up to 80%) [270, 272, 139, 273] and exhibits the potential for electrostatic immobilization of enzymes, as demonstrated in the last years for small redox proteins, such as cytochrome c and azurin.[260, 258] It was shown, that cyt c and azurin bind to the ATO surface by an electrostatic binding between the negatively charged ATO surface and the positively charged proteins. However, the protein-ATO binding interaction was rather weak and could easily be disrupted at high ionic strength.[260, 258] By additional reaction steps between the ATO surface and the protein, the protein-surface interaction could be tuned towards covalent binding with a high inherent stability. In such a way, an initial surface amination of the ATO surface was followed by amide formation via crosslinking the carboxylic acid at the surface to primary amines include carbodiimide compounds, such as EDC, to yield a stable covalent attachment of cyt c within mesoporous ATO electrodes, as shown by Müller et al.[258] Recently nanostructured ATO films have been developed in our group and the successful immobilization of hexa-histidine-tagged (his-tag) human sulfite oxidase (hSO) on these type of electrodes has been demonstrated.[157] It was speculated at that time that direct surface attachment of the his-tag hSO resulted from an interaction between the metal cation affine his-tag and the ATO surface. However, due to the small pore size (8 nm) of the ATO support used at that time, the amount of surface bound hSO on the porous ATO electrodes was not sufficient to observe either non-catalytic, direct electrochemical signals of the molybdenum-containing cofactor of the hSO or any spectroscopic signature by UV-Vis.

To optimize protein adsorption on this antimony tin oxide surfaces, a more sophisticated set up for IR studies was used in the present work, probing directly protein-surface interactions. Thereby, IR-spectroscopy serves a powerful tool to monitor proteins from a structural or mechanistic point of view in a variety of set-up configurations. In this context, the ATR-IR mode is one surface sensitive technique allowing to examine *in situ* processes such as adsorption/desorption of protein samples on electrode surface even at low protein concentrations and to reveal the integrity of the protein structure upon surface interaction. So far, *in situ* FTIR investigations on the adsorption behavior of proteins on transparent conducting oxides and other semiconductor surfaces have been, to the best of our knowledge, not reported yet.

In this chapter of the present thesis, a single reflection ATR-FTIR configuration is introduced allowing investigations of protein adsorption on TCO model electrodes. This technique is hereby applied to verify the hypothesis of a selective his-tag binding towards the ATO surface; hypothesis which is verified by studying the immobilization of native horse heart Cytochrome c (cyt c) and his-tagged horse heart Cytochrome c (his-cyt c) on planar ATO surfaces Hereby, we are aiming to establish the general applicability of ATO films for the effective and stable binding of proteins via a hexahistidine tag.

The following work presents the development of an ATR-IR set up for studies of immobilized enzymes on TCO surfaces.

5.2.1 Reference measurement

To resolve the contribution of inherent signal intensities from the protein solution within the evanescent ATR-IR wave, a reference measurement was carried out on a hydrophobic, H-terminated, uncoated Si-prism in contact with the protein-containing electrolyte. The Si-prism was pre-treated as usually before metal oxide coating or Au coating for SEIRA experiments following the standard polishing procedure (see chapter 3).

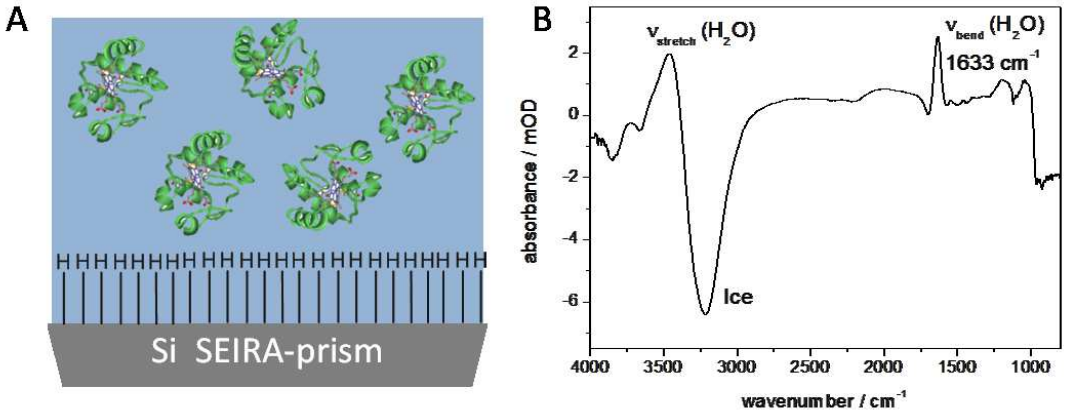

Figure 5.1: (A) Sketch of an ATR-FTIR set up with an H-terminated Si-prism, formed after etching process and incubation with a cyt c buffer solution as well as (B) ATR-FTIR spectrum of the 7µM cyt c incubation solution.

The hydrophobization of the surface is achieved by exposure to NH_4F solution. Thus, the H-terminated metal free surface of the Si-prism could be used to monitor the 7 µM his-cyt c incubation solution. The spectrum displayed in Figure 5.1 reveals only typical water adsorptions, related to O-H stretching and bending vibrations without any indication of amide bands. In conclusion, no specific IR signal of cyt c, i.e. amide I and amide II bands, could be observed from the 7 µM protein solution in the set up. This reference experiment shows that IR signals from the low concentrated protein solution cannot be detected and that the following section presenting amide I and amide II bands result from surface bound protein and cannot originating from dissolved protein in solution.

5.2.2 ATO thin film preparation and characterization

Planar ATO thin films were obtained by evaporation induced self-assembly of nanocrystalline antimony-doped tin dioxide (ATO) nanoparticles (NPs). The ATO nanoparticles were doped with 8 mol% of antimony. The 3.5 nm in diameter sized ATO NPs were synthesized following a benzyl alcohol assisted solvothermal approach, as reported previously.[274] In order to ease the wet-ability of the silicon prism, 2 wt% of F127 (m(F127)/m(ATO) = 0.02) were added as wetting agent ensuring the homogeneous deposition of planar ATO NPs thin films on the surface of the Si-prism (see Figure 5.2). The planar ATO-NPs-film surface exhibits a porosity based on the interparticle packing voids. Figure 5.2C displays a SEM cross section image of a planar ATO-coated Si wafer.

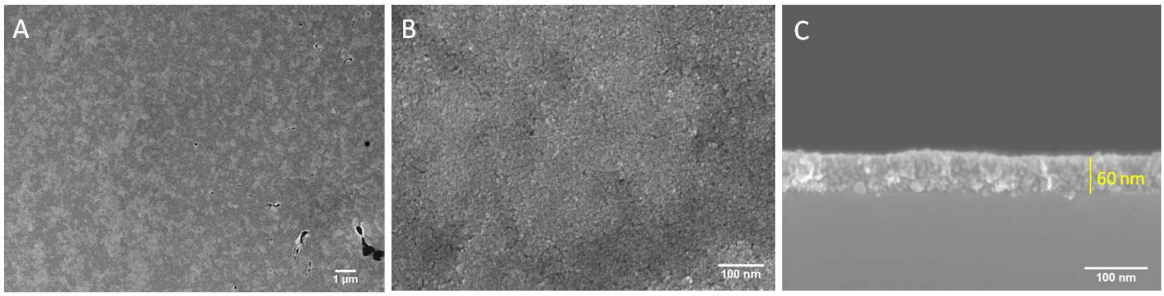

Figure 5.2: SEM micrographs of planar, ultrathin ATO films in top-view at (A) low and (B) medium magnification and (C) in cross-section view. The films were deposited on an IR transparent silicon prism for Single Reflection ATR-FTIR absorption spectroscopy and on a silicon wafer for cross-section measurements.

Conductivity and transparency measurements were performed by Dr. Anabel Molero and are discussed in detail in manuscript (Molero et al.; under preparation) . Electrical characterization of the as-prepared ATO thin films was carried out by 4-point probe measurements carried out on ATO coated ITO-glass substrates and revealed a low sheet resistance of ca. 103 ($\Omega/\square$), indicating a good conductivity of the nanostructured ATO-ITO "sandwich" electrodes. The transparency of the films in the visible region was determined by UV–Vis spectroscopy, exhibiting comparable transparency behavior to commercial thin ITO films.

5.2.3 Immobilization of horse heart Cytochrome c and his-tagged Cytochrome c on ATO

In order to gain deeper insights into the interactions between native and his-cyt c with the ATO surface, ATR-IR measurements on planar ATO NPs thin films were carried out (for set-up configuration see chapter 3). For this purpose, a silicon prism was coated with an ultrathin planar ATO film and used in an ATR-Kretschmann configuration to follow the in-situ adsorption and desorption kinetics of his-cyt c and cyt c. For both, cyt c and his–cyt c, two major band maxima, one characteristic for amide I absorptions centered at 1656 cm^{-1} and 1652 cm^{-1} for cyt c and his-cyt c respectively, and another band related to amide II absorptions located at 1549 cm^{-1} for both cases, were observed as displayed in Figure 5.3A and B. The amide I band (1700 - 1620 cm^{-1}) arises almost exclusively from the C=O stretching vibration of the backbone peptide bond and is sensitive to small variations in hydrogen bonding patterns and molecular geometry of the protein.21 The amide II band (1600–1500 cm^{-1}) originates from an out-of-phase combination of N-H in-plane bending and C-N stretching vibrations of peptide bonds.[275] It is generally accepted that the shape of the bands reflects the main protein chain conformation as described in detail in section 2.2.2.4.[276] The exact band positions of the secondary structure components of amide I and II vibrations are determined by second derivatives (*vide infra*). Figure 5.3C and D reveal the adsorption kinetics by monitoring amide I and amide II band intensities within an adsorption time of 2h. For both, cyt c and his-cyt c, the adsorption kinetics on ATO converges to different saturation values, i.e. protein coverages, as displayed by the course of amide absorption intensities. Figure 5.3C presents maximum amide I and amide II band intensities of cyt c on ATO with 0.77 mOD and 0.57 mOD, respectively. Compared to his-cyt c with 1.71 mOD and 1.31 mOD for amide I and amide II absorptions, respectively, cyt c bands occur with half of the intensities (45%) at the surface. The amide I / amide II ratio remains constant within the adsorption time of 2h for both cases with a ratio accounting for 1.3 for both, cyt c and his-cyt c.

Besides the difference in absolute intensities of the amide I and amide II absorption bands, which is about the double for his-cyt c compared to cyt c, the particular surface adsorption kinetics of cyt c and his-cyt c reveal a further difference. The time evolution of amide I and amide II intensities of cyt c and his-cyt c within the adsorption process can be appropriately fitted with a biexponential course as displayed in black lines in Figure 5.3C and D. Cyt c exhibits a fast first growth with a time constant of $\tau_1 = 1.77$ min, whereas the corresponding time constant for his-cyt c with $\tau_1 = 3.53$ min results in a two times slower binding process (see Table 5.1). The second overlapping process during surface adsorption for both, cyt c and his-cyt c is related to a very slow surface adsorption with time constants of $\tau_2 = 33.50$ min and 38.28 min, respectively.

To probe the interaction prevailing between the protein molecules and the surface, desorption experiments were carried out as displayed in Figure 5.3C and D. To elucidate the strength and reversibility of the binding, buffer exchange was performed, meaning surface attached protein films of cyt c and his-cyt c on ITO_{TR} were immersed in protein-free buffer several times. Thereby, the ionic strength of the buffer solution was increased stepwise, while the respective pH value was kept constant. The related desorption was monitored for each step till equilibrium was reached.

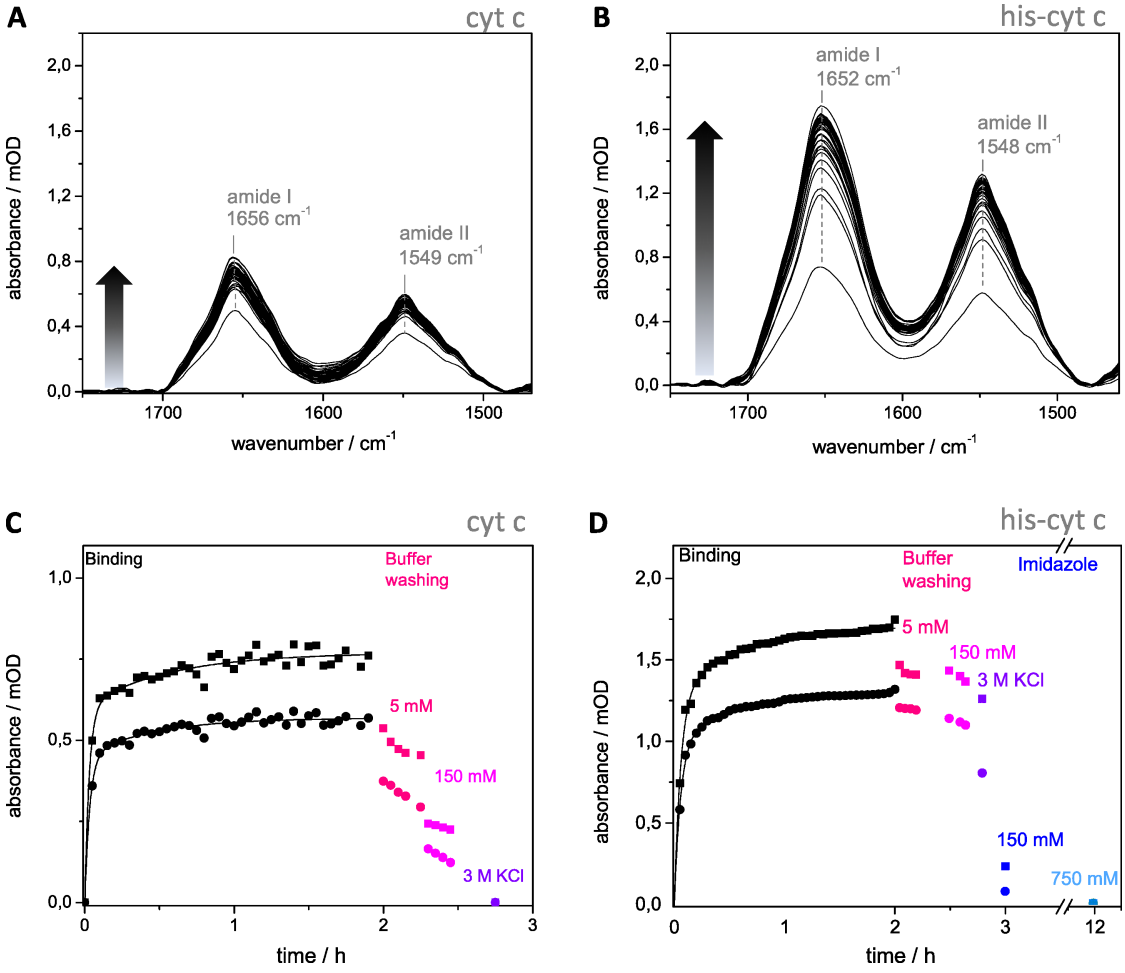

Figure 5.3: ATR-FTIR spectra of amide band region for (A) Cyt c and (B) his-Cyt c during immobilization on planar ATO thin films as well as the corresponding binding kinetics for (C) cyt c and (D) his-cyt c monitored by the maximal intensities (labeled in bold, black) of the amide I (■) and amide II (●) bands (black) as well are the related desorption processes upon washing with different buffer solutions with different ionic strength. Biexponential fits ($A = A_0 + A_1 \exp(-t/\tau_1) + A_2 \exp(-t/\tau_2)$) were applied in the time period of $0 < t < 2$h and are shown as black lines (C,D).

Table 5.1: Protein adsorption kinetics derived from selected amide I and amide II band intensities*

amide band	A_0 (mOD)	A_1 (mOD)	τ_1 (min)	A_2 (mOD)	τ_2 min
cyt c on ATO					
1656 cm^{-1}	0.77 ± 0.01	0.60 ± 0.04	1.77 ± 0.30	0.17 ± 0.02	33.50 ± 11.79
1549 cm^{-1}	0.57 ± 0.01	0.45 ± 0.03	1.98 ± 0.28	0.12 ± 0.2	27.37 ± 8.26
his-cyt c					
1652 cm^{-1}	1.71 ± 0.01	1.30 ± 0.04	3.53 ± 0.18	0.41 ± 0.02	38.28 ± 5.40
1548 cm^{-1}	1.31 ± 0.01	1.01 ± 0.02	3.46 ± 0.13	0.30 ± 0.01	30.43 ± 3.44

*Results from fitting the biexponential function $A = A_0 + A_1 \exp(-t/\tau_1) + A_2 \exp(-t/\tau_2)$ to the time course of the amide I band (1656 cm^{-1}, R^2 =0.9696) and amide II band (1549 cm^{-1}, $R^2 = 0.998$) bands for cyt c and to the corresponding amide I band (1652 cm^{-1}, $R^2 = 0.96597$) and amide II band (1548 cm^{-1}, $R^2 = 0.97599$), for his-cyt c. All applied in the time period $0 < t < 2h$.

For cyt c a simple buffer exchange after immobilization leads to a drastic loss of about 35% of the initial value of the amide band intensity. Buffer exchange exhibiting a higher ionic strength of 150 mM causes a further band intensity decrease down to 68% of the original intensity. Finally, by an exchange with a 3M KCl saturated buffer, the amide bands diminish entirely. Therefore, the ionic strengths induced protein desorption from the surface suggests a pure electrostatic binding between cyt c and the ATO surface.

In contrast, buffer exchange with varying ionic strength and even the addition of 3 M KCl had only minor effects on the amount of surface adsorbed his-cyt c (Figure 5.3D). The latter results indicate the existence of a strong, non- electrostatic interaction between his-cyt c and the ATO surface. Only an exchange with a buffer solution containing imidazole, a ligand with a high complexation affinity for metals and used as eluent in his-tag mediated metal ion affinity chromatography results in a quantitative desorption of his-cyt c from the ATO surface, as can be seen by the amide bands that finally vanish at high imidazole concentrations of 750 mM. Thus, a ligand exchange of the hexa-histidine tag complexed to a metal center of the ATO electrode surface can be achieved by the addition of imidazole molecules leading finally to a complete desorption of his-tagged proteins from the ATO surface. These results confirm the previously raised hypothesis of his-tag mediated binding between his-tagged proteins and the ATO surface as proposed by Frasca et al. for his-tagged hSO immobilized on mesoporous ATO electrodes.[157]

The investigated hypothesis of direct his-tag binding on ATO surfaces investigated in this work is illustrated in Figure 5.4. Proteins engineered with an attached his-tag are expected to bind via ligand-metal complexation between the histidine tag and presumably preferential the not fully coordinated tin surface cations rather than via an electrostatic interaction.

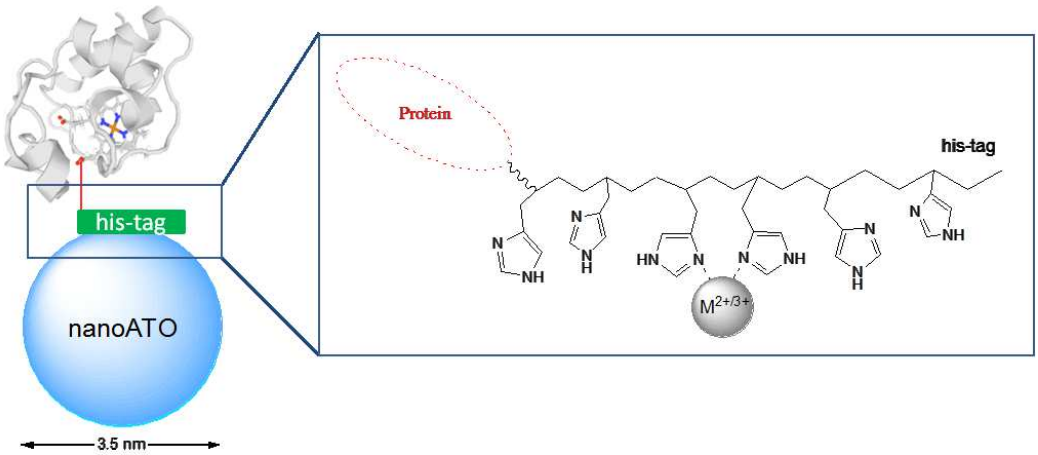

Figure 5.4: Proposed interaction between residues of the his-tag and exposed metal centers at the surface of the ATO nanoparticle. Due to the unknown surface details and functionality groups of the latter is not explicitly shown.

Imidazole is known to act as a ligand for metal cations. Nitrogen within the imidazole group of the hexahistidine tag binds via coordination to the exposed metal site.[277]

His-tagged proteins are usually purified by a preferential binding, most commonly to Ni^{2+},[278] but these type of metal chelate affinity is also known for a series of other metal cations such as Co^{2+}, Co^{3+} Cu^{2+}, Zn^{2+}.[279, 280, 278]

In the case of the observed electrostatic adhesion of cyt c to the ATO surface, the attachment can be attributed most likely to the positive surface charge of cyt c at neutral pH, which exhibits an isoelectric point of 10.2, which ensures an appropriate electrostatic binding on negatively charged surfaces. Alike many other metal oxides, ATO is expected to carry a substantial negative charge at neutral pH and an interaction with cyt c is assumed to be largely electrostatic and guided by its positively charged surface lysines.[281] However, the protein-surface interaction is relatively weak with the ATO developed in our group, which is in good agreement with other observations on the electrostatic binding of cyt c on various ATO materials.[260, 258]

5.2.4 Band assignment of Cytochrome c adsorbed on ATO

Minor shifts of up to four wavenumbers were found for the absolute maximum of the amide I band positions of cyt c (amide I at 1656 cm^{-1}; amide II at 1549 cm^{-1}) and his-cyt c (amide I at 1652 cm^{-1}; amide II at 1548 cm^{-1}), in Figure 5.3. Due to a strong overlap and large half-bandwidths of the underlying secondary structural components of the amide I and amide II vibrations, their exact band positions are determined by second derivative analysis of the ATR spectra, see Fig. 5.5. The observed values for each component are in line with those reported for adsorbed and solution cyt c, see Table 5.2. Thus, the large shift of four wavenumbers for the centered amide I band position observed only for the amide I band of cyt c may result from the significant differences in the band intensity distribution at 1656 cm^{-1} and 1643 cm^{-1}, which can be assigned to α-helix and random coil, respectively. These might derive from different binding interaction of cyt c and his-cyt c to the ATO surface. In addition, the intrinsic bandwidth for his-cyt c might be wider due to the artificially attached his-tag.

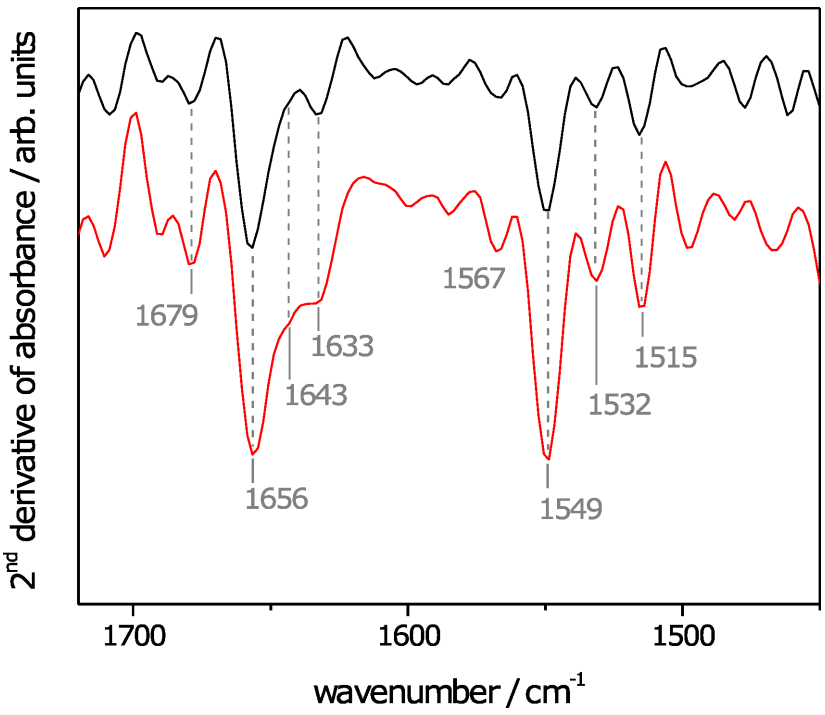

Figure 5.5: Second derivative of the corresponding ATR-IR spectra of cyt c (black) and his-cyt c (red) after 2h of adsorption on an ATO coated Si-prism.

Table 5.2: Assignment of the in Figure 5.5observed bands to the corresponding secondary structure elements and amino acid side chains

observed / cm^{-1} cyt c (his-cyt c)	assignment	designation	SEIRA values of cyt c on Au-SAM / cm^{-1} [232]	literature values / cm^{-1}	references
1679	amide I	β-turn	1680	1674 - 1675	[282, 283]
1656	amide I	α-helix and loop	1659	1650 - 1656	[282, 283]
1643	amide I	unordered/ β-sheet	1643	1641 - 1649	[283]
1633	amide I	extended β-strand	1633	1634 - 1636	[282, 283]
1567	amide II	β-turn	-	-	
1549	amide II	β-turn	1551	1547	[103, 6]
1515	tyrosine	in-plane ring vibration	1517	1517	[282, 283]

5.2.5 Conclusions

Antimony doped tin oxide (ATO) films were shown to be suitable, biocompatible electrodes for the immobilization of small redox proteins as exemplified on cytochrome c with *in situ* ATR-IR spectroscopy. The preservation of the native structure both for cyt c and his-cyt c after direct adsorption on the metal oxide surface could be verified by the similarity of the corresponding band positions of secondary structure elements and side chains with literature values of cyt c in solution as well as adsorbed species on SAM-coated Au-surfaces.[102] The adsorption of cyt c can be attributed to electrostatic interactions between the protein and the ATO surface. In the case of his-cyt c, a selective binding of the his-tag to the unmodified ATO nanoparticle surface can be established, which remains even under increasing ionic strengths of buffer solution. This

leads twice as high amide band intensities suggesting twice the protein coverage than in the case of an electrostatic binding. The difference in the binding behavior of cyt c and his-cyt c is even more pronounced when comparing their adsorption kinetics shown by different time regimes. While cyt c binds almost immediately to the ATO surface via electrostatic interactions, his-cyt c exhibits slower adsorption kinetics suggesting a more controlled and selective binding process. Complementary investigations for a better understanding of the different interaction types of cyt c and his-cyt c on ATO were performed by Dr. Stefano Frasca and Dr. Anabel Molero and are presently summarized for publication.

5.3 Tin-rich Indium Tin Oxide (ITO_{TR}) thin film electrodes for his-tagged horse heart Cytochrome c - immobilization strategy

5.3.1 Introduction

Among all different TCOs, ITO still is the most frequently used, due to its superior conductivity (range of 104 S cm^{-1}) and excellent transparency (up to 85%). For the introduction of the material see chapter section 2.3.3. In the field of bioelectrochemistry, ITO is often applied as a transparent electrode. Planar and mesoporous ITO have been used for the electrostatic and covalent attachment of small heme proteins23,24,11 as well as of bulky proteins such as photosystem II.[284, 285, 128, 286]

A promising low-cost alternative to commercial ITO (ITO; In_2O_3: Sn-doped with 10 mol% SnIV) is Tin-Rich ITO (ITO_{TR}), contains an In : Sn ratio of 1:1. Albeit the reduced amounts of In, ITO_{TR} exhibits comparable performance to commercial ITO in regard to its conductivity and transparency. ITO_{TR} has been originally developed as amorphous planar thin films via a single-source molecular precursor by Aksu et al. [143] as described in section 2.3.3. Recent works by Aksu et al. [143, 135] and Guiet et al. [146, 148, 147] describe the formation of nanostructured, porous ITO_{TR} via a soft-templating approach using block-copolymers. Particular beneficial of the one-step synthesis route developed by Guiet et al. in our group is the versatile tuneability with respect to composition, morphology, and pore size.[148] With respect to the variety of redox proteins regarding their surface properties and general size, the ITO_{TR} thin film synthesis approach describes a flexible and easy method for various designs of electrode platforms for individual protein adsorption. The formation of mesoporous structures offers high surface areas and thereby an increase of the protein loading, which is, in particular, interesting for biotechnology applications. However, several studies on the protein incorporation in mesoporous ITO or ITO_{TR} revealed some inactive fractions of the respective protein after immobilization. A fundamental understanding of the material-protein interaction is crucial, to achieve high loadings of functional protein.

In this work, planar, thin ITO_{TR} films were used as previously described (section 5.2) as a platform for the immobilization of the well-characterized redox protein cyt c.

The general applicability of mesoporous ITO_{TR} for the immobilization of biomolecules has been demonstrated by the stable binding and high loading of the redox protein cyt c within the mesoporous network under preservation of the native electrochemical properties.[134] However, higher protein loadings lead to a significant fraction of the adsorbed protein in an electrochemically inactive state. In this context, the authors suggested the occurrence of protein agglomeration within the pores of the material.

Even though, UV-vis absorption spectroscopy reveals information on the amount of adsorbed protein and the oxidation state of the heme iron, deeper insights with respect to an understanding of the protein-surface interplay are hard to derive from this technique. The effects of surface environment on the protein are crucial factors regarding the retention of its integrity upon immobilization. Conformational and orientational insights of the adsorbed protein are provided by more sophisticated spectroscopic vibrational techniques, such as IR and RR spectroscopy,

which are required for the optimization of the surface-protein binding. In this context, fundamental studies of such proteins immobilized on novel conducting platforms demand further spectro-electrochemical insights, which will be shown in chapter 6.

The following section discusses ITO_{TR} as a suitable electrode material with respect to its biocompatibility for the immobilization of cyt c and the electrocatalytic active enzyme, *Re* MBH, by ATR-IR spectro-electrochemistry and studies about a possible his-tag affinity on ITO_{TR} surfaces in comparison to those on ATO, *vide supra*.

5.3.2 ITO_{TR} thin film preparation and characterization

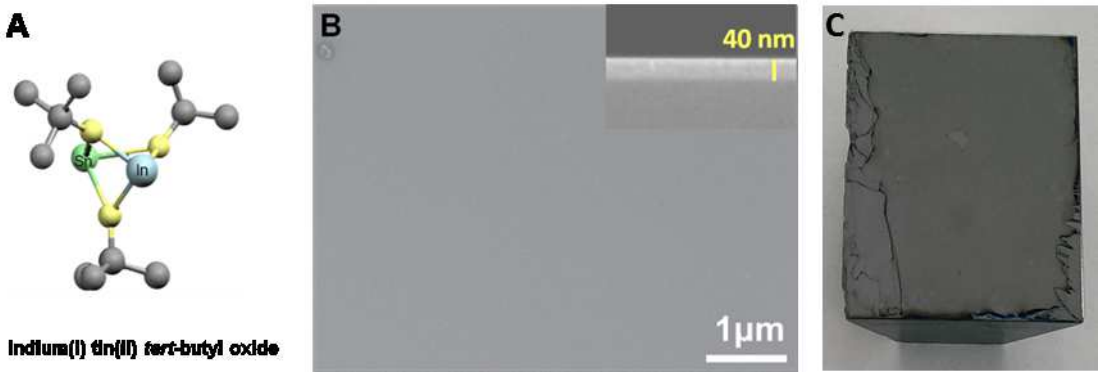

Figure 5.6: (A) Structure of the precursor indium(I)-tin(II)-tert-butyl oxide (ITBO), tin atom depicted in green, indium in light blue, oxygen atoms in yellow and carbon in black. (B) SEM image in low magnification and (C) photograph of an ITO_{TR}- film coated on a Si-prism using the procedure reported in the experimental part. Inset in (B) represents the cross section of an ITO_{TR}- film coated on a Si-wafer applying the same procedure.

Tin-Rich ITO (ITO_{TR}) was coated on the Si-prism to investigate its compatibility for protein interaction by ATR-IR spectroscopy. ITO_{TR} with an In to Sn ratio close to one is obtained by thermal decomposition of the molecular single-source precursor indium(I)-tin(II)-tert-butyl oxide (ITBO) (see Figure 5.6A). For the modification of the ATR-IR set-up, ITO_{TR} thin films were coated on the IR-transparent silicon prism, which acts here as the platform of the spectro-electrochemical cell as described in chapter 3. As shown in the HR-SEM micrograph in Figure 5.6B, thin films with a smooth surface and a homogeneous film thickness of approx. 40 nm ± 10 nm were obtained and occur as a light gray film on the surface of the Si-prism due to the light reflection as presented in Figure 5.6C. Coated on glass coated ITO films, ITO_{TR} films appear transparent. Conductivity measurements were performed on different ITO_{TR}-coated Si-prism samples (in the minimum for three different spots of each sample) exhibiting a mean resistivity of 0.04 Ω cm, i.e. a conductivity of 25 S/cm (commercial ITO: 104 S/cm). The sheet resistance of the films was determined by 4 point probe measurements resulting in an average sheet resistance of 1.4·105 Ω/□ after the first calcination under air and 7.2·104 Ω/□ after the second calcination under forming gas (10 % H_2, 90 % N2; flow rate ˜30 mL/min). Therefore, the synthesized films should in principle provide a sufficient conductivity and IR-transparency throughout the entire film for spectro-electrochemical studies.

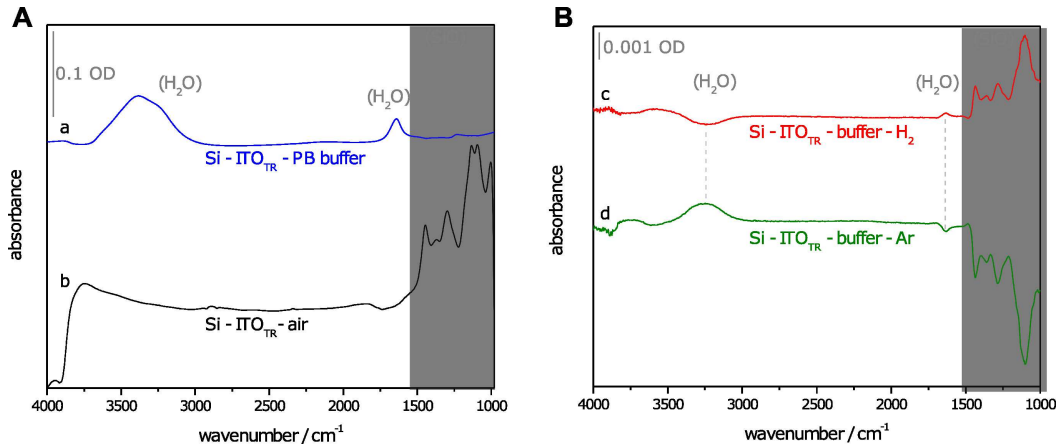

Figure 5.7: ATR-IR absorbance spectra of a bare ITO_{TR} film coated on a Si-prism. (A) black; reference spectrum: (a) ITO_{TR}-coated on Si-prism against air, and (b) after addition of potassium phosphate (PB) buffer (blue; b-a). (B) PB buffer on ITO_{TR}– PB purged with Ar (green; c-b) or with H_2 (red; d-c). Reference spectrum used for (a) monitored by uncoated Si-prism. For each spectrum from (b) to (d), the respective preceding spectrum was used as a reference spectrum.

In order to monitor the transparency of ITO_{TR} thin films in the mid-IR region, the IR spectrum of the bare Si-prism was measured before coating the prism with ITO_{TR} and subsequent to the calcination procedure as a reference in ATR mode. Figure 5.7A displays the Si-prism coated with ITO_{TR} thin film as prepared as a reference for all follow-up experiments. The black spectrum in Fig. 5.7A exhibits particularly strong bands below 1500 cm^{-1}, which can be assigned to Si-O vibrations. In general, Si-O surface layers are formed on Silicon within few minutes under exposure to air and can be even inherently existent in the Si-prism. The observed Si-O bands may also occur due to variations in the amount of Silicon oxide species between reference and sample spectrum, which were taken prior and after the ITO_{TR} film preparation, respectively. Especially the calcination step under air after the precursor film deposition may favor the formation of a Si-O layer. Since the Si-prism has to be disassembled and readjusted in the ATR-set up for the ITO_{TR} film coating, the spectral changes compared to the prior monitored reference spectrum may appear even stronger due to fluctuations of the measured area. Notably, the ITO_{TR} film exhibits a high overall transparency in the recorded mid-IR region from 3800 – 1000 cm^{-1}. Even if we have to account for possible spectral SiO contribution, the most interesting region for protein backbone investigations (in term of secondary structure) above 1500 cm^{-1} does hardly display any absorption. Thus, the spectrum recorded after the addition of potassium phosphate (PB) buffer just displays the typical water vibrations, such as a broad O-H stretching vibration at around 3400 cm^{-1} and the corresponding bending vibration at 1633 cm^{-1}. Moreover, the described transparency in the observed IR region is preserved upon gas saturation of the buffer solution with Ar and H_2, thus excluding significant baseline shifts upon gas exchange experiments. Only some spectral changes below 1500 cm^{-1} are observed. These can be attributed to temperature fluctuations occurring between the recording of background and sample spectrum; fluctuations which might also be related to the gas purging of the electrolyte. Thus, the prism inherent Si-O absorptions can be detected to some extent, see Figure 5.7B. This may even occur under temperature control by a thermostat.

5.3.3 Immobilization of horse heart Cytochrome c and his-tagged Cytochrome c on ITO_{TR}

Taking advantage of the transparency for IR light of the thin ITO_{TR} film(s), the protein adsorption during the immobilization process was monitored by IR spectroscopy in the ATR mode in the Kretschmann configuration. To compare the "performance" of the ITO_{TR} thin films in comparison to the previously studied ATO ones (section 5.2), two modifications of the heme protein cytochrome c (cyt c), i.e. cyt c equipped at its N-terminus with the his-tagged (his-cyt c) and non-tagged cyt c (cyt c) were used as probe proteins. Indeed, cyt c exhibits strong and well known vibrational bands, allowing to monitor the adsorption and state of cyt c on ITO_{TR} by ATR-IR.

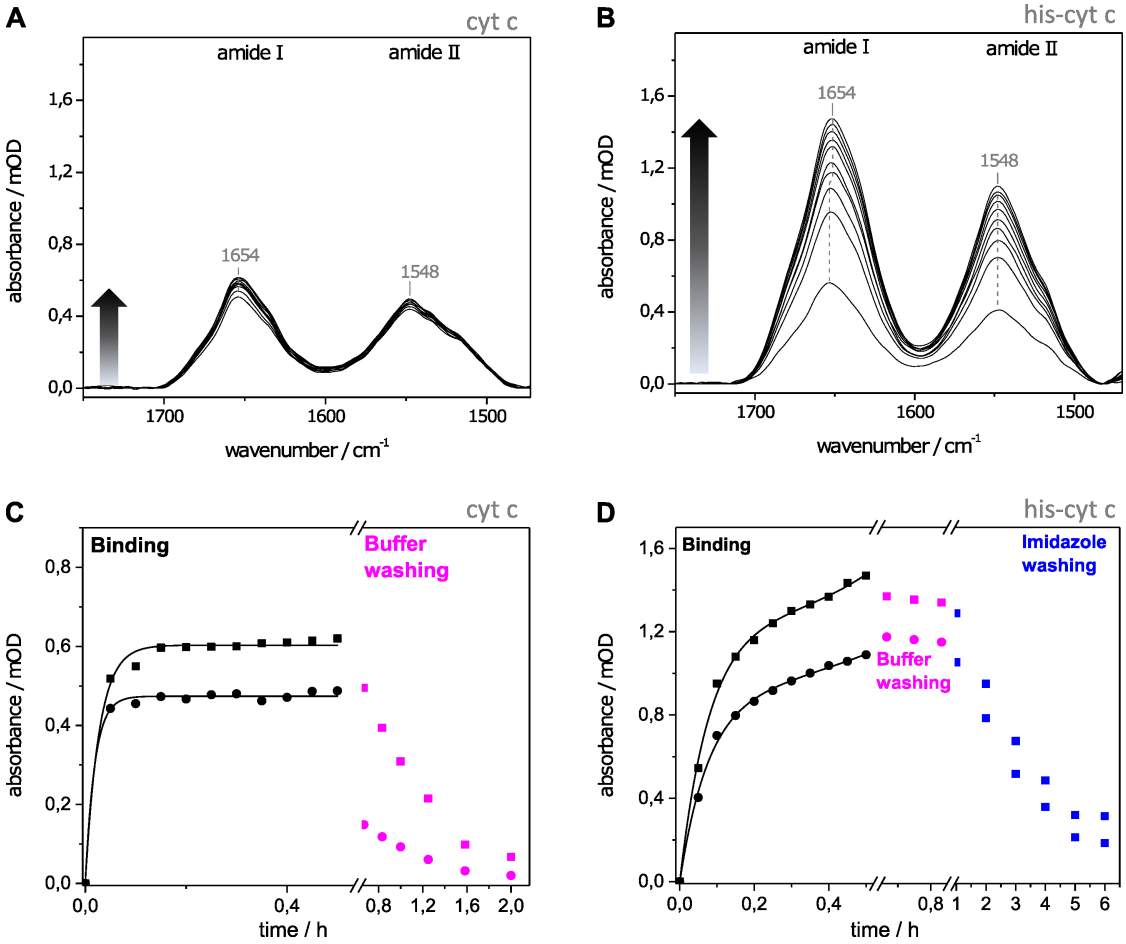

Figure 5.8: ATR-IR spectra of (A) cyt c and (B) his-cyt c during adsorption on an ITO_{TR} surface. Respective time courses of amide I (■) and amide II (●) band intensities for cyt c (C) and his-cyt c (D) upon ITO_{TR} surface adsorption and various washing procedures. Nonspecific binding is investigated by repeated washing with buffer solutions (pink data points). Only washing cycles with 750 mM imidazole buffer lead to a significant desorption of the specifically bound his-tagged cyt c (blue data points). (C) Monoexponential fits with $A = A_0 - A_1 \exp(-t/\tau_1)$ to the time courses of cyt c specific intensities and (D) Biexponential fits with $A = A_0 - A_1 \exp(-t/\tau_1) - A_2 \exp(-t/\tau_2)$ to the time courses of his-cyt c characteristic absorptions were carried out in the time period $0 < t < 30$ min and are depicted as black lines for binding process.

Figure 5.8A and B display the corresponding ATR-IR spectra of immobilized proteins recorded within 30 min of incubation. The bands located at 1654 cm^{-1} and 1548 cm^{-1} are assigned to

the amide I and II band, respectively, both arising from vibrations of the backbone structure of the protein (described in section 2.2.2.4). After 30 minutes of immobilization, the ATR-IR band intensities of the immobilized his-cyt c are about three times higher than those obtained for non-tagged cyt c, indicating a higher protein loading of the his-tagged protein on the ITO_{TR} surface (see Figure 5.8A,B). In both cases, the protein surface coverage was estimated by evaluating the protein concentration of the incubation solution by UV-Vis spectroscopy before and after incubation of the ITO_{TR} surfaces (see Figure 5.9).

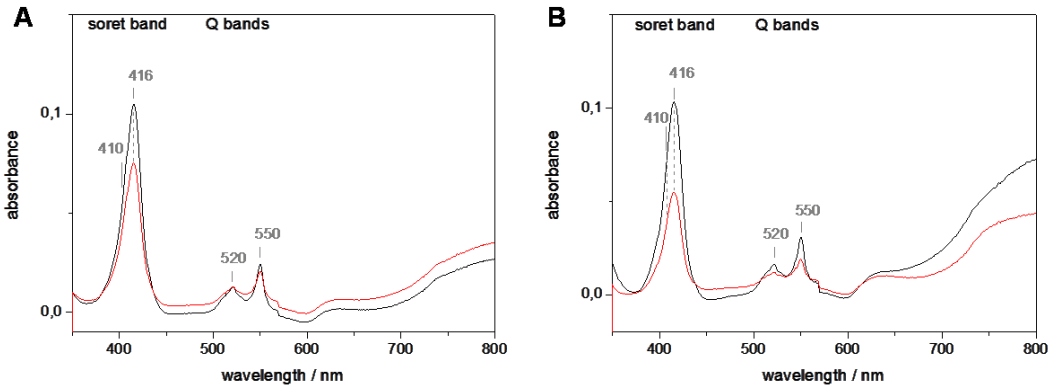

Figure 5.9: UV-Vis spectra of (A) cyt c and (B) his-cyt c solutions before (black) and after (red) 30 minutes of incubation of and ITO_{TR} coated Si-prism for ATR-IR measurements.

Figure 5.9 shows the corresponding UV-Vis spectra of the cyt c and his-cyt c solutions (7 µM protein in PB buffer) used for incubation of ITO_{TR}-covered Si-prism. The solutions were measured by UV-Vis spectroscopy just before and after incubation. From the intensity loss of the soret band at 416 nm the amount of surface adsorbed protein was estimated relative to the known concentration of protein in solution (7 µM/mL). In line with the IR results, a lower surface coverage of 4.5 pmol/cm² was determined for cyt c adsorption on ITO_{TR}, while an approx. three times higher surface coverage of about 16 pmol/cm² was determined for his-cyt c. Taking into account the theoretical maximum coverage for a cyt c monolayer (i.e. 15 pmol/cm²)[1] a submonolayer coverage was obtained for cyt c, while in the case of his-cyt c a coverage close to a monolayer was achieved.[287]

Furthermore, both cyt c and his-cyt c spectra display slightly shifted soret bands at 416 nm and Q bands at 520 nm and 550 nm, just as reported for the reduced state of native cyt c. This indicates that the proteins were purified in the reduced state.[288] To minor extends the oxidized species is covered by the spectra reduced spectra with soret bands at 410 nm and a broader band at 530 nm.

Kinetic analysis of the amide I and amide II band intensity evolution of cyt c (Fig. 5.8C) exhibit a fast growth; growth which can be fitted by a mono-exponential function. This suggests a fast attainment of the saturation level of protein at the surface, which is mostly reached within the acquisition time of the first spectrum. Final cyt c absorbance values of 0.6 mOD and 0.47 mOD are observed for amide I and amide II band intensities, respectively. In contrary, the kinetic analysis of his-cyt c adsorption reveals a biexponential growth and three times higher

[1] determined by using the size of horse heart cytochrome c determined by crystal structure analysis

final intensities for amide I and amide II intensities accounting for 1.14 mOD and 0.88 mOD, respectively. Both, cyt c and his-cyt c on ITO_{TR} exhibit constant amide I/amide II ratios of about 1.3 within the entire adsorption time. This correlates well with the previously observed ratio of cyt c and his-cyt c on ATO materials (*vide supra*) and also corresponds to the ratio recorded for native cyt c in solution.

Indications for the presence of a different binding mechanism of the tagged and untagged protein on the ITO_{TR} surface were provided by selective desorption experiments. Consecutively after the adsorption, desorption experiments carried out on untagged cyt c immobilized on planar ITO_{TR} (Fig. 5.8C, pink) show a complete desorption of the untagged protein from the ITO_{TR} surface already by a buffer exchange with a buffer of weak ionic strength (10 mM Tris buffer). As can be seen in Fig. 5.8, buffer exchange leads to a continuous and almost complete amide bands intensity loss (accounting for 95%). This points to a weak electrostatic binding between the untagged cyt c and the ITO_{TR} surface and agrees well with the in literature formulated hypothesis of a weak electrostatic interaction between native (un-tagged) cyt c and commercial ITO electrodes and is analog to our observations regarding the cyt c–ATO interaction, *vide supra*. In contrast, the same desorption experiment performed on his-cyt c adsorbed on ITO_{TR} (Fig. 5.8D) shows only a slight decrease of the IR intensities of the amide I and amide II bands. Even under usage of a high ionic strength buffer containing saturated KCl, the protein remained adsorbed at the metal oxide surface. These results point to a strong and non-electrostatic protein-surface interaction between his-cyt c and the ITO_{TR} surface. Only buffer exchanges with buffers containing high concentrations of imidazole (750 mM), a high affinity ligand for metal complexation, lead to a complete disappearance of the amide bands intensities. As such, a selective and quantitative desorption of his-cyt c is verified under the addition of imidazole as previously observed in the case of his-cyt c immobilized on planar ATO. This strongly indicates that, in contrast to the weak electrostatic cyt c-ITO_{TR} surface interaction, a strong hexa-histidine mediated complex-compound interaction between the his-cyt c and the ITO_{TR} surface take place. In this respect, complexation of metal ions on the ITO_{TR} surface such as Sn^{4+}, Sn^{2+} or In^{3+} by the hexa-histidine tag as for instance known for Ni^{2+} cations might be at the origin of this interaction. So far, complexes with Ni^{2+}, Zn^{2+}, Co^{2+} or Cu^{2+}[289] are known for highly selective interaction with histidine-tagged proteins, as well as Fe^{3+} complexes.[290] Fe^{2+} [291] exhibits also an affinity to imidazole binding, as well as Sn^{2+} and very rarely In^{3+} complexation is found, with only slightly lowered affinity towards his-tagged proteins.[292, 293, 294, 295] Also, this would explain why only imidazole could substantially remove the tag bound protein. Thereby, a binding via the nitrogen of the imidazole group to exposed metal centers at the ITO_{TR} surface can be assumed.

To clarify the necessity of exposed In^{3+} and Sn^{4+} ions enabling the coordination for the here observed his-tag affinity, a SiO_2 surface was incubated with his-cyt c. A thermally oxidized (calcination under air) Si-prism under air usually forms an amorphous silicon dioxide (SiO_2) surface layer at the prism surface. In contrast to the hydrophobic H-terminated Si-prism (see section 5.2.1), this oxygenated Si surface consists of siloxane (Si-O-Si) and silanol (Si-OH) groups and in contact with aqueous solutions, the outermost layer is hydrated to form predominantly silanol groups (SiOH).[296] The amphoteric property of such a silica surface is defined through deprotonation and protonation of its surface silanol groups, which can be classified into two groups with in-plane and outer-plane hydrogen bonds, related with the observation of two pKa values at around 5 and 7.5 to 9, respectively.[104, 297] Hence, it can be assumed that under neutral and basic conditions, the silica surface is neutral or slightly negatively charged. In this

regard, the SiO_2 surface should offer weak electrostatic binding sites for positively charged his-cyt c, and was therefore used to probe the corresponding protein-surface interaction without the presence of any metal ion for a selective complexation.

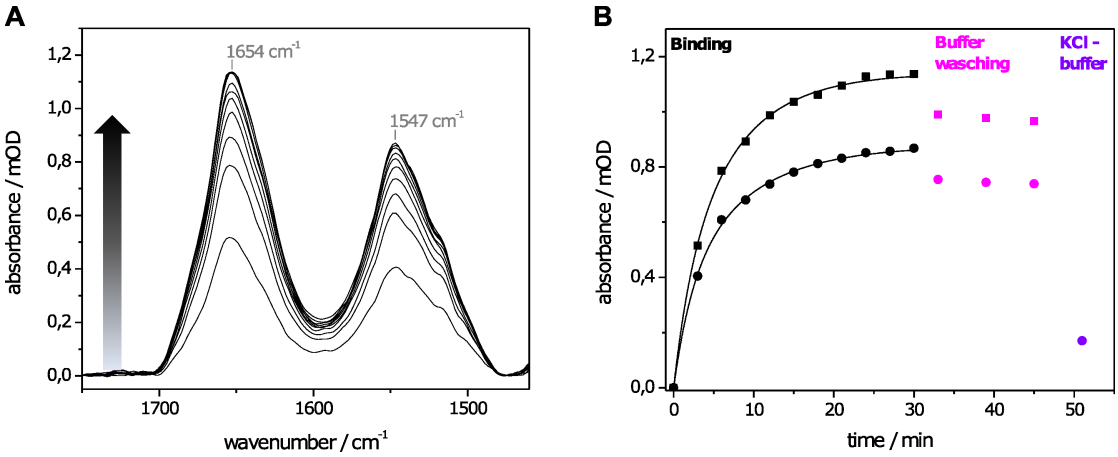

Figure 5.10: (A) ATR-IR spectra of his-cyt c recorded upon surface immobilization on a thermally oxidized Si-prism and (B) kinetic analysis of the adsorption monitored by the marked amide I (■) and amide II (●) band intensities during this process (black) and during desorption (pink and violet). Fractions of nonspecific binding are detected by repeated buffer washing procedures with phosphate buffer (pink) and with 3M KCl PB solution (violet). A biexponential fit with $A = A_0 + A_1 \exp(-t/\tau_1) + A_2 \exp(-t/\tau_2)$ was applied in the time period of $0 < t < 30$ min and is depicted as black line for the binding process.

Table 5.3: Kinetic analysis of selected amide I and amide II band intensities*

amide band	A_0 (mOD)	A_1 (mOD)	τ_1 (min)	A_2 (mOD)	τ_2 min
cyt c on ITO_{TR}					
1654 cm^{-1}	0.60 ± 0.23	0.60 ± 0.02	1.65 ± 0.16		
1547 cm^{-1}	0.47 ± 0.04	0.47 ± 0.01	1.13 ± 0.14		
his-cyt c on ITO_{TR}					
1654 cm^{-1}	1.49	1.25 ± 0.13	4.76 ± 0.72	0.27 ± 0.10	13.10 ± 3.35
1548 cm^{-1}	0.88	0.51 ± 0.08	8.70 ± 0.84	0.36 ± 0.05	2.34 ± 0.54
his-cyt c on SiO_x					
1654 cm^{-1}	1.15	0.39 ± 0.16	2.4 ± 0.83	0.76 ± 0.16	7.64 ± 0.85
1547 cm^{-1}	0.89	0.41 ± 0.07	2.52 ± 0.43	0.48 ± 0.07	9.67 ± 0.87

*Results of fitting the monoexponential function ($A = A_0 + A_1 \exp(-t/\tau_1)$) for native cyt c to the time course of its amide I (1654 cm^{-1}, $R^2 = 0{,}992$) and amide II (1547 cm^{-1}, $R^2 = 0{,}99466$) band intensities; respective fitting results of biexponential function ($A = A_0 + A_1 \exp(-t/\tau_1) + A_2 \exp(-t/\tau_2)$) for his-cyt c binding on ITO_{TR} film with amide I (1654 cm^{-1}, $R^2 = 0{,}996$) and amide II (1548 cm^{-1}, $R^2 = 0{,}99649$) band intensities and also for his-cyt c immobilization on oxidized Si-prism with amide I (1654 cm^{-1}, $R^2 = 0{,}9994$) and amide II (1548 cm^{-1}, $R^2 = 0{,}9988$) band intensities. All applied in the time period $0 < t < 30$ min.

Figure 5.10 displays the successful adsorption of his-cyt c on the oxidized Si-prism displayed by the steadily increasing amide band intensities recorded during the underlying binding process as

a function of time. Before the washing with 3M KCl, a buffer exchange with the 10 mM Tris buffer was carried out, which lead to a slight loss of amide I and amide II band intensities. After subsequent washing with 3M KCl buffer solution, the amide band intensities disappear almost entirely. Hence, a weak, electrostatic interaction of his-cyt at the oxidized interface is observed. The displayed adsorption interaction differs clearly from the previously observed interaction between his-cyt c and ITO_{TR}, which remained unaltered even under exposure to buffer solutions with higher ionic strengths. This indirectly verifies the specific affinity of the histidine tag for on the ITO_{TR} surface and in particular for the exposed surface cations such as Sn^{4+}, Sn^{2+} and In^{3+}. Considering that for both ATO and ITO_{TR} a his-tag affinity for the metal oxide surface could be revealed and that both oxides expose Sn^{4+} and possibly Sn^{2+} surface cations, it is more than likely that the actual binding occurs via the tin centers rather than the In^{3+} centers.

The different binding mechanism of the tagged and non-tagged protein on the ITO_{TR} surface is also reflected by the observed time evolution of amide band intensities upon immobilization as shown in Figure 5.10. Two different processes can be discriminated as a result of varying surface interactions. As expected for an unspecific binding, cyt c binds immediately to the surface, which is perceived as a fast increase of the amide band intensities until a saturation level is reached at 0.6 mOD for the amide I species. Table 5.3 displays the monoexponential fit applied to the obtained absorption intensities of amide I and amide II bands, exhibiting a time constant of τ = 1.65 min for amide I. This fast and mono-exponential adsorption course is often described by the Langmuir isotherm model. It is based on the assumption that only a monomolecular layer of non-interacting adsorbent molecules is formed at the surface of interest with all adsorption sites on this surface exhibiting equal adsorption energies. In other words, the adsorption of cyt c on ITO_{TR} can be assumed as a fast diffusion limited process which occurs without any slow preorientation processes in electrostatic interaction close to the surface before adsorption. Such an adsorption process would presumably result in a random surface binding of the protein with a high distribution of different protein orientations at the surface. In fact, this assumption will be further verified in chapter, *vide infra*.

In contrast to cyt c, his-cyt c shows a continuous amide band increase over the complete adsorption time, which can be described by two different adsorption growth phases within the observed time frame. An appropriate fit for the his-cyt c adsorption kinetic could be accomplished with a bi-exponential model. The first absorption regime is thereby the main and faster process with τ_1 = 4.76 min, yielding 86% of the total band intensity. This correlates with a comparable time range observed already for his-tag binding on planar ATO surfaces and differs from the slower time constant for unspecific cyt c binding on ITO_{TR}. The second, slower process is only related with an addition increase of 9% with respect to the overall adsorption intensity, exhibiting a time constant of τ_2 = 13.1 min. Subsequent washing procedures involving buffer exchanges carried out to remove unspecifically bound protein lead to a slight decrease of the amide band intensities. This is in line with desorption of a minor protein fraction, which is unspecifically bound to the surface.

5.3.4 Band assignment of Cytochrome c on ITO_{TR}

As displayed in Figure 5.11, cyt c immobilized electrostatically on ITO_{TR} and his-cyt c immobilized on oxidized Silicon reveal exactly the same band positions in the second derivatives of the absolute ATR-IR spectra. For his-cyt c coordinatively bound to the ITO_{TR} surface via the his-tag however, slight shifts for the bands at 1554 cm^{-1} and 1635 cm^{-1} with maximal 2 wavenumbers

are observed in the amide I region.

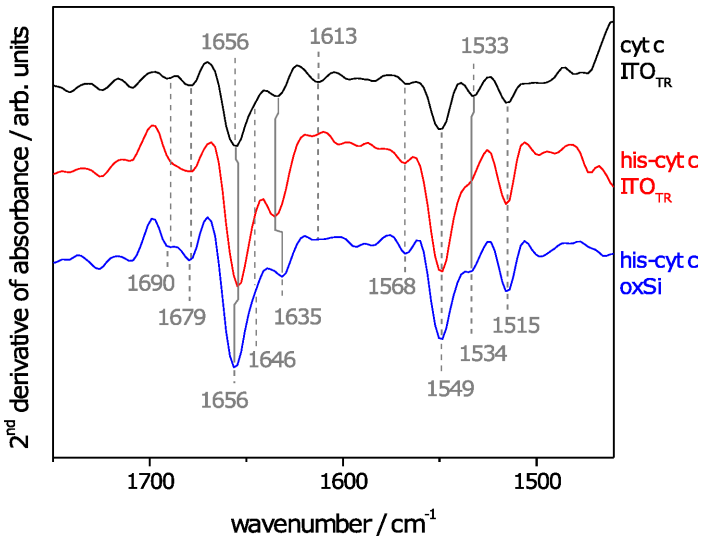

Figure 5.11: Second derivative of the ATR-IR spectra of cyt c (black) and his-cyt c (red) on ITO_{TR} and his-cyt c on an oxidized Si-prism (blue) after 30 min of adsorption.

Table 5.4: Assignment of the observed amide I and II bands related to secondary structure elements and side chains*

observed / cm^{-1} cyt c on ITO_{TR}	observed / cm^{-1} his-cyt c on ITO_{TR} and on oxidized Si	assignment	designation	SEIRA values of cyt c on Au-SAM / cm^{-1} [232]	literature values / cm^{-1} [283, 282]
-	- (1690)	amide I	β-turn	1680	1674 - 1675
1679	1679 (1679)	amide I	β-turn	1680	1674 - 1675
1656	1654 (1656)	amide I	α-helix and loop	1659	1650 - 1656
1646	1646 (1646)	amide I	unordered/ β-sheet	1643	1641 - 1649
1633	1635 (1632)	amide I	extended β-strand	1633	1634 - 1636
1613	- (-)		β-sheet		
1568	1568 (1568)	amide II	β-turn	-	-
1550	1549 (1549)	amide II	β-turn /alpha helix	1551	1547
1533	1534 (1534)	amide II			
1515	1515 (1515)	tyrosine	in-plane ring vibration	1517	1517

* references of literature values according to assigment in table 5.2.

5.3.5 Conclusion

It was shown that ATR-IR spectroscopy is a powerful tool for monitoring the adsorption processes of cyt c and his-cyt c on planar ITO_{TR} electrodes in order to understand the prevailing interactions between the proteins and the metal oxide surface. With moderate absorbance intensities in the range of 0.6 to 1.6 mOD, the amide I and amide II bands of the protein exhibited a comparable spectral pattern to previously reported ATR-IR works of cyt c on conductive surfaces, including those involving a surface enhancement effect (SEIRA). These findings prove that the mid-infrared (MIR) transparency of ITO_{TR} thin film coatings allows for a proper probing of adsorbed biomolecules even at submonolayer coverage. Moreover, the significantly increased band intensity of his-cyt c indicates a high binding affinity of the tagged protein towards the ITO_{TR} surface in comparison to the native, non-tagged cyt c. Also, the different adsorption and desorption behaviors observed for cyt c and his-cyt c clearly point to a change in interaction mechanism of tagged vs. non-tagged cyt c. While cyt c could be removed using only buffer solutions with high ionic strength, his-cyt c was only removed upon addition of highly concentrated imidazole solution. The latter fact points towards a strong interaction between the hexa-histidine tag and the ITO_{TR} surface. This selective binding type enables a direct, stable and reversible surface attachment without the requirement of any surface modifications, by for example Ni-Nitrilotriacetic acid (Ni-NTA) complexes. The ability to perform ATR-IR spectroscopy on transparent metal oxide coatings allows the monitoring of the adsorption behavior of a protein on these metal oxide thin films (even at sub-monolayer concentrations) as well as probe protein-metal surface interaction and compatibility. Hence, this setup provides a prospective powerful tool to characterize native secondary structure elements of proteins and their interaction with TCO surfaces.

Chapter 6

Spectro-electrochemical insights into Membrane-Bound [NiFe] Hydrogenase of Ralstonia eutropha on ITO_{TR} electrodes

6.1 Introduction

Despite the central role semiconductor-electrocatalyst interfaces play in recent research, the energetics and charge-transfer processes at these interfaces are only poorly understood to date. Especially, since the experimental tools for a direct measurement of the interfacial processes are lacking. Although the theory of semiconductor-electrolyte interfaces is well developed under dark conditions (see section 2.4.3) as well as under photoexcitation,[298] there has been only limited work in this context regarding surface-attached electrocatalysts. The observable current−voltage responses of semiconductor-electrocatalyst systems do require profound studies on a molecular level for an accurate interpretation. So far, previously established models do not involve the electrocatalytic process at the electrocatalyst-electrolyte interface independently from the charge separation process at the semiconductor-electrolyte interface, e.g. Gerischer model, see section.2.4.3.1 However, the latter model compromises only a simplified, partial aspect of a more complex interplay of the different compounds of the semiconductor-electrocatalyst-electrolyte systems.

Recently, works on enzyme catalysis performed on TCO semiconductors under exclusion of light revealed unexpected results, namely, high catalytic efficiencies even when product inhibition takes place and a shifted bias of the underlying catalytic reaction explained by the particular electronic properties of the semiconductor in direct electric contact with the enzyme of interest. Furthermore, electrochemical investigations on an [NiFeSe] hydrogenase adsorbed on n-type semiconductor film electrodes (TiO_2, CdS) were carried out by Bachmeier et al. [299] For both cases an enhanced H_2-production of the adsorbed hydrogenase is reported, even under highly restrictive product inhibition, i.e. under H_2-saturated electrolyte. The authors propose a junction between hydrogenase and semiconducting material for this remarkable effect by claiming an enhanced interfacial ET at the semiconductor electrode-hydrogenase interface, section 2.4.3.[299] A similar effect, namely, an enhanced hydrogen evolution reaction (HER) of the [FeFe] hydrogenase from Clostridium acetobutylicum was reported by King et al, when the enzyme was adsorbed on semiconducting carbon nanotubes.[300]

These findings emphasize the need for fundamental investigations by means of spectro-electrochemical approaches to obtain a fundamental understanding of the impact on the hydrogenase upon semiconductor-enzyme interactions, which is so far lacking. In this context, IR spectro-electrochemistry is a powerful tool to study and optimize the adsorption of hydrogenase for a fast and direct interfacial electron transfer as well as to study the prevailing redox states of the active site located close to the semiconductor-enzyme junction.

In the previous section a selective binding of his-tagged cyt c to metal oxide surfaces such as ITO_{TR} and ATO via a hexahistidine-tag extension, attached to the N-terminal of the protein (see section 5.4) could be verified.

The attachment of a polyhistidine-tag (polyhis-tag) to either the C-terminus or N-terminus of a protein is perhaps the most commonly used method in recombinant protein technology to facilitate their purification. Unlike other fusion protein strategies, the polyhis-tag approach can be applied to proteins in their native states as well as to small peptides. When used in protein based (bio)technological applications, this strategy effectively combines the steps of purification and his-tag mediated surface binding, as simultaneously a specific anchor was introduced. The corresponding bond via the coordination of histidines to a metal cation (see section 5.2.3; Table 5.4) is highly stable and can be only reversed in the presence of high concentration of competing

ligands such as imidazole. With the previously discussed successful immobilization of his-tag cyt c on ITO_{TR} and ATO (see chapter 5), the his-tag mediated direct binding with these metal oxide semiconductor surfaces and in particular with ITO_{TR} is extended to a far more complex enzyme, i.e. to the his-tagged membrane bound oxygen-tolerant hydrogenase from Ralstonia eutropha (his-MBH), in order to establish enzyme catalysis upon this type of his-tag mediated interaction.

The critical questions using such a large bio-electrocatalysts as demonstrated in chapter 4 are addressed in the following section. The focus lies on (i) the kinetic of enzyme immobilization, (ii) the mode of enzyme binding, and (iii) the enzyme-electrode interaction under turnover conditions. The latter is of particular interest since semiconductor-hydrogenase interactions are reported to enhance the specific catalytic activity of hydrogenases. Depending on the hydrogenase reaction (HER or HOR) and type of semiconductor (p- or n-type), the electron transfer rate (see section 2.4.3) can be enhanced with [270] or without light [299, 300].

The enhanced enzyme activities in response to semiconductor-enzyme interactions and the altered reaction biases will be investigated for MBH-ITO_{TR} systems and models for possible semiconductor–enzyme interactions explaining enhanced catalysis will be discussed.

6.2 Adsorption behavior of his-tagged MBH on ITO_{TR}

The adsorption of his-MBH on ITO_{TR} thin films was studied. Hereby, ATR-IR spectroscopy allows gaining insights into the enzyme's integrity as well as the state of the active site upon interaction with the ITO_{TR} surface. The direct binding interaction between the enzyme and the ITO_{TR} electrode is shown by desorption experiments, which verify the selective his-tag binding. Concomitant AFM measurements allowed an estimation of the enzyme coverage.

6.2.1 ATR-FTIR on his-tagged MBH on ITO_{TR}

Taking advantage of the high binding affinity of his-tags towards the ITO_{TR} surface, as shown in section5.8, a far more complex and highly interesting enzyme for biotechnological applications, i.e. the his-tagged membrane-bound [NiFe] hydrogenase (his-MBH) from Ralstonia eutropha (*Re*), was investigated for selective his-tag affinity binding on the ITO_{TR} surface.

Via facile variation in the purification process, the oxygen-tolerant membrane-bound hydrogenase from Ralstonia eutropha (*Re*) was engineered with a his-tag anchor (his-MBH) for selective his-tag binding directly on the ITO_{TR} surface. Figure 6.1A exhibits ATR-IR spectra of his-MBH upon its adsorption on a planar ITO_{TR} surface in the amide I and II band region (for SEM images of the planar surface see 5.3.2; Fig. 5.6). Within the adsorption time of 30 minutes, the corresponding amide I and amide II band intensities at 1650 cm^{-1} and 1548cm^{-1}, respectively, were monitored to elucidate the adsorption kinetics (Fig. 6.1B). By fitting a biexponential function to the data, two adsorption processes, a fast and a slow one, terminated at 10 and 30 minutes, respectively, were detected (see Table6.1). The completion of the first step of the biexponential adsorption process is indicated by a vertical dashed pink line in Fig. 6.1B, which seems essential for the activity of the ITO_{TR}-immobilized his-tagged MBH as demonstrated below (see Fig. 6.4).

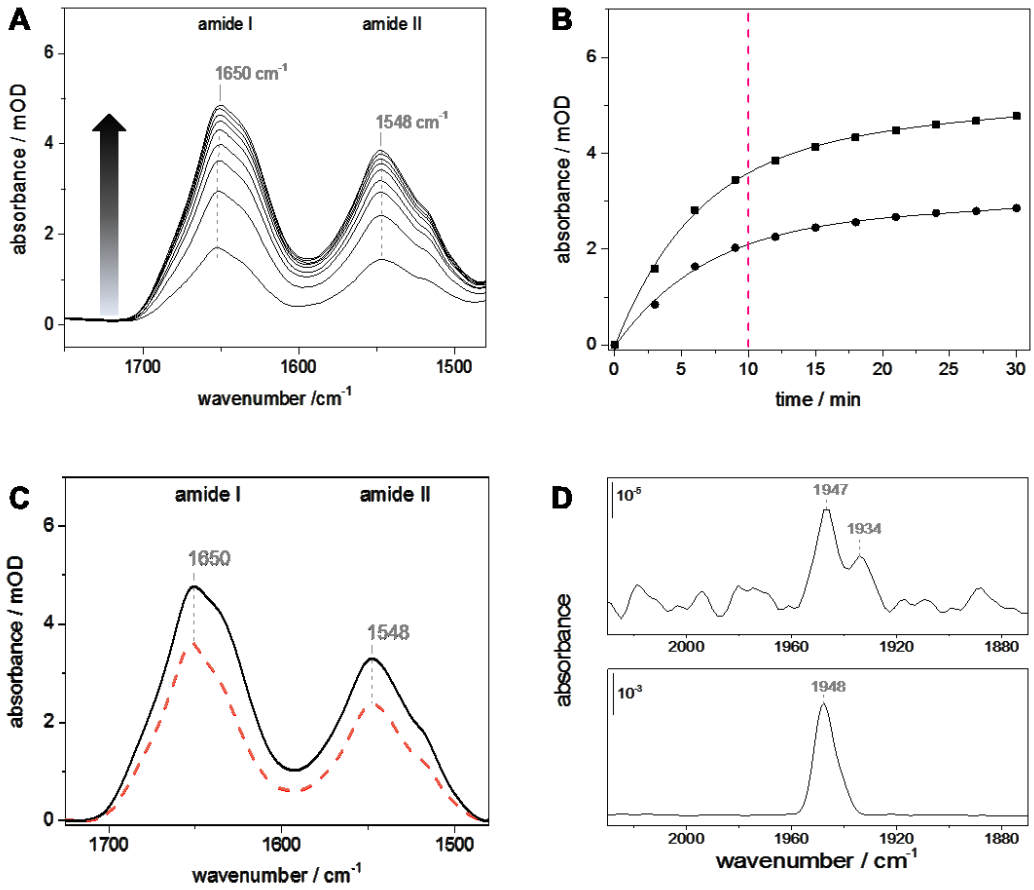

Figure 6.1: (A) ATR-IR spectra of his-MBH immobilized on planar ITO_{TR} within 30 min in 10 mM PB buffer at pH 7. (B) Binding kinetics monitored by the time course of the amide I (■) and amide II (●) band intensities (black). Biexponential fit ($A = A_0 + A_1 \exp(-t/\tau_1) + A_2 \exp(-t/\tau_2)$) was applied (results see Table 6.1). The dashed vertical pink line describes the time at which the first exponential growth is mostly completed. (C) ATR-IR spectrum of his-MBH on ITO_{TR} after completion of first (dashed pink) and second (final; solid black) exponential adsorption process, i.e. after 10 min and after 30 min, respectively; evaluated from results of biexponential fit. (D) Spectral region of the active site of ITO_{TR}-adsorbed his-MBH (top) and the related IR transmission data of his-MBH in bulk solution (bottom).

Table 6.1: Adsorption kinetics of amide I and amide II*

amide band	A_0 (mOD)	A_1 (mOD)	τ_1 (min)	A_2 (mOD)	τ_2 min
his-MBH on ITO_{TR}					
1650 cm^{-1}	4.78	3.77 ± 0.77	6.57 ± 0.49	1.31 ± 0.79	20.31 ± 8.52
1548 cm^{-1}	2.87	2.51 ± 0.81	6.70 ± 1.58	0.56 ± 0.08	26.22 ± 8.26

*Results of fitting the biexponential function $A = A_0 + A_1 \exp(-t/\tau_1) + A_2 \exp(-t/\tau_2)$ to the time course of the amide I (1650 cm^{-1}, R^2 = 0,99703) and amide II (1548 cm^{-1}, R^2 = 0,99703) band intensities of his-MBH during the entire adsorption process ($0 < t < 30$ min).

The time regimes determined for his-tag-MBH on ITO_{TR} (see Table 6.1) are similar to the previously determined time regimes for his-cyt c binding on ITO_{TR} (see section 5.3.3).

Figure 6.1C shows the amide I and II absorption bands of his-MBH immobilized on ITO_{TR} after 10 min and 30 min of immobilization, pink and black curves, respectively. In both cases, high IR band intensities (3.1 mOD and 4.8 mOD, respectively) were obtained, indicating a sufficient surface coverage of the enzyme on the ITO_{TR} surface for IR detection. Although no plasmonic surface enhancement is expected on ITO_{TR} surfaces in comparison to nanostructured Au surfaces (for a detailed discussion see chapter 7), the active site of the ITO_{TR}-immobilized his-MBH could still be monitored in the typical region characteristic for at least the CO ligand vibrational modes of the [NiFe] catalytic center (Figure 6.1D, upper graphic).

As can be seen in Figure 6.1D, two different redox states can be distinguished. The band at 1947 cm^{-1} is unambiguously assigned to the CO ligand present in the oxidized Ni_r-B state, which is ascribed to a reversibly inactivated state of the active site. The band at 1934 cm^{-1} in turn might be correlated to the CO stretching vibrations may be ascribed to $Ni_{r/a}$-S or Ni_{ia}-S state, representing a slightly more reduced redox state of the active site, with an EPR silent Ni^{2+} species harboring presumably a OH^- or an H_20 in the bridging position to the Fe^{2+}, or a modified Ni_{ia}-S form which appears irreversibly inactivated with respect to hydrogen exposure.[204, 5] For comparison, a solution spectrum in the spectral region characteristic for the active-site of his-MBH is shown in Fig. 6.1D (bottom graphic). The analysis of the solution spectrum of the protein batch used for immobilization revealed in line with literature reports, the presence of Ni_r-B in solution as well as of another typical and Ni_u-S subspecies (shoulder at 1942 cm^{-1}) in minor concentrations.[5] Hence, the additional state at 1934 cm^{-1} seems to be formed or at least enriched upon enzyme interaction with the ITO_{TR} surface after immobilization of the his-tagged MBH on ITO_{TR}.

6.2.2 AFM studies on his-tagged MBH coverage

AFM measurements confirm a compact coverage of his-MBH on the ITO_{TR} surface after 30 min of immobilization (see Fig. 6.2). AFM images are shown before and after enzyme incubation in Figure 6.2A and 6.2B, respectively. The planar ITO_{TR} exhibits an intrinsic surface structure with a low roughness due to its porosity with pore sizes of ca. 2 nm (Fig. 6.2A), possibly originating from the thermally induced decomposition during calcination of the organic fraction of the indium(I)-tin(II)-tri-tertbutyloxide (ITBO) precursor used for ITO_{TR} synthesis. Figure 6.2B presents the AFM image of an ITO_{TR} surface after 30 min of his-MBH immobilization, which obviously differs from the bare ITO_{TR} by the presence of large spherical units; units which can be attributed to his-MBH molecules. The corresponding diameter of a single unit can be determined from the lateral periodicity in the corresponding AFM height-profile to approximately 10.7 nm (Figure 6.2C). Consistently, similar unit sizes were determined by AFM for *strep*-MBH adsorbed on SAM-modified Au electrodes (see section 4.2.3). The size determination could not be accomplished by using the height in the z-profile, due to its limited resolution, which is given by the width of the AFM tips used in this study (7 nm in the present case). In contrast to the previous study on gold surfaces (see chapter 4), ellipsometric measurements could not be performed on the ITO_{TR}-coated Si-prism to corroborate the formation of a monolayer MBH film on the ITO_{TR} surface. Indeed, as the thickness of the planar ITO_{TR} films deposited on the

prism differs slightly for each coating and varies throughout the film, no suitable model could be developed for the corresponding data fitting of the ellipsometric data.

Determination of the average coverage of his-MBH on the ITO_{TR} films was realized by counting enzyme units for at least 10 different areas in each image in vertical and horizontal direction and averaged. This procedure was applied for every examined AFM sample at low magnification (2 µm x 2 µm) and higher magnifications (500 nm x 500 nm and 200 nm x 200 nm) with at least three images of three different sample areas for each magnification. By using this methodology, a his-MBH surface coverage of Γ_{his}-MBH= 0.54 pmol cm^{-2} was determined on ITO_{TR}. The theoretical, maximum coverage of his-MBH, assuming an ideal planar electrode surface and a solid sphere of approximately 7 nm in diameter (reasonable size based on the crystal structure of the MBH), leads to a maximal theoretical coverage of Γ_{theo}= 3.4 pmol cm^{-2}; i.e. a 6 times higher coverage than the experimental coverage determined by AFM.

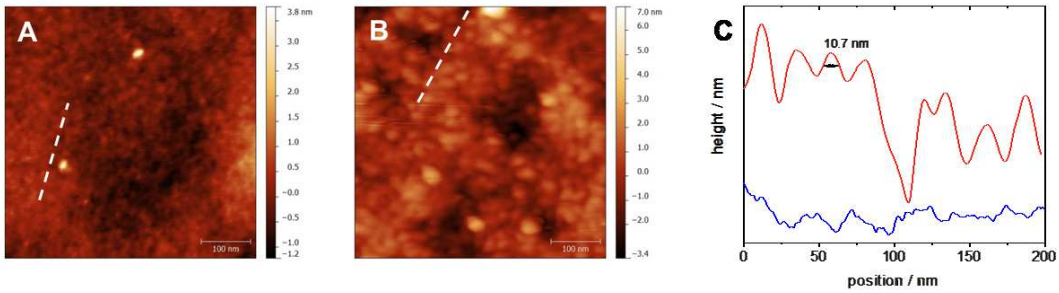

Figure 6.2: Topographic AFM mapping in the non-contact-mode of planar ITO_{TR} surface (A) before and (B) after 30 min of immobilization of his-MBH in 10 mM PB buffer at pH 7. The dashed line indicates the course of the height profiles shown in (C) prior (blue curve) and after his-MBH immobilization (orange curve).

The coverage of his-MBH on ITO_{TR} and *strep*-MBH on ITO_{TR} as well as on SAM-modified Au surfaces as well as its correlation with recorded IR band intensities will be compared and discussed in chapter 7, *vide infra*.

6.2.3 Desorption experiments of his-tagged MBH on ITO_{TR}

The binding interaction of his-MBH with the ITO_{TR} surface was studied in various desorption experiments as displayed in Figure 6.3.

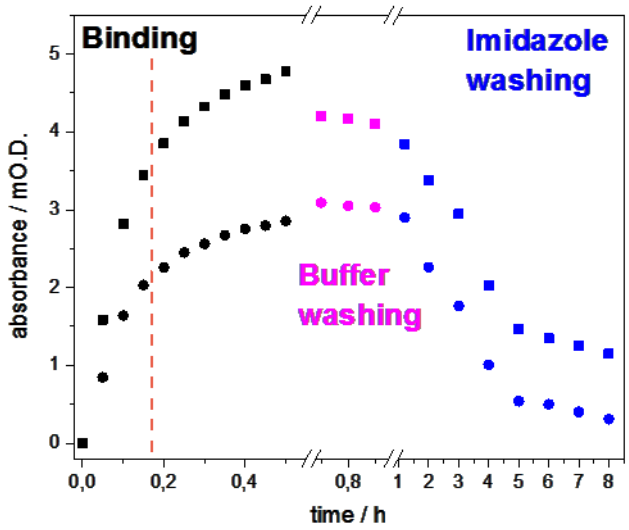

Figure 6.3: Kinetic analysis of the his-MBH surface binding on a planar ITO_{TR} surface during adsorption (black), monitored by the time course of amide I (■) and amide II (●) band intensities. Fractions of nonspecific interactions are elucidated by repeated buffer washing at higher ionic strengths (3M KCl) (pink). Only after iterated incubation with 750 mM imidazole buffer, the dominating portion of specifically bound his-MBH decreased significantly (blue).

Analogously to his-cyt c (chapter 5), the amide I and amide II band intensities remained unaffected by the washing procedures with buffer underlining the presence of a stable and non-electrostatic interaction between the his-MBH and the ITO_{TR} surface (Fig. 6.3). Imidazole addition could finally desorb the his-MBH selectively from the metal oxide surface. Hence, even for a much more complex enzyme with twice the size of his-cyt c, the adsorption is shown to be driven by its his-tag affinity to the ITO_{TR} surface.

6.2.4 Conclusions

This work presents studies of the adsorption behavior and observable redox states of a [NiFe] hydrogenase on a semiconductor surface by ATR-IR for the first time. His-MBH could be adsorbed on planar ITO_{TR} thin film electrodes. Upon adsorption on the ITO_{TR} surface, the integrity of the his-MBH protein backbone as well as of its active center was maintained. During the adsorption process, the amide I and amide II band intensities were monitored in situ revealing a biexponential adsorption behavior. By means of desorption experiments the selective his-tag binding of his-MBH to the ITO_{TR} surface could be revealed. Furthermore, the enzyme coverage of his-MBH was determined on ITO_{TR} by AFM measurements.

Contrary to the investigations of *strep*-MBH on SAM-covered gold electrodes, on which predominantly the Ni_r-B state was observed, in this case of his-MBH on ITO_{TR} surfaces, the $Ni_{r/a}$-S, partially reduced redox state, with an absorption band at 1934 cm^{-1} was found significantly enriched on the ITO_{TR} surface after immobilization of the his-MBH, suggesting a reductive effect by the semiconductor on the his-MBH.

When *strep*-MBH was immobilized on SAM-modified Au electrodes, only the Ni_r-B and rarely the irreversibly inactive Ni_{ia}-S species at 1930 cm^{-1} were detected (see chapter 4.2.2). This other state represents a partly reduced Ni(+2)-S species, the so-called Ni_r-S state, recently discussed by Siebert et al..[224].

6.2.5 Under turnover conditions

The ATR-IR set-up allowed concomitant electrochemical investigations of the adsorbed his-MBH on ITO_{TR} surfaces, i.e. protein film voltammetric studies, which are discussed in the following section.

6.2.5.1 Protein Film Voltammetry of his-MBH on ITO_{TR} electrodes

Protein film voltammetry was performed in the presence of H_2-saturated buffer after 10 min and 30 min of enzyme immobilization. Direct electron transfer (DET) between the immobilized his-MBH and the ITO_{TR} surface could be established (see Fig. 6.4). The voltammetric experiments revealed current densities for H_2 oxidation similar to those previously observed for *Re* MBH immobilized on graphite, Ag electrodes, and Au electrodes (see chapter 4) in a range of some µA cm^{-2}. The characteristic sigmoidal shape of the current-potential trace, as shown in Figure 6.4A, reflects the electrocatalytic activity of the immobilized enzyme for H_2 oxidation, including the typical current drop at higher potentials, related to the reversible oxidative inactivation of the *Re* MBH (see 2.21). This data indicates that the catalytic activity of his-MBH is preserved upon adsorption on the unmodified ITO_{TR} electrode. Notably, in comparison to the studies of *strep*-tagged MBH on charged SAM-functionalized gold electrodes (averaged values of 2-8 µAcm^{-2}; see section 4.2.4, Fig. 4.8) the adsorbed MBH on ITO_{TR} exhibits a high catalytic performance (15 µA cm^{-2}) with current densities up to three to four times higher (see section 4.2.1). Interestingly, previous attempts to immobilize his-tagged MBH on standard Ni^{2+}- Nitrilotriacetic acid (NTA) modified gold electrodes did not reveal any electrochemical activity,[67] which might be related to the large distance between the distal Fe-S cluster and the electrode surface, related to the presence of the large NTA-bearing linker hampering any direct electron transfer. In contrast, a direct his-tag mediated immobilization not only simplifies the electrode preparation (in the sense that no surface modification of the electrode is needed) but also provides a prevailing orientation, which favors direct electron transfer between the immobilized enzyme and the electrode. This is particularly important, as especially complex and large biocatalysts such as the MBH may easily risk their use in electrocatalytic applications due to “misorientation” on the electrode surface.

Electrochemical studies of CV measurements performed after different immobilization times on ITO_{TR}-coated ITO/glass (ITO_{TR}/ITO/glass) (see appendix Fig. 6.1) revealed the highest catalytic current densities after 10 min of incubation (Fig. 6.4A).

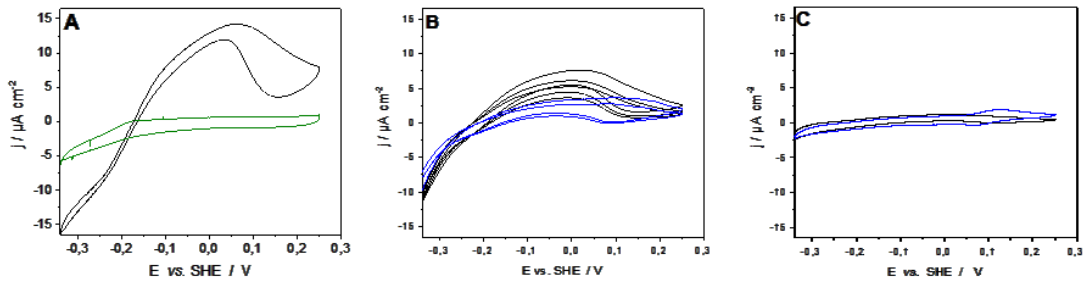

Figure 6.4: (A) Consecutive voltammetric traces of blank ITO_{TR}/Si-prism (dashed black) and *Re* his-MBH immobilized on ITO_{TR} for 10 min as well as (B) his-MBH immobilized for 30 min; before (black) and after addition of 10µM methylene blue as mediator (blue) in the presence of H_2-saturated buffer. The decreases of hydrogen oxidation and evolution reaction (HOR and HER) performed by his-MBH in consecutive CVs are indicated by arrows. All voltammetric measurements were carried out in 10 mM PB buffer at pH 5.5, at room temperature with a scan rate of 5 mV s^{-1}. Potentials are given with respect to the SHE reference electrode.

No effect of mediator addition was observed on the catalytic current density of hydrogen oxidation, indicating a homogeneous and an optimal distribution of his-MBH orientations on the electrode surface, enabling solely direct ET (Fig. 6.4A). For longer incubation times of 30 min (see Figure 6.4B), a drastic loss (80-90%) of current density related to a direct electron transfer is observed, although the intensity of the amide bands suggests a 25% higher enzyme coverage on the ITO_{TR} surface when compared to an incubation time of 10 min (see Figure 6.1). Upon addition of a redox mediator, however, an increase of about twice the catalytic current for DET was observed. In conclusion, increasing adsorption times and thus higher enzyme loadings lead to a loss of enzyme activity concomitant with a less defined orientation of the his-MBH on the ITO_{TR} surface. This immense loss of catalytic activity within 30 min of incubation (80-90%) might be caused by long-term instability of the enzyme. Indeed due to residual oxygen in solution, a certain enzyme instability upon successive CV cycling or upon prolonged immobilization time is commonly observed regardless of the substrate material in use.[203, 33] Hence, the loss of catalytic activity is not ascribed necessarily to the prolonged his-MBH-ITO_{TR} interaction.

Fig. 6.4A shows the subsequently recorded voltammetric cycles of his-MBH on ITO_{TR}, whereby each cycle leads to a certain current density loss of the hydrogen oxidation reaction (HOR) and the hydrogen evolution reaction (HER). However, the reason for the activity loss is not understood in detail, yet.

Different factors can be considered for such catalytic current losses, such as active site damage, enzyme structure denaturation or even enzyme crowding effects. *Re* heterodimer MBH exhibits denaturation at its active site due to residual oxygen as reported for MBH in solution.[58] The ATR-IR spectra of the CO ligand vibrational mode does not indicate a significant damage at its active site, which usually can be monitored via the irreversibly inactivated Ni_{ia}-S state (Fig. 6.1D). Also, enzyme functionality loss may be caused by alterations in the protein structure, which might occur upon long-time exposure to the electrode substrate. However, in the case of his-MBH on ITO_{TR} changes in the amide band pattern within the immobilization time are not detected (Fig. 6.1A).

A possible explanation for activity loss with increasing enzyme coverage might be an effect due

to enzyme crowding. In fact, enzyme crowding effect, deactivating the enzyme's functionality was recently shown in adsorption studies of bilirubin oxidase from *Myrothecium verrucaria* (*Mv* BOD) on SAM-modified gold electrodes.[301] The trend of enzymatic activity loss by prolonged immobilization times is discussed. In agreement with the results on his-MBH on ITO_{TR}, these findings for *Mv* BOD on SAM-coated gold electrodes confirm that incubations with higher enzyme concentration or over a longer time period result in a compact monolayer rather than a preferential submonolayer, yielding to lower enzymatic activities.[301] As stated for *Mv* BOD, longer immobilization times, and thus also higher enzyme coverages, resulting in loss of catalytic currents was additionally accompanied with a reorientation of the enzyme molecules.

A further reason for the observed his-MBH activity loss upon interaction should be considered by active site leaching or even metal ion leaching should be considered as a possible origin for activity loss in case of metal oxide surfaces.

The his-tag directed/governed, well-aligned enzyme orientation on the surface has an impact on certain electrochemical properties of the adsorbed MBH. Two major aspects were observed, which can be related to the direct electronic contact of his-MBH to ITO_{TR} electrode. Firstly, the shape of the CV should be discussed. According to the work of Leger et al.,[213] broad current traces originate from a highly diverse distribution of enzyme orientations with different ET rates. In contrast, narrow traces can be related to a more homogeneous orientational enzyme distribution at the surface. Therefore, the very narrow CV traces recorded for his-MBH immobilized for 10 min on ITO_{TR} compared to those where his-MBH is adsorbed on PGE might be indicating a more homogeneous orientation of his-MBH on ITO_{TR} than on PGE. Secondly, the OCP under H_2 atmosphere of his-MBH on ITO_{TR} (E_{OCP}=-290 mV vs SHE) is altered in comparison to the ones observed for his-MBH on PGE and *strep*-MBH immobilized on negatively charged SAM-coated Au surfaces (E_{OCP}=- 240 mV). The OCP of blank ITO_{TR} without MBH adsorption is not affected by H_2. The corresponding even slightly more negative OCP value may be a further indication for an established direct and fast interfacial electron exchange, which seems to be caused by the his-tag anchoring. Contemplating OCP as an empirical factor, the his-MBH on ITO_{TR} seems to indicate apparently affords not only a homogeneous distribution but also an efficient electrode-enzyme heterogeneous ET, which so far is the best achieved enzyme-surface interaction in this work. This conclusion could be derived from the comparison of all observed OCP values of *strep*-MBH on Au surfaces and his- MBH on ITO_{TR}, under Ar as well as H_2 atmosphere. The values are given in Table 7.4; chapter 7.

The CV traces of immobilized MBH represent also the involved redox states that prevail in different potential regions. Upon cyclic scanning, catalytically inactive states are reactivated in a redox process, marked empirically by a potential, denoted as E_{switch}, which is defined as an inflection point, which can be extracted from the CV's first derivative.[242] Remarkably, voltammetric traces of his-MBH on ITO_{TR} and on PGE differ with respect to their detectable switch potentials (E_{switch}) by 100 mV, suggesting a shift of the reactivation of his-MBH on ITO_{TR} to lower potentials.

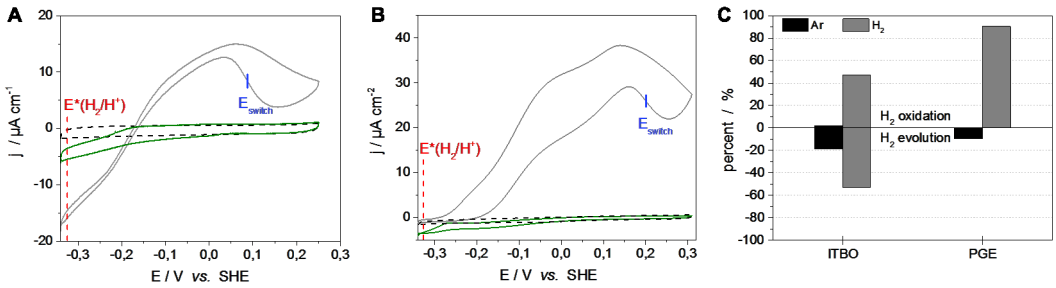

Figure 6.5: First recorded voltammetric traces before (dashed black line) and after 10 min of *Re* his-MBH immobilization (solid line) on (A) ITO_{TR} electrodes and (B) PGE electrodes in the presence of Ar-saturated (green) and H_2-saturated (grey) 10mM PB electrolyte at pH 5.5. The indicated vertical dashed red line corresponds to the standard potential of the H_2/H^+ couple. (C) comparison of normalized current densities involving proton oxidation and proton reduction of his-MBH on $ITO_{TR}$and PGE electrodes under Ar (black) and H_2 (grey) atmosphere, respectively. The presented activities were normalized to the sum of maximal current densities of both, H_2 oxidation and of H_2 evolution. All voltammetric measurements were carried out at room temperature with a scan rate of 5 mV s^{-1}. Potentials are given with respect to the SHE reference electrode.

As often observed for hydrogenases showing HER, e.g. standard hydrogenases, such as Hyd-2 from *E. coli* or [FeFe]-hydrogenases, the related E_{switch} value is found at lower potentials when compared to hydrogenases with less extended HER capabilities. E_{switch} is thereby less regarded as a thermodynamic equilibrium property but more as an empirical feature indicating the conversion from "ready" Ni_r-B to active Nia-S redox states. Generally, it was observed that a shift of the switch potential to more positive potentials can be correlated with an increase in catalytic activity of the hydrogenase towards hydrogen oxidation.[246] More interesting in the present context is a comparison of the width of the potential windows where H_2 oxidation occurs, which is located between the catalytic onset potential and E_{switch}. In this respect, the CV current-potential trace of his-MBH on ITO_{TR} appears as a compressed trace with a higher onset and a lower switch potential compared to the CVs of MBH immobilized on PGE or Au-SAM systems. On ITO_{TR}, the width of the potential window for H_2 oxidation is situated between E_{onset}=-180 mV and E_{switch}=+100 mV corresponding to a potential window of ΔE=280 mV. Contrarily, in the case of his-MBH immobilization on PGE electrode, the corresponding width of the potential region between E_{onset}=-250 mV and E_{switch}=+200 mV is much larger, accounting for ΔE=450 mV. The recorded CVs of the latter demonstrate only HOR current densities, whereby the same his-MBH on ITO_{TR} reveals both, HOR and HER, even in similar relative quantities. Similar correlations between the observable potential window between the onset and switch potential and the hydrogenases bias between towards the HOR and HER reactions were discussed for E coli Hyd-2 and Hyd-1, respectively.[246] Hyd-2 displays a smaller potential window but reveals only HER activity, whereas *E. coli* Hyd-1 exhibits HOR and no HER. The comparison of the exposed potential window width should be treated as an empirical trend. Even if a differentiation for the corresponding hydrogenase bias was detectable for different hydrogenases, the same observation was also made for the same *Re* MBH by placing on different surfaces, which exhibit varying surface interactions. Already for *strep*-MBH on SAM-coated, nanostructured Au surfaces with different surface charges displayed a maximal potential difference of ΔE=50 mV for E_{switch} values depending on the surface charge and probably the capability for interfacial electron transfers (see section 4.2.1).

As displayed in Figure 6.5A (gray line), strong negative currents at potentials below -180 mV vs SHE were detected in the CV traces for his-MBH adsorbed on ITO_{TR} in H_2 saturated buffer, while no such currents are recorded for the bare ITO_{TR} (dashed line) recorded as a reference. Surprisingly, this behavior is only observed when the electrolyte is purged with H_2 and not as usually observed for hydrogenases after purging the electrolyte with Ar. This result is in contradiction to the reported product inhibition of the MBH. To exclude any effect from the enzyme preparation batch itself, the enzyme was adsorbed under the same conditions on a standard PGE electrode (see Figure 6.5B). In line with previously reported experiments, only H_2 oxidation, but no H_2 evolution was observed for the his-MBH immobilized on PGE.[205, 207] Figure 6.5C shows the percentage of current density related to catalytic hydrogen oxidation (j_{ox}) and proton reduction (j_{red}) normalized to the total of maximal faradaic current densities observed for both reactions in sum, e.g.

$$j_{ox}\% = \frac{j_{ox}}{j_{ox}+j_{red}} \cdot 100 \text{ and } j_{red}\% = \frac{j_{red}}{j_{ox}+j_{red}} \cdot 100$$

As can be derived from Figure 6.5C, similar electrocatalytic current densities at same overpotentials for HER and HOR were observed for his-MBH on ITO_{TR} surfaces. Upon comparing the HER activity under Ar of his-MBH on PGE (j_{HER}=-3.6 µAcm^{-2}) and of his-MBH on ITO_{TR} (j_{HER}=-5 µAcm^{-2}), an increased absolute, as well as relative to the normalized value of HER activity of the his-MBH on the ITO_{TR} surface is found (Fig. 6.5C). It should be noted that the higher HOR current densities of his-MBH on PGE electrodes can be explained most likely by the typically rougher PGE surface (as shown by SEM images in reference,[33] which favors a higher MBH surface coverage than the planar ITO_{TR}.

For clarification for the following discussion, the onset potential is thenceforth defined as the onset potential for both, HER and HOR of the his-MBH on ITO_{TR}, as seen in Fig. 6.5A. In addition to the increased HER activity upon adsorption on ITO_{TR}, a strong positive shift in the onset potential of his-MBH on ITO_{TR} can be observed. This is shown in Figure 6.5A. The negative catalytic currents start reproducibly at a potential around $E(H_2/H^+)$=-180 mV (vs SHE), while the equilibrium potential of the H_2/H^+ couple at pH 5.5 is located at $E_{eq}(H_2/H^+)$=-325 mV (vs SHE; $E_{eq} = E^0$- 0.0059 * pH) as indicated by the vertical, dashed red line in Figure 6.5. This negative potential shift of more than -145 mV is very puzzling and points to an effect that is not yet described for other semiconductor-enzyme systems in literature. As possible origins of such a shift a -induced potential at the ITO_{TR} electrolyte interface or at the Si/ITO_{TR} junction has to be considered as possible explanation, which however could be excluded by comparing experiments on ITO_{TR}/ITO/glass, intrinsic ITO_{TR}/Si and p-doped Si/ITO_{TR} electrodes (see appendix Fig. A.14).

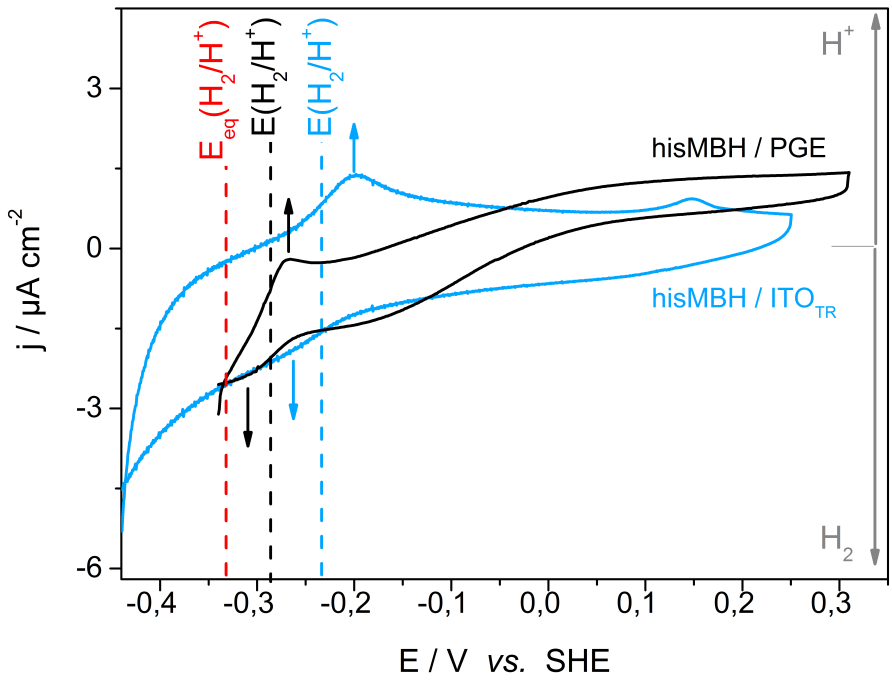

Figure 6.6: Cyclic voltammograms in Ar saturated buffer solution (10 mM PB buffer at pH5.5) after 10 min of his-MBH immobilization on an ITO_{TR} electrode (blue) and a PGE electrode (black), respectively. Further indicated as vertical, dashed lines are the corresponding equilibrium potentials of H_2/H^+ calculated for pH 5.5 from standard potential (red line) and the determined potentials from the related peaks of H_2 oxidation and H_2 production, indicated by arrows on the voltammograms of his-MBH on ITO_{TR} (blue) and PGE (black) as well as the associated mid-point potentials. The underlying scan rate is 5 mV s^{-1}.

Cyclic voltammograms (CVs) recorded on an ITO_{TR} and a PGE electrode are shown in Figure 6.6, where the observed peak-like Faradaic current maxima/minima ascribed to HOR and HER are due to substrate depletion due to the usage of stationary electrodes. The potential of the oxidation and reduction waves of his-MBH on PGE ($E(H^+)_{ox}$ = -260 mV and $E(H_2)_{red}$ = -300 mV vs SHE, respectively; pH 5.5) agree well with previous reports of *strep*-MBH from the same organism immobilized on on PGE [58] or on Ag-SAM electrodes [203]. In contrast, the his-MBH immobilized on ITO_{TR} displays for both, oxidation and reduction waves shifts of their maxima/minima to more positive potentials. The oxidation peak $E(H^+)$ is shifted to - 194 mV while the reduction peak $E(H_2)$ is shifted to - 260 mV (vs SHE; pH 5.5). This observation reflects the fact that the electrocatalytic properties of the his-MBH immobilized on ITO_{TR} is not anymore solely controlled by the redox properties of the enzyme, but indicates a strong impact of the semiconductor-enzyme interaction. The small oxidation peak observed in Figure 6.6 at +125 mV vs SHE can probably be assigned to a hydroxylation reaction taking place at the ITO_{TR} surface. This feature is observed with and without the adsorbed protein species and does therefore not seem to be related nor interfere with the enzyme catalysis (see appendix Fig. A.15 and A.17).

In Fig. 6.7, the CVs of his-MBH on ITO_{TR} and PGE under Ar and H_2 initially shown in Fig. 6.2, are magnified to show the overlay of the CVs under Ar and H_2, respectively, green and gray. The shift of the peak-like H_2/H^+ oxidation/reduction currents (indicated by arrows in Fig. 6.7) of his-MBH on ITO_{TR} under Ar has been discussed, *vide supra*. The overlayed CV of his-MBH under H_2 atmosphere show the Faradaic current densities towards both reactions, HOR and HER, at same potentials as the peak-like H_2/H^+ currents under Ar occurs. This suggests that the recorded negative current densities of his-MBH under H_2 indeed can be ascribed to a HER performed by the enzyme, even if these currents occur at a much more positive potentials than predicted by the Nernst equation (E_{eq} (-325 mV; pH 5.5)).

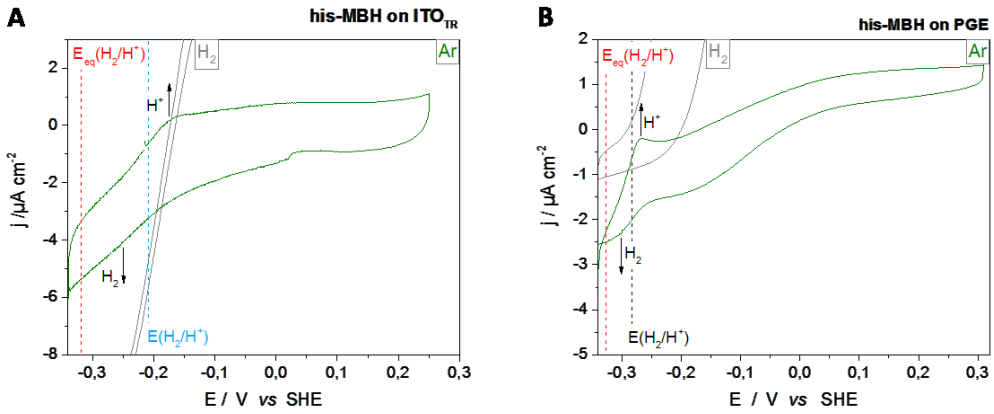

Figure 6.7: Voltammetric traces after 10 min of his-MBH immobilization on (A) ITO_{TR}- and (B) PGE electrodes in the presence of Ar-saturated (green) and H_2-saturated (gray) 10mM PB electrolyte at pH 5.5. Indicated vertical dashed lines correspond to the equilibrium potential of the H_2/H^+ couple at pH 5.5 as determined by the Nernst equation (E_{eq};in red) and experimentally determined by recorded peak-like oxidation/reduction (arrows) of the H_2/H^+ couple by his-MBH on ITO_{TR} (blue) and PGE (black). All voltammetric measurements were carried out at room temperature with a scan rate of 5 mV s^{-1}. Potentials are given with respect to the SHE reference electrode.

Similarly, as seen in the CV in Fig. 6.7B, the his-MBH on PGE reveals faradaic current densities for H_2 oxidation at potentials at which peak-like H_2 oxidation occurs under Ar.

An assignment of the reductive current to a redox transition above the value of $E_{eq}(H_2/H^+)$= -325 mV as it could be originating from a reduction of the his-MBH enzyme itself is rather unlikely. Although the redox potential of the distal Fe-S cluster in the *Re* MBH could not be determined by EPR titrations yet, it is most likely to be the lowest redox couple present in the enzyme, as determined for other hydrogenases previously.[1] For example, the determination of the redox potentials of the distal Fe-S cluster of other O_2-tolerant [NiFe] hydrogenases revealed a redox transition at approximately -69 mV (vs SHE) for *E. coli* Hyd-1, and -78 mV (vs SHE) for *A. aquifex* Hase I [302]; redox potentials which were more positive in comparison to the redox transition of the distal cluster of their O_2-sensitive counterparts.[303] In line with the potential determined for the redox transition of the distal iron-sulfur cluster of other O_2-tolerant hydrogenases, the redox potential of the distal Fe-S cluster of the *Re* MBH can thus be assumed to be in the same potential range; i.e. at potentials above -100 mV (vs SHE). A reduction of the distal Fe-S cluster of his-MBH immobilized on ITO_{TR} would, therefore contribute to the total

current density by a negative current density at potentials above -100 mV (vs SHE) and could therefore not explain the reductive currents observed below -180 mV (vs SHE). Therefore, the negative currents observed at potentials below -180 mV (vs SHE) can be excluded to originate from the reduction of the distal Fe-S cluster, the most negative Fe-S cluster, which is exposed in a direct electron transfer configuration to the ITO_{TR} electrode surface.

Hydrogenases are commonly characterized by their bias for the reversible hydrogen splitting, normally determined by solution assays. However, the one has to notice that catalytic reaction bias of hydrogenases and here his-MBH are strongly dependent on experimental condition settings such as pH, electrolyte, the partial pressure of H_2 as well as support electrode. All these aspects do not only influence the current densities for either HOR or HER, but also affect the favored bias of the reaction. In this respect, Armstrong presented recently a detailed study on the HER ability of hydrogenases depending on these experimental parameters, which is discussed in the following section (6.2.6).

6.2.6 Hydrogen production of hydrogenases

Armstrong proposes a model rationalizing the tendency of a substrate-saturated hydrogenase to operate preferentially in a particular direction, i.e. being biased towards hydrogen oxidation or proton reduction.[246] Thereby, the interfacial ET occurs at the electron entry/exit site of the hydrogenase, i.e. at the distal Fe-S cluster, with a reduction potential defined as $E^0{}_{ox/red}$ in the following. The catalytic bias is thereby predicted by the following equation, where n is the overall number of electrons involved in the reaction ($H_2 \rightleftarrows H^+ + 2e^-$) and the electrode and $E^0(H_2/H^+)$ is the equilibrium standard potential imposed by the oxidized and reduced substrate, while kc and ka present the ET reaction rates for cathodic and anodic reaction, respectively.[246]

$$catalytic\ bias = \frac{k_c}{k_a} = exp\left[-\frac{nF}{RT}\left(E - E_{eq}\left(H_2/H^+\right)\right)\right]$$

The model highlights the role of the distal [4Fe−4S] cluster as the electrochemical control center for the enzymatic reaction bias.[191] The catalytic bias depends on the difference between the redox potential of the distal Fe-S cluster ($E_{ox/red}$) and the H_2/H^+ couple ($E^0(H_2/H^+)$). From this model one can see, that a hydrogenase with an $E_{ox/red}$ close to $E^0(H_2/H^+)$ works reversibly. The potential-dependent rate of interfacial ET can thereby be modeled by the Butler−Volmer model, whereas the description of the overall rate constant requires also the consideration of intramolecular ET processes, while the catalysis is assumed to be potential-independent.

In summary, the model applied by Armstrong to hydrogenases questions the general definitions of a hydrogenases capability of performing either solely HOR or HER according to the observable catalytic bias, which is commonly determined in solution assays or by using standard electrodes such as PGE or SAM covered Au electrodes. Hydrogenases are complex electrocatalysts and are intrinsically capable of performing both reactions. Thereby it has to be considered that the observed catalytic bias is an effect of enzyme-electrode interaction and experimental conditions.

Therefore, the extraordinary bi-directional property of the his-MBH when adsorbed on ITO_{TR} is not an intrinsically defined as unusual behavior, but rather the result of the experimental conditions.

The unusual tendency of his-MBH to produce H_2 in the presence of H_2 when it is immobilized on ITO_{TR} can only result from the enzyme-ITO_{TR} interaction in combination with the presence

of H_2, as this effect is exclusively limited to the adsorbed enzyme on ITO_{TR} and is not observed for bare ITO_{TR}, i.e. in absence of the enzyme, see Fig. 6.9. This effect is neither observed on PGE electrodes (Figure 6.5). It is therefore evident that the interplay between semiconducting ITO_{TR}-MBH system is responsible for the unusual potential onset shift, but only when all three components in an ITO_{TR}– his-MBH – electrolyte(H_2) system are taken into account, the remarkable enhanced HER might be explained.

In the following, possible explanations will be discussed to disentangle the origin of the observed phenomena of his-MBH on ITO_{TR}, namely a) the altered bias of his-MBH on ITO_{TR} in favor of H_2 production, b) the enhanced HER effect under product inhibition conditions (H_2 atmosphere) and c) the positive potential shift of its onset potential.

6.2.7 His-tagged MBH - semiconductor interface

As discussed by Bachmeier et al. for n-type semiconductors like TiO_2 and CdS band bending is expected at the MO-electrolyte interface.[299] Generally, the electrochemical determination of the flat band position (E_{fb}) of ITO materials is challenging since it supposedly lies below the potentials for the In^{3+} and Sn^{4+} metallic reduction. The corresponding reduction potentials of In^{3+} and Sn^{4+} in the ITO_{TR} material to metallic state occur at similar, overlapping values; at the chosen experimental conditions at pH 5.5 around -480 mV (vs SHE),[304] which impedes an electrochemical determination. The flat band potential is strongly dependent on electrolyte and ionic strengths. Consistent with the proposed potential value for the CB, values for the work functions of regular ITO (i.e. Sn-doped In_2O_3) obtained via different synthesis routes have been reported in the range between 4.3 eV to 4.7 eV. These correspond to values between -0.2 V and +0.2 V (vs SHE) in absolute electrode scale (see 2.14), where 0V is defined by the redox couple H_2/H^+, see chapter 2.3.1; Fig. 2.14.[305, 306, 307] However, the higher tin content in ITO_{TR} in comparison to regular ITO will surely affect its band structure, see Fig. 2.13. Regardless, as shown by Franzen et al, a highly tin-doped ITO material is considered as n-type semiconductor.[308]

At open circuit potentials (OCP) and in contact with electrolyte solutions with chemical potentials below the Fermi level of the MO or upon adsorption of proteins with redox potentials below the Fermi level of the MO, which is usually the case for n-type semiconductors, electrons from the MO surface are transferred to the redox couple attached at the surface and will lead to an upward bending of the band edges of CB and VB resulting in positive charge at the MO surface (see Figure 6.8A), for more detailed description see chapter 2, section 2.3.1.

The exact position of the flat band potential for the ITO_{TR}- system is unknown. Flat band potentials of semiconductors typically depend on the chemical potential of the solution in contact with their surface and strongly on the pH as well as on the redox potential of the adsorbed species (see chapter 2, 2.4.3). According to the Gerischer model, an n-type semiconductor in contact with an enzyme-electrolyte interface will establish a depletion layer in the space charge region by charge transfer processes, see chapter 2.3.1. Generally, n-type semiconductors are presupposed with more negative Fermi-level potentials than the redox potential/chemical potential of enzymes/electrolyte, which therefore leading to reductive charge transfer from the semiconductor to the enzyme/electrolyte.[173] When negative potentials are applied below the flat band potential of the semiconductor, an accumulation layer in the conduction band is induced, which

forwards the electron bias. The implications of the theoretical background will be discussed on this example below, see Fig. 6.8.

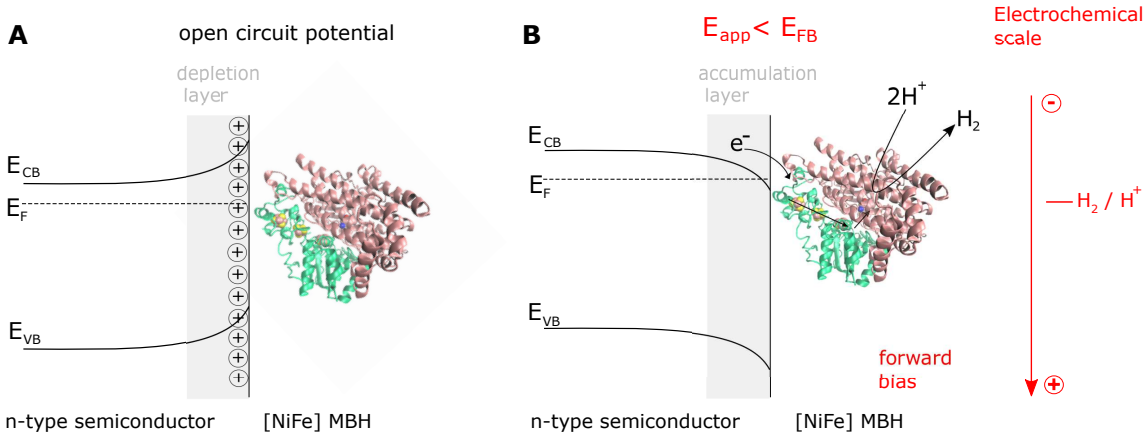

Figure 6.8: Band diagram for a n-type semiconductor-enzyme junction. Schematic depiction of the suggested band bending at equilibrium conditions with an adsorbed hydrogenase on ITO_{TR} (A) at OCP under formation of a depletion layer and (B) at negative applied potentials i.e. below the flat band potential (forward bias) inducing an accumulation layer. Thereby, EF represents the Fermi level and EFB the flat band potential of the semiconductor. Electrochemical scale is indicated in red and the hypothetical H_2/H^+ couple allowing catalysis by his-MBH.

The reductive effect of the surface adsorbed enzyme on an n-type semiconductor as sketched in Fig. 6.8 An experimental hint for the such a (at least partial) reduction of the his-MBH might be given by the IR spectroscopic results and in particular by the presence of significant amounts of a his-MBH redox state with a CO absorption at 1934 cm^{-1} (Fig. 6.1D), which is more than likely related to a partially reduced $Ni(+2)_r$-S state rather than to a $Ni(+2)_{ia}$-S state.

The formation of such an enzyme – semiconductor electron junction between the his-MBH and the ITO_{TR}surface might also be at the origin of the observed HER. The observed junction for his-MBH could however not be observed in a similar manner for his-cyt c (section 5.3.3) as his-cytc was present as a mixture of oxidized and reduced states in solution.

Upon potential application below the flat band potential, an accumulation layer is generated with an excess of electrons that might be able to flow under forward bias towards the distal Fe-S cluster of his-MBH. As a result of the potential induced forward bias, an accelerated ET kinetic for the interfacial ET might occur, which should be highly beneficial for a constant reduction of the active site, which in turn might be able to enforce a proton reduction even under conditions where normally product inhibition of the HER occurs (Fig. 6.5B). This atypical behavior is ascribed to the n-type semiconducting properties of ITO_{TR} in line with recent results reported by Bachmeier et al. for hydrogenases immobilized on n-type TiO_2 and CdS surfaces.[299] Bachmeier et al. proposed a mechanism for H_2 production under product inhibition conditions for hydrogenases immobilized on TiO_2 and CdS, both n-type semiconductors. This mechanism is based on the formation of an electron accumulation layer at the semiconductor electrode/hydrogenase interface.[299] Also Svedružić et al. reported this type of HER enhancement for hydrogenases immobilized on n-type semiconducting single-wall carbon nanotubes.[300] The enhancement of HER is hereby predominantly observed under Ar atmosphere conditions and in reduced quanti-

ties even present under H_2 by overcoming ruling product inhibition conditions. Even though, we also can report an enhanced HER under Ar the effect of HER under H_2 is even more enhanced on his-MBH on ITO_{TR}. However, in our case, this cannot explain the increased H_2 evolution under H_2 atmosphere; even higher than observed under Ar. In the present case of his-MBH /ITO_{TR}, not only does the semiconductor surface but in particular, the semiconductor surface in contact with H_2 saturated electrolyte seems to activate the HER for his-MBH–ITO_{TR} electrodes.

In this respect, the high electron density in the accumulation layer might enable a fast and effective ET from the electrode to the distal [4Fe4S] cluster, thereby boosting HER of his-MBH. Investigations of Co based HER catalysts adsorbed on TiO_2 showed that, indeed, very fast ET occurs between attached redox center and the CB of the metal oxide.[309]

6.2.8 Effect of H_2 on ITO_{TR}-MBH hybrid electrode – Enhanced HER activity

The enhanced HER activity of his-MBH adsorbed on ITO_{TR} electrodes (in comparison to other electrode surfaces) is in particular observed upon H_2 saturation of the electrolyte. In the interplay of the three components of the ITO_{TR}-MBH-electrolyte (H_2), his-MBH acts solely as the catalyst by its intrinsic properties. Whereas H_2 might interact with the ITO_{TR} surface, resulting in an additive effect (see section 6.2.6) and hence, allowing his-MBH to catalyze H_2 production with a high turnover rate. This unusual bi-directional biased catalysis of the *Re* MBH might be in particular facilitated through direct and a fast electron exchange between the ITO_{TR} electrode and the selectively via the hexahistidine-tag – surface bound his-MBH. Thus, H_2 seems to initiate the enhancement towards HER of his-MBH by means of an electron boost, an increased ET kinetics, additional to the semiconductor junction effect between the ITO_{TR}-MBH systems. Control experiments on bare ITO_{TR} under Ar and H_2 show that a blank, enzyme-free, ITO_{TR} surface does not exhibit a catalytic activity for HER (nor any other reaction in this potential range), see section 6.9. However, in the presence of H_2, ITO_{TR} seems to act as a more electron-enriched surface, enhancing the electron transfer towards his-MBH, which works on ITO_{TR}works as a catalyst for H_2 evolution. While the onset potential of his-MBH on ITO_{TR} is shifted to a higher potential, the respective switch potential is shifted to lower potential than observed on PGE, see Fig. 6.5. It should be noted that this ITO_{TR}-MBH hybrid exhibits two main characteristics, firstly a boosted HER caused by H_2 addition to the electrolyte and secondly a shifted onset potential probably enabled by the ITO_{TR}-his-MBH interaction. Besides, the oxidized Ni_r-B state, the EPR-silent partially reduced $Ni(+2)_r$-S state with a CO absorption at 1934 cm^{-1} could be monitored in significant amounts already upon surface interaction at low positive oxidative potentials (E_{OCP}=+50 mV vs SHE). *Strep*-MBH on Au-SAM electrodes did not exhibit hints for a formation of this particular Ni-S state at such low oxidative potentials (at OCP). The ITO_{TR} surface seems to function as reducing agent for the enzyme, which might be eased through the direct electron transfer configuration of the his-MBH on the ITO_{TR} surface achieved thanks to the his-tag mediated selective surface adsorption. A fast electron exchange with a forward bias from the ITO_{TR} surface towards the his-MBH would also explain the enhanced HER under Ar atmosphere on ITO_{TR} surface when compared to his-MBH immobilized on PGE, where such a HER enhancement does not occur.

6.2.9 Hydrogen affinity towards ITO_{TR}surfaces

Regarding the metal oxide – substrate interaction, it should be noted that the affinity of H_2 in particular to metallic Indium is known to be strong (Pourbaix diagram).[296] Even if in the present, analyzed potential range no faradaic conversion of H_2/H^+ is expected (see reference experiments in section 6.2.11), H_2 binding can still take place at the ITO_{TR} surface due to the high hydrogen affinity towards the In and Sn cations. Therefore, the effect of molecular H_2 on ITO materials is often used for H_2-sensoring.[310] 6.2.11.3. ATR-IR spectroscopic investigations of a long-term stored (> 1 year) batch of synthesized ITO_{TR}, which exhibits a poor conductivity, could give an idea of the effect on ITO_{TR} upon H_2 exposures even at OCP, see section 6.2.11.3..

6.2.10 Shift of the hydrogenases onset potential

Previously mentioned, the hydrogen affinity (see section 6.11) towards the ITO_{TR} substrate on which the his-MBH is immobilized, might explain the observed potential deviation from the expected standard potential of H_2/H^+ [$E^0(H_2/H^+)$] by lowering the activation energy for HER. Possible reasons for such effects will be discussed below.

The planar thin ITO_{TR} film harbors an intrinsic porosity made of 2 nm large pores. In this respect, H_2 affinity towards the substrate might be even enlarged by gas penetration into the thin film.

A shift of the enzyme onset potential to a more positive potential is observed for his-MBH on ITO_{TR} relative to the standard potential of $E^0(H_2/H^+)$ = -325 mV. Thus, the onset potential for the H_2 oxidation reaction of his-MBH on ITO_{TR} shifts from the value of the standard potential about ΔE= + 145 mV to $E_{onset}(ITO_{TR})$=-180mV (vs SHE) in comparison to the corresponding onset potential value of his-MBH on PGE, where only a shift of ΔE = + 85 mV to the onset potential at E_{onset}(PGE) = -240 mV is observed. In conclusion, an increased onset potential for hydrogen oxidation and a reduced potential for HER, can be detected (Fig. 6.5A).

Fig. 6.7 displays the CV of his-MBH on ITO_{TR} under Ar, in which the depletive peak-like oxidation and reductive peaks are shifted to higher potentials in comparison to the same voltammetric traces of his-MBH on PGE. Hence, the onset potential shift of his-MBH on ITO_{TR} under H_2 is also and as such a results of the interaction between ITO_{TR}-enzyme. Subsequent addition of H_2 to the system leads further to enhanced current densities for HER under a remaining onset potential of $E_{onset}(ITO_{TR})$=-180 mV (vs SHE). These results indicate that the interaction of H_2 with the ITO_{TR} thin films leads to a surface-substrate (ITO_{TR}-H_2) interplay which enables the his-MBH to catalyze the production of H_2 at more positive potentials.

The CV of his-MBH on ITO_{TR} displays particular differences regarding the position of the switch potential compared to his-MBH on PGE (Fig 6.5) or *strep*-MBH on Au-SAMs (see chapter 4). The switch potential of his-MBH on ITO_{TR} is negatively shifted by about E = -100 mV when compared to the switch potential of his-MBH on PGE. Generally, the switch potential describes the reactivation of a hydrogenase and is believed to correspond to the potential at which the redox transition between the Ni_r-B and Ni_a-S states takes place.

With a reactivation of his-MBH on ITO_{TR} occurring at lower potentials (E_{switch} = +90 mV) than his-MBH on PGE (E_{switch} = +200 mV), an eased reactivation of the his-MBH on ITO_{TR} electrodes is suggested. However, it also could indicate that the applied potential at the ITO_{TR} electrode is not consistent with the effective potential induced at the electrode surface. If the onset potential shift would occur due to an instrumental error and a discrepancy in accurately measuring the applied potentials, one would expect potential shifts for the switch and onset potential in the same direction; which is not the case in the present example, see section 6.5. Therefore, an instrumentational error can be excluded as the origin for onset potential shift.

H_2might induce band structure changes in ITO_{TR} via chemical modifications since H_2 generally shows a high affinity to ITO. In this regard, an exposure of ITO_{TR} to H_2 could result in an electron enrichment at its surface, which therefore can induce a different chemical potential at its interface accompanied by the kinetically enhanced HER effect by boosting electrons towards the catalyst. Studies focused on work function changes on ITO upon gas exposure such as H_2, revealed changes in particular of the surface work function.[311] These effects might explain the here observed thermodynamic underpotential for HER, shifting its onset potential to $E_{onset}(ITO_{TR})$=-180mV, i.e. to more positive values than the standard potential at $E^0(H_2/H^+)$=-340 mVin the dark. The applied potential might not coincide with the potential established effectively at the MO surface. It might be possible to disentangle this effect by replacing H_2 with other reductive agents, which would only interact with the ITO_{TR} surface but not with the his-MBH.

An increase of the local proton concentration at the ITO_{TR} surface due to a splitting (reaction) of the adsorbed H_2 might be considered at first as a possible origin for the onset potential shift. However, this can be excluded here. Indeed, the absolute energy positions of the valence and conduction band edges of semiconducting metal oxides follow a Nernstian relation, exhibiting a variation of 0.059 V per pH unit at 25 °C at 1 atm H_2. Therefore, a change in the local proton concentration change would induce the potential of the conduction and valence band edges of the semiconductor in the same way than the redox potential of the H_2/H^+ couple itself.[312] An increase of the local proton concentration would, however affect the his-MBH catalysis. The MBH catalysis for HER is indeed facilitated by an increase of the proton concentration and the reaction equilibrium of the reversible reaction $H_2 \rightleftarrows 2H^+ + 2e^-$ would be shifted close to the electrode surface on the H_2 production side with increasing concentration of H^+.

A variety of metal oxide semiconductors are known for their gas sensor abilities.[310] ITO is reported among them, but is not as extensively studied as others. The hydrogen sensing mechanism taking place in MOs is complex and has been investigated by many researchers. The commonly accepted mechanism is however based on the variation of the surface electron depletion region due to the reaction between hydrogen and the oxygen species at the metal oxide surface. The redox reaction is exothermic and results in the fast desorption of produced H_2O molecules from the surface. The released electrons will reduce the thickness of the depletion region, and therefore decrease the resistance of the semiconductor. The surface chemisorption of dissociated hydrogen may also play an important role in the hydrogen sensing behavior. As reported, hydrogen

molecules at the surface of a semiconductor induce an intermediate energy level for the transfer of charges from hydrogen to the conduction band. In such way, an accumulation layer of electrons can be created leading to a metalized region near the surface, which decreases the semiconductor resistance.[310, 313, 314] Typical features of such sensing mechanisms result in a shift of the potential (V) in the current-potential (I-V) curves. Even though, the explanation for the origin of the potential shift is still discussed controversially, these findings fit surprisingly well with the observations made for the his-MBH-ITO_{TR} systems described in this work; i.e. the enhanced HER as well as the positive potential shift for the hydrogen oxidation and hydrogen evaluation reactions.

A different explanation for the observed potential shift may be H_2 stabilization by surface interaction with ITO_{TR}. Generally, hydrogen underpotentials are characterized by the rise of the free Gibbs energy through the energy gain by the hydrogen adsorption to the material and are often described in the sense of hydrogen underpotential deposition. In summary, hydrogen molecules interacting with the substrate surface can lead to a decrease of ΔG, thus shift the H_2/H^+ equilibrium potential towards higher potentials as described by the following correlation:

$E_{eq} = -\frac{\Delta G_{eq}}{nF}$ with $\Delta G_{eq}\,(H_2/H^+) < \Delta G^0\,(H_2/H^+)$

In the case that hydrogen is stabilized at the electrode surface, the equilibrium potential of the H_2/H^+ couple could be shifted to more positive , therefore approaching the E^0(ox/red) potential of the his-MBH's distal [4Fe4S] cluster, which in principle, following Armstrong's model (see 6.2.7), should allow the the his-MBH to function as a bi-directional HOR and HER electrocatalyst.

In contrast to the thermodynamic equilibrium for H_2/H^+ conversion, the redox potential of the distal cluster is independent of pH and given intrinsically by the enzyme.

The rise of free Gibbs energy in case of highly affine H_2-metal interactions can lead to a shifted potential of the H_2/H^+ equilibrium, which might be the case for ITO_{TR} in the presence of hydrogen. Interestingly, the OCP under the turnover condition for the his-MBH on ITO_{TR} is as low as -290mV. This is the lowest OCP value observed for an immobilized *Re* MBH-electrode system in comparison to the OCP observed for his-MBH on PGE, *strep*-MBH on Au-SAM as well as for *strep*-MBH on ITO_{TR}, see Table 7.4. Under good direct interfacial electron connection between *strep*-MBH and the latter electrode surfaces, the recorded OCP was observed to reach only a value of maximum –240 mV. None of these MBH-surfaces showed any strong HER activity as his-MBH on ITO_{TR} under the same experimental conditions.

In order to investigate the observed unusual negative current densities at such positive potentials, and to confirm the correlation to a HER process, several reference experiments are required to clarify the origin of the reductive current densities as discussed in the following section.

Typically, a thermodynamic underpotential can be observed by a photovoltage induced by light excitation of the semiconductors. To investigate if the here observed shifts of the onset potential result from light exposure, specific reference experiments were carried out (see section 6.12), which led to the exclusion of any photo-induced effects.

6.2.11 Reference experiments

6.2.11.1 Blank ITO_{TR}

As reference measurement, cyclic voltammetry was performed on blank ITO_{TR} electrodes under Ar and H_2 atmosphere to probe any catalytic activity for HOR and HER originating from the metal oxide itself in the potential window used for the his-MBH studies.

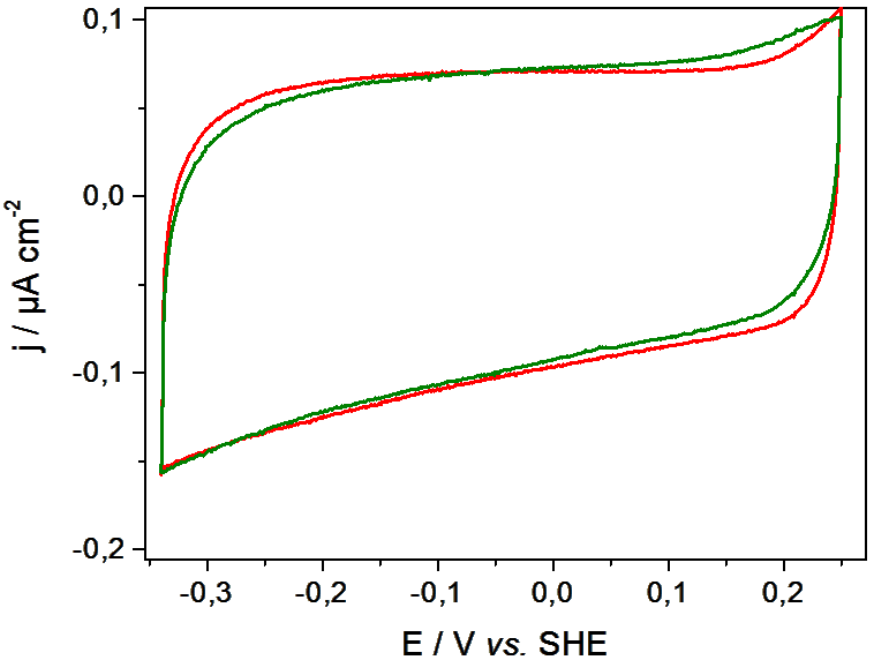

Figure 6.9: Cyclic voltammograms recorded in Ar (green) and H_2 (red) saturated buffer solution (10 mM PB buffer, pH5.5) in the dark in a potential window between -0.35 V and 0.35 V comparable to the CV study of his-MBH on ITO_{TR}. The applied scan rate is 5 mV s^{-1}.

Figure 6.9 exhibits the CVs of ITO_{TR} recorded under Ar (green) and H_2 (red) atmosphere, in which no significant changes in the applied potential can be observed. This negative experiment allows excluding any catalytic activity of ITO_{TR} itself for hydrogen oxidation or hydrogen evolution. However, an adsorption of hydrogen to the ITO_{TR} surface cannot be completely excluded as high affinities are reported for H_2 adhesion to ITO surfaces.[310]

6.2.11.2 Oxygen Reduction on ITO_{TR}

Another possible explanation of the reductive current densities could be a concomitant reaction which takes place at the electrode surface or in the enzyme itself overlapping with the catalytic H_2 oxidation signal of the his-MBH. O_2 reduction at the ITO_{TR} surface or the Sn/In reduction of the material itself could be herewith possible reason for generating the reductive current densities and hence misleading the shift of the real onset potential to higher potentials as exemplified in [315]. An overlapping reduction of ITO_{TR} overlapping with the his-MBH catalytic reaction can be excluded. ITO_{TR} can be reduced to lower valence or metallic Sn and In states at a potential

around -0.48 V (vs SHE at pH 5.5).[304] No redox features which might be related to an ITO_{TR} reduction itself are observable and thus, can be excluded as a concurrent reaction in the applied potential window. A further possible reaction, which might be considered, is O_2 reduction at the electrode surface due to residual O_2 contamination in the buffer solution, which generally defines a possible source of error. In order to exclude reductive currents originating from O_2 reduction at the ITO_{TR} surface, CVs of the blank ITO_{TR} electrode in buffer solutions saturated with 20% O_2 were taken, see Fig. 6.10.

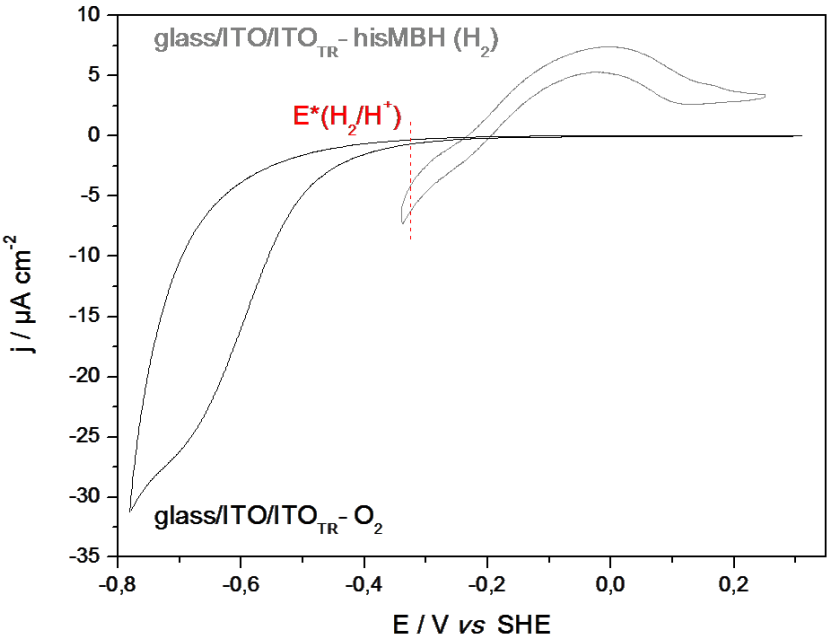

Figure 6.10: Cyclic voltammogram of an ITO_{TR}-coated ITO-glass slide measured in air saturated 10 mM PB buffer at pH5.5 (black) in comparison with his-MBH immobilized for 10 min on ITO_{TR}-coated ITO-glass in H_2-saturated 10 mM PB buffer solution at pH 5.5 The vertical dashed line in red indicates the theoretical equilibrium potential of the H_2/H^+ couple at pH 5.5. The applied scan rate is 5 mV s^{-1}.

The O_2 reduction at the ITO_{TR} surface in 10 mM PB buffer at pH 5.5, as displayed in Figure 6.10, shows a commence of the reductive currents below -400 mV. For comparison, the his-MBH on ITO_{TR}/ITO/glass is plotted in the same Figure 6.10. As can be seen, the oxygen reduction O_2 reduction current on the pristine ITO_{TR}surface cannot be the origin of the observed HER current densities. Thus, the reductive current densities observed for his-MBH catalytic activity immobilized on $ITO_{TR}$are unlikely to originate from an overlap of hydrogenase catalysis and oxygen reduction.

6.2.11.3 Hydrogen Effect on Low Conductive ITO_{TR}

Early ATR-IR experiments on ITO_{TR} preparations, which exhibited low conductivity, revealed that the ITO_{TR} thin films were strongly affected by exposure to hydrogen.

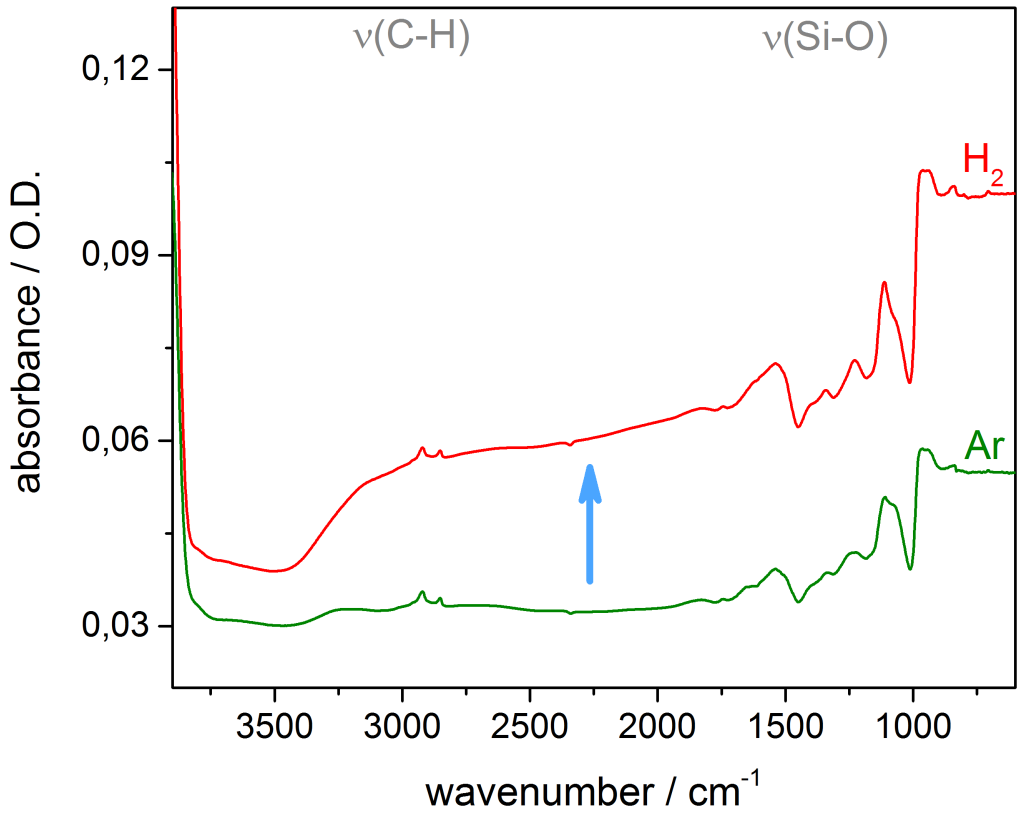

Figure 6.11: ATR-IR spectra of an ITO_{TR} preparation with low conductivities coated on an undoped Si-prism recorded under Ar (green) and H_2 (red) atmosphere reveal a strong shift of the baseline upon H_2 saturation of the 10 mM PB electrolyte (pH 5.5) at room temperature; both spectra measured at OCP (+250 mV).

Figure 6.11 shows the effect of H_2 exposure on an ITO_{TR} material with low conductivity. H_2 is known to increase the conductivity of TCO materials during calcination. Among different technological applications, commercial ITO can be used as a component in H_2 sensors, which also explains the specific H_2-ITO_{TR} interaction. Upon H_2 supply or the application of negative potentials the baseline of the ITO_{TR} spectrum shifts drastically as a result of lowered transparency. Such effects on ITO_{TR} occurred, when the thin ITO_{TR} films were synthesized from long-term stored ITBO precursor batches (precursor age older than 1 year). ITBO, the ITO_{TR} molecular single-source precursor, is in general highly sensitive to temperature fluctuations, as well as to and oxygen and water exposure. Low conductivities of such ITO_{TR} samples were also corroborated by electrochemical experiments and in particular CV experiments, which exhibited high capacitive currents for same film preparations (see appendix Fig. A6.3).

6.2.11.4 HER under Light Exposure

To rule out any light-induced effects on the increased HER of his-MBH on ITO_{TR}, experiments under light irradiation were performed using a halogen light source. Halogen lamps generate a continuous distribution of light across the visible spectrum, although most of the energy emitted

by these lamps is dissipated as heat in the infrared range, while generally a smaller luminous efficacy is exhibited in the visible region. Due to their relatively weak emission in the UV part of their spectrum, halogen lamps are not as useful for examining specimens that must be illuminated with wavelengths below 400 nm. Most of the experiments were performed under laboratory light exposure. Laboratory light was based on mercury tubes, which emit district wavelengths under filtering the UV contribution. To rule out any light effects originating from the laboratory light illumination, electrochemical experiments were performed under complete light exclusion by covering the set-up with aluminum foil.

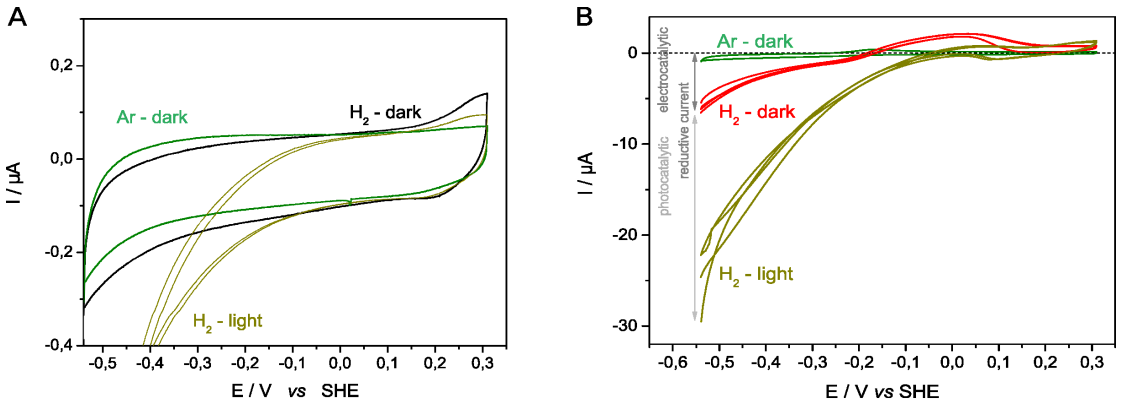

Figure 6.12: Cyclic Voltammetry on pristine ITO_{TR} films in the dark under Ar (green) and under H_2 atmosphere in the dark (black) as well under halogen light exposure (dark yellow): (A) without enzyme and (B) after his-MBH immobilization. Experiments were performed in 10mM PB solution at pH 5.5 with a scan rate of 5 mV s^{-1}.

Figure 6.12A shows CVs of the bare ITO_{TR} surface under Ar and H_2 atmosphere in the dark and under illumination by means of a halogen light source. The CVs of pristine ITO_{TR} under Ar and H_2 recorded in the dark and at the beginning of the light irradiation show only very small, practically negligible changes. However, after several minutes of light exposure (5min), a reductive current could be observed on bare ITO_{TR} under H_2.Figure 6.12B shows the recorded CVs of his-MBH on ITO_{TR} under H_2 under light exposure with a halogen lamp (yellow CV) and in the dark (red CV). The red CVs display the previously observed electrocatalytic responses of his-MBH on ITO_{TR} with biases towards H_2 oxidation and H_2 evolution. After 5min of light illumination, the reductive currents in the CV increase tremendously and seem to shift the catalytic response of his-MBH for H_2 oxidation. The strong reduction observed under extended illumination seems to result from a concomitant reaction; it might be the same as observed already in the reference CVs taken on bare ITO_{TR} in Fig. 6.12A. Typically n-type semiconductors upon light excitations are used as photoanodes [316] and therefore enhance oxidation reactions through generated charge carriers in the valence band, i.e. holes (see 2.3.1) . Since no evidence of any simultaneously enhanced oxidation is observed in the CV upon illumination, the here recorded reductive currents argue against a light-induced effect for the H_2 evolution of his-MBH and rather indicate the occurrence of a second reaction taking place at the ITO_{TR} surface. Conclusively, the HER of his-MBH in the dark can be assigned to a purely electrochemical effect induced by the his-MBH-ITO_{TR} enzyme-semiconductor interaction and at very low potentials there might be an overlap with oxygen reduction as displayed already in section 6.2.11.2.

6.2.12 Preactivation of his-tagged MBH on ITO_{TR}

As discussed previously in chapter 4 (Au-SAM), a subsequent preactivation step at a potential of -340 mV (vs SHE) can result in a homogenization of the enzyme orientations and an increase of catalytic current density caused by the adsorbed enzyme. Therefore, a CV without and subsequently with a preactivation of his-MBH on ITO_{TR} electrode under H_2 atmosphere was subsequently recorded. Figure 6.13 shows a CV before (black) and after (red) applying a potential of -340 mV vs SHE for 5 min under H_2. As can be seen in Figure 6.13, a decrease of current density by 12% is observed after the preactivation. As such the positive preactivation effect on the HOR catalysis obtained for the *strep*-MBH/NH_2-Au system could not be transferred to the his-MBH/ITO_{TR} system. The decay of catalytic activity under extended application of a reductive potential, seen by the decrease in current density, is however in line with literature reports linking this decrease with enzyme damage under applied potential as well as to enzyme loss / surface desorption.[33]

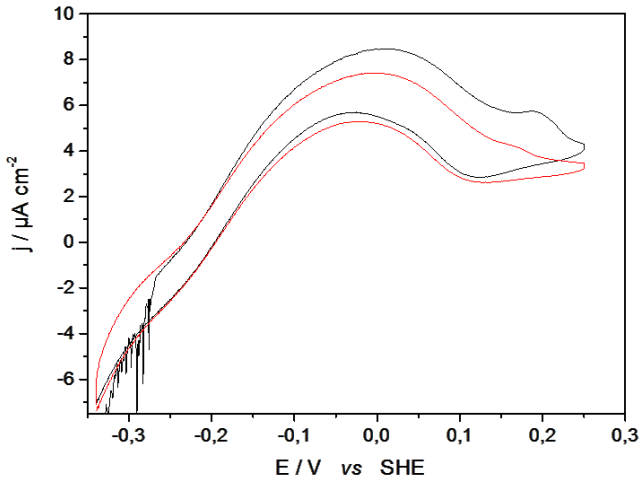

Figure 6.13: Cyclic voltammetry of his-MBH on ITO_{TR} measured before (black) and after (red) a subsequent 5 min long preactivation step at -340 mV vs SHE in the presence of H_2 saturated electrolyte. All voltammetric measurements were carried out in 10 mM PB buffer at pH 5.5 at room temperature and a scan rate of 5 mV s^{-1}.

6.2.13 ITO_{TR}stability for electrochemical studies

SEM images of an ITO_{TR}-coated Si-prism were taken to study the stability and retention of the ITO_{TR} film under standard utilization for spectro-electrochemical ATR-IR measurements. Figure 6.14 displays an ITO_{TR} film before and after 30 min of his-MBH incubation and subsequently conducting CV investigations.

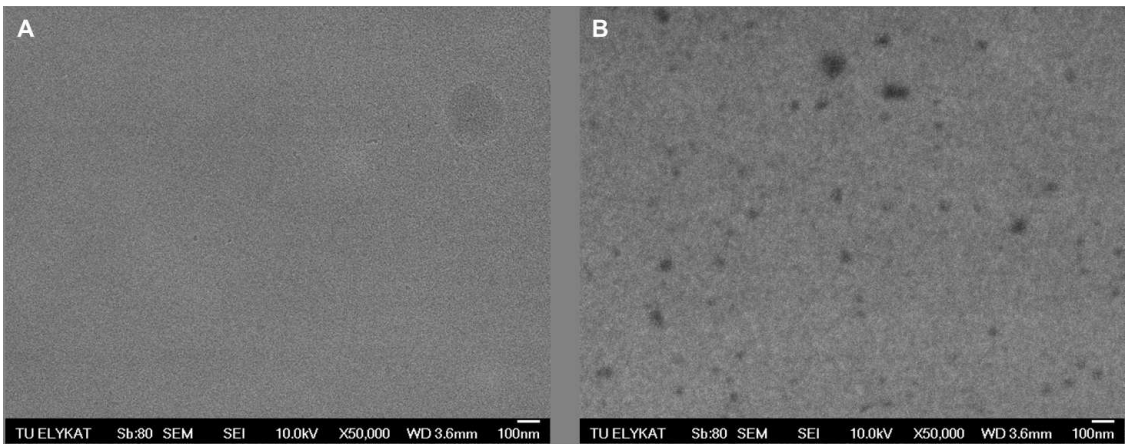

Figure 6.14: ITO_{TR} coated on an undoped Si-prism (A) before and (B) after 30 min of his-MBH immobilization and subsequent CV studies. All voltammetric measurements were carried out in H_2-saturated, 10 mM PB buffer at room temperature with a scan rate at 5 mV s^{-1}.

Figure 6.14B exhibits dark areas with fine-distributed smaller and some minor amounts of bigger sized dark spots on the ITO_{TR} surface by HR-SEM. These dark areas originate most likely from the adsorbed protein on the surface, leading to dark contrasts due to its organic-nature yielding less secondary electrons. Well-distributed small his-MBH units, and secondly also bigger agglomerations of his-MBH clusters, both already observed within AFM studies. Unfortunately, the overlaying protein film of adsorbed his-MBH was too thin to be measured by Energy-dispersive X-ray (EDX) spectroscopy.

Cross sections of ITO_{TR} coated on undoped Si wafers could show that the ITO_{TR} film itself was unaffected and a dark contrasted very thin film was coated on top (see Fig. 6.15). However, also here the thickness of the his-MBH film was sufficiently thin so that any verification of its organic composition by EDX spectroscopy in a line-scan mode was impossible.

In summary, electrochemical measurements under the described experimental conditions did not visibly affect or change the ITO_{TR} film structure, as seen from SEM images recorded before and after enzyme immobilization as well as electrochemical measurements (Fig. 6.14; Fig. 6.15). Herewith, the compatibility and stability of ITO_{TR} thin film electrodes are demonstrated for enzyme investigations.

Reduction of ITO_{TR} (E (ITO_{TR})= -480 mV vs SHE, pH 5.5) leads to irreversible changes of the electrode, affecting both its electrical and optical properties. During cycling or when it is held at potentials more negative than the ITO_{TR} reduction potential, the ITO_{TR} electrode is observed to turn from transparent into metallic color due to the metal cation reduction, resulting in a significant decrease in its transparency.

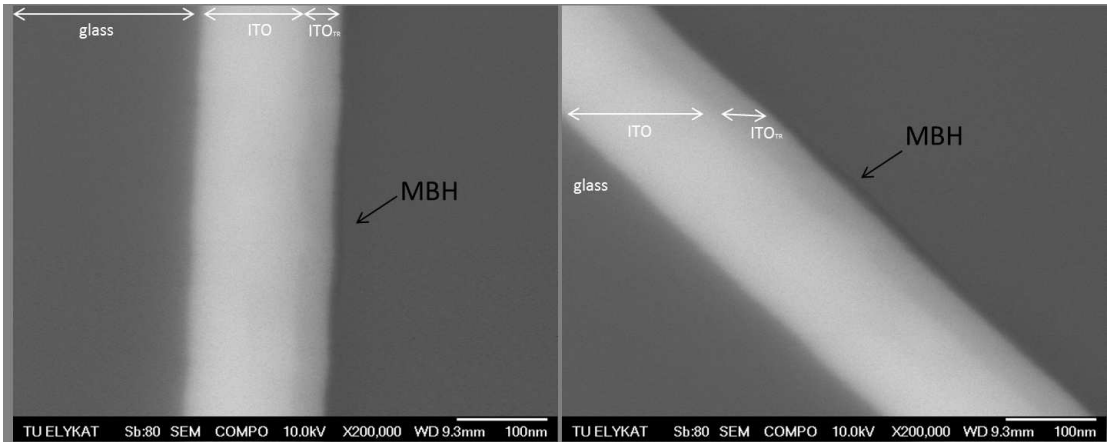

Figure 6.15: Cross section of MBH adsorbed on ITO_{TR} coated ITO-glass slide in the HR-SEM COMBO modus for a better distinction of conductive support and non-conductive adsorbed enzyme. Two images in different tilt angles of the film cross section have been carried out to minimize any artificially created thin dark line observed at the edge on ITO_{TR} support in the HR-SEM combo modus and therefore verifying the MBH adsorbate. Assignments of different support layers are noted by white arrows and enzyme with a black arrow in both images.

6.2.14 Conclusions

Exploiting the his-tag affinity of the ITO_{TR}, it was possible to immobilize his-MBH while preserving its catalytic activity towards H_2 on ITO_{TR} thin film electrodes. This constitutes a major achievement as for the first time a simultaneous IR spectro-electrochemical investigation of a highly relevant enzyme for hydrogen technology could be performed. In contrast to previous works that focus on resonance Raman spectroscopic investigations, this ATR-IR approach is not limited to enzymes harboring strongly absorbing chromophores to provide the necessary resonance enhancement for probing (sub)monolayer coverages.[92] In fact, his-MBH was immobilized for 30 min on ITO_{TR}, leading to relatively high intensities of the amide I and II bands of roughly 5 mOD. Very similar absorbance intensities were observed for immobilized his-MBH on SAM-modified Au electrodes by SEIRA spectroscopy (˜ 6 mOD).[67] The adsorption and desorption of the his-tagged MBH followed similar patterns as observed for the his-tagged cyt c. This leads to the conclusion that also in the case of his-MBH the protein-surface interaction is mediated via the histidine-tag instead of electrostatic or hydrophobic forces. The most important finding is related to the observable increased hydrogen evolution reaction (HER) capability of his-MBH immobilized on ITO_{TR}, caused by a specific enzyme-ITO_{TR} interaction. In comparison to the related studies on a PGE electrode, his-MBH adsorbed on ITO_{TR} surfaces reveals a slightly enhanced HER under Ar atmosphere, and a dramatically enhanced HER under H_2 supply. This particular behavior is exclusively observed upon adsorption of the his-MBH on ITO_{TR} film. The second phenomena observed on this hybrid system is the shift in onset potential above the expected standard potential value of the H_2/H^+ couple at $E^0(H_2/H^+)$=-325 mV vs SHE. An indication of the existence of a possible electron injection/donation effect might be the spontaneous partial reduction of his-MBH upon adsorption on ITO_{TR} (depletion layer formation) resulting in the enrichment of an EPR silent Ni(+2) state characterized by a CO absorption band at 1934 cm^{-1}. The formation of such an interfacial depletion layer at the ITO_{TR}-electrolyte interface might also be a crucial factor enabling the observed HER.

The role of the H_2 presence remains puzzling. Although previous works on immobilized hydrogenases describe an enhanced proton reduction activity of hydrogenases at MO surfaces, these experiments were conducted under Ar atmosphere, where no product inhibition is expected. Conversely, in our case the highest activities for proton reduction were observed only under product addition, i.e. H_2 saturated electrolyte, which is, in fact, difficult to understand. Moreover, ITO_{TR} electrodes without enzyme loading did not exhibit any differences regarding observable electrochemical signals under H_2 exposure compared to those recorded under Ar atmosphere. No significant changes of the open circuit potential were observed, nor any indication of a material induced proton reduction/hydrogen oxidation in the investigated potential window. A high affinity of H_2 towards ITO materials however is reported in literature and can have significant effects on its electronic structure. ATR-IR experiments on ITO_{TR} batches with poor conductivity displayed changes in its IR transparency upon H_2 supply. A lower transparency could suggest an electron enrichment of the material. This observation points to the fact that H_2 – material interactions might induce changes that play an important role for the unusually high H_2 production by the hydrogenase.

Finally, somehow the combination of the three components - ITO_{TR}, H_2, his-MBH - is the reason for for allowing unbiased high H_2 production by his-MBH. However, whether the modified catalytic activity results from a subtle change of the ITO_{TR} surface by H_2 or a possible pre-reduction of MBH facilitating subsequently easier proton reduction and, last but not least, an interplay between an enhanced ET between enzyme and ITO_{TR} during MBH catalysis cannot be distinguished here.

To ensure that the reductive currents at such negative potentials are resulting from H_2 production of his-MBH, mass spectroscopy experiments were carried out in D_2O under H_2 saturation of the electrolyte (for experimental details see chapter 3). These results could not be unambiguously interpreted, since the Pt counter electrode may have also an impact on the H_2 conversion during the whole experiment. Since *Re* MBH converts H_2 even at OCP under zero net current, the results have to be taken into account out carefully. For a more accurate discrimination, a membrane-separated electrochemical cell may provide more precise results. Furthermore, a ring disc electrode set up was also used to identify the H_2 production by coating the graphite electrodes with ITO_{TR} layers. However, these experiments could also not provide conclusive results, mainly due to the small electrode areas leading to a too small H_2 production for detection at the Pt ring electrode. For an unequivocal identification of the converted product or intermediates, differential electrochemical mass spectrometry (DEMS) measurements would need to be performed in the future.

6.3 Adsorption behavior of *strep*-tagged MBH on ITO_{TR}

To elucidate the enhanced HER activity observed for his-MBH adsorption to ITO_{TR}, *strep*-MBH was immobilized on ITO_{TR} for comparison substituting thereby the hexa-histidine affinity tag by a *strep*-affinity tag

6.3.1 ATR-IR studies of immobilized *strep*-tagged MBH on ITO_{TR}

Strep-MBH could be successfully adsorbed on planar ITO_{TR} electrodes. The corresponding adsorption process was probed *in situ* by ATR-IR spectroscopy as shown in Figure 6.16A.

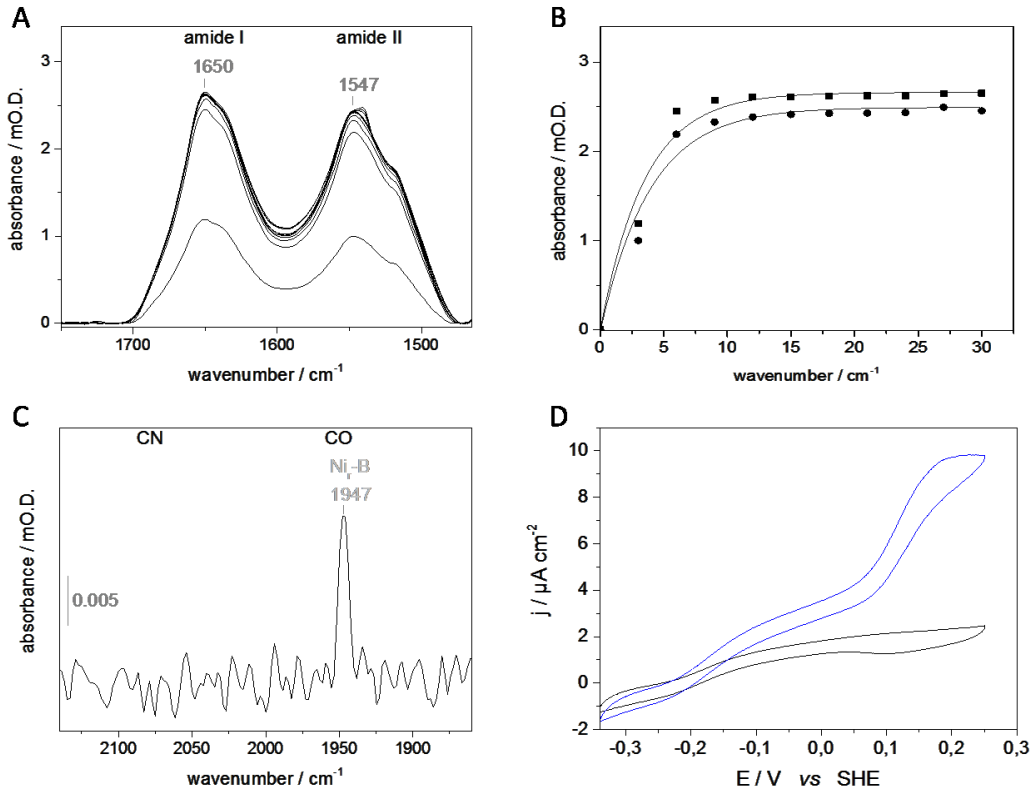

Figure 6.16: (A) ATR-IR spectra of immobilized *strep*-MBH on planar ITO_{TR} recorded during the 30 min lasting adsorption process, (B) binding kinetics monitored by changes amide I (■) and amide II (●) band intensities (black). Monoexponential fits ($A = A_0 + A_1 \exp(-t/\tau_1)$) were applied in the time period of $0 < t < 30$ min and are displayed as black lines for binding process. (C) ATR-IR spectral region characteristic for the active site from adsorbed *strep*-MBH. (D) Voltammetric traces of *strep*-MBH measured before (black) and after (blue) addition of methylene blue (10µM) recorded in H_2-saturated PB buffer (10mM) at pH5.5 with a scan rate of 5 mV s^{-1}.

Table 6.2: Adsorption kinetics derived from amide I and amide II bands*

amide band	A_0 (mOD)	A_1 (mOD)	τ_1 (min)
strep-MBH on ITO_{TR}			
1650 cm^{-1}	2.65	2.82 ± 0.17	2.68 ± 0.77
1547 cm^{-1}	2.45	2.59 ± 0.14	3.28 ± 0.42

*Results of fitting the monoexponential function $A = A_0 + A_1 \exp(-t/\tau_1)$ to the time course of the amide I (1650 cm^{-1}, R^2 = 0,99703) and amide II (1547 cm^{-1}, R^2= 0,99703) band intensities during strep-MBH absorption in the time period $0 < t < 30$ min.

Similar to the band positions of his-MBH observed on ITO_{TR} amide I and amide II bands are centered at 1650 cm^{-1} and 1547 cm^{-1}, respectively, and exhibit also the same band features, which will be elucidated in more detail in section 7.2. Contrarily to the previously discussed his-MBH (see Fig. 6.16), *strep*-MBH adsorbs rapidly in a monoexponential manner with a fast

kinetic as displayed in Figure 6.16B. The corresponding results of the fit are summarized in Table 6.2. The monoexponential fit reveals a time constant of 2.68 min for the amide I band intensity, which appears relatively fast compared to the kinetics of his-MBH adsorption (Table 6.2). Already the second spectrum taken after 6 min of protein incubation shows a practically completed *strep*-MBH adsorption demonstrated. An extension of the incubation time does not affect the amide band intensities, thus no further increase of the protein coverage on the ITO_{TR} surface can be monitored. This fast adsorption behavior was already observed non-tagged cyt c on several ITO_{TR} as well as ATO (chapter 5). Thereby, the non-tagged cyt c electrostatically bound to the TCO surfaces. ATR-IR spectra of the electrostatically bound *strep*-MBH displays a CO absorption band at 1948 cm^{-1}, characteristic of the Ni_r-B state of the active site (Figure 6.16C). Compared to the active site spectrum of his-MBH on ITO_{TR}, the *strep*-MBH does not exhibit any partially reduced state EPR silent Ni(+2)-S state with a CO vibrational band at 1934 cm^{-1} upon its interaction with the ITO_{TR} surface. Related cyclic voltammograms reveal the characteristic sigmoidal shape characteristic for H_2 oxidation catalysis (Fig. 6.16D). After 30 min of *strep*-MBH adsorption on ITO_{TR}, only a weak DET process for the H_2 oxidation is observable. Even though, minor amounts of HER below -200 mV can be detected, the HER compared to HOR current densities is not pronounced as can be observed for his-MBH bound to ITO_{TR}. Upon mediator addition, a significant increase in current density along the entire voltammetric trace can be observed. The displayed current densities for MET as well as the DET are both increased when methylene blue (MB) is added to the electrolyte solution. Since the MB is a compatible mediator for the H_2 oxidation reaction with the reduction potential of its redox couple situated in the region of the maximum H_2 uptake of the *Re* MBH (around +80mV). This effect can be clearly observed via the sudden increase of current density at 80 mV (Fig. 6.16D). Thus, a high fraction of the immobilized *strep*-MBH is adsorbed initially in an unfavored orientation. Additions of mediator lead to a significant increase of the current densities over the entire potential range, also characteristic for DET from -340 mV to + 310mV. Both, slightly HER by 30% (below -200mV), as well as the H_2 oxidation by 50% (above -200 mV), are increased upon addition of MB. MB as a hydrophobic molecule can also interact with the hydrophobic parts of *strep*-MBH e.g. the large hydrophobic tail, or even hydrophobic fractions of the ITO_{TR} surface. In such way, a certain reorganization of the enzyme molecules on the surface towards a more optimized orientation for DET processes might be induced. However, even upon anchoring, at least a fraction of the immobilized enzyme remains in an unfavorable orientation for DET.

Also, a series of electrochemical experiments was carried out, varying thereby the incubation time for *strep*-MBH on ITO_{TR} to reveal the most efficient immobilization conditions. *Strep*-MBH on ITO_{TR} showed maximum catalytic efficiencies after an adsorption time of 5 min (see appendix Fig. A6.5). An effect after mediator addition was observed for all incubation times.

6.3.2 Preactivation of *strep*-tagged MBH on ITO_{TR}

A subsequent preactivation step at a potential of -340 mV vs SHE was also applied for *strep*-MBH after its immobilization on ITO_{TR}. Figure 6.17 displays the two subsequent CVs of *strep*-MBH on the ITO_{TR} electrode under H_2 atmosphere with the first CV before (black) and a second after (red) a potential application of -340 mV for 5 min under H_2 resulted in a drastic decrease of the current density, similar to those observations made after preactivation of his-MBH on ITO_{TR}, see section 6.13.

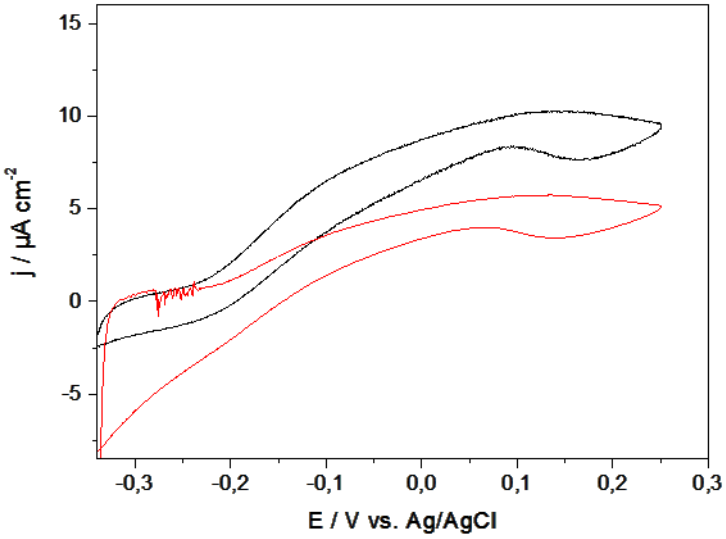

Figure 6.17: Cyclic voltammetric studies of *strep*-MBH bound to ITO_{TR}, measured before (black) and after (red) a subsequent 5 min preactivation step at -340 mV in the presence of H_2. All voltammetric measurements were carried out in 10 mM PB buffer at room temperature and with a scan rate of 5 mV s^{-1}.

For both, his-MBH and *strep*-MBH bound via coordination and electrostatic interactions to the metal oxide surface, respectively, the current densities decreased in general upon consecutive cycling, which is also reported for *Re* MBH adsorbed on PGE in the works of Vincent and Armstrong.[33] The catalytic current for *strep*-MBH on ITO_{TR} decreases by 50% after only 5 min of potential application. In contrast, the corresponding current decrease for selective bound his-MBH under same conditions was just 12%.

6.3.3 Conclusions

Compared to the coordinatively bound his-MBH discussed in 6.2, the electrostatically adsorbed MBH exhibits several differences in its interaction with the ITOTR. This emphasizes the importance of a selective binding, as direct and fast ET via the semiconductor platform is observed for his-MBH binding on ITO_{TR}. *Strep*-MBH binds rapidly to the ITO_{TR} surface with a mono-exponential kinetic rate. The active site can be monitored by one CO stretching mode after adsorption, which is characteristic of the oxidized Nir-B state, although its intensity is quite low. In addition to the IR spectroscopic observation of a fast *strep*-MBH adsorption, the corresponding subsequently recorded CVs with and without mediator suggests a broad distribution of orientations. The mediator affected not only the observable MET but also led to a re-organization of the adsorbed *strep*-MBH in such way as to also increase the DET. Pre-activation experiments show an instability of the adsorbed *strep*-MBH on ITO_{TR} via the observed loss in current densities of about 50%.

Chapter 7

Comparison of adsorbed protein on Au-SEIRA and ITO_{TR}-ATR electrodes

7.1 Comparisons of spectro-electrochemical surfaces used for Cytochrome c

This last chapter will summarize the findings for cyt c and MBH immobilized on the two different electrode surfaces, the commonly used surface-enhancing nanostructured Au-covered with SAMs and the recently established ITO_{TR} surface, both integrated into a Kretschmann ATR-IR set up.

Cyt c immobilized on SAM-coated Au-electrodes has been extensively studied by SEIRA spectroscopy in the work of [67, 102, 103]. Cyt c and his-cyt c adsorbed on ITO_{TR} surfaces can be compared with respect to their deduced amide I band intensities as well as their corresponding protein coverages relative to the already obtained values of cyt c on SEIRA sensitive SAM-coated Au-electrodes in reference [102] (Table 7.1).

Table 7.1: Cyt *c* surface coverages and amide I band intensities*

surface	coverage (Γ) pmol cm^{-2}	amide I intensity mOD	amide I / coverage mOD cm^2 $pmol^{-1}$	reference
Au-C_{11}COOH – cyt *c*	9 (CV)	14 (SEIRA)	1.56	[102]
ITO_{TR}– cyt c	4.5 (UV-Vis)	0.6 (ATR)	0.11	this work/ chapter 5
ITO_{TR}– his-cyt c	16.0 (UV-Vis)	1.49 (ATR)	0.10	this work/ chapter 5
SiO_x – his-cyt c	10.4 (UV-Vis)	1.1 (ATR)	0.11	This work/ appendix

*Comparison of cyt c on Au-SAM, cyt c on ITO_{TR} and his-cyt c on ITO_{TR}. Methods applied to determine protein coverage are denoted in brackets. Amide I band intensities are also normalized to the corresponding enzyme's surface coverage. For determination of his-MBH coverage on SiOx by UV-Vis see appendix Fig. A.18.

Table 7.1 displays the values for protein coverages and amide I absorbance intensities of cyt c on Au-SAM and (his-)cyt c on ITO_{TR} surfaces. The normalization of the amide I band intensity to the surface coverage value (amide I/coverage) represents a crude estimation of the molecular absorption of the immobilized enzyme. Thereby, it allows a comparison of immobilized enzyme on Au-electrodes used for SEIRA spectroscopy and ITO_{TR}-ATR electrodes. Cyt c and his-cyt c on the ITO_{TR}, as well as his-cyt c on oxidized Si-prism, show all consistently the same values of 0.1 mOD cm^2 $pmol^{-1}$. In comparison, cyt c on Au-SAM exhibits approximately 16 times higher absorbance intensity normalized to the determined coverages. Thus, surface-enhancement of cyt c on the SAM-modified nanostructured Au can be roughly estimated by a factor of about 16 compared to the (his-)cyt c on ITO_{TR} measured in ATR-IR modus. In this first crude estimation of the molecular aborbances for the different spectro-electrochemical platforms, the contribution of angular and surface distance dependencies of the SEIRA absorption are disregarded. However, the estimated value for an enhancement of the surface sensitive Au in the SEIRAs studies compared to ITO_{TR} used for ATR investigations agrees well with the enhancement factor of about 20 observed stated by Osawa [267, 112] and Hartstein[99], which were obtained by comparing adsorbed SAMs on surface-enhancing Au electrodes with SAMs in solution studied in transmission–IR. It also has to be noted that the coverage of cyt c on Au-SAM was previously determined by CV and an accurate value can only be then obtained,

if all adsorbed cyt c molecules are electrochemically active i.e. oriented for exclusive DET on the electrode surface and preserved in its native state. In contrast, the cyt c and his-cyt c coverage on ITO_{TR} were determined via UV-Vis spectroscopy, measuring the protein incubation solution with a known concentration before and after enzyme immobilization. by means of the UV-Vis concentration, the determined protein coverage includes the quantification of all electrochemically active, as well as inactive proteins, which might lead to an error comparing to the electrochemically determined protein coverage. The attempts to determine cyt c and his-cyt c coverage on ITO_{TR} surfaces electrochemically did not result in any clear detectable redox signals in the corresponding CVs.

An adsorption of his-cyt c on the oxidized Si-prism (without the layer of ITO_{TR}) also reveals a very similar ratio for in its amide I band intensity (see Figure 5.10) relative to the surface coverage determined by UV-Vis spectroscopic measurements of the SAM solution before and incubation, just in same manners as described before. Since similar amide I band intensity/coverage ratios are observed for cyt c and his-cyt c on planar ITO_{TR} as well as on the undoped Si crystal a surface-enhancement caused by the thin ITO_{TR} film can be excluded. Previously, plasmonic effects on highly doped ITO were discussed in literature, presumably induced by either highly doping effects or material design.[308, 317, 318] In the case of the latter, surface-enhanced IR Spectroscopy of ITO could be performed by means of confined ITO antennas [319, 320, 321] as also shown for SERS.[322] In conclusion, contrarily to the highly doped ITO in literature an enhancement in the MIR region at the surface of the ITO_{TR} material seems highly unlikely.

7.2 Comparison of electrode surfaces suitable for spectro-electrochemical studies on Membrane-Bound [NiFe] Hydrogenase from *Re*

Similar to the discussion in the previous subchapter amide I band intensities and surfaces coverages of various *Re* MBH variants immobilized on different electrodes for spectro-electrochemical studies are compared in Table 7.2. Namely, *strep*-MBH data on Au-SAM surfaces from previous SEIRAS studies (see chapter 4) are compared to *strep*- and his-MBH IR studies on ITO_{TR} (see chapter 6), at which the spectral data is obtained in a modified ATR-IR setup.

The amide I band intensity normalized to the surface coverage (amide I/coverage) gives a rough idea of the molecular absorption of the immobilized enzyme, and thereby allows to estimate an enhancement factor by a comparison of spectral SEIRA and ATR-IR data. Indeed, *strep*-MBH bound to on both Au-SAM surfaces, Au-C_6NH_2 and Au-C_5COOH, reveals almost identical values of 14.3 and 14.4 mOD cm^2 $pmol^{-1}$, respectively. Also *strep*- and his-MBH on ITO_{TR} exhibits similar amide I/coverage ratio values of 9.3 and 9.7 mOD cm^2 $pmol^{-1}$. Since the use of the amide I/coverage ratio is a very crude estimate for the determining a surface enhancement, a more appropriate estimation was calculated by the integrated amide I band intensity per enzyme unit, including the investigated areas for each ATR- and SEIRA measurement and the number of adsorbed molecules calculated from the surface coverage.

Table 7.2: MBH surfaces coverages on different bio-compatible electrodes compared to amide I band intensities*

surface	coverage (Γ) pmol cm^{-2}	amide I intensity mOD	amide I / coverage mOD cm^2 $pmol^{-1}$	Integrated amide I band intensity / enzyme unit
Au-C_6NH_2 – *strep*-MBH	0.44 (AFM)	6.3 (SEIRA)	14.3	3.8 10^{-12}
Au-C_5COOH – *strep*-MBH	0.09 (AFM)	1.3 (SEIRA)	14.4	4.7 10^{-12}
ITO_{TR}– *strep*-MBH	0.29 (UV-Vis)	2.7 (ATR)	9.3	5.2 10^{-12}
ITO_{TR}– his-MBH	0.36 (UV-Vis)	3.5 (ATR)	9.7	2.6 10^{-12}

*Comparison of available date for *strep*-MBH on Au-SAM, on ITO_{TR} and his-MBH on ITO_{TR}. Methods for the determination of protein coverage are denoted in brackets. Furthermore, the integrated amide band intensity per enzyme unit is estimated.

Also, these values are located in very similar ranges independent of the type of spectroscopic technique (SEIRAs or normal ATR measurement). Compared to the cyt c findings, *vide supra*, where a maximum enhancement factor of 16 could be estimated, the same spectroscopic technique reveals much lower values for the larger MBH protein. A reason for this discrepancy regarding the enhancement factor may origin from the diverging protein sizes. The amide bands encode the secondary structure of the protein and arise from couple amide bond vibrations of the polypeptide chain. Since surface enhancement declines rapidly with distance (d) correlated with d^{-6} and the signal decays within a maximum distance of 8 nm from the surface, the impacting on small proteins/molecules located close at the surface is higher compared to larger molecules. In contrast, ATR-IR is known for an exponential decay of the evanescent wave within the µm range. Therefore, an enhancement will be stronger for small molecules, which are situated in close proximity to the surface. The larger the molecule is, the smaller the contribution of the relative enhancement. For cyt c a size of 3.4 nm is reported,[323] while the MBH with 7-10 nm exhibits almost twice the size of a cyt c molecule. This may be the reason for the observed hardly enhanced absorption intensities per enzyme unit of MBH on Au-SAM, whereas, for the half sized cyt c, the enhancement still affects the observable signal intensities drastically. The effect and possible contributions of a surface enhancement by SEIRA spectroscopy in contrast to ATR-IR studies on ITO_{TR} becomes evident within a closer look at the amide band positions of the adsorbed MBH.

Fig. 7.1 shows the absorbance spectra and the corresponding second derivative of these spectra in spectral region characteristic for the the amide I and II bands of *strep*-MBH immobilized on all five different Au-SAM surfaces monitored by SEIRA as discusses in chapter 4 and of *strep*-MBH as well as his-MBH on ITO_{TR} measured by ATR-IR spectroscopy, in chapter 5. However, distinct differences can be observed for the corresponding amide band positions. SEIRA spectra display shifts of the MBH amide I and amide II bands of about 10 cm^{-1} and 4 cm^{-1} to higher wavenumbers, respectively, compared to MBH immobilized on ITO_{TR}. The second derivative (Fig. 7.1B) disentangles distinctive amide band positions more easily, while in the corresponding absorbance spectra strong band overlaps are dominating, and thus do not allow proper assignments. Fig. 7.1B reveals that the absorptions of the secondary structure elements contributing to the enveloping amide I and II bands are located at exactly the same positions. The apparent shifts in the original absorbance spectra (Fig. 7.1A) are therefore more likely

due to a diversely pronounced enhancement of the various secondary structure elements of the protein backbone, which dependents on the particular orientation and the relative distance to Au surface, according to surface selection rules. Hence, the apparent amide band positions in the absorbance spectrum differ.

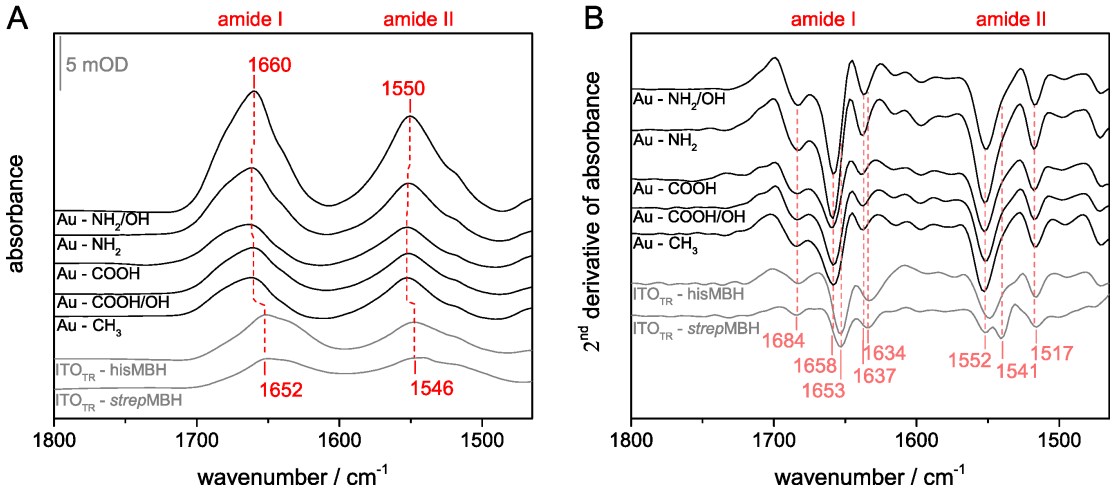

Figure 7.1: (A) SEIRA spectra of *strep*-MBH on different SAMs (black) compared to ATR-IR spectra of his-MBH and *strep*-MBH on ITO_{TR} surface (gray) after 30 min of immobilization with (B) the corresponding second derivatives of the spectra.

For a comparison of the catalytic efficiency, the turnover frequency (k_{cat}) of *Re* MBH on all different electrode surfaces with known coverage was calculated and summarized in Table 7.3. It has to be noted that the electrochemical measurements were performed on stationary electrodes. Since diffusion is the strongest limiting factor for stationary electrodes, the determined k_{cat} is used here as an indication of the efficiency of interfacial ET upon MBH–surface interaction. However, these k_{cat} values cannot be compared to the corresponding values in other works, where rotating disc electrodes are used, that overcome the diffusion limitation.

Table 7.3: Overview on *Re* MBH turnover frequencies on different electrode surfaces*

surface	coverage (Γ) pmol cm²	amide I intensity mOD	j_{max} µA cm²	k_{cat} s^{-1}
Au-C_5NH_2 – *strep*-MBH	0.44 (AFM)	6.3 (SEIRA)	2.0	24
Au-C_5COOH – *strep*-MBH	0.09 (AFM)	1.3 (SEIRA)	1.0	58
ITO_{TR}– *strep*-MBH	0.29 (UV-Vis)	2.7 (ATR)	3.1	54
ITO_{TR}– his-MBH	0.36 (UV-Vis)	3.5 (ATR)	13.0	187

*Comparison of values for surface coverage (Γ), amide I band intensity, maximal current densities (j_{max}) and the resulting turnover frequencies (k_{cat}), which were determined for *strep*-MBH on Au-SAM, on ITO_{TR} as well as his- MBH on ITO_{TR}. Applied methods for the protein coverage determination are denoted in brackets.

The maximum turnover frequency, k_{cat}, was calculated for stationary electrodes by

$k_{cat} = \frac{j_{max}}{nF\Gamma}$

with jmax as maximum current density, n is the number of transferred electrons in the catalytic reaction and F is the faraday constant (96 485 C mol^{-1}). The determined k_{cat} show the lowest value for the MBH adsorbed on NH_2-coated surface, which was estimated already due to its orientational drawback suggesting a slow ET in chapter 4. In surprisingly well agreement is the corresponding values for *Re* MBH adsorbed on negatively charged Au-C_5COOH as well as adsorbed on ITO_{TR} with k_{cat} of 58 s^{-1} and 54 s^{-1}. If the surface of a metal oxide is not pretreated, the surfaces contain mixtures of functional groups such as hydroxyl or carboxylic groups. Even though the exact distribution and the amount of functional groups of ITO_{TR} surface are not known, the corresponding k_{cat} values are similar. The turnover frequency of his-MBH on PGE electrode could not be determined here, since an enzyme coverage was not estimated.

Table 7.4 displays the observed OCP values for *strep*-MBH on Au-SAMs and ITO_{TR} as well as his-MBH on ITO_{TR} under Ar and H_2. As discussed previously, a correlation between OCP and catalytic efficiencies depending on the enzyme-surface interaction can be derived.

Table 7.4: MBH turnover frequency and reported open circuit potentials under Ar and H_2*

surface	coverage (Γ) pmol cm^{-2}	k_{cat} s^{-1}	$E_{OCP}(Ar)$ mV (vs SHE)	$E_{OCP}(H_2)$ mV (vs SHE)
Au-C_6NH_2 – *strep*-MBH	0.44 (AFM)	24	+130	-40
Au-C_5COOH – *strep*-MBH	0.09 (AFM)	58	+130	-240
ITO_{TR}– *strep*-MBH	0.29 (UV-Vis)	54	+300	-240
ITO_{TR}– his-MBH	0.36 (UV-Vis)	187	+300	-290

*Comparison of values for surface coverage (Γ), turnover frequencies (k_{cat}) and open circuit potentials observed under Ar ($E_{OCP}(Ar)$) and H_2 ($EOCP(H_2)$) atmosphere, determined for *strep*-MBH on Au-SAM, on ITO_{TR} and his-MBH on ITO_{TR}. Chosen methods for the protein coverage determination are denoted in brackets.

Thereby, the lowest OCP value might indicate the best so far achieved enzyme-surface interaction, exhibiting an adequate direct and fast ET from the enzymes to the electrode surface. This is based on the hypothesis discussed in literature, that the closer the OCP to the redox potential of the enzyme or of a predominant reaction which is taking place, the more efficient the DET occurs between enzyme and the surface.[241] In case of the hydrogenase, the OCP can be used as a guideline representing the zero net current. The closer the OCP to the zero net current (onset potential), the better is the DET efficiency. In fact, also the previously conducted experiments on Au modified surfaces could verify a correlation of the observed OCP of adsorbed *Re* MBH on diverse surfaces with the efficiency of the DET (see chapter 4). In this respect, preferential orientations through the transmembrane helix, either *strep*-tag or his-tag, apparently provide not only a homogeneous orientational distribution but also an efficient heterogeneous ET between electrode and enzyme.

For the sake of completeness, it is worth to mention that enzyme coverage is also known to affect the OCP value.[241] The smaller the enzyme coverage is, the higher becomes the expected OCP value. However, AFM experiments showed loadings of similar values for his-MBH on ITO_{TR} and *strep*-MBH on SAM-coated Au. Therefore, the effect of enzyme coverage on the OCP can be assumed to be negligible in the present case.

7.3 Conclusions

In conclusion, the simple ATR-IR setup in a Kretschmann configuration is a powerful alternative method for monitoring protein (sub)monolayers on planar surfaces without the need for any plasmonic enhancement. Furthermore, a certain surface sensitivity can be achieved for this chosen set up. *In situ* measurements following the immobilization process as well as electrochemical characterization could be performed without the interference of water bands, which are usually a problem during ATR experiments, especially on adsorbed (sub)monolayer species.

In contrast to the exponential decay of the signal intensity in ATR-IR spectroscopy, the surface enhancement of the IR signal in SEIRA spectroscopy decays more rapidly by a factor of d^{-6}. The larger the adsorbed enzyme on the Au surface, the smaller the impact of the enhancement effect on the absolute intensity of amide I and amide II bands. The SEIRA effect becomes most evident when comparing the secondary structure component intensities, which resulted in a shift of centered amide I and amide II bands. The enhancement effect in SEIRA spectroscopy can be advantageous when estimating orientations as a result of the angular selection rule, but cannot provide immediate quantitative determination. The latter can be easier achieved by ATR-IR spectroscopy and optical theory.

In future, an enhancement of spectral intensity could be achieved by an increasing protein loading for example by providing larger surfaces within 3D materials. Replacing planar TCO films by thin porous materials should easily lead to greater signal intensities. Thus, some of those 3D materials based on ITO_{TR} were tested for *strep*-MBH immobilization. Initial results are displayed in appendix Fig. A.19, A.20.

Bibliography

[1] Wolfgang Lubitz, Hideaki Ogata, Olaf Rudiger, and Edward Reijerse. Hydrogenases. *Chemical reviews*, 114(8):4081–4148, 2014.

[2] Tymoczko Berg. Stryer: Biochemie, spektrum, akad, 2003.

[3] Christophe Leger and Patrick Bertrand. Direct electrochemistry of redox enzymes as a tool for mechanistic studies. *Chemical reviews*, 108(7):2379–2438, 2008.

[4] Shi-Gang Sun, Paul A Christensen, and Andrzej Wieckowski. *In-situ spectroscopic studies of adsorption at the electrode and electrocatalysis*. Elsevier, 2011.

[5] M. Saggu, I. Zebger, M. Ludwig, O. Lenz, B. Friedrich, P. Hildebrandt, and F. Lendzian. Spectroscopic insights into the oxygen-tolerant membrane-associated [nife] hydrogenase of ralstonia eutropha h16. *Journal of Biological Chemistry*, 284(24):16264, 2009.

[6] D. Moss, E. Nabedryk, J. Breton, and W. Mï¿½ntele. Redox-linked conformational changes in proteins detected by a combination of infrared spectroscopy and protein electrochemistry. *European Journal of Biochemistry*, 187(3):565–572, 1990.

[7] F. Baymann, D.A. Moss, and W. Maentele. An electrochemical assay for the characterization of redox proteins from biological electron transfer chains. *Analytical biochemistry*, 199(2):269–274, 1991.

[8] Marjory Stephenson and Leonard Hubert Stickland. Hydrogenase: a bacterial enzyme activating molecular hydrogen: The properties of the enzyme. *Biochemical Journal*, 25(1):205, 1931.

[9] T. Buhrke, S. Loescher, O. Lenz, E. Schlodder, I. Zebger, L.K. Andersen, P. Hildebrandt, W. Meyer-Klaucke, H. Dau, B. Friedrich, et al. Reduction of unusual iron-sulfur clusters in the h2-sensing regulatory ni-fe hydrogenase from ralstonia eutropha h16. *Journal of Biological Chemistry*, 280(20):19488, 2005.

[10] Richard Cammack. The catalytic machinery. *Hydrogen as a Fuel. Learning from Nature*, pages 159–180, 2001.

[11] Paulette M Vignais, Bernard Billoud, and Jacques Meyer. Classification and phylogeny of hydrogenases. *FEMS microbiology reviews*, 25(4):455–501, 2001.

[12] Hannah S Shafaat, Olaf Ruediger, Hideaki Ogata, and Wolfgang Lubitz. [nife] hydrogenases: a common active site for hydrogen metabolism under diverse conditions. *Biochimica et Biophysica Acta (BBA)-Bioenergetics*, 1827(8):986–1002, 2013.

[13] Bent Sørensen. *Hydrogen and fuel cells: emerging technologies and applications*. Academic Press, 2011.

[14] John Benemann. Hydrogen biotechnology: progress and prospects. *Nature biotechnology*, 14(9):1101–1103, 1996.

[15] PP Edwards, VL Kuznetsov, and WIF David. Hydrogen energy. *Philosophical Transactions of the Royal Society of London A: Mathematical, Physical and Engineering Sciences*, 365(1853):1043–1056, 2007.

[16] Anne K Jones, Emma Sillery, Simon PJ Albracht, and Fraser A Armstrong. Direct comparison of the electrocatalytic oxidation of hydrogen by an enzyme and a platinum catalyst. *Chemical Communications*, (8):866–867, 2002.

[17] Kylie A Vincent, James A Cracknell, Oliver Lenz, Ingo Zebger, Baerbel Friedrich, and Fraser A Armstrong. Electrocatalytic hydrogen oxidation by an enzyme at high carbon monoxide or oxygen levels. *Proceedings of the National Academy of Sciences of the United States of America*, 102(47):16951–16954, 2005.

[18] Maria-Eirini Pandelia, Pascale Infossi, Marie Therese Giudici-Orticoni, and Wolfgang Lubitz. The oxygen-tolerant hydrogenase i from aquifex aeolicus weakly interacts with carbon monoxide: an electrochemical and time-resolved ftir study. *Biochemistry*, 49(41):8873–8881, 2010.

[19] Gabrielle Goldet, Annemarie F Wait, James A Cracknell, Kylie A Vincent, Marcus Ludwig, Oliver Lenz, Baerbel Friedrich, and Fraser A Armstrong. Hydrogen production under aerobic conditions by membrane-bound hydrogenases from ralstonia species. *Journal of the American Chemical Society*, 130(33):11106–11113, 2008.

[20] AA Karyakin, SV Morozov, EE Karyakina, NA Zorin, VV Perelygin, and S Cosnier. Hydrogenase electrodes for fuel cells. *Biochemical Society Transactions*, 33(1):73–75, 2005.

[21] Kylie A Vincent, Natalie A Belsey, Wolfgang Lubitz, and Fraser A Armstrong. Rapid and reversible reactions of [nife]-hydrogenases with sulfide. *Journal of the American Chemical Society*, 128(23):7448–7449, 2006.

[22] A Ciaccafava, A De Poulpiquet, V Techer, MT Giudici-Orticoni, S Tingry, C Innocent, and E Lojou. An innovative powerful and mediatorless h 2/o 2 biofuel cell based on an outstanding bioanode. *Electrochemistry Communications*, 23:25–28, 2012.

[23] Paulette M Vignais and Bernard Billoud. Occurrence, classification, and biological function of hydrogenases: an overview. *Chemical reviews*, 107(10):4206–4272, 2007.

[24] Paula Tamagnini, Rikard Axelsson, Pia Lindberg, Fredrik Oxelfelt, Roebbe Wuenschiers, and Peter Lindblad. Hydrogenases and hydrogen metabolism of cyanobacteria. *Microbiology and Molecular Biology Reviews*, 66(1):1–20, 2002.

[25] Paula Tamagnini, Elsa Leitaeo, Paulo Oliveira, Daniela Ferreira, Filipe Pinto, David James Harris, Thorsten Heidorn, and Peter Lindblad. Cyanobacterial hydrogenases: diversity, regulation and applications. *FEMS microbiology reviews*, 31(6):692–720, 2007.

[26] Rudolf K Thauer, Anne-Kristin Kaster, Meike Goenrich, Michael Schick, Takeshi Hiromoto, and Seigo Shima. Hydrogenases from methanogenic archaea, nickel, a novel cofactor, and h2 storage. *Annual review of biochemistry*, 79:507–536, 2010.

[27] L-F Wu and MA Mandrand. Microbial hydrogenases: primary structure, classification, signatures and phylogeny. *FEMS microbiology reviews*, 10(3-4):243–269, 1993.

[28] J.C. Fontecilla-Camps, A. Volbeda, C. Cavazza, and Y. Nicolet. Structure/function relationships of [nife]-and [fefe]-hydrogenases. *Chemical reviews*, 107(10):4273–4303, 2007.

[29] Juan C Fontecilla-Camps, Patricia Amara, Christine Cavazza, Yvain Nicolet, and Anne Volbeda. Structure–function relationships of anaerobic gas-processing metalloenzymes. *Nature*, 460(7257):814–822, 2009.

[30] Beatrix Schwoerer, Victor M Fernanez, Carmen Zirngibl, and Rudolf K Thauer. H2-forming n5, n10-methylenetetrahydromethanopterin dehydrogenase from methanobacterium thermoautotrophicum. *European Journal of Biochemistry*, 212(1):255–261, 1993.

[31] Seigo Shima, Oliver Pilak, Sonja Vogt, Michael Schick, Marco S Stagni, Wolfram Meyer-Klaucke, Eberhard Warkentin, Rudolf K Thauer, and Ulrich Ermler. The crystal structure of [fe]-hydrogenase reveals the geometry of the active site. *Science*, 321(5888):572–575, 2008.

[32] Randolph P Happe, Winfried Roseboom, Antonio J Pierik, Simon PJ Albracht, Kimberly A Bagley, et al. Biological activation of hydrogen. *Nature*, (385):126–126, 1997.

[33] K.A. Vincent, A. Parkin, and F.A. Armstrong. Investigating and exploiting the electrocatalytic properties of hydrogenases. *Chemical reviews*, 107(10):4366–4413, 2007.

[34] Antonio L De Lacey, Victor M Fernandez, Marc Rousset, and Richard Cammack. Activation and inactivation of hydrogenase function and the catalytic cycle: spectroelectrochemical studies. *Chemical reviews*, 107(10):4304–4330, 2007.

[35] Gabrielle Goldet, Caterina Brandmayr, Sven T Stripp, Thomas Happe, Christine Cavazza, Juan C Fontecilla-Camps, and Fraser A Armstrong. Electrochemical kinetic investigations of the reactions of [fefe]-hydrogenases with carbon monoxide and oxygen: comparing the importance of gas tunnels and active-site electronic/redox effects. *Journal of the American Chemical Society*, 131(41):14979–14989, 2009.

[36] Sven T Stripp, Gabrielle Goldet, Caterina Brandmayr, Oliver Sanganas, Kylie A Vincent, Michael Haumann, Fraser A Armstrong, and Thomas Happe. How oxygen attacks [fefe] hydrogenases from photosynthetic organisms. *Proceedings of the National Academy of Sciences*, 106(41):17331–17336, 2009.

[37] Thorsteinn I Sigfusson. Pathways to hydrogen as an energy carrier. *Philosophical Transactions of the Royal Society of London A: Mathematical, Physical and Engineering Sciences*, 365(1853):1025–1042, 2007.

[38] Tanja Burgdorf, Oliver Lenz, Thorsten Buhrke, Eddy Van Der Linden, Anne K Jones, Simon PJ Albracht, and Baerbel Friedrich. [nife]-hydrogenases of ralstonia eutropha h16: modular enzymes for oxygen-tolerant biological hydrogen oxidation. *Journal of molecular microbiology and biotechnology*, 10(2-4):181–196, 2006.

[39] Rainer Cramm. Genomic view of energy metabolism in ralstonia eutropha h16. *Journal of molecular microbiology and biotechnology*, 16(1-2):38–52, 2008.

[40] Jens Appel, Saranya Phunpruch, Klaus Steinmuller, and Rudiger Schulz. The bidirectional hydrogenase of synechocystis sp. pcc 6803 works as an electron valve during photosynthesis. *Archives of microbiology*, 173(5-6):333–338, 2000.

[41] Lucas J Stal and Roy Moezelaar. Fermentation in cyanobacteria. *FEMS microbiology reviews*, 21(2):179–211, 1997.

[42] Olga Troshina, Larissa Serebryakova, Marina Sheremetieva, and Peter Lindblad. Production of h 2 by the unicellular cyanobacterium gloeocapsa alpicola calu 743 during fermentation. *International Journal of Hydrogen Energy*, 27(11):1283–1289, 2002.

[43] MICHAEL Kuhn, A Steinbuchel, and HANS G Schlegel. Hydrogen evolution by strictly aerobic hydrogen bacteria under anaerobic conditions. *Journal of bacteriology*, 159(2):633–639, 1984.

[44] Simon PJ Albracht. Intimate relationships of the large and the small subunits of all nickel hydrogenases with two nuclear-encoded subunits of mitochondrial nadh: ubiquinone oxidoreductase. *Biochimica et Biophysica Acta (BBA)-Bioenergetics*, 1144(2):221–224, 1993.

[45] Simon PJ Albracht. Nickel hydrogenases: in search of the active site. *Biochimica et Biophysica Acta (BBA)-Bioenergetics*, 1188(3):167–204, 1994.

[46] Simon PJ Albracht, A Mariette, and Ph de Jong. Bovine-heart nadh: ubiquinone oxidoreductase is a monomer with 8 fe-s clusters and 2 fmn groups. *Biochimica et Biophysica Acta (BBA)-Bioenergetics*, 1318(1):92–106, 1997.

[47] Philippe Constant, Soumitra Paul Chowdhury, Jennifer Pratscher, and Ralf Conrad. Streptomycetes contributing to atmospheric molecular hydrogen soil uptake are widespread and encode a putative high-affinity [nife]-hydrogenase. *Environmental microbiology*, 12(3):821–829, 2010.

[48] Philippe Constant, Soumitra Paul Chowdhury, Laura Hesse, Jennifer Pratscher, and Ralf Conrad. Genome data mining and soil survey for the novel group 5 [nife]-hydrogenase to explore the diversity and ecological importance of presumptive high-affinity h2-oxidizing bacteria. *Applied and environmental microbiology*, 77(17):6027–6035, 2011.

[49] Caspar Schaefer, Baerbel Friedrich, and Oliver Lenz. Novel, oxygen-insensitive group 5 [nife]-hydrogenase in ralstonia eutropha. *Applied and environmental microbiology*, 79(17):5137–5145, 2013.

[50] Diplom-Ingenieur Biotechnologie and Marius Horch. Structure-function relationships of metalloenzymes.

[51] Oliver Lenz, Marcus Ludwig, Torsten Schubert, Ingmar Burstel, Stefanie Ganskow, Tobias Goris, Alexander Schwarze, and Barbel Friedrich. H2 conversion in the presence of o2 as performed by the membrane-bound [nife]-hydrogenase of ralstonia eutropha. *ChemPhysChem*, 11(6):1107–1119, 2010.

[52] Johannes Fritsch, Oliver Lenz, and Barbel Friedrich. Structure, function and biosynthesis of o2-tolerant hydrogenases. *Nature Reviews Microbiology*, 11(2):106–114, 2013.

[53] Oliver Lenz, Andrea Gleiche, Angelika Strack, and Baerbel Friedrich. Requirements for heterologous production of a complex metalloenzyme: the membrane-bound [nife] hydrogenase. *Journal of bacteriology*, 187(18):6590–6595, 2005.

[54] Anne Volbeda, Elsa Garcin, Claudine Piras, Antonio L de Lacey, Victor M Fernandez, E Claude Hatchikian, Michel Frey, and Juan Carlos Fontecilla-Camps. Structure of the [nife] hydrogenase active site: Evidence for biologically uncommon fe ligands. *Journal of the American Chemical Society*, 118(51):12989–12996, 1996.

[55] Yael Montet, Patricia Amara, Anne Volbeda, Xavier Vernede, E Claude Hatchikian, Martin J Field, Michel Frey, and Juan C Fontecilla-Camps. Gas access to the active site of ni-fe hydrogenases probed by x-ray crystallography and molecular dynamics. *Nature structural biology*, 4(7):523, 1997.

[56] Isaiah Sumner and Gregory A Voth. Proton transport pathways in [nife]-hydrogenase. *The Journal of Physical Chemistry B*, 116(9):2917–2926, 2012.

[57] Anne Volbeda, Juan C Fontecilla-Camps, Martin J Field, et al. A qm/mm study of proton transport pathways in a [nife] hydrogenase. *Proteins: Structure, Function, and Bioinformatics*, 73(1):195–203, 2008.

[58] T. Goris, AM. Wait, M.F. Saggu, J Fritsch, N. Heidary, M. Stein, I. Zebger, F. Lendzian, F.A. Armstrong, B. Friedrich, and O. Lenz. A unique iron-sulfur cluster is crucial for oxygen tolerance of a [nife]-hydrogenase. *Nature Chemical Biology*, 7:310–318, 2011.

[59] Johannes Fritsch, Patrick Scheerer, Stefan Frielingsdorf, Sebastian Kroschinsky, Baerbel Friedrich, Oliver Lenz, and Christian MT Spahn. The crystal structure of an oxygen-tolerant hydrogenase uncovers a novel iron-sulphur centre. *Nature*, 479(7372):249–252, 2011.

[60] Stefan Frielingsdorf, Torsten Schubert, Anne Pohlmann, Oliver Lenz, and Barbel Friedrich. A trimeric supercomplex of the oxygen-tolerant membrane-bound [nife]-hydrogenase from ralstonia eutropha h16. *Biochemistry*, 50(50):10836–10843, 2011.

[61] Marianne Brugna-Guiral, Pascale Tron, Wolfgang Nitschke, Karl-Otto Stetter, Benedicte Burlat, Bruno Guigliarelli, Mireille Bruschi, and Marie Therese Giudici-Orticoni. [nife] hydrogenases from the hyperthermophilic bacterium aquifex aeolicus: properties, function, and phylogenetics. *Extremophiles*, 7(2):145–157, 2003.

[62] D. Millo, P. Hildebrandt, M.E. Pandelia, W. Lubitz, and I. Zebger. Seira spectroscopy of the electrochemical activation of an immobilized [nife] hydrogenase under turnover and non-turnover conditions. *Angewandte Chemie International Edition*, 50(11):2632–2634, 2011.

[63] Maria-Eirini Pandelia, Vincent Fourmond, Pascale Tron-Infossi, Elisabeth Lojou, Patrick Bertrand, Christophe Leger, Marie-Therese Giudici-Orticoni, and Wolfgang Lubitz. Membrane-bound hydrogenase i from the hyperthermophilic bacterium aquifex aeolicus: enzyme activation, redox intermediates and oxygen tolerance. *Journal of the American Chemical Society*, 132(20):6991–7004, 2010.

[64] Alexandre Ciaccafava, Pascale Infossi, Marianne Ilbert, Marianne Guiral, Sophie Lecomte, Marie Therese Giudici-Orticoni, and Elisabeth Lojou. Electrochemistry, afm, and pm-irra spectroscopy of immobilized hydrogenase: Role of a hydrophobic helix in enzyme orientation for efficient h2 oxidation. *Angewandte Chemie International Edition*, 51(4):953–956, 2012.

[65] Miguel Saggu, Christian Teutloff, Marcus Ludwig, Marc Brecht, Maria-Eirini Pandelia, Oliver Lenz, Baerbel Friedrich, Wolfgang Lubitz, Peter Hildebrandt, Friedhelm Lendzian, et al. Comparison of the membrane-bound [nife] hydrogenases from r. eutropha h16 and d. vulgaris miyazaki f in the oxidized ready state by pulsed epr. *Physical Chemistry Chemical Physics*, 12(9):2139–2148, 2010.

[66] Maria-Eirini Pandelia, Pascale Infossi, Matthias Stein, Marie-Therese Giudici-Orticoni, and Wolfgang Lubitz. Spectroscopic characterization of the key catalytic intermediate ni–c in the o 2-tolerant [nife] hydrogenase i from aquifex aeolicus: evidence of a weakly bound hydride. *Chemical Communications*, 48(6):823–825, 2012.

[67] Nattawadee Wisitruangsakul, Oliver Lenz, Marcus Ludwig, Baerbel Friedrich, Friedhelm Lendzian, Peter Hildebrandt, and Ingo Zebger. Monitoring catalysis of the membrane-bound hydrogenase from ralstonia eutropha h16 by surface-enhanced ir absorption spectroscopy. *Angewandte Chemie International Edition*, 48(3):611–613, 2009.

[68] Ricardo Hidalgo, Philip A Ash, Adam J Healy, and Kylie A Vincent. Infrared spectroscopy during electrocatalytic turnover reveals the ni-l active site state during h2 oxidation by a nife hydrogenase. *Angewandte Chemie*, 127(24):7216–7219, 2015.

[69] Hideaki Ogata, Shun Hirota, Asuka Nakahara, Hirofumi Komori, Naoki Shibata, Tatsuhisa Kato, Kenji Kano, and Yoshiki Higuchi. Activation process of [nife] hydrogenase elucidated by high-resolution x-ray analyses: conversion of the ready to the unready state. *Structure*, 13(11):1635–1642, 2005.

[70] Maurice van Gastel, Matthias Stein, Marc Brecht, Olga Schroder, Friedhelm Lendzian, Robert Bittl, Hideaki Ogata, Yoshiki Higuchi, and Wolfgang Lubitz. A single-crystal endor and density functional theory study of the oxidized states of the [nife] hydrogenase from desulfovibrio vulgaris miyazaki f. *JBIC Journal of Biological Inorganic Chemistry*, 11(1):41–51, 2006.

[71] Anne Volbeda, Lydie Martin, Christine Cavazza, Michael Matho, Bart W Faber, Winfried Roseboom, Simon PJ Albracht, Elsa Garcin, Marc Rousset, and Juan C Fontecilla-Camps. Structural differences between the ready and unready oxidized states of [nife] hydrogenases. *JBIC Journal of Biological Inorganic Chemistry*, 10(3):239–249, 2005.

[72] JW Van der Zwaan, SPJ Albracht, RD Fontijn, and EC Slater. Monovalent nickel in hydrogenase from chromatium vinosum. *FEBS letters*, 179(2):271–277, 1985.

[73] Gerard Davidson, Suranjan B Choudhury, Zhijie Gu, Kurethara Bose, Winfried Roseboom, Simon PJ Albracht, and Michael J Maroney. Structural examination of the nickel site in chromatium vinosum hydrogenase: redox state oscillations and structural changes accompanying reductive activation and co binding. *Biochemistry*, 39(25):7468–7479, 2000.

[74] S. Foerster, M. Stein, M. Brecht, H. Ogata, Y. Higuchi, and W. Lubitz. Single crystal epr studies of the reduced active site of [nife] hydrogenase from desulfovibrio vulgaris miyazaki f. *Journal of the American Chemical Society*, 125(1):83–93, 2003.

[75] Stefanie Foerster, Maurice Van Gastel, Marc Brecht, and Wolfgang Lubitz. An orientation-selected endor and hyscore study of the ni-c active state of desulfovibrio vulgaris miyazaki f hydrogenase. *JBIC Journal of Biological Inorganic Chemistry*, 10(1):51–62, 2005.

[76] Elisabeth Siebert, Marius Horch, Yvonne Rippers, Johannes Fritsch, Stefan Frielingsdorf, Oliver Lenz, Francisco Velazquez Escobar, Friedrich Siebert, Lars Paasche, Uwe Kuhlmann, et al. Resonance raman spectroscopy as a tool to monitor the active site of hydrogenases. *Angewandte Chemie International Edition*, 52(19):5162–5165, 2013.

[77] Marius Horch, Janna Schoknecht, Maria Andrea Mroginski, Oliver Lenz, Peter Hildebrandt, and Ingo Zebger. Resonance raman spectroscopy on [nife] hydrogenase provides structural insights into catalytic intermediates and reactions. *Journal of the American Chemical Society*, 136(28):9870–9873, 2014.

[78] Mario Kampa, Maria-Eirini Pandelia, Wolfgang Lubitz, Maurice van Gastel, and Frank Neese. A metal–metal bond in the light-induced state of [nife] hydrogenases with relevance to hydrogen evolution. *Journal of the American Chemical Society*, 135(10):3915–3925, 2013.

[79] Francois Dole, Andre Fournel, Valerie Magro, E Claude Hatchikian, Patrick Bertrand, and Bruno Guigliarelli. Nature and electronic structure of the ni-x dinuclear center of desulfovibrio gigas hydrogenase. implications for the enzymatic mechanism. *Biochemistry*, 36(25):7847–7854, 1997.

[80] Hongxin Wang, CY Ralston, DS Patil, RM Jones, W Gu, M Verhagen, M Adams, P Ge, C Riordan, CA Marganian, et al. Nickel l-edge soft x-ray spectroscopy of nickel-iron hydrogenases and model compounds evidence for high-spin nickel (ii) in the active enzyme. *Journal of the American Chemical Society*, 122(43):10544–10552, 2000.

[81] Hongxin Wang, Daulat S Patil, Weiwei Gu, Lilian Jacquamet, Stephan Friedrich, Tobias Funk, and Stephen P Cramer. L-edge x-ray absorption spectroscopy of some ni enzymes: probe of ni electronic structure. *Journal of Electron Spectroscopy and Related Phenomena*, 114:855–863, 2001.

[82] Hideaki Ogata, Koji Nishikawa, and Wolfgang Lubitz. Hydrogens detected by sub-atomic resolution protein crystallography in a [lsqb] nife [rsqb] hydrogenase. *Nature*, 520(7548):571–574, 2015.

[83] Lindsey A Flanagan and Alison Parkin. Electrochemical insights into the mechanism of nife membrane-bound hydrogenases. *Biochemical Society Transactions*, 44(1):315–328, 2016.

[84] Petra Kellers, Maria-Eirini Pandelia, Leslie J Currell, Helmut Gorner, and Wolfgang Lubitz. Ftir study on the light sensitivity of the [nife] hydrogenase from desulfovibrio vulgaris miyazaki f: Ni–c to ni–l photoconversion, kinetics of proton rebinding and h/d isotope effect. *Physical Chemistry Chemical Physics*, 11(39):8680–8683, 2009.

[85] Hulin Tai, Koji Nishikawa, Seiya Inoue, Yoshiki Higuchi, and Shun Hirota. Ft-ir characterization of the light-induced ni-l2 and ni-l3 states of [nife] hydrogenase from desulfovibrio vulgaris miyazaki f. *The Journal of Physical Chemistry B*, 119(43):13668–13674, 2015.

[86] Milagros Medina, Ruth Williams, Richard Cammack, and E Claude Hatchikian. Studies of light-induced nickel epr signals in desulfovibrio gigas hydrogenase. *Journal of the Chemical Society, Faraday Transactions*, 90(19):2921–2924, 1994.

[87] Sten O Nilsson Lill and Per EM Siegbahn. An autocatalytic mechanism for nife-hydrogenase: reduction to ni (i) followed by oxidative addition. *Biochemistry*, 48(5):1056–1066, 2009.

[88] DW Smith and RJP Williams. The spectra of ferric haems and haemoproteins. In *Structure and Bonding*, pages 1–45. Springer, 1970.

[89] Albrecht Messerschmidt. *Handbook of metalloproteins*. Wiley, 2001.

[90] Philip A Anfinrud, Manho Lim, and Timothy A Jackson. Femtosecond ir spectroscopy: methods and applications to protein dynamics. In *OE/LASE'94*, pages 107–115. International Society for Optics and Photonics, 1994.

[91] Philipp Kukura, David W McCamant, and Richard A Mathies. Femtosecond stimulated raman spectroscopy. *Annu. Rev. Phys. Chem.*, 58:461–488, 2007.

[92] Friedrich Siebert and Peter Hildebrandt. *Vibrational spectroscopy in life science*. John Wiley & Sons, 2008.

[93] Martin A Green and Mark J Keevers. Optical properties of intrinsic silicon at 300 k. *Progress in Photovoltaics: Research and Applications*, 3(3):189–192, 1995.

[94] HH Li. Refractive index of silicon and germanium and its wavelength and temperature derivatives. *Journal of Physical and Chemical Reference Data*, 9(3):561–658, 1980.

[95] HH Li. Refractive index of zns, znse, and znte and its wavelength and temperature derivatives. *Journal of physical and chemical reference data*, 13(1):103–150, 1984.

[96] Joan C Sauerwein and Geraldine R Dalton. *Standard Reference Data Publications, 1964-1984*, volume 708. Office of Standard Reference Data, National Bureau of Standards, 1985.

[97] RA Synowicki. Spectroscopic ellipsometry characterization of indium tin oxide film microstructure and optical constants. *Thin Solid Films*, 313:394–397, 1998.

[98] E Shanthi, V Dutta, A Banerjee, and KL Chopra. Electrical and optical properties of undoped and antimony-doped tin oxide films. *Journal of Applied Physics*, 51(12):6243–6251, 1980.

[99] A Hartstein, JR Kirtley, and JC Tsang. Enhancement of the infrared absorption from molecular monolayers with thin metal overlayers. *Physical Review Letters*, 45(3):201, 1980.

[100] M. Osawa and M. Ikeda. Surface-enhanced infrared absorption of p-nitrobenzoic acid deposited on silver island films: contributions of electromagnetic and chemical mechanisms. *The Journal of Physical Chemistry*, 95(24):9914–9919, 1991.

[101] J.M. Chalmers and P.R. Griffiths. *Handbook of vibrational spectroscopy*, volume 3. Wiley New York, 2002.

[102] Nattawadee Wisitruangsakul, Ingo Zebger, Khoa H Ly, Daniel H Murgida, Sanong Ekgasit, and Peter Hildebrandt. Redox-linked protein dynamics of cytochrome c probed by time-resolved surface enhanced infrared absorption spectroscopy. *Physical chemistry chemical physics*, 10(34):5276–5286, 2008.

[103] Kenichi Ataka and Joachim Heberle. Functional vibrational spectroscopy of a cytochrome c monolayer: Seidas probes the interaction with different surface-modified electrodes. *Journal of the American Chemical Society*, 126(30):9445–9457, 2004.

[104] Kenichi Ataka, Frank Giess, Wolfgang Knoll, Renate Naumann, Sabina Haber-Pohlmeier, Bjorn Richter, and Joachim Heberle. Oriented attachment and membrane reconstitution of his-tagged cytochrome c oxidase to a gold electrode: in situ monitoring by surface-enhanced infrared absorption spectroscopy. *Journal of the American Chemical Society*, 126(49):16199–16206, 2004.

[105] Xiue Jiang, Martin Engelhard, Kenichi Ataka, and Joachim Heberle. Molecular impact of the membrane potential on the regulatory mechanism of proton transfer in sensory rhodopsin ii. *Journal of the American Chemical Society*, 132(31):10808–10815, 2010.

[106] Jacek Kozuch, Conrad Weichbrodt, Diego Millo, Karin Giller, Stefan Becker, Peter Hildebrandt, and Claudia Steinem. Voltage-dependent structural changes of the membrane-bound anion channel hvdac1 probed by seira and electrochemical impedance spectroscopy. *Physical Chemistry Chemical Physics*, 16(20):9546–9555, 2014.

[107] Oscar Gutierrez-Sanz, Marta Marques, Ines AC Pereira, Antonio L De Lacey, Wolfgang Lubitz, and Olaf Rudiger. Orientation and function of a membrane-bound enzyme monitored by electrochemical surface-enhanced infrared absorption spectroscopy. *The Journal of Physical Chemistry Letters*, 4(17):2794–2798, 2013.

[108] Swantje Wiebalck, Jacek Kozuch, Enrico Forbrig, C Christoph Tzschucke, Lars JC Jeuken, and Peter Hildebrandt. Monitoring the transmembrane proton gradient generated by cytochrome bo 3 in tethered bilayer lipid membranes using seira spectroscopy. *The Journal of Physical Chemistry B*, 120(9):2249–2256, 2016.

[109] Xiue Jiang, Anne Zuber, Joachim Heberle, and Kenichi Ataka. In situ monitoring of the orientated assembly of strep-tagged membrane proteins on the gold surface by surface enhanced infrared absorption spectroscopy. *Physical Chemistry Chemical Physics*, 10(42):6381–6387, 2008.

[110] A. Wokaun, JP Gordon, and PF Liao. Radiation damping in surface-enhanced Raman scattering. *Physical Review Letters*, 48(14):957–960, 1982.

[111] S.L. McCall, P.M. Platzman, and P.A. Wolff. Surface enhanced Raman scattering. *Physics Letters A*, 77(5):381–383, 1980.

[112] O. Osawa. Surface-enhanced infrared absorption spectroscopy. *John Wiley & Sons Ltd,*, 2002.

[113] G.T. Merklin and P.R. Griffiths. Influence of chemical interactions on the surface-enhanced infrared absorption spectrometry of nitrophenols on copper and silver films. *Langmuir*, 13(23):6159–6163, 1997.

[114] Andreas Barth and Christian Zscherp. What vibrations tell about proteins. *Quarterly reviews of biophysics*, 35(04):369–430, 2002.

[115] Andreas Barth. Infrared spectroscopy of proteins. *Biochimica et Biophysica Acta (BBA)-Bioenergetics*, 1767(9):1073–1101, 2007.

[116] Jacek Artur Kozuch. *Structure-function relationships of membrane proteins-spectroelectrochemical investigation of artificial membranes*. PhD thesis, Universitätsbibliothek der Technischen Universität Berlin, 2012.

[117] A. Volbeda and J.C. Fontecilla-Camps. The active site and catalytic mechanism of nife hydrogenases. *Dalton Transactions*, (21):4030–4038, 2003.

[118] C. Fichtner, C. Laurich, E. Bothe, and W. Lubitz. Spectroelectrochemical characterization of the [nife] hydrogenase of desulfovibrio vulgaris miyazaki f. *Biochemistry*, 45(32):9706–9716, 2006.

[119] A.L. De Lacey, V.M. Fernandez, M. Rousset, C. Cavazza, and C.E. Hatchikian. Spectroscopic and kinetic characterization of active site mutants of desulfovibrio fructosovorans ni-fe hydrogenase. *Journal of Biological Inorganic Chemistry*, 8(1):129–134, 2003.

[120] M. Saggu, M. Ludwig, B. Friedrich, P. Hildebrandt, R. Bittl, F. Lendzian, O. Lenz, and I. Zebger. Impact of amino acid substitutions near the catalytic site on the spectral properties of an o2-tolerant membrane-bound [nife] hydrogenase. *ChemPhysChem*, 11(6):1215–1224, 2010.

[121] Antonio J Pierik, Winfried Roseboom, Randolph P Happe, Kimberly A Bagley, and Simon PJ Albracht. Carbon monoxide and cyanide as intrinsic ligands to iron in the active site of [nife]-hydrogenases nife (cn) 2co, biologys way to activate h2. *Journal of Biological Chemistry*, 274(6):3331–3337, 1999.

[122] Gregory J Exarhos and Xiao-Dong Zhou. Discovery-based design of transparent conducting oxide films. *Thin solid films*, 515(18):7025–7052, 2007.

[123] KL Chopra, S Major, and DK Pandya. Transparent conductors - a status review. *Thin solid films*, 102(1):1–46, 1983.

[124] Peter P Edwards, Adrian Porch, Martin O Jones, David Vernon Morgan, and R Marc Perks. Basic materials physics of transparent conducting oxides. *Dalton Transactions*, (19):2995–3002, 2004.

[125] K. Badeker. Ueber die elektrische leitfaehigkeit und die thermoelektrische kraft einiger schwermetallverbindungen. *Annalen der Physik*, 327(4):749–766, 1907.

[126] G Haacke. Transparent conducting coatings. *Annual Review of Materials Science*, 7(1):73–93, 1977.

[127] Sebastian C Dixon, David O Scanlon, Claire J Carmalt, and Ivan P Parkin. n-type doped transparent conducting binary oxides: an overview. *Journal of Materials Chemistry C*, 4(29):6946–6961, 2016.

[128] Klaus Ellmer. Past achievements and future challenges in the development of optically transparent electrodes. *Nature Photonics*, 6(12):809–817, 2012.

[129] Katarzyna Skorupska, Mohammed Aggour, Michael Kanis, Michael Lublow, Helmut Jungblut, and Joachim J Lewerenz Hans. Electrochemically induced self-organized nanostructures on silicon for realization of a novel nanoemitter solar cell concept. *ECS Transactions*, 2(20):1–9, 2007.

[130] S Shanthi, C Subramanian, and P Ramasamy. Growth and characterization of antimony doped tin oxide thin films. *Journal of Crystal Growth*, 197(4):858–864, 1999.

[131] Tadatsugu Minami. Transparent conducting oxide semiconductors for transparent electrodes. *Semiconductor Science and Technology*, 20(4):S35, 2005.

[132] Sangwook Lee, Jun Hong Noh, Shin-Tae Bae, In-Sun Cho, Jin Young Kim, Hyunho Shin, Jung-Kun Lee, Hyun Suk Jung, and Kug Sun Hong. Indium- tin- oxide-based transparent conducting layers for highly efficient photovoltaic devices. *The Journal of Physical Chemistry C*, 113(17):7443–7447, 2009.

[133] NG Patel, PD Patel, and VS Vaishnav. Indium tin oxide (ito) thin film gas sensor for detection of methanol at room temperature. *Sensors and Actuators B: Chemical*, 96(1):180–189, 2003.

[134] Stefano Frasca, Till von Graberg, Jiu-Ju Feng, Arne Thomas, Bernd M Smarsly, Inez M Weidinger, Frieder W Scheller, Peter Hildebrandt, and Ulla Wollenberger. Mesoporous indium tin oxide as a novel platform for bioelectronics. *ChemCatChem*, 2(7):839–845, 2010.

[135] Yilmaz Aksu, Stefano Frasca, Ulla Wollenberger, Matthias Driess, and Arne Thomas. A molecular precursor approach to tunable porous tin-rich indium tin oxide with durable high electrical conductivity for bioelectronic devices. *Chemistry of Materials*, 23(7):1798–1804, 2011.

[136] Jizhong Song and Haibo Zeng. Transparent electrodes printed with nanocrystal inks for flexible smart devices. *Angewandte Chemie International Edition*, 54(34):9760–9774, 2015.

[137] Yuankun Zhu, Rueben J Mendelsberg, Jiaqi Zhu, Jiecai Han, and Andre Anders. Transparent and conductive indium doped cadmium oxide thin films prepared by pulsed filtered cathodic arc deposition. *Applied Surface Science*, 265:738–744, 2013.

[138] Yude Wang, Torsten Brezesinski, Markus Antonietti, and Bernd Smarsly. Ordered mesoporous sb-, nb-, and ta-doped sno2 thin films with adjustable doping levels and high electrical conductivity. *Acs Nano*, 3(6):1373–1378, 2009.

[139] Vesna Mueller, Matthias Rasp, Jiri Rathousky, Benedikt Schutz, Markus Niederberger, and Dina Fattakhova-Rohlfing. Transparent conducting films of antimony-doped tin oxide with uniform mesostructure assembled from preformed nanocrystals. *Small*, 6(5):633–637, 2010.

[140] Michael Veith, Sven Hill, and Volker Huch. Synthese und charakterisierung von iniii–snii-halogenido-alkoxiden und von indiumtri-tert-butoxid. *Zeitschrift für anorganische und allgemeine Chemie*, 627(7):1495–1504, 2001.

[141] Michael Veith. Molecular precursors for (nano) materials - a one step strategy. *Journal of the Chemical Society, Dalton Transactions*, (12):2405–2412, 2002.

[142] M Veith, C Bubel, and M Zimmer. A novel precursor system and its application to produce tin doped indium oxide. *Dalton Transactions*, 40(22):6028–6032, 2011.

[143] Yilmaz Aksu and Matthias Driess. A low-temperature molecular approach to highly conductive tin-rich indium tin oxide thin films with durable electro-optical performance. *Angewandte Chemie International Edition*, 48(42):7778–7782, 2009.

[144] Kerim Samedov, Yilmaz Aksu, and Matthias Driess. Facile molecular approach to transparent thin-film field-effect transistors with high-performance using new homo-and heteroleptic indium (iii)–tin (ii) single-source precursors. *Chemistry of Materials*, 24(11):2078–2090, 2012.

[145] Michael Veith and Klaus Kunze. On the differing lewis basicity of ini compared with snii in molecular indium-tin and thallium-tin alkoxides. *Angewandte Chemie International Edition in English*, 30(1):95–97, 1991.

[146] Amandine Guiet, Tobias Reier, Nina Heidary, Diana Felkel, Benjamin Johnson, Ulla Vainio, Helmut Schlaad, Yilmaz Aksu, Matthias Driess, Peter Strasser, et al. A one-pot approach to mesoporous metal oxide ultrathin film electrodes bearing one metal nanoparticle per pore with enhanced electrocatalytic properties. *Chemistry of Materials*, 25(23):4645–4652, 2013.

[147] Amandine Guiet, Caren Gobel, Katharina Klingan, Michael Lublow, Tobias Reier, Ulla Vainio, Ralph Kraehnert, Helmut Schlaad, Peter Strasser, Ivelina Zaharieva, et al. Hydrophobic nanoreactor soft-templating: A supramolecular approach to yolk@ shell materials. *Advanced Functional Materials*, 25(39):6228–6240, 2015.

[148] Amandine Guiet. *Hydrophobic Nanoreactor Templating for Nanostructured Metal-Tin-rich ITO Materials*. PhD thesis, TU Berlin, 2014.

[149] B Stjerna, E Olsson, and CG Granqvist. Optical and electrical properties of radio frequency sputtered tin oxide films doped with oxygen vacancies, f, sb, or mo. *Journal of Applied Physics*, 76(6):3797–3817, 1994.

[150] Ivar Hamberg, J Stefan EM Svensson, Tord S Eriksson, Claes-Goran Granqvist, Per Arrenius, and Fredrik Norin. Radiative cooling and frost formation on surfaces with different thermal emittance: theoretical analysis and practical experience. *Applied optics*, 26(11):2131–2136, 1987.

[151] TD Senguttuvan and LK Malhotra. Sol gel deposition of pure and antimony doped tin dioxide thin films by non alkoxide precursors. *Thin Solid Films*, 289(1):22–28, 1996.

[152] S Jager, B Szyszka, J Szczyrbowski, and G Brauer. Comparison of transparent conductive oxide thin films prepared by ac and dc reactive magnetron sputtering. *Surface and coatings technology*, 98(1):1304–1314, 1998.

[153] E Kh Shokr. Optimization of the electrical and optical properties of sb-sn-o thin films. *Semiconductor science and technology*, 15(3):247, 2000.

[154] C Terrier, JP Chatelon, and JA Roger. Electrical and optical properties of sb: Sno 2 thin films obtained by the sol-gel method. *Thin solid films*, 295(1):95–100, 1997.

[155] MIB Bernardi, LE Soledade, IA Santos, ER Leite, Elson Longo, and Jose Arana Varela. Influence of the concentration of sb 2 o 3 and the viscosity of the precursor solution on the electrical and optical properties of sno 2 thin films produced by the pechini method. *Thin Solid Films*, 405(1):228–233, 2002.

[156] F Javier Yusta et al. Cvd preparation and characterization of tin dioxide films for electrochemical applications. *Journal of Materials Chemistry*, 7(8):1421–1427, 1997.

[157] Stefano Frasca, Anabel Molero Milan, Amandine Guiet, Caren Goebel, Fernando Perez-Caballero, Konstanze Stiba, Silke Leimkuhler, Anna Fischer, and Ulla Wollenberger. Bioelectrocatalysis at mesoporous antimony doped tin oxide electrodes - electrochemical characterization and direct enzyme communication. *Electrochimica Acta*, 110:172–180, 2013.

[158] Antonio Facchetti and Tobin Marks. *Transparent electronics: from synthesis to applications*. John Wiley & Sons, 2010.

[159] Christopher P Smith and Henry S White. Theory of the interfacial potential distribution and reversible voltammetric response of electrodes coated with electroactive molecular films. *Analytical chemistry*, 64(20):2398–2405, 1992.

[160] Lucia Becucci, Ivan Guryanov, Flavio Maran, Federica Scaletti, and Rolando Guidelli. A procedure for estimating the surface dipole potential of monolayers adsorbed on electrodes. *Soft Matter*, 8(33):8601–8607, 2012.

[161] Giulietta Smulevich and Thomas G Spiro. Surface enhanced raman spectroscopic evidence that adsorption on silver particles can denature heme proteins. *The Journal of Physical Chemistry*, 89(24):5168–5173, 1985.

[162] Frank Schreiber. Self-assembled monolayers: from simplemodel systems to biofunctionalized interfaces. *Journal of Physics: Condensed Matter*, 16(28):R881, 2004.

[163] J Christopher Love, Lara A Estroff, Jennah K Kriebel, Ralph G Nuzzo, and George M Whitesides. Self-assembled monolayers of thiolates on metals as a form of nanotechnology. *Chemical reviews*, 105(4):1103–1170, 2005.

[164] Johannes G Vos, Robert J Forster, and Tia E Keyes. *Interfacial supramolecular assemblies*. John Wiley & Sons, 2003.

[165] Daniel H Murgida and Peter Hildebrandt. Electron-transfer processes of cytochrome c at interfaces. new insights by surface-enhanced resonance raman spectroscopy. *Accounts of chemical research*, 37(11):854–861, 2004.

[166] Daniel H Murgida and Peter Hildebrandt. Redox and redox-coupled processes of heme proteins and enzymes at electrochemical interfaces. *Physical chemistry chemical physics*, 7(22):3773–3784, 2005.

[167] Hongjun Yue, D Khoshtariya, DH Waldeck, J Grochol, P Hildebrandt, and DH Murgida. On the electron transfer mechanism between cytochrome c and metal electrodes. evidence for dynamic control at short distances. *The Journal of Physical Chemistry B*, 110(40):19906–19913, 2006.

[168] Valentin Radu, Stefan Frielingsdorf, Stephen D Evans, Oliver Lenz, and Lars JC Jeuken. Enhanced oxygen-tolerance of the full heterotrimeric membrane-bound [nife]-hydrogenase of ralstonia eutropha. *Journal of the American Chemical Society*, 136(24):8512–8515, 2014.

[169] Jacek Kozuch, Claudia Steinem, Peter Hildebrandt, and Diego Millo. Combined electrochemistry and surface-enhanced infrared absorption spectroscopy of gramicidin a incorporated into tethered bilayer lipid membranes. *Angewandte Chemie International Edition*, 51(32):8114–8117, 2012.

[170] Daniel K Schwartz. Mechanisms and kinetics of self-assembled monolayer formation. *Annual Review of Physical Chemistry*, 52(1):107–137, 2001.

[171] Debasis Samanta and Amitabha Sarkar. Immobilization of bio-macromolecules on self-assembled monolayers: methods and sensor applications. *Chemical Society Reviews*, 40(5):2567–2592, 2011.

[172] H Gerischer. Electrochemical behavior of semiconductors under illumination. *Journal of the Electrochemical Society*, 113(11):1174–1182, 1966.

[173] Rüdiger Memming and Detlef Bahnemann. *Semiconductor electrochemistry*. John Wiley & Sons, 2015.

[174] C. Leger, S.J. Elliott, K.R. Hoke, L.J.C. Jeuken, A.K. Jones, and F.A. Armstrong. Enzyme electrokinetics: Using protein film voltammetry to investigate redox enzymes and their mechanisms. *Biochemistry*, 42(29):8653–8662, 2003.

[175] Patrick C Hallenbeck and John R Benemann. Biological hydrogen production; fundamentals and limiting processes. *International Journal of Hydrogen Energy*, 27(11):1185–1193, 2002.

[176] Fraser A Armstrong, Natalie A Belsey, James A Cracknell, Gabrielle Goldet, Alison Parkin, Erwin Reisner, Kylie A Vincent, and Annemarie F Wait. Dynamic electrochemical investigations of hydrogen oxidation and production by enzymes and implications for future technology. *Chemical Society Reviews*, 38(1):36–51, 2009.

[177] Chelsea L McIntosh, Frauke Germer, Ruediger Schulz, Jens Appel, and Anne K Jones. The [nife]-hydrogenase of the cyanobacterium synechocystis sp. pcc 6803 works bidirectionally with a bias to h2 production. *Journal of the American Chemical Society*, 133(29):11308–11319, 2011.

[178] Y Martin, Clayton C Williams, and H Kumar Wickramasinghe. Atomic force microscope–force mapping and profiling on a sub 100-å scale. *Journal of Applied Physics*, 61(10):4723–4729, 1987.

[179] Gerhard Meyer and Nabil M Amer. Erratum: Novel optical approach to atomic force microscopy[appl. phys. lett. 53, 1045(1988)]. *Applied Physics Letters*, 53(24):2400, 1988.

[180] U Durig, JK Gimzewski, and DW Pohl. Experimental observation of forces acting during scanning tunneling microscopy. *Physical review letters*, 57(19):2403, 1986.

[181] Rufus Lumry, Emil L Smith, and Ruby R Glantz. Kinetics of carboxypeptidase action. i. effect of various extrinsic factors on kinetic parameters1. *Journal of the American Chemical Society*, 73(9):4330–4340, 1951.

[182] Johannes Fritsch, Simone Loescher, Oliver Sanganas, Elisabeth Siebert, Ingo Zebger, Matthias Stein, Marcus Ludwig, Antonio L De Lacey, Holger Dau, Baerbel Friedrich, et al. [nife] and [fes] cofactors in the membrane-bound hydrogenase of ralstonia eutropha investigated by x-ray absorption spectroscopy: insights into o2-tolerant h2 cleavage. *Biochemistry*, 50(26):5858–5869, 2011.

[183] W Brent R Pollock, Federico I Rosell, Mark B Twitchett, Mark E Dumont, and A Grant Mauk. Bacterial expression of a mitochondrial cytochrome c. trimethylation of lys72 in yeast iso-1-cytochrome c and the alkaline conformational transition. *Biochemistry*, 37(17):6124–6131, 1998.

[184] Rachel B Kapust, Jozsef Tozser, Terry D Copeland, and David S Waugh. The p1 specificity of tobacco etch virus protease. *Biochemical and biophysical research communications*, 294(5):949–955, 2002.

[185] Hiroto Miyake, Shen Ye, and Masatoshi Osawa. Electroless deposition of gold thin films on silicon for surface-enhanced infrared spectroelectrochemistry. *Electrochemistry Communications*, 4(12):973–977, 2002.

[186] Urs Oesch and Jiri Janata. Electrochemical study of gold electrodes with anodic oxide films - formation and reduction behaviour of anodic oxides on gold. *Electrochimica Acta*, 28(9):1237–1246, 1983.

[187] S Trasatti and OA Petrii. Real surface area measurements in electrochemistry. *Pure and applied chemistry*, 63(5):711–734, 1991.

[188] Paulette M Vignais. H/d exchange reactions and mechanistic aspects of the hydrogenases. *Coordination chemistry reviews*, 249(15):1677–1690, 2005.

[189] AT Yahiro, SM Lee, and DO Kimble. Bioelectrochemistry: I. enzyme utilizing bio-fuel cell studies. *Biochimica et Biophysica Acta (BBA)-Specialized Section on Biophysical Subjects*, 88(2):375–383, 1964.

[190] Paul W King. Designing interfaces of hydrogenase–nanomaterial hybrids for efficient solar conversion. *Biochimica et Biophysica Acta (BBA)-Bioenergetics*, 1827(8):949–957, 2013.

[191] Christophe Leger, Sean J Elliott, Kevin R Hoke, Lars JC Jeuken, Anne K Jones, and Fraser A Armstrong. Enzyme electrokinetics: using protein film voltammetry to investigate redox enzymes and their mechanisms. *Biochemistry*, 42(29):8653–8662, 2003.

[192] Elisabeth Lojou. Hydrogenases as catalysts for fuel cells: strategies for efficient immobilization at electrode interfaces. *Electrochimica Acta*, 56(28):10385–10397, 2011.

[193] Anne Volbeda, Patricia Amara, Claudine Darnault, Jean-Marie Mouesca, Alison Parkin, Maxie M Roessler, Fraser A Armstrong, and Juan C Fontecilla-Camps. X-ray crystallographic and computational studies of the o2-tolerant [nife]-hydrogenase 1 from escherichia coli. *Proceedings of the National Academy of Sciences*, 109(14):5305–5310, 2012.

[194] Yasuhito Shomura, Ki-Seok Yoon, Hirofumi Nishihara, and Yoshiki Higuchi. Structural basis for a [lsqb] 4fe-3s [rsqb] cluster in the oxygen-tolerant membrane-bound [lsqb] nife [rsqb]-hydrogenase. *Nature*, 479(7372):253–256, 2011.

[195] Kylie A Vincent, James A Cracknell, Jeremy R Clark, Marcus Ludwig, Oliver Lenz, Baerbel Friedrich, and Fraser A Armstrong. Electricity from low-level h 2 in still air–an ultimate test for an oxygen tolerant hydrogenase. *Chemical communications*, (48):5033–5035, 2006.

[196] Annemarie F Wait, Alison Parkin, Gregory M Morley, Luciano dos Santos, and Fraser A Armstrong. Characteristics of enzyme-based hydrogen fuel cells using an oxygen-tolerant hydrogenase as the anodic catalyst. *The Journal of Physical Chemistry C*, 114(27):12003–12009, 2010.

[197] Sadagopan Krishnan and Fraser A Armstrong. Order-of-magnitude enhancement of an enzymatic hydrogen-air fuel cell based on pyrenyl carbon nanostructures. *Chemical Science*, 3(4):1015–1023, 2012.

[198] S Calabrese Barton. Enzyme catalysis in biological fuel cells. *Handbook of Fuel Cells*, 2010.

[199] Jingdong Zhang, Alexander M Kuznetsov, Igor G Medvedev, Qijin Chi, Tim Albrecht, Palle S Jensen, and Jens Ulstrup. Single-molecule electron transfer in electrochemical environments. *Chemical reviews*, 108(7):2737–2791, 2008.

[200] Elena E Ferapontova, Sergey Shleev, Tautgirdas Ruzgas, Leonard Stoica, Andreas Christenson, Jan Tkac, Alexander I Yaropolov, and Lo Gorton. Direct electrochemistry of proteins and enzymes. *Perspectives in bioanalysis*, 1:517–598, 2005.

[201] Nicolas Plumeré, Olaf Rüdiger, Alaa Alsheikh Oughli, Rhodri Williams, Jeevanthi Vivekananthan, Sascha Pöller, Wolfgang Schuhmann, and Wolfgang Lubitz. A redox hydrogel protects hydrogenase from high-potential deactivation and oxygen damage. *Nature chemistry*, 6(9):822–827, 2014.

[202] E Lojou, X Luo, M Brugna, N Candoni, S Dementin, and MT Giudici-Orticoni. Biocatalysts for fuel cells: efficient hydrogenase orientation for h2 oxidation at electrodes modified with carbon nanotubes. *JBIC Journal of Biological Inorganic Chemistry*, 13(7):1157–1167, 2008.

[203] Murat Sezer, Stefan Frielingsdorf, Diego Millo, Nina Heidary, Tillman Utesch, Maria-Andrea Mroginski, Baerbel Friedrich, Peter Hildebrandt, Ingo Zebger, and Inez M Weidinger. Role of the hoxz subunit in the electron transfer pathway of the membrane-bound [nife]-hydrogenase from ralstonia eutropha immobilized on electrodes. *The Journal of Physical Chemistry B*, 115(34):10368–10374, 2011.

[204] Elisabeth Siebert, Yvonne Rippers, Stefan Frielingsdorf, Johannes Fritsch, Andrea Schmidt, Jacqueline Kalms, Sagie Katz, Oliver Lenz, Patrick Scheerer, Lars Paasche, et al. Resonance raman spectroscopic analysis of the [nife] active site and the proximal [4fe-3s]

cluster of an o2-tolerant membrane-bound hydrogenase in the crystalline state. *The Journal of Physical Chemistry B*, 119(43):13785–13796, 2015.

[205] K.A. Vincent, A. Parkin, O. Lenz, S.P.J. Albracht, J.C. Fontecilla-Camps, R. Cammack, B. Friedrich, and F.A. Armstrong. Electrochemical definitions of o2 sensitivity and oxidative inactivation in hydrogenases. *Journal of the American Chemical Society*, 127(51):18179–18189, 2005.

[206] Christopher C Page, Christopher C Moser, Xiaoxi Chen, and P Leslie Dutton. Natural engineering principles of electron tunnelling in biological oxidation–reduction. *Nature*, 402(6757):47–52, 1999.

[207] James A Cracknell, Kylie A Vincent, and Fraser A Armstrong. Enzymes as working or inspirational electrocatalysts for fuel cells and electrolysis. *Chemical Reviews*, 108(7):2439–2461, 2008.

[208] Tillmann Utesch, Diego Millo, Maria Ana Castro, Peter Hildebrandt, Ingo Zebger, and Maria Andrea Mroginski. Effect of the protonation degree of a self-assembled monolayer on the immobilization dynamics of a [nife] hydrogenase. *Langmuir*, 29(2):673–682, 2013.

[209] Diego Millo, Maria-Eirini Pandelia, Tillmann Utesch, Nattawadee Wisitruangsakul, Maria A Mroginski, Wolfgang Lubitz, Peter Hildebrandt, and Ingo Zebger. Spectroelectrochemical study of the [nife] hydrogenase from desulfovibrio vulgaris miyazaki f in solution and immobilized on biocompatible gold surfaces. *The Journal of Physical Chemistry B*, 113(46):15344–15351, 2009.

[210] Yvonne Rippers, Tillmann Utesch, Peter Hildebrandt, Ingo Zebger, and Maria Andrea Mroginski. Insights into the structure of the active site of the o 2-tolerant membrane bound [nife] hydrogenase of r. eutropha h16 by molecular modelling. *Physical Chemistry Chemical Physics*, 13(36):16146–16149, 2011.

[211] Francesco Oteri, Alexandre Ciaccafava, Anne De Poulpiquet, Marc Baaden, Elisabeth Lojou, and Sophie Sacquin-Mora. The weak, fluctuating, dipole moment of membrane-bound hydrogenase from aquifex aeolicus accounts for its adaptability to charged electrodes. *Physical Chemistry Chemical Physics*, 16(23):11318–11322, 2014.

[212] Duncan GG McMillan, Sophie J Marritt, Gemma L Kemp, Piers Gordon-Brown, Julea N Butt, and Lars JC Jeuken. The impact of enzyme orientation and electrode topology on the catalytic activity of adsorbed redox enzymes. *Electrochimica acta*, 110:79–85, 2013.

[213] Christophe Leger and Patrick Bertrand. Direct electrochemistry of redox enzymes as a tool for mechanistic studies. *Chemical reviews*, 108(7):2379–2438, 2008.

[214] P Zuo, T Albrecht, PD Barker, DH Murgida, and P Hildebrandt. Interfacial redox processes of cytochrome b 562. *Physical Chemistry Chemical Physics*, 11(34):7430–7436, 2009.

[215] Waldemar A Marmisolle, Daiana A Capdevila, Ezequiel de la Llave, Federico J Williams, and Daniel H Murgida. Self-assembled monolayers of nh2-terminated thiolates: Order, p k a, and specific adsorption. *Langmuir*, 29(17):5351–5359, 2013.

[216] Tesfaye Hailu Degefa, Peter Schön, Dirk Bongard, and Lorenz Walder. Elucidation of the electron transfer mechanism of marker ions at sams with charged head groups. *Journal of Electroanalytical Chemistry*, 574(1):49–62, 2004.

[217] Jianwei Zhao, Liqiang Luo, Xiurong Yang, Erkang Wang, and Shaojun Dong. Determination of surface pka of sam using an electrochemical titration method. *Electroanalysis*, 11(15):1108–1113, 1999.

[218] Mark A Bryant and Richard M Crooks. Determination of surface pka values of surface-confined molecules derivatized with ph-sensitive pendant groups. *Langmuir*, 9(2):385–387, 1993.

[219] Colin D Bain and George M Whitesides. A study by contact angle of the acid-base behavior of monolayers containing. omega.-mercaptocarboxylic acids adsorbed on gold: an example of reactive spreading. *Langmuir*, 5(6):1370–1378, 1989.

[220] Li Sun, Larry J Kepley, and Richard M Crooks. Molecular interactions between organized, surface-confined monolayers and vapor-phase probe molecules: Hydrogen-bonding interactions. *Langmuir*, 8(9):2101–2103, 1992.

[221] http://webclu.bio.wzw.tum.de/stride/

[222] http://swift.cmbi.ru.nl/gv/dssp/

[223] Jonas Schartner, Joern Gueldenhaupt, Bastian Mei, Matthias Roegner, Martin Muhler, Klaus Gerwert, and Carsten Koetting. Universal method for protein immobilization on chemically functionalized germanium investigated by atr-ftir difference spectroscopy. *Journal of the American Chemical Society*, 135(10):4079–4087, 2013.

[224] Elisabeth Siebert. *Vibrational Spectroscopy of the Active Site and Iron Sulfur Clusters of the Membrane Bound Hydrogenase from Ralstonia Eutropha*. PhD thesis, TU Berlin, 2015.

[225] C Hinnen, Roger Parsons, and Katsumi Niki. Electrochemical and spectroreflectance studies of the adsorbed horse heart cytochrome c and cytochrome c 3 from d. vulgaris, miyazaki strain, at gold electrode. *Journal of Electroanalytical Chemistry and Interfacial Electrochemistry*, 147(1):329–337, 1983.

[226] David E Reed and Fred M Hawkridge. Direct electron transfer reactions of cytochrome c at silver electrodes. *Analytical chemistry*, 59(19):2334–2339, 1987.

[227] Fraser A Armstrong. Probing metalloproteins by voltammetry. In *Bioinorganic chemistry*, pages 137–221. Springer, 1990.

[228] Robert A Latour. Molecular simulation of protein-surface interactions: Benefits, problems, solutions, and future directions (review). *Biointerphases*, 3(3):FC2–FC12, 2008.

[229] M Ozboyaci, DB Kokh, and RC Wade. Three steps to gold: mechanism of protein adsorption revealed by brownian and molecular dynamics simulations. *Physical Chemistry Chemical Physics*, 18(15):10191–10200, 2016.

[230] Nina Heidary, Tillmann Utesch, Maximilian Zerball, Marius Horch, Diego Millo, Johannes Fritsch, Oliver Lenz, Regine von Klitzing, Peter Hildebrandt, Anna Fischer, et al. Orientation-controlled electrocatalytic efficiency of an adsorbed oxygen-tolerant hydrogenase. *PloS one*, 10(11):e0143101, 2015.

[231] Daniel H Murgida and Peter Hildebrandt. Heterogeneous electron transfer of cytochrome c on coated silver electrodes. electric field effects on structure and redox potential. *The Journal of Physical Chemistry B*, 105(8):1578–1586, 2001.

[232] N. Wisitruangsakul. *Signal Enhancement of Infrared spectrum by surface enhanced infrared absorption spectroscopy.* PhD thesis, Technical University Berlin, 2008.

[233] Wesley Crowell Sanders. *Examining the Effects of Applied Potential on the Surface Charge of Functionalized Monolayers for Site-Directed Ionic Self Assembly.* PhD thesis, Virginia Polytechnic Institute and State University, 2008.

[234] Pablo Ramírez, Rafael Andreu, Ángel Cuesta, Carmen J Calzado, and Juan José Calvente. Determination of the potential of zero charge of au (111) modified with thiol monolayers. *Analytical chemistry*, 79(17):6473–6479, 2007.

[235] Derek Marsh, Martin Müller, and Franz-Josef Schmitt. Orientation of the infrared transition moments for an α-helix. *Biophysical journal*, 78(5):2499–2510, 2000.

[236] Adam J Healy, Philip A Ash, Oliver Lenz, and Kylie A Vincent. Attenuated total reflectance infrared spectroelectrochemistry at a carbon particle electrode; unmediated redox control of a [nife]-hydrogenase solution. *Physical Chemistry Chemical Physics*, 15(19):7055–7059, 2013.

[237] Alexey Silakov, Christina Kamp, Eduard Reijerse, Thomas Happe, and Wolfgang Lubitz. Spectroelectrochemical characterization of the active site of the [fefe] hydrogenase hyda1 from chlamydomonas reinhardtii. *Biochemistry*, 48(33):7780–7786, 2009.

[238] Kenichi Ataka, Sven Timo Stripp, and Joachim Heberle. Surface-enhanced infrared absorption spectroscopy (seiras) to probe monolayers of membrane proteins. *Biochimica et Biophysica Acta (BBA)-Biomembranes*, 1828(10):2283–2293, 2013.

[239] Murat Sezer, Diego Millo, Inez M Weidinger, Ingo Zebger, and Peter Hildebrandt. Analyzing the catalytic processes of immobilized redox enzymes by vibrational spectroscopies. *IUBMB life*, 64(6):455–464, 2012.

[240] J. Fritsch, S. Loescher, O. Sanganas, E. Siebert, I. Zebger, M. Stein, M. Ludwig, A. De Lacey, H. Dau, B.I. Friedrich, O. Lenz, and M. Haumann. [nife] and [fes] cofactors in the membrane-bound hydrogenase of ralstonia eutropha investigated by x-ray absorption spectroscopy: Insights into o2-tolerant h2 cleavage. *Biochemistry*, 2011.

[241] Abdelkader Zebda, Chantal Gondran, Alan Le Goff, Michael Holzinger, Philippe Cinquin, and Serge Cosnier. Mediatorless high-power glucose biofuel cells based on compressed carbon nanotube-enzyme electrodes. *Nature communications*, 2:370, 2011.

[242] Abbas Abou Hamdan, Pierre-Pol Liebgott, Vincent Fourmond, Oscar Gutiérrez-Sanz, Antonio L De Lacey, Pascale Infossi, Marc Rousset, Sébastien Dementin, and Christophe Léger. Relation between anaerobic inactivation and oxygen tolerance in a large series of nife hydrogenase mutants. *Proceedings of the National Academy of Sciences*, 109(49):19916–19921, 2012.

[243] Lars Lauterbach and Oliver Lenz. Catalytic production of hydrogen peroxide and water by oxygen-tolerant [nife]-hydrogenase during h2 cycling in the presence of o2. *Journal of the American Chemical Society*, 135(47):17897–17905, 2013.

[244] Marta Carepo, David L Tierney, Carlos D Brondino, Tran Chin Yang, Ana Pamplona, Joshua Telser, Isabel Moura, José JG Moura, and Brian M Hoffman. 17o endor detection of a solvent-derived ni-(oh x)-fe bridge that is lost upon activation of the hydrogenase from desulfovibrio gigas. *Journal of the American Chemical Society*, 124(2):281–286, 2002.

[245] Abbas Abou Hamdan, Bénédicte Burlat, Oscar Gutiérrez-Sanz, Pierre-Pol Liebgott, Carole Baffert, Antonio L De Lacey, Marc Rousset, Bruno Guigliarelli, Christophe Léger, and Sébastien Dementin. O2-independent formation of the inactive states of nife hydrogenase. *Nature chemical biology*, 9(1):15–17, 2013.

[246] Fraser A Armstrong, Rhiannon M Evans, Suzannah V Hexter, Bonnie J Murphy, Maxie M Roessler, and Philip Wulff. Guiding principles of hydrogenase catalysis instigated and clarified by protein film electrochemistry. *Accounts of chemical research*, 49(5):884–892, 2016.

[247] Masaru Kato, Jenny Z Zhang, Nicholas Paul, and Erwin Reisner. Protein film photoelectrochemistry of the water oxidation enzyme photosystem ii. *Chemical Society Reviews*, 43(18):6485–6497, 2014.

[248] DS Ghosh, L Martinez, S Giurgola, P Vergani, and V Pruneri. Widely transparent electrodes based on ultrathin metals. *Optics letters*, 34(3):325–327, 2009.

[249] Alexander Böker and Patrick van Rijn. *Bio-synthetic Hybrid Materials and Bionanoparticles: A Biological Chemical Approach Towards Material Science*. Number 16. Royal Society of Chemistry, 2015.

[250] Itamar Willner and Eugenii Katz. *Bioelectronics: from theory to applications*. John Wiley & Sons, 2006.

[251] Anna Reynal, Fezile Lakadamyali, Manuela A Gross, Erwin Reisner, and James R Durrant. Parameters affecting electron transfer dynamics from semiconductors to molecular catalysts for the photochemical reduction of protons. *Energy & Environmental Science*, 6(11):3291–3300, 2013.

[252] Nicholas D Spencer. *Tailoring surfaces: modifying surface composition and structure for applications in tribology, biology and catalysis*, volume 5. World scientific, 2011.

[253] P Hubert Mutin, Gilles Guerrero, and André Vioux. Hybrid materials from organophosphorus coupling molecules. *Journal of Materials Chemistry*, 15(35-36):3761–3768, 2005.

[254] Yu Tai Tao. Structural comparison of self-assembled monolayers of n-alkanoic acids on the surfaces of silver, copper, and aluminum. *Journal of the American Chemical Society*, 115(10):4350–4358, 1993.

[255] C Garcia Nunez, M Sachsenhauser, B Blashcke, A Garcia Marin, Jose A Garrido, and Jose L Pau. Effects of hydroxylation and silanization on the surface properties of zno nanowires. *ACS applied materials & interfaces*, 7(9):5331–5337, 2015.

[256] Michael Brumbach and Neal R Armstrong. Modification of transparent conducting oxide (tco) electrodes through silanization and chemisorption of small molecules. *Encyclopedia of Electrochemistry*, 2007.

[257] Marcos Pita, Cristina Gutierrez-Sanchez, David Olea, Marisela Velez, Cristina Garcia-Diego, Sergey Shleev, Victor M Fernandez, and Antonio L De Lacey. High redox potential cathode based on laccase covalently attached to gold electrode. *The Journal of Physical Chemistry C*, 115(27):13420–13428, 2011.

[258] Vesna Mueller, Jiri Rathousky, and Dina Fattakhova-Rohlfing. Covalent immobilization of redox protein within the mesopores of transparent conducting electrodes. *Electrochimica Acta*, 116:1–8, 2014.

[259] Emmanuel Topoglidis, Colin J Campbell, Anthony EG Cass, and James R Durrant. Factors that affect protein adsorption on nanostructured titania films. a novel spectroelectrochemical application to sensing. *Langmuir*, 17(25):7899–7906, 2001.

[260] Patrick Kwan, Dominik Schmitt, Alex M Volosin, Chelsea L McIntosh, Dong-Kyun Seo, and Anne K Jones. Spectroelectrochemistry of cytochrome c and azurin immobilized in nanoporous antimony-doped tin oxide. *Chemical Communications*, 47(45):12367–12369, 2011.

[261] E McCafferty and JP Wightman. Determination of the concentration of surface hydroxyl groups on metal oxide films by a quantitative xps method. *Surface and Interface Analysis*, 26(8):549–564, 1998.

[262] Sophie J Marritt, Gemma L Kemp, Li Xiaoe, James R Durrant, Myles R Cheesman, and Julea N Butt. Spectroelectrochemical characterization of a pentaheme cytochrome in solution and as electrocatalytically active films on nanocrystalline metal-oxide electrodes. *Journal of the American Chemical Society*, 130(27):8588–8589, 2008.

[263] Emmanuel Topoglidis, Thierry Lutz, Richard L Willis, Christopher J Barnett, Anthony EG Cass, and James R Durrant. Protein adsorption on nanoporous tio 2 films: a novel approach to studying photoinduced protein/electrode transfer reactions. *Faraday discussions*, 116:35–46, 2000.

[264] Emmanuel Topoglidis, Thierry Lutz, James R Durrant, and Emilio Palomares. Interfacial electron transfer on cytochrome-c sensitised conformally coated mesoporous tio 2 films. *Bioelectrochemistry*, 74(1):142–148, 2008.

[265] Hainer Wackerbarth and Peter Hildebrandt. Redox and conformational equilibria and dynamics of cytochrome c at high electric fields. *ChemPhysChem*, 4(7):714–724, 2003.

[266] Arthur Lesk. *Introduction to protein science: architecture, function, and genomics*. Oxford university press, 2010.

[267] Kazuhiro Nakanishi, Takaharu Sakiyama, and Koreyoshi Imamura. On the adsorption of proteins on solid surfaces, a common but very complicated phenomenon. *Journal of Bioscience and Bioengineering*, 91(3):233–244, 2001.

[268] James L Willit and Edmond F Bowden. Adsorption and redox thermodynamics of strongly adsorbed cytochrome c on tin oxide electrodes. *Journal of Physical Chemistry*, 94(21):8241–8246, 1990.

[269] Christian Herrero, Annamaria Quaranta, Winfried Leibl, A William Rutherford, and Ally Aukauloo. Artificial photosynthetic systems. using light and water to provide electrons and protons for the synthesis of a fuel. *Energy & Environmental Science*, 4(7):2353–2365, 2011.

[270] Erwin Reisner, Daniel J Powell, Christine Cavazza, Juan C Fontecilla-Camps, and Fraser A Armstrong. Visible light-driven h2 production by hydrogenases attached to dye-sensitized tio2 nanoparticles. *Journal of the American Chemical Society*, 131(51):18457–18466, 2009.

[271] Z Ghorannevis, E Akbarnejad, and M Ghoranneviss. Structural and morphological properties of ito thin films grown by magnetron sputtering. *Journal of Theoretical and Applied Physics*, 9(4):285–290, 2015.

[272] Eric Arsenault, Navid Soheilnia, and Geoffrey A Ozin. Periodic macroporous nanocrystalline antimony-doped tin oxide electrode. *Acs Nano*, 5(4):2984–2988, 2011.

[273] Li Luo, Deniz Bozyigit, Vanessa Wood, and Markus Niederberger. High-quality transparent electrodes spin-cast from preformed antimony-doped tin oxide nanocrystals for thin film optoelectronics. *Chemistry of Materials*, 25(24):4901–4907, 2013.

[274] Vesna Mueller, Matthias Rasp, Goran Setefanic, Jianhua Ba, Sebastian Guenther, Jiri Rathousky, Markus Niederberger, and Dina Fattakhova-Rohlfing. Highly conducting nanosized monodispersed antimony-doped tin oxide particles synthesized via nonaqueous sol-gel procedure. *Chemistry of materials*, 21(21):5229–5236, 2009.

[275] Samuel Krimm and Jagdeesh Bandekar. Vibrational spectroscopy and conformation of peptides, polypeptides, and proteins. *Advances in protein chemistry*, 38:181–364, 1986.

[276] Heino Susi and D Michael Byler. [13] resolution-enhanced fourier transform infrared spectroscopy of enzymes. *Methods in enzymology*, 130:290–311, 1986.

[277] Richard J Sundberg and R Bruce Martin. Interactions of histidine and other imidazole derivatives with transition metal ions in chemical and biological systems. *Chemical Reviews*, 74(4):471–517, 1974.

[278] Yubing Xie. *The Nanobiotechnology Handbook*. CRC Press, 2012.

[279] Seraphine V Wegner and Joachim P Spatz. Cobalt (iii) as a stable and inert mediator ion between nta and his6-tagged proteins. *Angewandte Chemie International Edition*, 52(29):7593–7596, 2013.

[280] Sho-hei Fujishima, Hiroshi Nonaka, Sho-hei Uchinomiya, Yoshiyuki Alex Kawase, Akio Ojida, and Itaru Hamachi. Design of a multinuclear zn (ii) complex as a new molecular probe for fluorescence imaging of his-tag fused proteins. *Chemical Communications*, 48(4):594–596, 2012.

[281] Katsumi Niki, W Reef Hardy, Michael G Hill, H Li, James R Sprinkle, Emanuel Margoliash, Kyoko Fujita, Ryutaro Tanimura, Nobufumi Nakamura, Hiroyuki Ohno, et al.

Coupling to lysine-13 promotes electron tunneling through carboxylate-terminated alkanethiol self-assembled monolayers to cytochrome c. *The Journal of Physical Chemistry B*, 107(37):9947–9949, 2003.

[282] Aichun Dong, Ping Huang, and Winslow S Caughey. Protein secondary structures in water from second-derivative amide i infrared spectra. *Biochemistry*, 29(13):3303–3308, 1990.

[283] Julia F Calvert, Jennifer L Hill, and Aichun Dong. Redox-dependent conformational changes are common structural features of cytochrome c from various species. *Archives of biochemistry and biophysics*, 346(2):287–293, 1997.

[284] Masaru Kato, Tanai Cardona, A William Rutherford, and Erwin Reisner. Covalent immobilization of oriented photosystem ii on a nanostructured electrode for solar water oxidation. *Journal of the American Chemical Society*, 135(29):10610–10613, 2013.

[285] Masaru Kato, Tanai Cardona, A William Rutherford, and Erwin Reisner. Photoelectrochemical water oxidation with photosystem ii integrated in a mesoporous indium–tin oxide electrode. *Journal of the American Chemical Society*, 134(20):8332–8335, 2012.

[286] Delphine Schaming, Christophe Renault, Ryan T Tucker, Stephanie Lau-Truong, Jean Aubard, Michael J Brett, Veronique Balland, and Benot Limoges. Spectroelectrochemical characterization of small hemoproteins adsorbed within nanostructured mesoporous ito electrodes. *Langmuir*, 28(39):14065–14072, 2012.

[287] Xiaoxi Chen, Rosaria Ferrigno, Jerry Yang, and George M Whitesides. Redox properties of cytochrome c adsorbed on self-assembled monolayers: a probe for protein conformation and orientation. *Langmuir*, 18(18):7009–7015, 2002.

[288] E Margoliash and OF Walasek. [61] cytochrome c from vertebrate and invertebrate sources. *Methods in enzymology*, 10:339–348, 1967.

[289] R Bruce Martin. Pyrrole hydrogen ionization of imidazole derivatives in metal ion complexes and carbonic anhydrase. *Proceedings of the National Academy of Sciences*, 71(11):4346–4347, 1974.

[290] Craig R Johnson, Rex E Shepherd, Bonnie Marr, Stephen O'Donnell, and Walter Dressick. Affinities of imidazolate and imidazole ligands for pentacyanoiron (iii). *Journal of the American Chemical Society*, 102(20):6227–6235, 1980.

[291] Eric Victor, Sunghee Kim, and Stephen J Lippard. Synthesis of bis (imidazole) metal complexes and their use in rapid no detection and quantification devices. *Inorganic chemistry*, 53(24):12809–12821, 2014.

[292] Diane A Blake, Pampa Chakrabarti, Mehraban Khosraviani, Frank M Hatcher, Connie M Westhoff, Peter Goebel, Dwane E Wylie, and Robert C Blake. Metal binding properties of a monoclonal antibody directed toward metal-chelate complexes. *Journal of Biological Chemistry*, 271(44):27677–27685, 1996.

[293] Samantha J Dammer, Pavlo V Solntsev, Jared R Sabin, and Victor N Nemykin. Synthesis, characterization, and electron-transfer processes in indium ferrocenyl-containing porphyrins and their fullerene adducts. *Inorganic chemistry*, 52(16):9496–9510, 2013.

[294] JM Barbe, C Ratti, P Richard, C Lecomte, R Gerardin, and R Guilard. Tin (ii) porphyrins: synthesis and spectroscopic properties of a series of divalent tin porphyrins. x-ray crystal structure of (2, 3, 7, 8, 12, 13, 17, 18-octaethylprophinato) tin (ii). *Inorganic chemistry*, 29(20):4126–4130, 1990.

[295] James M Harrington, Karen A Oscarson, S Bart Jones, Joseph H Reibenspies, Libero J Bartolotti, and Robert D Hancock. The affinity of indium (iii) for nitrogen-donor ligands in aqueous solution. a study of the complexing of indium (iii) with polyamines by differential pulse voltammetry, density functional theory, and crystallography. *Zeitschrift für Naturforschung B*, 62(3):386–396, 2007.

[296] N De Zoubov, C Vanleugenhaghe, M Pourbaix, and M Pourbaix Copper. Atlas of electrochemical equilibria in aqueous solutions. *Pergamon Press, New York*, 1966.

[297] Alberto Mendez, Elisabeth Bosch, Martı Roses, and Uwe D Neue. Comparison of the acidity of residual silanol groups in several liquid chromatography columns. *Journal of Chromatography A*, 986(1):33–44, 2003.

[298] Howard Reiss. Photocharacteristics for electrolyte-semiconductor junctions. *Journal of The Electrochemical Society*, 125(6):937–949, 1978.

[299] Andreas Bachmeier, Vincent CC Wang, Thomas W Woolerton, Sophie Bell, Juan C Fontecilla-Camps, Mehmet Can, Stephen W Ragsdale, Yatendra S Chaudhary, and Fraser A Armstrong. How light-harvesting semiconductors can alter the bias of reversible electrocatalysts in favor of h2 production and co2 reduction. *Journal of the American Chemical Society*, 135(40):15026–15032, 2013.

[300] Drazenka Svedruzic, Jeffrey L Blackburn, Robert C Tenent, John-David R Rocha, Todd B Vinzant, Michael J Heben, and Paul W King. High-performance hydrogen production and oxidation electrodes with hydrogenase supported on metallic single-wall carbonnanotube networks. *Journal of the American Chemical Society*, 133(12):4299–4306, 2011.

[301] Cristina Gutierrez-Sanchez, Alexandre Ciaccafava, Pierre Yves Blanchard, Karen Monsalve, Marie Thérèse Giudici-Orticoni, Sophie Lecomte, and Elisabeth Lojou. Efficiency of enzymatic o2 reduction by myrothecium verrucaria bilirubin oxidase probed by surface plasmon resonance, pmirras, and electrochemistry. *ACS Catalysis*, 6(8):5482–5492, 2016.

[302] Maria-Eirini Pandelia, Wolfgang Nitschke, Pascale Infossi, Marie-Thérèse Giudici-Orticoni, Eckhard Bill, and Wolfgang Lubitz. Characterization of a unique [fes] cluster in the electron transfer chain of the oxygen tolerant [nife] hydrogenase from aquifex aeolicus. *Proceedings of the National Academy of Sciences*, 108(15):6097–6102, 2011.

[303] Bonnie J Murphy, Frank Sargent, and Fraser A Armstrong. Transforming an oxygen-tolerant [nife] uptake hydrogenase into a proficient, reversible hydrogen producer. *Energy & Environmental Science*, 7(4):1426–1433, 2014.

[304] Jesse D Benck, Blaise A Pinaud, Yelena Gorlin, and Thomas F Jaramillo. Substrate selection for fundamental studies of electrocatalysts and photoelectrodes: inert potential windows in acidic, neutral, and basic electrolyte. *PloS one*, 9(10):e107942, 2014.

[305] Yvonne Gassenbauer, Robert Schafranek, Andreas Klein, Spiros Zafeiratos, Michael Hävecker, Axel Knop-Gericke, and Robert Schlögl. Surface states, surface potentials, and segregation at surfaces of tin-doped in 2 o 3. *Physical Review B*, 73(24):245312, 2006.

[306] Yongsup Park, V Choong, Yongli Gao, Bing R Hsieh, and Ching Wan Tang. Work function of indium tin oxide transparent conductor measured by photoelectron spectroscopy. *Applied Physics Letters*, 68(19):2699–2701, 1996.

[307] R Schlaf, H Murata, and ZH Kafafi. Work function measurements on indium tin oxide films. *Journal of Electron Spectroscopy and Related Phenomena*, 120(1):149–154, 2001.

[308] Scott H Brewer and Stefan Franzen. Calculation of the electronic and optical properties of indium tin oxide by density functional theory. *Chemical Physics*, 300(1):285–293, 2004.

[309] Fezile Lakadamyali, Anna Reynal, Masaru Kato, James R Durrant, and Erwin Reisner. Electron transfer in dye-sensitised semiconductors modified with molecular cobalt catalysts: Photoreduction of aqueous protons. *Chemistry–A European Journal*, 18(48):15464–15475, 2012.

[310] Haoshuang Gu, Zhao Wang, and Yongming Hu. Hydrogen gas sensors based on semiconductor oxide nanostructures. *Sensors*, 12(5):5517–5550, 2012.

[311] John A Chaney and Pehr E Pehrsson. Work function changes and surface chemistry of oxygen, hydrogen, and carbon on indium tin oxide. *Applied surface science*, 180(3):214–226, 2001.

[312] Yong Xu and Martin AA Schoonen. The absolute energy positions of conduction and valence bands of selected semiconducting minerals. *American Mineralogist*, 85(3-4):543–556, 2000.

[313] Sukon Phanichphant. Semiconductor metal oxides as hydrogen gas sensors. *Procedia Engineering*, 87:795–802, 2014.

[314] Satyendra K Mishra and Banshi D Gupta. Surface plasmon resonance-based fiber-optic hydrogen gas sensor utilizing indium–tin oxide (ito) thin films. *Plasmonics*, 7(4):627–632, 2012.

[315] Ian J McPherson and Kylie A Vincent. Electrocatalysis by hydrogenases: lessons for building bio-inspired device. *Journal of the Brazilian Chemical Society*, 25(3):427–441, 2014.

[316] J Augustyński, B Alexander, and R Solarska. Metal oxide photoanodes for water splitting. *Photocatalysis*, pages 1–38, 2011.

[317] Ting Wang and Pavle V Radovanovic. Free electron concentration in colloidal indium tin oxide nanocrystals determined by their size and structure. *The Journal of Physical Chemistry C*, 115(2):406–413, 2010.

[318] Crissy Rhodes, Stefan Franzen, Jon-Paul Maria, Mark Losego, Donovan N Leonard, Brian Laughlin, Gerd Duscher, and Stephen Weibel. Surface plasmon resonance in conducting metal oxides. *Journal of Applied Physics*, 100(5):054905, 2006.

[319] Martina Abb, Yudong Wang, Nikitas Papasimakis, CH De Groot, and Otto L Muskens. Surface-enhanced infrared spectroscopy using metal oxide plasmonic antenna arrays. *Nano letters*, 14(1):346–352, 2013.

[320] Sebastien D Lounis, Evan L Runnerstrom, Amy Bergerud, Dennis Nordlund, and Delia J Milliron. Influence of dopant distribution on the plasmonic properties of indium tin oxide nanocrystals. *Journal of the American Chemical Society*, 136(19):7110–7116, 2014.

[321] Peijun Guo, Richard D Schaller, John B Ketterson, and Robert PH Chang. Ultrafast switching of tunable infrared plasmons in indium tin oxide nanorod arrays with large absolute amplitude. *Nature Photonics*, 2016.

[322] Shi-Qiang Li, Peijun Guo, D Bruce Buchholz, Wei Zhou, Yi Hua, Teri W Odom, JB Ketterson, Leonidas E Ocola, Kazuaki Sakoda, and Robert PH Chang. Plasmonic–photonic mode coupling in indium-tin-oxide nanorod arrays. *ACS Photonics*, 1(3):163–172, 2014.

[323] Galina P Gorbenko. Structure of cytochrome c complexes with phospholipids as revealed by resonance energy transfer. *Biochimica et Biophysica Acta (BBA)-Biomembranes*, 1420(1):1–13, 1999.

Appendix A

Appendix

Appendix to Chapter 4

A4.1 Structure of the MBH heterodimer

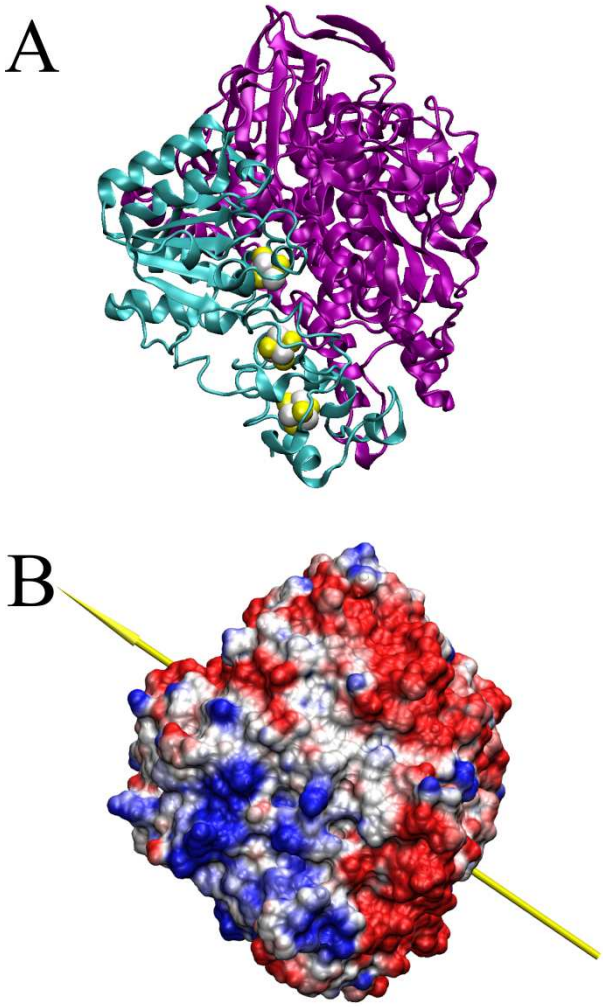

Figure A.1: Panel A shows the secondary structure of the MBH. The small and large subunits are colored in cyan and purple, respectively. Additionally, the FeS clusters are indicated as spheres. In panel B, the electrostatic potential surface calculated with the APBS tool is displayed. Red and blue indicate negatively and positively charged regions, respectively. The yellow arrow demonstrates the direction of the dipole moment of the dimer.

A4.2 Experimental series of *strep*-MBH on negatively charged SAMs of mixtures C_5COOH-SAM and C_6OH-SAM on Au electrodes.

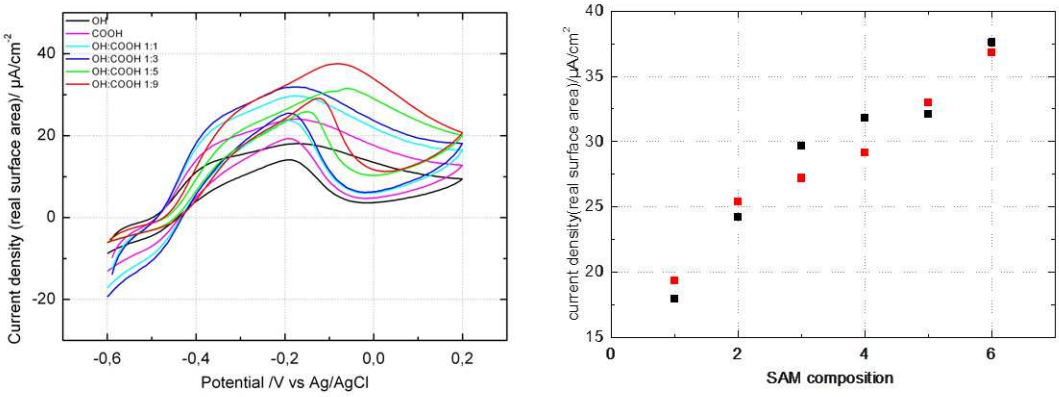

Figure A.2: Cyclic voltamogramms of *strep*-MBH in H_2 saturated 10 mM $NaPO_4$-buffer at pH 5.5, on stationary electrode; *Strep*-MBH immobilization and measurements at pH 5.5; Immobilization time 4h; Immobilization temperature at 4°C; Measurements performed at room temperature; Scan rate 5 mV/s. Experiments performed by Dr. Nastaran Ranjbar/ Strasser group.

A4.3 Time dependencies of *strep*-MBH on Au-C_5COOH/C_6OH (1:9; v:v)

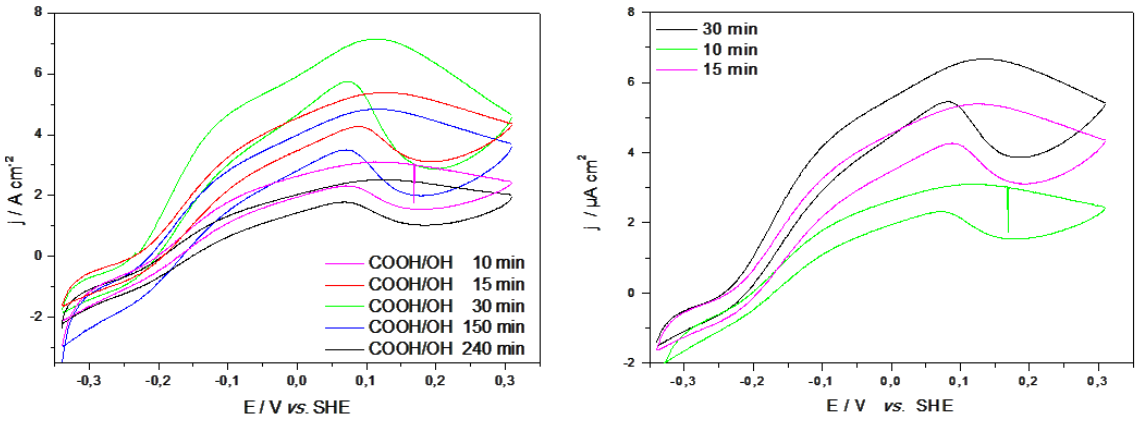

Figure A.3: First recorded cyclic voltamogramms of *strep*-MBH on Au-coated C_5COOH/C_6OH (1:9; v:v) in H_2 saturated 10 mM $NaPO_4$-buffer at pH 5.5 at varying enzyme incubation times: 10 min, 15 min, 30 min, 150 min, 240 min; on stationary Au-pen electrode; measured in two repeated experimental passages. *Strep*-MBH immobilization and measurements at pH 5.5; Immobilization temperature at 4°C; Measurements performed at room temperature; Scan rate 5mV/s.

A4.4 pH dependencies of *strep*-MBH on Au-C_5COOH

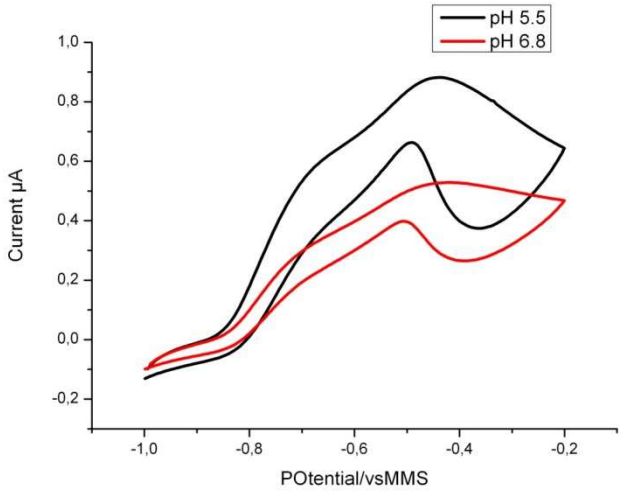

Figure A.4: Cyclic voltamogramms of *strep*-MBH on Au-C_5COOH in H_2-saturated electrolyte (10 mM phosphate buffer; pH 5.5), stationary electrode, scan rate 5 mV/s, hydrogenase immobilization in pH 5.5 10 mM buffer performed by Dr. Nastaran Ranjbar/ Strasser group/ TU Berlin.

A4.5 *Strep*-MBH immobilization essayed on various SAMs at various pHs

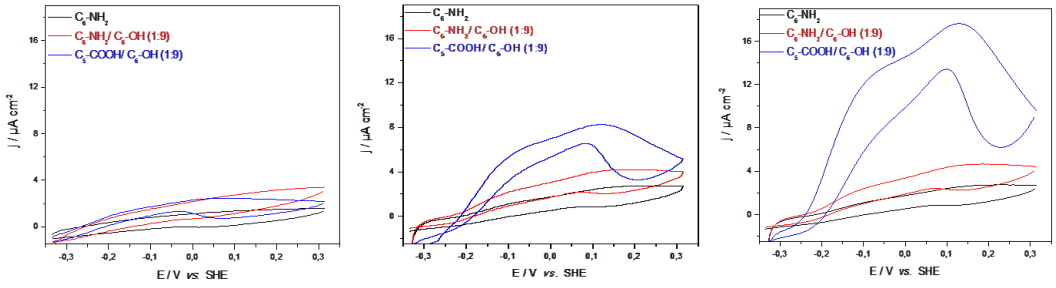

Figure A.5: Cyclic voltammograms of *strep*-MBH under H_2 atmosphere on Au-coated C_6NH_2 (black trace), C_6NH_2/C_6OH (red trace) and C_5COOH/C_6OH (blue trace) carried out in 10 mM $NaPO_4$-buffer (A) immobilization as well as measurement at pH 7 (with pre-activation at -550 mV for 5 min), (B) immobilization at pH 7, subsequent measurements performed at pH 5.5, (C) immobilization and measurement at pH 5.5. Immobilization time 30 min; Immobilization temperature was set to 4°C; Measurements performed at room temperature; Scan rate 5mV/s.

A4.6 Correlation between immobilization time and current densities for *strep*-MBH on Au-C_5COOH/C_6OH

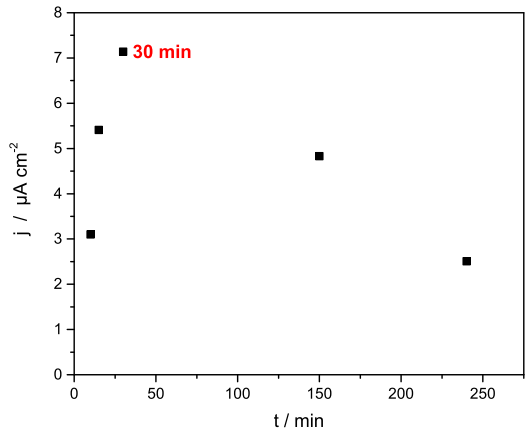

Figure A.6: Results of maximum current density efficiencies of *strep*-MBH adsorbed as a function of immobilization time on Au-C_5COOH/C_6OH (1:9; v:v). Maximum current densities evaluated each from first recorded cycle at +100mV. Immobilization in 10 mM PB buffer at pH 5.5 at 4°C; CV measurements in 10 mM PB buffer at pH 5.5 at room temperature. Evaluated from Nastaran Ranjbar's experiments.

A4.7 Electrochemical desorption of the amino-1-hexanethiol SAM

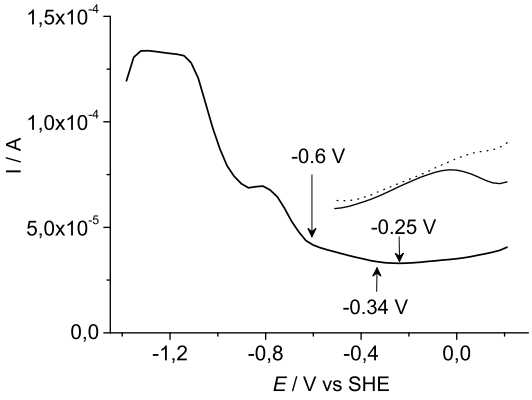

Figure A.7: Reductive desorption of the amino-1-hexanethiol SAM. The chemically modified Au electrode was subjected to an AC voltammetric sweep from +0.2 to -1.4 V in a buffered solution at pH 5.5 under Ar atmosphere. Scan rate, frequency, and potential amplitude were 50 mV s^{-1}, 100 Hz, and 4 mV, respectively. In the potential region between 0 and -0.8 V, the amplitude of the capacitive current of the electrical double layer (I) is essentially constant, and its value is about half that of the bare Au electrode, hereby used as a blank (dotted line). At poised potentials lower than -0.6 V, current increases exponentially, as expected for SAM desorption. The capacitive current measured after SAM desorption (short thick line) is twice that of the Au-SAM electrode and is similar to that of the blank (dotted line). Please note that the minimum of the AC trace at -250 mV for the SAM-coated electrodes corresponding to the point of zero charge of the system is very close to -340 mV.

A4.8 CV of methylene blue mediator on Au-SAM

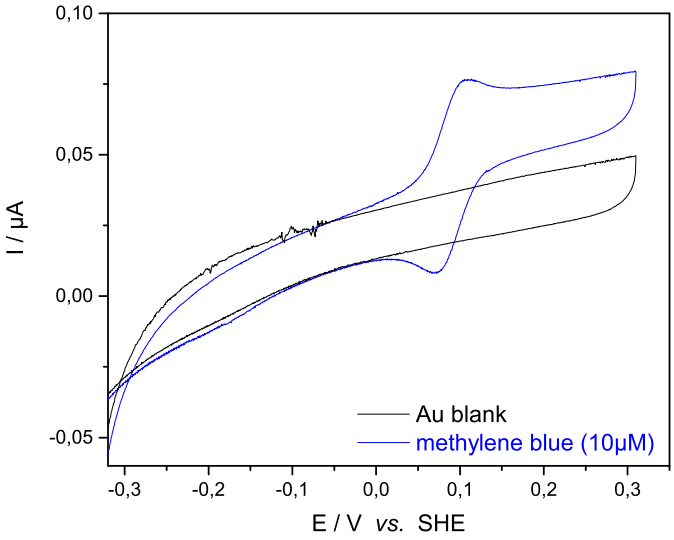

Figure A.8: CV of 10 µM methylene blue in 10 mM PB buffer at pH 5.5 on Au-C_6NH_2. Scan rate 5 mV/s.

A4.9 pKa determination of Au coated SAMs

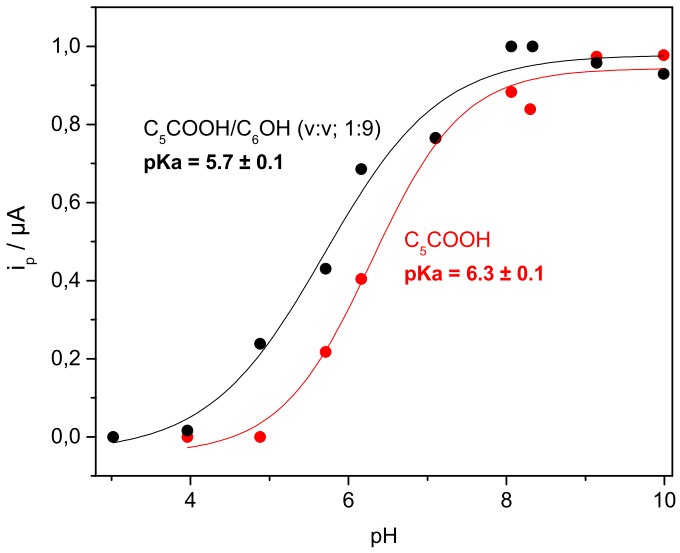

Figure A.9: pKa titration of C5COOH- and C5COOH/C6OH-SAM-coated on Au electrodes for *strep*-MBH immobilization. Surface pKa values of the SAMs were determined by the peak current (ip) of a given probe redox couple in buffers varying the pH. Experiments were carried out after protocol described by Degafa et. al performed by Dr. Maria Ana Castro / Murgida group.

A4.10 Ellipsometric Measurements

Ellipsometry has been applied to determine the thickness of the protein layer adsorbed on gold electrodes coated with an amino-terminated SAM. For the protein-coated SAM/Au/Si-prism or wafer a one-box model was assumed, in which the continuum media were air (n=1.000) and gold (n=0,144; k=3,178). The refractive index and the absorption constant of gold were determined by measuring 5 different spots on the bare gold surface. With respect to its small thickness the SAM layer could be neglected. In such way the thickness of the protein layer has been fitted. The obtained average ellipsometric angles Δ and Ψ were determined to be 100.19° and 43.29°. As thin films (<10nm) were investigated only the respective Δ values change significantly. The refractive index of the enzyme layer n was estimated to a value of 1.48. Figure FigA.10 displays changes of the ellipsometric angle Δ in dependence of the thickness with respect to the applied model.

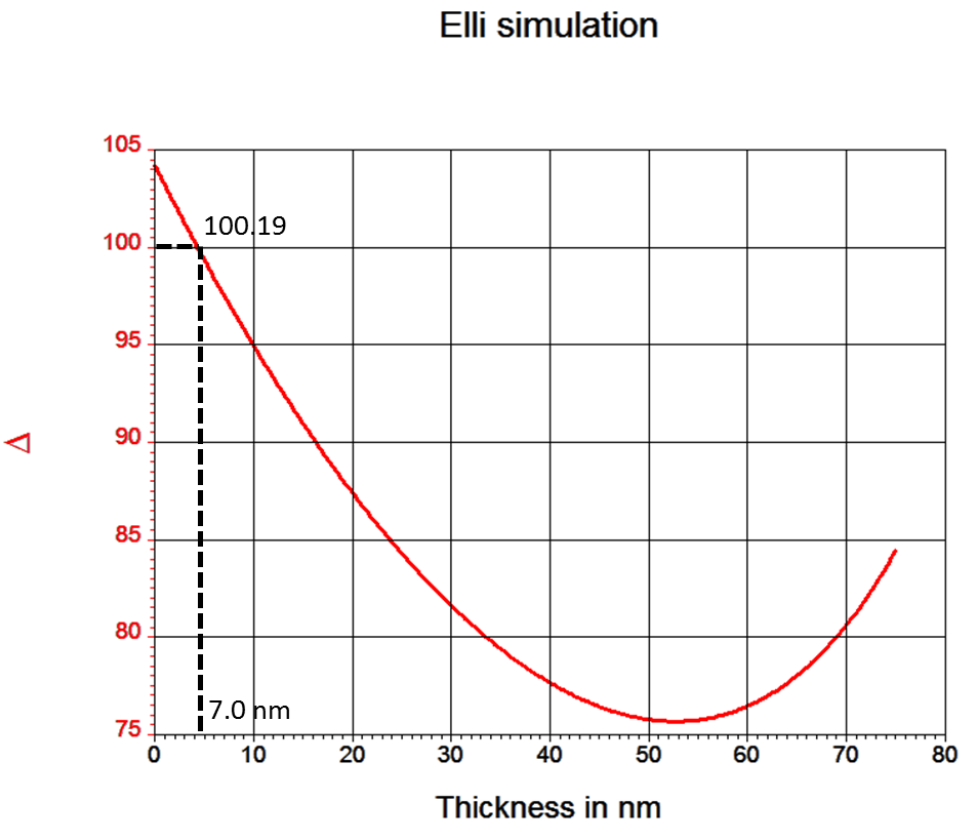

Figure A.10: Simulation of the ellipsometric angle Δ in dependence of the thickness according to the applied model. The measured average Δ value of 100.19° represents a thickness of ca. 7 nm.

A4.11 Protein Film Voltammetry of absorbed *strep*-MBH compared to the bare C_6NH_2-SAM/Au

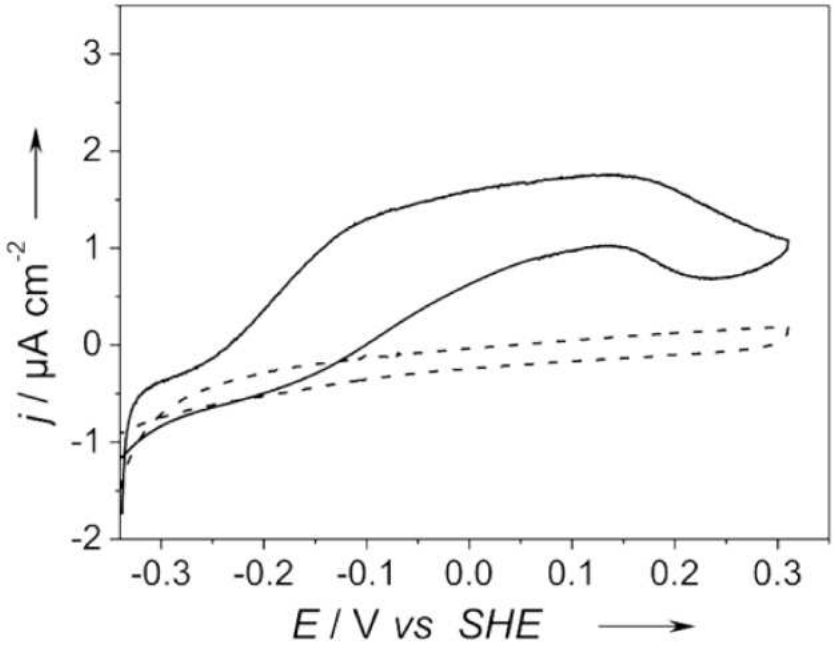

Figure A.11: Voltammetric traces of immobilized *Re* MBH on a SAM-coated Au electrode in the presence of H_2-saturated buffer (10 mM PB buffer; pH 5.5) (solid line), corresponding amino-1-hexanethiol SAM-coated Au electrode prior to immobilization (dashed line).

A4.12 Potential dependent changes of strep-MBH active site adsorbed on C_6NH_2–SAM/Au

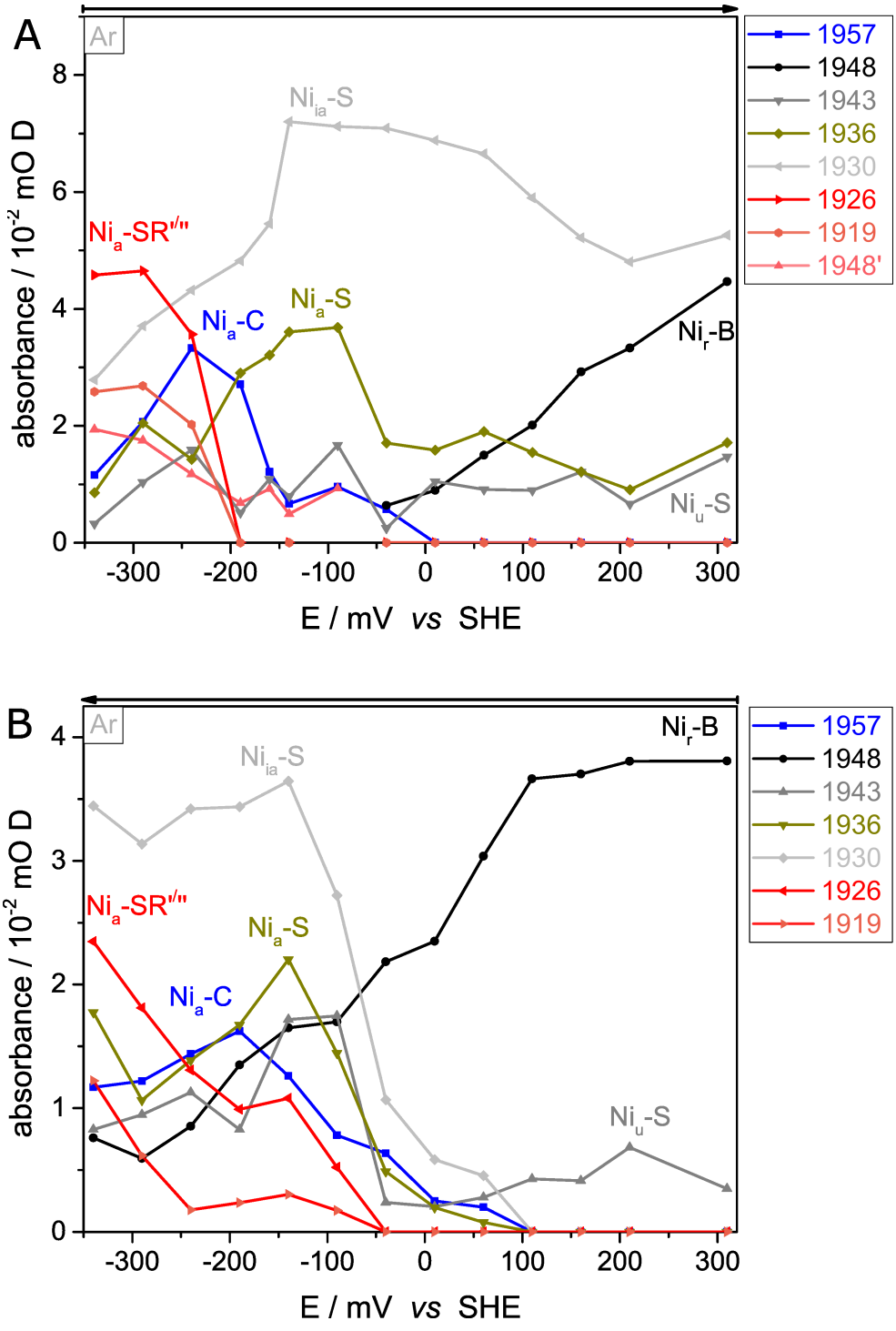

Figure A.12: Potential dependent band intensities for CO absorptions, characteristic for different states of the active site, providing thereby crude courses of various redox transitions, which were determined for two different samples of *strep*-MBH adsorbed on C_6NH_2/Au. The displayed potentials were applied stepwise until spectral equilibrium was reached; potential steps were applied from negative to positive values (A) and (B) in the reversed manner (positive to negative values). Measurements were performed in 10 mM PB solution at pH 5.5 under Ar atmosphere at 4°C.

Appendix to Chapter 6

A6.1 Time dependencies of *strep*-MBH on

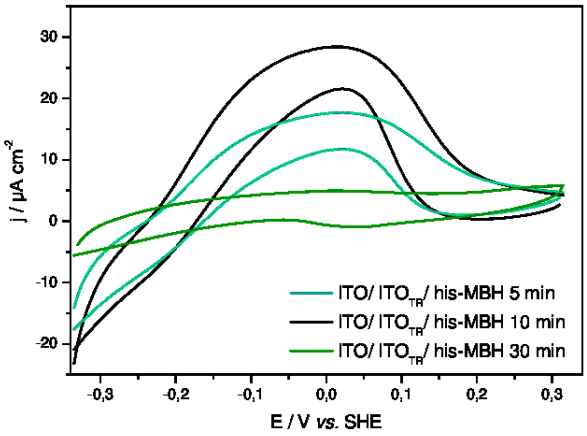

Figure A.13: First recorded cyclic voltamogramms of his-MBH on ITO_{TR}/ITO/glass in H_2 saturated 10 mM $NaPO_4$-buffer at pH 5.5. His-MBH immobilization and measurements at pH 5.5; Immobilization temperature at 4°C; Measurements performed at room temperature; Scan rate 5mV/s.

A6.2 His-MBH adsorbed on various substrate materials

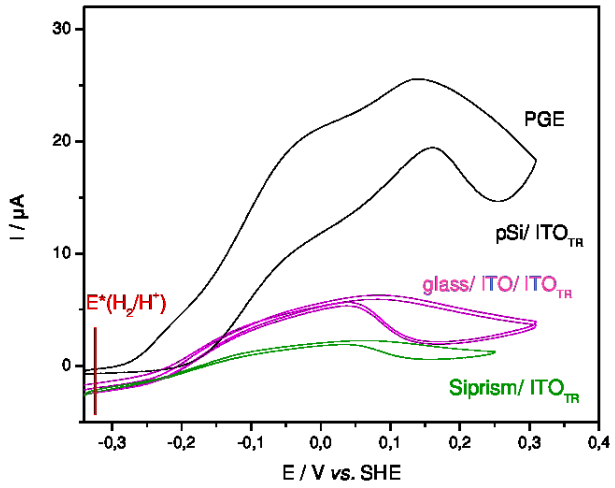

Figure A.14: First recorded cyclic voltamogramms of his-MBH on varying material electrodes: PGE, ITO_{TR}-coated on Si-prism, on p-doped Si wafer, on ITO/glass in H_2 saturated 10 mM $NaPO_4$-buffer at pH 5.5 for 10 min immobilization. His-MBH immobilization and measurements at pH 5.5; Immobilization temperature at 4°C; Measurements performed at room temperature; Scan rate 5mV/s.

A6.3 Protein Film Voltammetry of absorbed *strep*-MBH on low conductive ITO_{TR} thin films

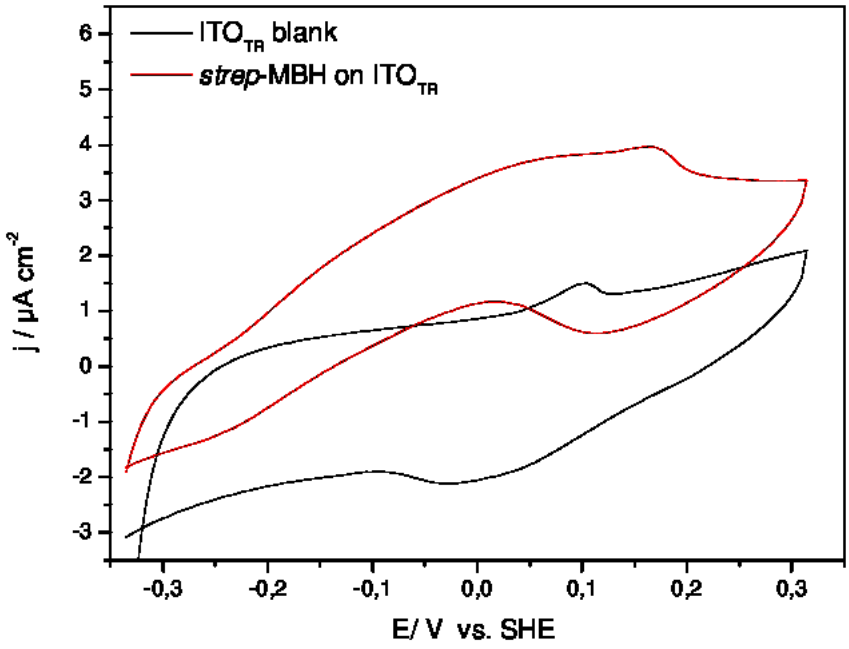

Figure A.15: CVs of low conductive ITO_{TR} thin film before (black trace) and after immobilization of *strep*-MBH (red trace).

A6.4 Mass Spectra

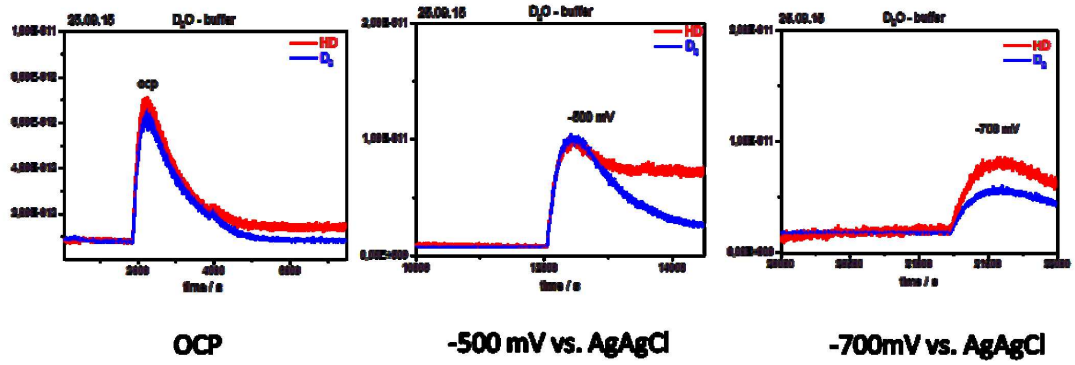

Figure A.16: Mass spectroscopic analysis of electrolyte solution (10 mM PB buffer at pH 5.5) from his-MBH adsorbed on ITO_{TR} surface after cronoamperometric treatment of 1h at (A) OCP, (B) below (-500 mV) and above (-700 mV) the standard H_2/H^+ couple (E^0=H_2/H^+ = -550 mV). All potentials are depicted vs Ag/AgCl reference electrode.

A6.5 Time dependencies of *strep*-MBH on ITO_{TR}

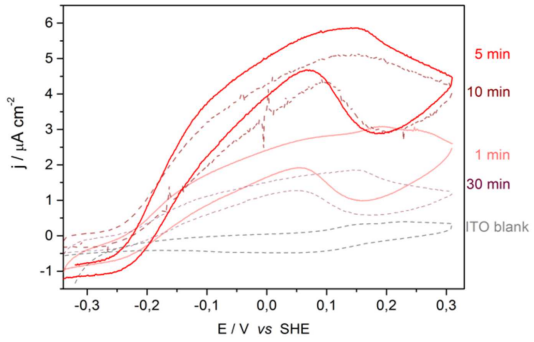

Figure A.17: CVs of blank ITO_{TR} (grey) and *strep*-MBH on ITO_{TR} upon variation of incubation time of 1, 5, 10 and 30 min with a 1 µM *strep*-MBH in a 10 mM phosphate solution at pH 5.5. ITO_{TR} exposes small and broad peaks around 0.2 V, which occur through hydroxylation of metal exposed surface. Experiments at pH 7 showed much lower DET.

Appendix to Chapter 7

A7.1 Determination of his-MBH coverage on oxidized Si-prism (SiO_x-surface)

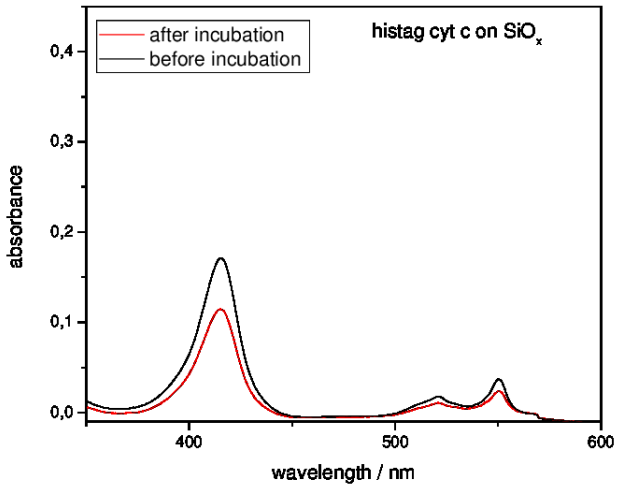

Figure A.18: UV-Vis spectra of his-cyt c solutions before (black) and after (red) 30 minutes of incubation of and SiO_x surface on Si prism for ATR-IR measurements.

A7.2 3D structures of ITO_{TR} and SnO_2 nanostructured materials

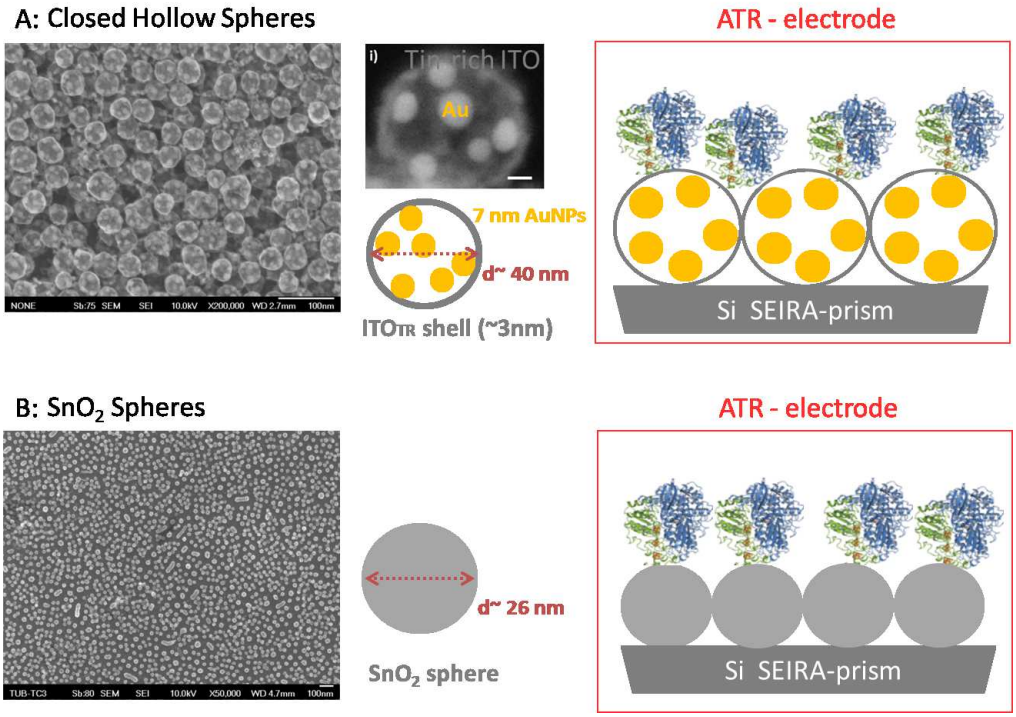

Figure A.19: SEM images and illustrations of (A) Au nanoparticle (AuNPs) - loaded ITO_{TR} closed hollow spheres and (B) submonolayer of SnO_2 spheres coated on Si prism for enzyme immobilization in ATR-IR mode.

A7.3 *Strep*-MBH immobilization on 3D structures of ITO_{TR} and SnO_2 materials

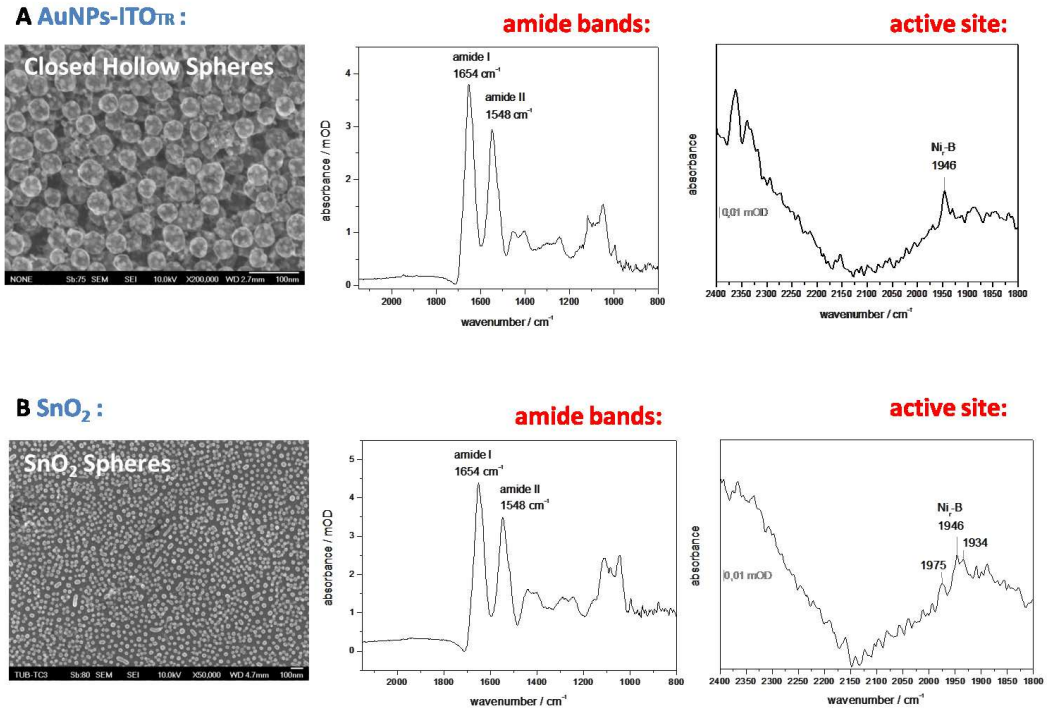

Figure A.20: SEM imags of (A) Au nanoparticle (AuNPs) - loaded ITO_{TR} closed hollow spheres and (B) submonolayer of SnO_2 spheres coated on Si prism and ATR-IR spectra of corresponding *strep*-MBH adsorption after 30 min presenting region characteristic for amide and active site.